Au-based multimetallic nanoparticles for NO direct decomposition

Taha Elgayyar

N°d'ordre NNT : 2022LYSE1084

THESE de DOCTORAT DE L'UNIVERSITE DE LYON
opérée au sein de
L'Université Claude Bernard Lyon 1

Ecole Doctorale N° 206
Ecole Doctorale de Chimie de Lyon

Spécialité de doctorat : Catalyse et Environnement
Discipline : Chimie

Soutenue publiquement le 14/06/2022, par :
Taha Elgayyar

Au-based multimetallic nanoparticles for NO direct decomposition

---

Devant le jury composé de :

EPRON, Florence Directrice de Recherche, CNRS Poitiers UMR 7285 - IC2MP	Présidente

EPRON, Florence Directrice de Recherche, CNRS Poitiers UMR 7285 - IC2MP	Rapporteure
MARCEAU, Eric Maître de Conférences, Université Lille UMR 8181 – UCCS	Rapporteur
CHRIST, Lorraine Professeure des Universités, Université Lyon 1 UMR 5256 – IRCELYON	Examinatrice
GUESMI, Hazar Chargée de Recherche, CNRS Montpellier UMR 5253 -ICG	Examinatrice
MEUNIER, Frédéric Directeur de Recherche, CNRS Lyon UMR 5256 – IRCELYON	Directeur de thèse
TUEL, Alain Directeur de Recherche, CNRS Lyon UMR 5256 – IRCELYON	Co-directeur de thèse
SCHUURMAN, Yves Directeur de Recherche, CNRS Lyon UMR 5256 – IRCELYON	Invité

Abstract

The goal of the “DecompNOx” project is the formulation of supported Au-(noble metal) bimetallic nanoalloys active for NO decomposition below 500°C. We have already published four articles presenting our results. Monometallic (Au, Pd and Pt) and bimetallic nanoparticles were prepared using several supports (SiO_2, LTA and Al_2O_3). SiO_2 and LTA-based catalysts were investigated for the deNOx activity. Alumina-based samples (previously prepared, characterized and tested for NO decomposition by my colleague Ranin ATWI) were investigated for the CO adsorption/desorption kinetics. For Pd-Au/SiO_2, the alloying enhanced and stabilized the deNOx catalytic activity of Pd, though decreased N_2 selectivity. For Pt-Au@LTA, the samples displayed deactivation under NO, possibly due to the oxidation of Pt or due to S and Cl used during the preparation. Au did not result in an activity enhancement. For Pt-Au/Al_2O_3, the alloying lead to a limited bridge adsorption (i.e. the dilution of Pt by Au) and a faster CO desorption than that over the monometallic Pt (i.e. a weaker CO adsorption on Pt). Despite the evidenced modified properties of the metals by alloying with Au, there is as till a scope to improve the deNOx catalytic activity compared to other literature reports.

Keywords: NOx, alloy, bimetallic nanoparticles, Au, Pd, Pt, XRD, CO adsorption, DRIFTS

En français :

L'objectif du projet “DecompNOx” est l’élaboration formulation de nano-alliages bimétalliques Au-(métal noble) supportés, actifs pour la décomposition du NO en dessous de 500°C. Nous avons déjà publié quatre articles présentant nos résultats. Des nanoparticules monométalliques (Au, Pd et Pt) et bimétalliques ont été préparées en utilisant des plusieurs supports (SiO_2, LTA et Al_2O_3). Les catalyseurs à base de SiO_2 et de LTA ont été étudiés pour l'activité deNOx. Les échantillons à base d'alumine (précédemment préparés, caractérisés et testé pour la décomposition du NO par ma collègue Ranin ATWI) ont été étudiés pour la cinétique d'adsorption/désorption du CO. Pour les échantillons Pd-Au/SiO_2, l'alliage a amélioré et stabilisé l'activité catalytique deNOx de Pd, bien qu'il ait diminué la sélectivité de N_2. Les échantillons Pt-Au@LTA présentaient une désactivation sous NO, peut-être due à l'oxydation du Pt ou à cause du S et Cl utilisés lors de la préparation. L’or n'a entraîné aucune amélioration de l'activité. Pour l’échantillon bimétallique Pt-Au/Al_2O_3, l'alliage a conduit à la dilution du Pt et à une désorption de CO plus rapide que celle sur Pt (une adsorption de CO plus faible sur Pt allié avec Au). Malgré les propriétés modifiées des métaux par l’alliage avec Au, il y a encore une marge pour améliorer l'activité deNOx en comparaison avec la littérature.

Mots-clés: NOx, alliage, nanoparticules, Au, Pd, Pt, DRX, CO adsorption, DRIFTS

Table of Contents

Acknowledgement

First and foremost, I am extremely grateful to my supervisors (Dr. Frédéric MEUNIER, Dr. Alain TUEL, and Dr. Yves SCHUURMAN) for their invaluable advice, continuous support, and patience during my PhD study. Even during the COVID-19 pandemic, their support continued so as to adapt to the necessary measures and precautions. Their precious knowledge and experience have encouraged me in all the time during and after my stay at IRCELYON institute (CNRS-UCBL) and even in my daily life. I also express my honor and gratitude for the presence and guidance of my thesis defense jury members. Moreover, I also acknowledge the financial support from ANR.

Furthermore, I acknowledge the wonderful experience and help that I had during our collaboration with our colleagues at the LRS laboratory (CNRS-Sorbonne university): Josephine SCHNEE, Cyril THOMAS, and Laurent DELANNOY.

I would also like to thank everyone at IRCELYON especially my colleagues in the ING team (Ranin ATWI, William DE REZENDE LOCATEL, Corentin CHATELARD, Emmanuel LANDRIVON, Jérome CANIVET), my other colleagues at IRCELYON (Dr. Nadine ESSAYEM, Eya ZGHAB, Sarah KHEIREDDIN and Frédéric DAPPOZE) with whom I have shared the best moments and some language exchange as well. Everyone contributed to make my life in Lyon an amazing experience.

I also would like to acknowledge the tremendous efforts of the technical support teams at IRCELYON: PXRD experiments by Françoise BOSSELET and Yoan AIZAC, TEM-EDX analysis by Laurence BUREL, and ICP-OES analysis by Nicolas BONNET.

No words can express my sincere and special gratitude to my parents and everyone in my family, who have been supporting me since a very young age, and especially in the past few years. A major drive in my life is to make them proud. A special thank you is to my brother Fouad ELGAYAR who has been helping and supporting me in Lyon and with the preparation of my thesis defense.

The guidance and encouragement from my university professors were also unparalleled whether in Cairo, Egypt (Pr. Ibrahim BADR, Pr. Gamal ELMELIGI, Pr. Attia ELSAYED) or in Lyon, France (Pr. Peter GOEKJIAN, Pr. Shashank MISHRA and Pr. Anne GIROIR-FENDLER)

I also show my gratitude to my friends Abdallah ABDELMOTTALEB, Ahmed ABDELHAKEM, Aboubakr HAMAD, Ahmed DIAAEDDIN, Ibrahim BADR, Eslam ELKALLA, Muhamed SALEM and Shaimaa SHERIF for the sincere support and encouragement.

Finally, I would like to add a special acknowledgement to the first inspiration in my life Dr. Ahmed ZEWAIL, the Egyptian Nobel prize laureate who left our world in 2016.

List of abbreviations

ANR	Association Natioanle de Recherche
APTMS	AminoPropylTriMethoxySilance
ATR	Attenuated Total Reflectance
Au-CO	CO adsorbed on Au
B-CO	Bridge adsorbed CO
BET	Brunauer-Emmett-Teller theory
Ca-LTA	Calcium-Linde Type A Zeolite
Ca^{2+}-CO	Co adsorbed on Calcium ions
CNRS	Centre nationale de recherche scientifique
Co-DP	Co-Deposititon Preciptation
Co-DPNaOH	Co-Deposititon Preciptation by NaOH
DP	Deposititon Preciptation
DPNaOH	Deposititon Preciptation by NaOH
DPU	Deposititon Preciptation by Urea
DRIFTS	Diffusion Reflectance Infrared Fourier Transform Spectroscopy
DTGS	Deuterated TriGlycine Sulfate detector
$deNO_X$	NOx decomposition
d_i	Particle Diameter
d_{NW}	Number Weighed Diameter (average particle diameter)
d_{SW}	Surface Weighed Diameter
EDX	Energy Dispersive X-ray Spectroscopy
EEA	European Environment Agency
EN	Electronegativity
ETEM	Environmental Transmission Electron Microscopy
Eq.	Equation
Ex situ	Latin, meaning off site
et al.	Latin *et alii*, meaning and co-workers
e.g.	Latin *exempli gratia*, meaning for example
FAU	Faujasite (Zeolite)
FCC	Face Centered Cubic
Fig.	Figure
FTIR	Fourier Transform Infrared spectroscopy

FWHM	Full Width at Half Maximum intensity
GHSV	Gas Hourly Space Velocity
HCs	Hydrocarbons
HRTEM	High Resolution Transmission Electron Microscopy
ICDD	International Center for Diffraction Data
ICP-OES	Inductively Coupled Plasma Optical Emission Spectroscopy
In situ	Latin, meaning on site
IRCELYON	Institut de Recherche sur la Catalyse et l'Environnement de Lyon
i.e.	Latin *id est*, meaning that is
L-CO	Linearly adsorbed CO
LRS	Laboratoire de Réactivité et Surface
LTA	Linde Type A (Zeolite)
MCT	Mercury Cadmium Telluride detector
MFI	Mobil Five (Zeolite framework)
MFC	Mass Flow Controller
MPTMS	MercaptoPropylTriMethoxySilance
MW	Molecular Weight
N_{ads}	Adsorbed Nitrogen
NSR	NOx Storage Reduction
O_{ads}	Adsorbed Oxygen
OH-CO	Co adsorbed on OH groups
PEG	Poly-Ethylene Glycol
PDF	Powder Diffraction File
Pt-CO	CO adsorbed on Pt
PXRD	Powder X-ray Diffraction
PZC	Point of Zero Charge
RAIRS	Reflection Adsorption Infrared Spectroscopy
RT	Room Temperature
SAA	Single Atom Alloy
SAC	Single Atom Catalyst
SCR	Selective Catalytic Reduction
SEA	Strong Electrostatic Adsorption
SEM	Scanning Electron Microscopy
SNCR	Selective Non-Catalytic Reduction

TEM	Transmission Electron Microscopy
TIR	Transmission Infrared
TPD	Temperature Programmed Desorption
TPR	Temperature Programmed Reduction
TWC	Three-Way Catalyst
UCBL	Université Claude Bernard Lyon-1
UMR	Unité Mixte de Recherche
W/F	Weight/Flow ratio
WGS	Water Gas Shift
wt.%	Weight Percentage
XPS	X-ray Photoelectron Spectroscopy
ZSM5	Zeolite Socony Mobile-5
$\Delta_f H°$	Enthalpy change of formation
$\Delta_r H°$	Enthalpy change of reaction
Θ	Bragg's angle
β	XRD peak width (in radians) at half maximum intensity
λ	XRD source wavelength;
	Air/fuel ratio
μ	Micro-
Σ	Summation

Résumé

Monoxyde d'azote est un polluant majeur des gaz d'échappement qui représente une menace sérieuse pour la santé et l'environnement. Le projet 'DecompNOx' est financé par l'ANR et est dédié à la formulation de nanoparticules bimétalliques supportées à base d'Au actives pour la décomposition directe du NO en dessous de 500°C. Ce processus est thermodynamiquement favorable dans cette gamme de température (La fig. R.1) où pour la formation de NO ($\Delta_f H°$= 90,2 kJ/mol à 25 °C [1][2]). Cependant, la réaction montre une très grande barrière cinétique de ~335 kJ/mol [1][2].

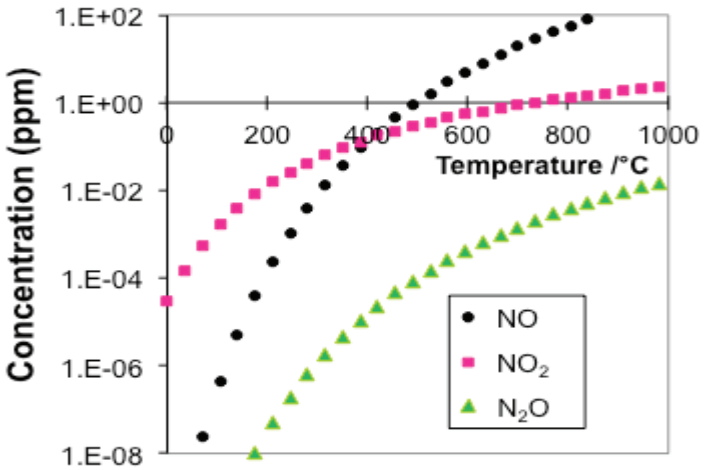

Figure R.1: Concentrations d'équilibre calculées par le logiciel HSC Chemistry 6.2 de NO, NO_2 et N_2O en fonction de la température en supposant une composition de départ de 200 ppm NO + 10% O_2 /N_2.

Tout au long du projet, plusieurs méthodes ont été utilisées pour la préparation des nanoparticules bimétalliques Pd-Au et Pt-Au supportées sur plusieurs supports (SiO_2, LTA et Al_2O_3). On a étudié l'effet de l'alliage des métaux nobles actifs avec de l'or sur l'activité catalytique deNO_X des catalyseurs à base de SiO_2 et LTA.

Des catalyseurs à base d'alumine ont été préparés, caractérisés (par TEM-EDX et DRX) et testé par ma collègue Ranin Atwi [3]. Dans ce travail, les échantillons ont été étudiés par la cinétique d'adsorption/désorption du CO en tant qu'un outil de la caractérisation des nanoalliages bimétalliques.

Les nanoparticules Pd-Au/SiO_2 ont été préparés par l'imprégnation humide et la méthode redox de surface. L'analyse TEM a montré des petites nanoparticules d'Au (<5 nm), tandis que les échantillons contenant du Pd ont montré une fraction significative de particules plus grosses (>9 nm). Les analyses PXRD *in situ* et TEM-EDX ont révélé l'alliage entre Au et Pd après chauffage à 450°C sous H_2. PXRD a également révélé une composition d'alliage seuil de $Pd_{0,2}Au_{0,8}$ résistant à l'oxydation à l'air à 500°C. Sous NO à 450°C, Au était inactif. L'échantillon de Pd(4) contenant ~4% en poids de Pd a

montré une activité mesurable et une sélectivité élevée en N_2, bien que continuellement désactivée en raison de l'empoisonnement de surface par l'oxygène produit.

L'alliage entre Pd et Au (à un rapport molaire Au/Pd de 0,12) dans l'échantillon Pd(4)Au(1) a amélioré et stabilisé l'activité catalytique deNO_X. L'analyse PXRD post-réaction a montré la présence de PdO en plus de Pd métallique et d'une phase d'alliage de PdAu. Cependant, la charge d'or plus élevée dans le Pd(4)Au(4) a entraîné une activité catalytique stable mais plus faible et une sélectivité en N_2 améliorée. Cela suggère que la réaction se déroule probablement via un mécanisme de formation de dimères de NO. La charge d'or plus élevée a probablement inhibé la formation de dimères et amélioré la décomposition du N_2O formé. La fig. R.2 montre la décomposition des NO_X sur tous les échantillons en termes de produit ($N_2 + N_2O$).

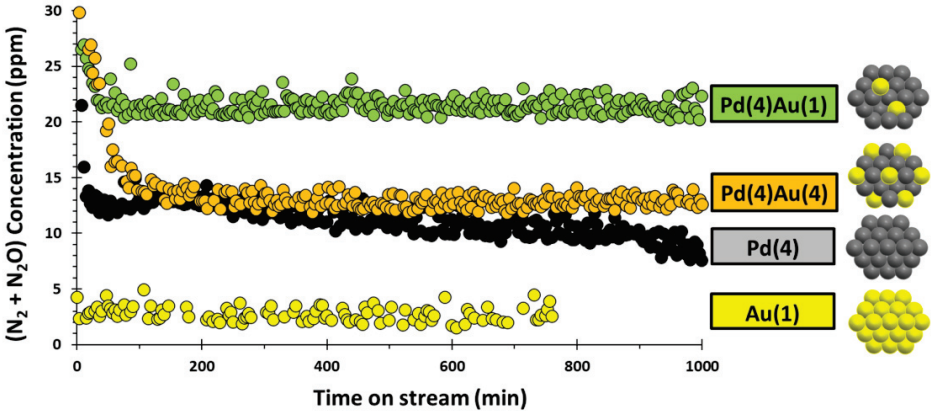

Figure R.2: L'évolution de la conversion du NO en ($N_2 + N_2O$) sur 100 mg sur les échantillons à base de SiO_2 lors du test catalytique. Alimentation : 500 ppm NO/ ArHe , 50 mL/min, 450 °C.

Des nanoparticules de Pt-Au ont été encapsulées dans la structure LTA. Un procédé d'échange d'ions Ca^{2+} a également été réalisé afin d'augmenter la taille des pores de la structure LTA. La structure LTA a été analysée par DRX. Les images TEM-EDX ont montré des petites nanoparticules (2-3 nm), en plus du S et du Cl qui ont été utilisés lors de la préparation. Après réduction sous H_2 à 350°C, le support LTA ainsi que l'or présentaient une faible adsorption linéaire. Le Pt a montré une forte adsorption linéaire de CO, en plus d'une certaine adsorption en mode ponté. L'échantillon bimétallique présentait une adsorption de pont limitée en raison de la dilution de Pt par Au. Tous les échantillons présentaient une désactivation sous NO, peut-être due à l'oxydation du Pt ou en raison de la présence du S et du Cl. L'or n'a ajouté aucune amélioration apparente de l'activité.

Les nanoparticules Pt-Au/Al_2O_3 ont été préparés par imprégnation humide. L'analyse TEM-EDX a principalement détecté de petites nanoparticules (<4 nm) dans tous les échantillons et des alliages métalliques. L'échantillon Au(2) contenant ~2 % Au en poids a montré une faible adsorption linéaire de CO et la formation de carbonates. L'échantillon du Pt présentait une forte adsorption linéaire de

CO et une faible adsorption en pont. L'alliage dans les échantillons bimétalliques conduit à une adsorption pontée limitée (c'est-à-dire la dilution de Pt par Au). L'échantillon bimétallique a également montré une désorption de CO plus rapide que celle de l'échantillon de Pt monométallique. Cela pourrait être dû à une adsorption de CO plus faible sur Pt en raison de l'alliage avec Au, ou à une désorption se produisant sur l'or après une migration de CO en surface. La fig. R.3 montre l'évolution de la surface de bande des bandes d'adsorption linéaire après l'arrêt du CO sur tous les échantillons. En effet, nous avons réussi à utiliser la cinétique de désorption en tant qu'un moyen de caractériser les nanoparticules de PtAu alliées.

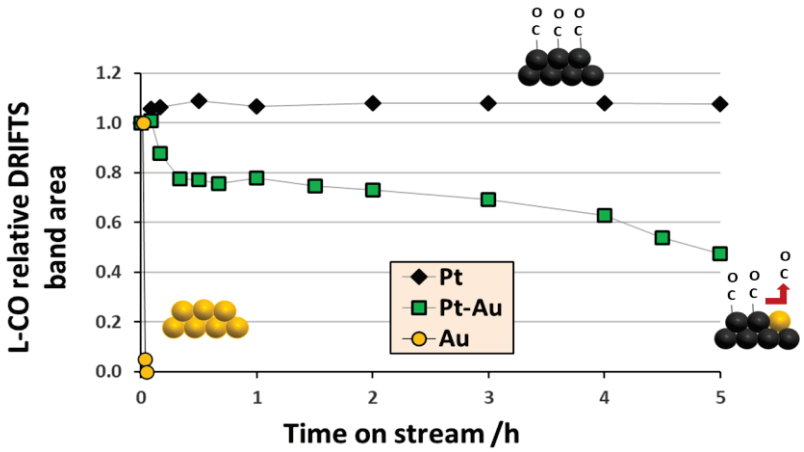

Figure R.3 : Le changement des aires relatives des bandes pendant la désorption de Pt L-CO sur Pt sur Pt(1.3), Pt(2)Au(0.3), et la désorption de Au L-CO sur Au(2)/Al_2O_3 . Alimentation : He, 100 mL/min, 50°C. Les échantillons ont été préalablement laissés sous CO pendant 15 min.

Les résultats de ce travail ont donné lieu à 4 publications :

1- **Contributions and limitations of IR spectroscopy of CO adsorption to the characterization of bimetallic and nanoalloy catalysts** [4]**.** Une revue qui s'articule sur les avantages et les limites de caractérisations pour l'adsorption du CO par DRIFTS.
2- **Au-Modified Pd catalyst exhibits improved activity and stability for NO direct decomposition** [5]**.** Cet article présente les performances catalytiques obtenues sur les nanoparticules de Pd-Au/SiO_2.
3- **Evidencing Pt-Au alloyed domains on supported bimetallic nanoparticles using CO desorption kinetics** [6]**.** Dans cet article on a développé la cinétique d'adsorption-désorption du CO sur des échantillons à base d'alumine.
4- **Stability of Pt-adsorbed CO on catalysts for room temperature oxidation of CO** [7]**.** Cette publication rapporte sur l'effet de l'utilisation de plusieurs supports à base de Pt avec des différentes propriétés redox (alumine, oxyde de titane et oxyde de cérium) et leurs performances catalytiques dans l'oxydation du CO.

Nous avions aussi publié un autre article traitant de la restructuration des nanoparticules d'Au sous CO [8]. Cependant, nous avons dû retirer cet article car nous n'avons pas pu reproduire nos résultats après avoir changé la cellule DRIFTS qui s'est avérée corrodée. Nous avons découvert que l'évolution du profil d'adsorption sur l'or était simplement due à la contamination par le Ni du matériau cellulaire corrodé. Une conclusion similaire a été récemment rapportée ailleurs [9]. Par conséquent, nous avons également soumis une note de rétractation [10] au journal d'édition soulignant la mauvaise interprétation majeure des données qui pourrait résulter des contaminations.

Ce travail a prouvé la capacité d'allier Au avec des métaux nobles (Pd) pour favoriser leur activité vers la décomposition des NO_X en dessous de 500°C. Cependant, la meilleure activité obtenue est encore limitée par rapport à d'autres substances catalytiques rapportées dans la littérature telles que Cu-ZSM5. Par conséquent, d'autres formulations et/ou méthodes d'activation doivent également être envisagées pour obtenir des activités compétitives.

Références

[1] F. Garin, "Mechanism of NOx decomposition," *Appl. Catal. A Gen.*, vol. 222, no. 1–2, pp. 183–219, 2001, doi: 10.1016/S0926-860X(01)00827-4.

[2] H. Wise and M. F. Frech, "Kinetics of decomposition of nitric oxide at elevated temperatures. I. Rate measurements in a quartz vessel," *J. Chem. Phys.*, vol. 20, no. 1, pp. 22–24, 1952, doi: 10.1063/1.1700189.

[3] R. A. (PhD Dissertation), "NO direct decomposition in the presence of excess oxygen over gold-based catalysts," 2021.

[4] T. Elgayyar, R. Atwi, A. Tuel, and F. C. Meunier, "Contributions and limitations of IR spectroscopy of CO adsorption to the characterization of bimetallic and nanoalloy catalysts," *Catal. Today*, vol. 373, pp. 59–68, 2021, doi: 10.1016/j.cattod.2021.01.009.

[5] T. Elgayyar *et al.*, "Au-Modified Pd catalyst exhibits improved activity and stability for NO direct decomposition," *Catal. Sci. Technol.*, vol. 11, no. 8, pp. 2908–2914, 2021, doi: 10.1039/d1cy00301a.

[6] T. Elgayyar, R. Atwi, A. Tuel, L. Burel, Y. Schuurman, and F. C. Meunier, "Evidencing Pt-Au alloyed domains on supported bimetallic nanoparticles using CO desorption kinetics," *Appl. Catal. A Gen.*, vol. 639, no. April, p. 118643, 2022, doi: 10.1016/j.apcata.2022.118643.

[7] F. C. Meunier, T. Elgayyar, K. Dembélé, and H. Kaper, "Stability of Pt-Adsorbed CO on Catalysts for Room Temperature-Oxidation of CO," *Catalysts*, vol. 12, no. 5, pp. 1–12, 2022, doi: 10.3390/catal12050532.

[8] R. Atwi, T. Elgayyar, F. J. Cadete Santos Aires, A. Tuel, and F. C. Meunier, "Revisiting the Evolution of IR Spectra of CO Adsorbed on Au Nanoparticles Supported on Non-reducible Supports," *Top. Catal.*, vol. 63, no. 15–18, pp. 1596–1605, 2020, doi: 10.1007/s11244-020-01372-2.

[9] Y. Yao, L. Chen, X. Mao, Y. Yang, J. Chen, and L. Zhou, "In Situ PM-IRRAS Study of CO Adsorption on Au Surfaces: Solving the Puzzle," *J. Phys. Chem. C*, vol. 125, no. 16, pp. 8606–8619, 2021, doi: 10.1021/acs.jpcc.1c01638.

[10] R. Atwi, T. Elgayyar, F. J. Cadete Santos Aires, A. Tuel, and F. C. Meunier, "Retraction Note to: Revisiting the Evolution of IR Spectra of CO Adsorbed on Au Nanoparticles Supported on Non-reducible Supports," *Top. Catal.*, vol. 64, no. 17–20, pp. 1054–1055, 2021, doi: 10.1007/s11244-021-01467-4.

Introduction

This thesis is funded by the ANR project "DecompNO_X". It is a joint endeavor between IRCELYON institute (UMR5256: UCBL-CNRS) and LRS laboratory (UMR 7197: Sorbonne university-CNRS). The aim of the project is the formulation of Au-based bimetallic nanoparticles (supported on oxide supports or encapsulated in zeolites) active for NO direct decomposition.

1. NO_X emissions control

Nitric oxide (NO) is considered a health hazard as it contributes to acid rains, reacts with ozone, and is also oxidized in air forming NO_2 which is dangerous for the respiratory system. These emissions could also lead to the formation of ground level ozone, which can cause the ecosystem damage. These emissions can be formed due to the thermal reaction of N_2 with O_2 at elevated temperatures, with an activation energy as high as ~500 kJ/mol [1] or ~400 kJ/mol [2]. In addition, NO_X can be formed due to the combustion of N-containing fuels. This means that these emissions may be formed at any combustion engines or high temperature industrial process. According to the European Environment Agency (EEA-33), in 2011, the main NO_X emissions sources were road transport (41%), energy production (23%) and commercial households (13%) [3].

Regulation have been implemented to control the NO_X emissions. The latest regulation in Europe is the standard Euro 6 for light-duty vehicles (or Euro VI for heavy duty). Euro 6 sets the NO_X emissions limit to 80 mg/km, while Euro VI sets the limit to 460 mg/km [4].

Various processes have been developed for the removal of the NO_X emissions. NO_X Storage-Reduction (NSR) is used with lean-burn engines where the NO_X are stored then reduced using HCs. The limitations are that toxic NH_3 may be produced, and catalyst poisoning by SO_2 [5]. The three-way catalyst (TWC) [6][7] is based on the catalytic ability of noble metals (Pd, Pt or Rh) to oxidize CO and HCs and to reduce NO simultaneously. The reduction of NO is favored with excess fuel (controlled O_2 level) such as with gasoline engines and not diesel engines with lean (O_2-rich) conditions. Selective Catalytic Reduction (SCR) [8] and Selective Non-Catalytic Reduction (SNCR) [9] are used with fixed exhaust sources and involve the conversion of NO to N_2 via the reduction with NH_3, Urea or HCs. Both processes are costly and hazardous due to the high toxicity of the reagents used. SNCR does not use a catalyst and is less efficient than SCR [9]. More details of these processes are shown in chapter 1.

2. NO Direct Decomposition

Direct NO decomposition to N_2 and O_2 is a process that does not involve the use of reductants and does not form toxic emissions. The process is also thermodynamically favored below 500°C (Fig. I.1) since NO formation has a $\Delta_f H°$ of 90.2 kJ/mol at 25 °C [10][11]. Nonetheless, the reaction displays a very large kinetic barrier of ~335 kJ/mol [10][11].

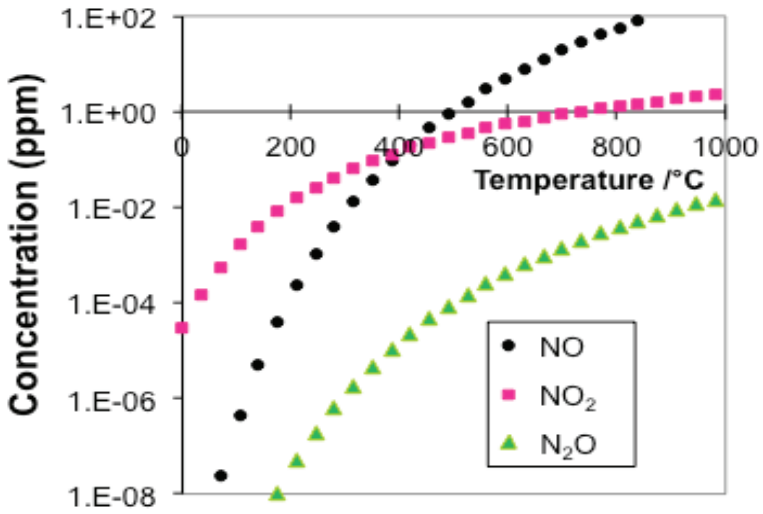

Figure I.1 : Calculated equilibrium concentrations by HSC Chemistry 6.2 software of NO, NO_2 and N_2O as a function of temperature assuming a starting composition of (200 ppm NO + 10% O_2/N_2).

Several catalytic substances have been reported in the literature. Metal oxides showed high activities at high temperatures [12][13][14][15][16]. The presence of O_2 lead to the activity inhibition [12][13]. Perovskites showed high activities at high temperatures [17][18][19]. Heteropoly acids displayed great affinity for NO adsorption and decomposition [20][21][22]. Similarly, O_2 lead to the activity inhibition [23]. Cu-ZSM5 catalysts showed high activities at moderate temperatures (300-600°C) [24][25][26] even in the presence of O_2 [27]. However, SO_2 lead to the catalyst poisoning [28]. Noble metals showed activity at high temperatures [12][29][30]. The poisoning by O_2 was a major reported limitation [29][12] as also reported by Amirnazmi *et al.* [31] using the rate equation below:

$$\mathbf{r} = \frac{\mathbf{N} \times \boldsymbol{k} \times \mathbf{P_{NO}}}{\mathbf{1} + \boldsymbol{\alpha} \times \mathbf{K} \times \mathbf{P_{O_2}}} \qquad \textbf{Eq. I.1}$$

where N is Avogadro's number, *k* is the reaction rate constant, α is a conversion factor, and K is the adsorption equilibrium constant. More details of these catalysts are shown in chapter 1.

3. The objective of the DecompNOx project

The objective of the project is to formulate a noble metal(s)-based catalyst active for NO direct decomposition to N_2 and O_2 at moderate temperatures (200-500°C) and stable against oxidation.

Fig. I.2 shows the Gibbs Energy of the decomposition of various bulk metal oxides in the presence of 10 kPa of O_2 into the corresponding metals. Gold oxide (Au_2O_3) is unstable over the whole temperature range while the other metal oxides are stable up to high temperatures.

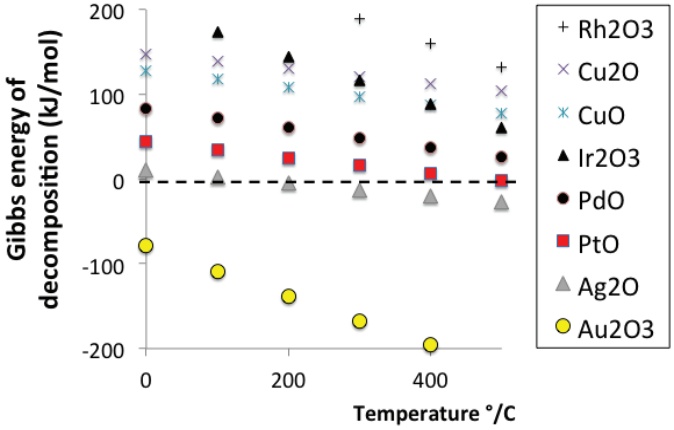

Figure I.2 : Gibbs energy of decomposition $MO_X \rightarrow M + {}^{X}/_{2}\ O_2$ for several bulk metal oxides (in equilibrium with 10 kPa of O_2). The data were obtained using the HSC Chemistry 6.2 software.

Therefore, the proposed idea of the project is to combine the activity of noble metals and the oxidation resistance of Au via the formulation of bimetallic Au-Metal nanoalloy catalysts supported on oxide supports or encapsulated in zeolites. Alloying the active metal with Au is expected to enhance the oxidation resistance of the active metal.

Several metals are of interest such as Pd, Ag, Pt, Rh, Ir and Cu. Fig. I.3, I.4 and I.5 and I.6 show the phase diagrams of binary Au-M systems; where M is Pd, Ag, Cu and Pt, respectively. Pd, Ag and Cu show excellent miscibility with Au. In contrast, Pt displays a large miscibility gap with Au. Yet, a better miscibility could be expected at the nanoscale. Moreover, the surface tension of Au is lower than that of most noble metals (Table I.1). This would favor the presence of Au at surface sites in Au-M alloy nanoparticles. This could enable the efficient protection of the metal surface against oxygen.

Table I.1 : Surface tension [32] and atomic sizes [33] of the metals of interest.

Physical quantity	Ag	**Au**	Cu	Pd	Pt	Rh	Ir
Surface tension (mN/m)	925	**1145**	1330	1482	1763	1925	2264
Atomic radius (pm)	144	**144**	128	138	138	134	136

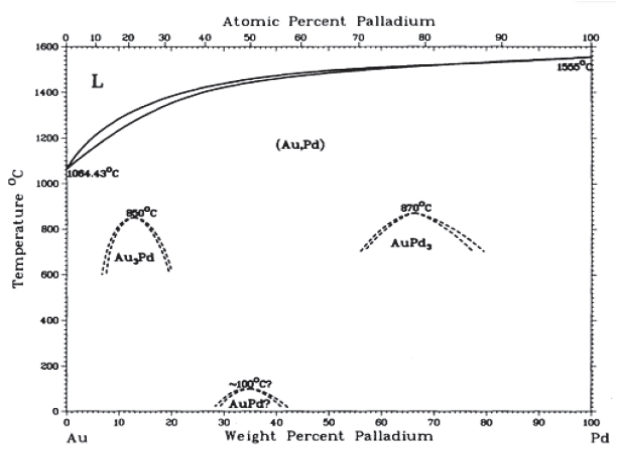

Figure I.3 : phase diagram of Au-Pd system. [34]

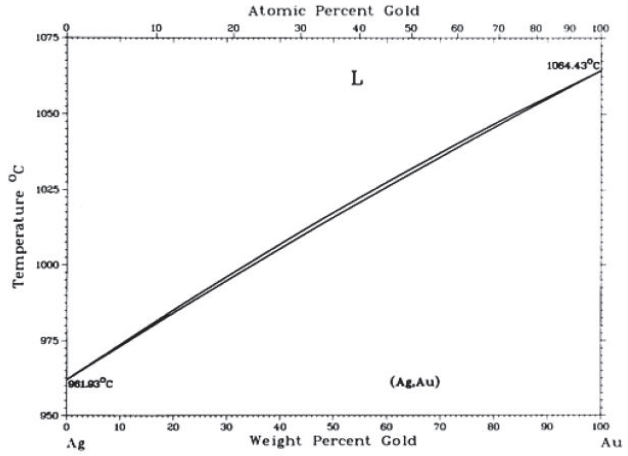

Figure I.4 : Phase diagram of Au-Ag system. [34]

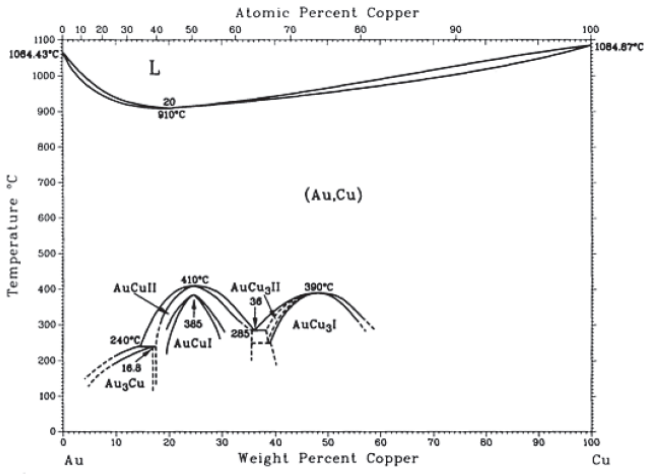

Figure I.5 : Phase diagram of Au-Cu system. [35]

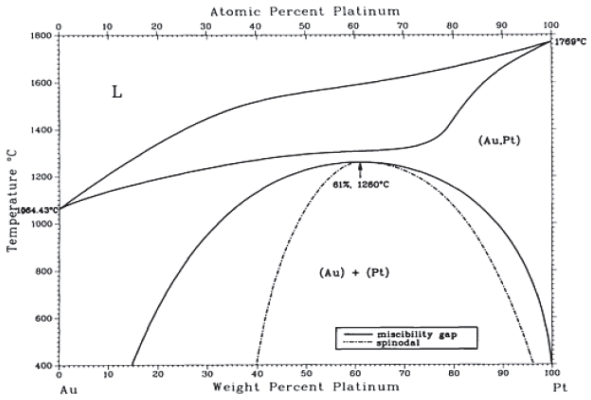

Figure I.6 : phase diagram of Au-Pt system. [34]

The project involves the catalyst preparation, characterization and catalytic testing. The PhD thesis consists of five chapters (in addition to a final chapter of the conclusions and perspectives):

Chapter 1. State of the Art. The chapter presents a brief literature review of all the relevant topics. These include the various catalytic applications, preparation methods and characterization techniques of Au-based bimetallic nanoparticles. In addition, the various NO_X emissions removal technologies are discussed with a focus on the NO direct decomposition.

Chapter 2. Experimental. The chapter presents details of the experimental catalyst preparation procedures. Moreover, the chapter describes the experimental conditions as well as technical and theoretical details of the characterization techniques and catalytic tests.

Chapter 3. Silica-supported Pd-Au nanoparticles. The chapter discusses the characterization (by ICP-OES, TEM-EDX and PXRD) and the catalytic activity of Pd, Au and Pd-Au/SiO_2 nanoparticles.

Chapter 4. LTA-encapsulated Pt-Au nanoparticles. The chapter discusses the characterization (by ICP-OES, TEM-EDX, PXRD and DRIFTS CO adsorption analyses) and the catalytic activity of monometallic Pt, Au and bimetallic Pt-Au@LTA nanoparticles. It must be mentioned that several other metals (Pd, Rh, Ir, Ag and Cu) were used for the preparation and catalytic testing of monometallic and Au-based bimetallic counterparts. Yet, only the Pt-based samples displayed measurable activities. Therefore, only the results of the Pt-Au system are discussed.

Chapter 5. Alumina-supported Pt-Au nanoparticles. The chapter discusses the characterization by CO adsorption by DRIFTS of Pt, Au and bimetallic Pt-Au/Al_2O_3 nanoparticles, as a tool to characterize bimetallic nanoparticles. This characterization tool could be useful and informative considering the possible limitations of the other characterization techniques. These samples were previously prepared, characterized (by ICP-OES, TEM-EDX and PXRD analyses), and tested for the deNO_X activity by my colleague Ranin ATWI where these samples were inactive.

List of publications

This work lead to the successful publication of four articles in peer-reviewed journals:

1- **Contributions and limitations of IR spectroscopy of CO adsorption to the characterization of bimetallic and nanoalloy catalysts** [36]**.** A review article discussing the advantages and limitations of the characterization using CO adsorption by DRIFTS.
2- **Au-Modified Pd catalyst exhibits improved activity and stability for NO direct decomposition** [37]**.** An article presenting our catalytic results over the Pd-Au/SiO_2 nanoparticles.
3- **Evidencing Pt-Au alloyed domains on supported bimetallic nanoparticles using CO desorption kinetics** [38]**.** An article discussing the CO adsorption and desorption kinetics over the alumina-based sample.
4- **Stability of Pt-adsorbed CO on catalysts for room temperature oxidation of CO** [39]**.** An article presenting the effect of using different supports with different redox properties (alumina, titania and ceria) on the stability of CO adsorbed on Pt.

References

[1] Y. B. Zeldovich, “The Oxidation of Nitrogen in Combustion and Explosions,” *Acta Physicochim.*, vol. 21, pp. 577–628, 1946.

[2] H. S. Click, J. J. Klein, and W. Squire, “Single-pulse shock tube studies of the kinetics of the reaction N 2+O2⇄2NO between 2000-3000°K,” *J. Chem. Phys.*, vol. 27, no. 4, pp. 850–857, 1957, doi: 10.1063/1.1743864.

[3] EEA, “https://www.eea.europa.eu/data-and-maps/indicators/eea-32-nitrogen-oxides-nox-emissions-1/assessment.2010-08-19.0140149032-3.”

[4] EC, “https://ec.europa.eu/environment/air/sources/road.htm.”

[5] N. Miyoshi and S. N. I. Mastumoto, “NOx storage-reduction catalyst (NSR catalyst) for automotive engines: Sulfur poisoning mechanism and improvement of catalyst performance,” *Stud. Surf. Sci. Catal.*, vol. 121, pp. 245–250, 1999, doi: 10.1016/s0167-2991(99)80074-3.

[6] R. J. Farrauto and R. M. Heck, “Catalytic converters : state of the art and perspectives,” *Catal. Today*, vol. 51, no. 3–4, pp. 351–360, 1999.

[7] S. Nandi *et al.*, “Relationship between design strategies of commercial three-way monolithic catalysts and their performances in realistic conditions,” *Catal. Today*, vol. 384–386, no. April 2021, pp. 122–132, 2022, doi: 10.1016/j.cattod.2021.05.005.

[8] H. Kim *et al.*, “Current Catalyst Technology of Selective Catalytic Reduction (SCR) for NO x Removal in South Korea,” *Catalysts*, vol. 10, no. 1, p. 52, 2020.

[9] E. S. P. B. V, “Formation and control of nitrogen oxides,” *Catal. Today*, vol. 2, no. 4, pp. 369–379, 1988, doi: 10.1016/0920-5861(88)80002-6.

[10] F. Garin, “Mechanism of NOx decomposition,” *Appl. Catal. A Gen.*, vol. 222, no. 1–2, pp. 183–219, 2001, doi: 10.1016/S0926-860X(01)00827-4.

[11] H. Wise and M. F. Frech, “Kinetics of decomposition of nitric oxide at elevated temperatures. I. Rate measurements in a quartz vessel,” *J. Chem. Phys.*, vol. 20, no. 1, pp. 22–24, 1952, doi: 10.1063/1.1700189.

[12] M. Iwamoto and H. Hamada, “Catalysis Today, 10 (1991) 67-71,” *Catal. Today*, vol. 10, p. 57, 1991.

[13] E. R. S. Winter, “The catalytic decomposition of nitric oxide by metallic oxides,” *J. Catal.*, vol. 22, no. 2, pp. 158–170, 1971, doi: 10.1016/0021-9517(71)90182-5.

[14] H. Hamada, Y. Kintaichi, M. Sasaki, and T. Ito, “Silver-promoted Cobalt Oxide Catalysts for Direct Decomposition of Nitrogen Monoxide,” *Chemistry Letters*, vol. 19, no. 7. pp. 1069–1070, 1990, doi: 10.1246/cl.1990.1069.

[15] G. K. Reddy, T. C. Peck, and C. A. Roberts, “CeO2-M xO y (M = Fe, Co, Ni, and Cu)-Based Oxides for Direct NO Decomposition,” *J. Phys. Chem. C*, vol. 123, no. 47, pp. 28695–28706, 2019, doi: 10.1021/acs.jpcc.9b07736.

[16] S. Tsujimoto, K. Yasuda, T. Masui, and N. Imanaka, “Effects of Tb and Ba introduction on the reaction mechanism of direct NO decomposition over C-type cubic rare earth oxides based on Y2O 3,” *Catal. Sci. Technol.*, vol. 3, no. 8, pp. 1928–1936, 2013, doi: 10.1039/c3cy20746c.

[17] H. Iwakuni, Y. Shinmyou, H. Yano, H. Matsumoto, and T. Ishihara, “Direct decomposition of NO into N2 and O2 on BaMnO3-based perovskite oxides,” *Appl. Catal. B Environ.*, vol. 74, no. 3–4, pp. 299–306, 2007, doi: 10.1016/j.apcatb.2007.02.020.

[18] T. Ishihara *et al.*, “Direct decomposition of NO into N2 and O2 over La(Ba)Mn(In)O3 perovskite oxide,” *J. Catal.*, vol. 220, no. 1, pp. 104–114, 2003, doi: 10.1016/S0021-9517(03)00265-3.

[19] J. Zhu, D. Xiao, J. Li, X. Xie, X. Yang, and Y. Wu, “Recycle - New possible mechanism of NO decomposition over perovskite(-like) oxides,” *J. Mol. Catal. A Chem.*, vol. 233, no. 1–2, pp. 29–34, 2005, doi: 10.1016/j.molcata.2005.02.011.

[20] R. T. Yang and N. Chen, “A New Approach to Decomposition of Nitric Oxide Using Sorbent/Catalyst without Reducing Gas: Use of Heteropoly Compounds,” *Ind. Eng. Chem. Res.*, vol. 33, no. 4, pp. 825–831, 1994, doi: 10.1021/ie00028a007.

[21] Z. Zhang, L. Zhu, J. Ma, S. Ren, and X. Yang, “Temperature programmed desorption-mass spectrometry study of no desorption and decomposition by Titania supported 12-tungstophosphoric acid,” *React. Kinet. Catal. Lett.*, vol. 76, no. 1, pp. 93–101, 2002, doi: 10.1023/A:1015669529142.

[22] R. L. McCormick, S. K. Boonrueng, and A. M. Herring, “In situ IR and temperature programmed desorption-mass spectrometry study of NO absorption and decomposition by silica supported 12-tungstophosphoric acid,”

Catal. Today, vol. 42, no. 1–2, pp. 145–157, 1998, doi: 10.1016/S0920-5861(98)00085-6.

[23] J. Schnee, L. Delannoy, G. Costentin, and C. Thomas, "Unraveling the Direct Decomposition of NO xover Keggin Heteropolyacids and Their Deactivation Using a Combination of Gas-IR/MS and in Situ DRIFT Spectroscopy," *J. Phys. Chem. C*, vol. 124, no. 41, pp. 22459–22470, 2020, doi: 10.1021/acs.jpcc.0c05945.

[24] M. Iwamoto, H. Yahiro, K. Tanda, N. Mizuno, Y. Mine, and S. Kagawa, "Removal of nitrogen monoxide through a novel catalytic process. 1. Decomposition on excessively copper ion exchanged ZSM-5 zeolites," *J. Phys. Chem.*, vol. 95, no. 9, pp. 3727–3730, 1991, doi: 10.1021/j100162a053.

[25] T. Curtin, P. Grange, and B. Delmon, "The direct decomposition of nitrogen monoxide," *Catal. Today*, vol. 35, no. 1–2, pp. 121–127, 1997, doi: 10.1016/S0920-5861(96)00138-1.

[26] G. Spoto *et al.*, "Cu(I)-ZSM-5 zeolites prepared by reaction of H-ZSM-5 with gaseous CuCl: Spectroscopic characterization and reactivity towards carbon monoxide and nitric oxide," *Appl. Catal. B, Environ.*, vol. 3, no. 2–3, pp. 151–172, 1994, doi: 10.1016/0926-3373(93)E0032-7.

[27] P. Yang, J. Zhou, and Z. Wang, "Direct decomposition of NO into N2 and O2 over Cu /ZSM-5 containing Ce and Zr as promoter," *Adv. Mater. Res.*, vol. 113–116, pp. 1735–1739, 2010, doi: 10.4028/www.scientific.net/AMR.113-116.1735.

[28] M. Iwamoto, H. Yahiro, S. Shundo, Y. Yu-u, and N. Mizuno, "Influence of sulfur dioxide on catalytic removal of nitric oxide over copper ion-exchanged ZSM-5 zeolite," *Appl. Catal.*, vol. 69, no. 1, pp. 0–4, 1991, doi: 10.1016/S0166-9834(00)83286-8.

[29] G. K. Reddy, C. Ling, T. C. Peck, and H. Jia, "Understanding the chemical state of palladium during the direct NO decomposition-influence of pretreatment environment and reaction temperature," *RSC Adv.*, vol. 7, no. 32, pp. 19645–19655, 2017, doi: 10.1039/c7ra00836h.

[30] M. Haneda, Y. Kintaichi, I. Nakamura, T. Fujitani, and H. Hamada, "Comprehensive study combining surface science and real catalyst for NO direct decomposition," *Chem. Commun.*, vol. 2, no. 23, pp. 2816–2817, 2002, doi: 10.1039/b207619e.

[31] A. Amirnazmi, J. E. Benson, and M. Boudart, "Oxygen inhibition in the decomposition of NO on metal oxides and platinum," *J. Catal.*, vol. 30, no. 1, pp. 55–65, 1973, doi: 10.1016/0021-9517(73)90051-1.

[32] B. J. Keene, "Review of data for the surface tension of pure metals," *Int. Mater. Rev.*, vol. 38, no. 4, pp. 157–192, 1993, doi: 10.1179/imr.1993.38.4.157.

[33] J. Emsley, "The Elements," *3rd Ed. Oxford Clarendon Press*, 1998.

[34] H. Okamoto and TB. Massalski, "Phase Diagrams of Binary Gold Alloys," *ASM Int.*, 1987.

[35] H. Okamoto, D. J. Chakrabarti, D. E. Laughlin, and T. B. Massalski, "The Au- Cu (gold-copper) system," *J. Phase Equilibria*, vol. 8, no. 5, pp. 454–474, 1987.

[36] T. Elgayyar, R. Atwi, A. Tuel, and F. C. Meunier, "Contributions and limitations of IR spectroscopy of CO adsorption to the characterization of bimetallic and nanoalloy catalysts," *Catal. Today*, vol. 373, pp. 59–68, 2021, doi: 10.1016/j.cattod.2021.01.009.

[37] T. Elgayyar *et al.*, "Au-Modified Pd catalyst exhibits improved activity and stability for NO direct decomposition," *Catal. Sci. Technol.*, vol. 11, no. 8, pp. 2908–2914, 2021, doi: 10.1039/d1cy00301a.

[38] T. Elgayyar, R. Atwi, A. Tuel, L. Burel, Y. Schuurman, and F. C. Meunier, "Evidencing Pt-Au alloyed domains on supported bimetallic nanoparticles using CO desorption kinetics," *Appl. Catal. A Gen.*, vol. 639, no. April, p. 118643, 2022, doi: 10.1016/j.apcata.2022.118643.

[39] F. C. Meunier, T. Elgayyar, K. Dembélé, and H. Kaper, "Stability of Pt-Adsorbed CO on Catalysts for Room Temperature-Oxidation of CO," *Catalysts*, vol. 12, no. 5, pp. 1–12, 2022, doi: 10.3390/catal12050532.

Chapter 1. State of the art

This chapter presents the state-of-the-art of the topics relevant to the DecompNOx thesis project. The chapter introduces the main features of heterogeneous catalysis. Some catalytic reactions are also presented in which, the different effects of monometallic vs. bimetallic nanoparticle catalysts are demonstrated, especially Au-based bimetallic nanoparticles. The chapter presents reported preparation and characterization methods of the Au-based bimetallic nanoparticles supported on oxide supports and encapsulated in zeolites. The chapter discusses the various processes reported in the literature on the removal of NO_X. A more detailed discussion is then presented on various catalysts used for the direct NO decomposition to N_2 and O_2 (especially noble metals). One of the major drawbacks of noble metals is the poisoning by oxygen (produced and/or introduced in the feed) at moderate temperatures up to 500°C. Tackling down this major drawback may lead to a noble metal-based catalyst which is active for NO decomposition and stable.

1. Heterogeneous Catalysis

Heterogeneous catalysis describes a catalytic process where the catalyst and the reactant(s) are in different phases; typically, a solid catalyst and gaseous reactant(s). Fig. 1.1.1 shows a typical heterogeneous catalysis process.

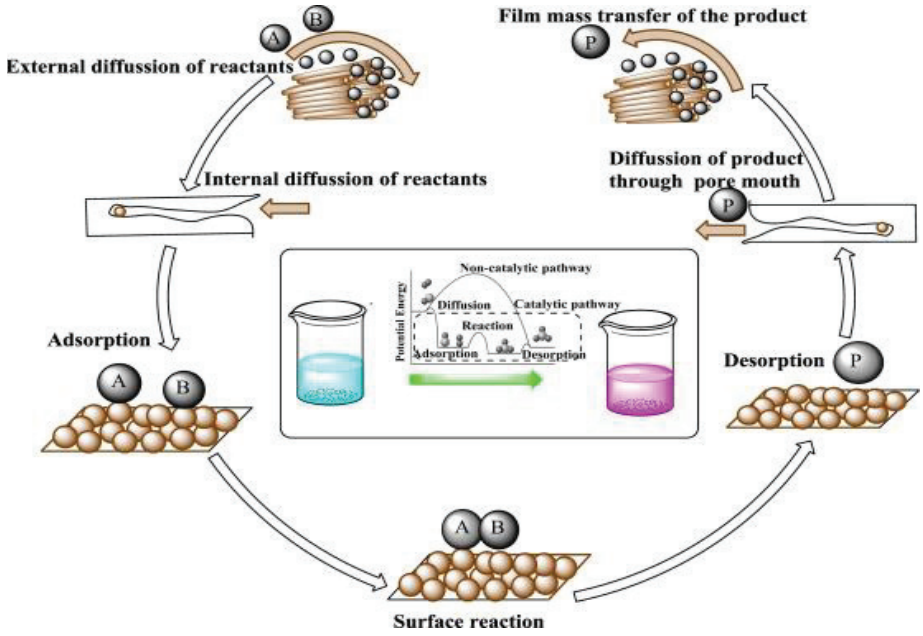

Figure 1.1.1 : Heterogeneous catalysis reaction steps. [45]

Various reasons could lead to the deactivation of the heterogeneous catalyst such as sintering, poisoning, the formation of an inactive phase due to the reaction with the gases, mechanical failure, or pore/site blockage [46].

1.1. Metal Nanoparticles

Nanoparticles (1-100 nm) display physical, chemical and mechanical properties different from those observed with bulk structures due to the quantum size effect [47][48]. Moreover, at such a small particle size, the fraction of surface atoms is greatly increased. Obviously, this adds an economic advantage to using nanoparticle catalysts, as catalysis depends on the surface properties. Metal nanoparticles have been widely used in polymer industry, electronics, biomedical applications, and catalysis.

1.2. Monometallic and bimetallic nanoparticle catalysts

Many metals have been used as monometallic nanoparticle catalysts. In the work of Hirai et al. [49][50][51], polymer-stabilized Pd, Pt, Rh and Ir nanoparticles were investigated for the hydrogenation of olefins. Also, Hutchings [52] studied the use of carbon-supported metal chlorides for the hydrochlorination of acetylene.

Bimetallic nanoparticles may display an enhanced catalytic activity compared to their monometallic counterparts. Bimetallics could combine the advantages of both metals used, while the monometallic catalysts would display a limited activity or undergo deactivation. The catalytic activity could be enhanced through electronic or geometrical effects depending on nanoparticle structure, which depends on the nature of the metals and the preparation method. Bimetallic nanoparticles can take the form of a random alloy, intermetallic alloy compounds, segregated phases, or core-shell structures depending on various parameters (Fig. 1.1.2).

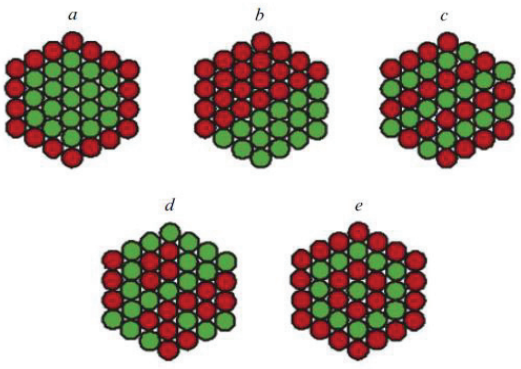

Figure 1.1.2 : Types of bimetallic nanoparticles: (a) core-shell, (b) segregated subclusters, (c) intermetallic alloy, (d) random alloy, and (e) multi-shell. [53]

The alloy formation depends on the similarity of the metal lattice parameters and surface energies [54]. The formation of intermetallic compounds is thermodynamically controlled [55] and could be promoted by annealing in an inert gas [56]. The core-shell structure provides several advantages such as enhancing the optical properties and electronic coupling. The shell thickness is a major parameter governing the particle properties [57].

Examples of bimetallic nanoparticle catalysts are Fe-based bimetallic nanoparticles used for the elimination of pollutants [58][59][60], Pd-based bimetallic nanoparticles [61][62][63], and single atom alloys (SAA) such as single Pd atoms in Ag matrix [64][65] or in Au matrix [66].

1.3. Au-based bimetallic nanoparticle catalysts

In the past, gold has been considered as an inert noble metal and used in the manufacturing of jewelries and coins. Many metals can form alloys with gold modifying its thermal stability, strength and color. Gold alloys have also been used as alternatives in jewelry industry.

The work of Bond et al. [67] was the first to demonstrate the catalytic activity of Au catalysts. After that, Also, Hutchings [52] used Au to catalyze acetylene hydrochlorination. Also, Haruta et al. [68] used Au nanoparticle catalysts for CO oxidation. Au displays an excellent oxidation resistance and is one of the best choices for catalytic reaction performed under an oxidative atmosphere.

Alloying Au with Pd has proven to enhance the catalytic activity and oxidation resistance of Pd nanoparticles in various reactions such as the hydrochlorination of aryl chlorides [69] or tertrachloromethane [70], the oxidation of alcohols [71][72][73][74], and the dehydrosulfurization (HDS) of thiophene [75]. Also, Au enhanced the oxidation resistance of Pt [37] and the Pt utilization for electrocatalysis [76]. Au also enhanced the activity of Fe/HZSM-5 used for methane dehydroaromatization [77].

2. Preparation methods of Au-based bimetallic nanoparticles reported in the literature

This section discusses the preparation and corresponding characterizations of nanoparticles supported on oxide supports and encapsulated in zeolites reported in the literature.

2.1. Oxide-supported nanoparticles

2.1.1. Preparation of oxide-supported monometallic nanoparticles

2.1.1.1. Wet impregnation

The preparation of supported monometallic nanoparticles was reported using the wet impregnation method. The Pd precursor to be used was $Pd(NO_3)_2$ [35][66], $PdCl_2$ [78][79], $Pd(NH_3)_4(NO_3)_2$ [78][80] or $(NH_4)_2PdCl_4$ [81]. The typical Au precursor used is $HAuCl_4$. During the synthesis, different reductants were used, such as a freshly prepared $NaBH_4$ solution [66][82] or hydrazine [79] both at room temperature or heating under H_2 [83][81][35][78].

In water, the surface of silica is negatively charged due to its very low PZC (Point of Zero Charge) of ~2 [84]. Therefore, metal precursors anions such as $AuCl_4^-$ or $PtCl_6^{-2}$ would display repulsion towards the silica surface. Consequently, an organic amine is grafted on silica such as APTES (3-aminopropyltriethoxysilane) [85][86] or APTMS (3-aminopropyltrimethoxysilane) [5], or a precursor that contains an organic amine moiety is used such as $Au(en)_2Cl_3$ [87][88].

Wet impregnation can also be used for the preparation of Rh/SiO_2 where $Rh(NO_3)_3$ [89] or $RhCl_3$ [90] were used as the precursor. After the preparation, the sample was reduced in H_2 flow at 623K [89]. Termetallic nanoparticles (Rh-Mn-Li/SiO_2) were prepared and activated by reduction in H_2.

2.1.1.2. Incipient wetness impregnation (dry impregnation)

Incipient wetness impregnation method was also used for the preparation of Rh/SiO_2 and Rh/Al_2O_3 nanoparticles [91]. After the impregnation, the sample was heated to 343 K then calcined at 823 K under an air flow for 6 h. No reductant was used during the impregnation. However, prior to the characterization by CO and H_2 chemisorption, the catalysts were reduced in H_2 flow at 673 K. Table 1.2.1 shows the dispersion calculated for two catalysts using the two chemisorption measurements. The loading of Rh is similar in both samples; yet using silica as the support resulted in a lower dispersion.

Table 1.2.1 : Rh loading and dispersion of the catalysts used in this study [91].

Catalyst	Rh wt.% loading	Dispersion (%)[a]	Dispersion (%)[b]
Rh/Al_2O_3	2.4	50	75
Rh/SiO_2	1.9	20	27

[a] Estimated by FT-IR study CO chemisorption at RT.
[b] Estimated by H_2 chemisorption at RT.

2.1.1.3. Ion exchange (or strong electrostatic adsorption "SEA")

For the SEA synthesis, $Pd(NH_3)_4Cl_2$ [81] or $Pd(NH_3)_4(NO_3)_2$ [83][85] were used as the Pd precursors. Typically, the pH of the aqueous solution is adjusted to ~11 [81][92] or 9 [83] before addition of the support. Under these conditions the metal support interaction is maximized due to the strong interaction between the cationic ion precursor in solution and the negative charge generated on silica whose PZC (point of zero charge) is ~2 [84]. Fig. 1.2.1 shows a representation of the interaction between the metal complex with the support at pH values higher and lower than the PZC.

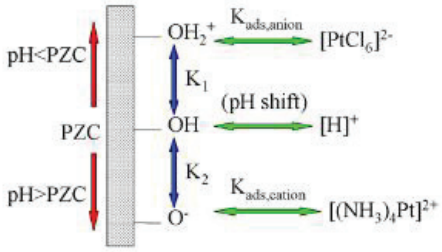

Figure 1.2.1 : Mechanism of electrostatic adsorption. [92]

In another work [83], heating under He or O_2 prior to the reduction with H_2 at 400°C lead to an enhanced dispersion compared to directly performing a reduction treatment (Table 1.2.2 and Fig. 1.2.2).

Table 1.2.2 : Dispersion measurements obtained using different pretreatments. [83]

Catalyst	Pretreatment	D_{CO} (%)	D_{H2} (%)	TEM[100/d(nm)]
$[Pd(NH_3)_4]^{2+}/SiO_2$	H_2 400°C	11	26	20
$[Pd(NH_3)_4]^{2+}/SiO_2$	O_2 100°C, H_2 400°C	40	44	37
$[Pd(NH_3)_4]^{2+}/SiO_2$	O_2 200°C, H_2 400°C	42	37	31
$[Pd(NH_3)_4]^{2+}/SiO_2$	He (Ar) 300°C, H_2 400°C	37	38	24
$[Pd(NH_3)_4]^{2+}/SiO_2$	O_2 100°C, H_2 400°C	67	71	70-80

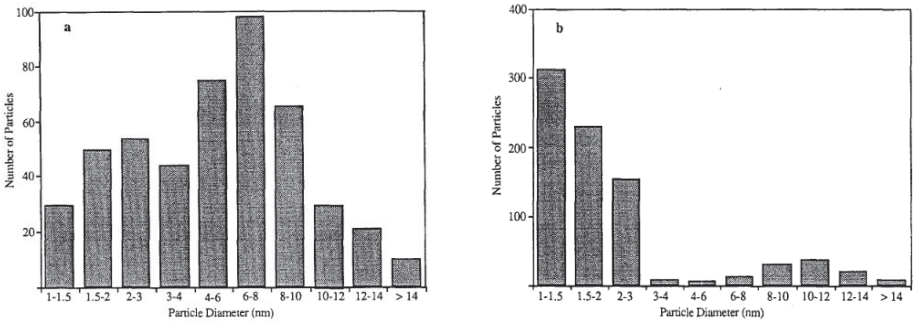

Figure 1.2.2 : Particle size distribution of $[Pd(NH_3)_4]^{2+}/SiO_2$ following pretreatments: (a) H_2 400°C (b) O_2 100°C, H_2 400°C. [83]

Another group [81] investigated the influence of the ion exchange method and the incipient wetness impregnation method on the preparation of Pd/SiO_2 nanoparticles. For the dry impregnation method, $(NH_4)_2PdCl_4$ and $Pd(NH_3)_4Cl_2$ were used as the Pd precursors. Both precursors showed similar particle size. After impregnation and drying, two protocols were used for the treatment. Maximum achievable Pd loading by the SEA method was 4.4 wt. %.

2.1.1.4. Deposition-Precipitation (DP)

Deposition-Precipitation was performed using urea (DPU) or NaOH (DPNaOH) [93]. Using urea, a final calcination step is required to get rid of these hydrocarbons present. Using the $DPNH_4OH$ method reported [94], Au/TiO_2 could be prepared. DPU can be used for the preparation of supported Rh nanoparticles (Rh/SiO_2) [95]. Fig. 1.2.3 shows the TEM analysis of 4.4% Rh/SiO_2 and indicates the very narrow particle size distribution of 0.5-1.7 nm.

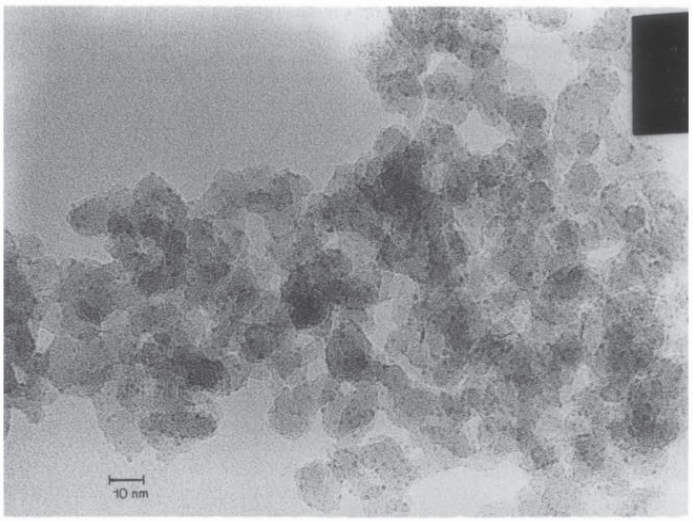

Figure 1.2.3 : TEM micrograph of Rh/SiO_2 catalyst (containing 4.4 wt% Rh). This sample had been reduced at 250°C and exhibited a hydrogen uptake of H/Rh = 0.88. [95]

2.1.2. Preparation of oxide-supported Au-based bimetallic nanoparticles

2.1.2.1. Co-impregnation

As reported [96], a solution of the mixture of the precursors of both Au and Pd ($HAuCl_4$ and $PdCl_2$) is added to a suspension of silica (in ethanol. After the impregnation, ethanol is evaporated using a water bath at 70°C. Reduction was performed at 200°C at a rate of 3°C/min for 2 h. A final calcination step was also performed in air at 300°C for 4 h. The alloy formation was observed for the sample $Pd_{0.4}Au$ (2.53 wt.% Au + 0.7 wt.% Pd /SiO_2) as the (111) peak shifts slightly toward a higher angle, from 38.1° to 38.4° of 2θ (Fig. 1.2.4).

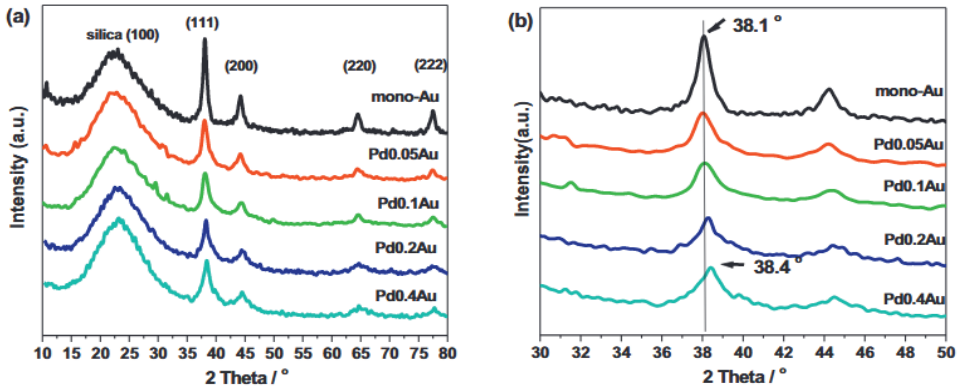

Figure 1.2.4 : XRD patterns of the catalysts: full patterns (a) and regional patterns of PdAu/MSN catalysts with various metal compositions (b). Au loading in all samples is ~2.5 wt. % and Pd loading is 0.08-0.7 wt. %. [96]

2.1.2.2. Successive impregnation

Simply, any of the two metals could be impregnated first, followed by the impregnation of the other.

2.1.2.3. Surface redox method (electroless deposition) [78]

Supported monometallic Pd or Pt can be prepared first using wet impregnation method and then used as a parent catalyst. Then, H_2 is bubbled into a suspension of the parent catalyst in water. Hydrogen can adsorb dissociatively on the surface of the metal due to its low activation energy of adsorption and dissociation on Pd for instance (4.8 kJ/mol [97] and 23.4 kJ/mol [98], respectively). In turn, the adsorbed H atoms can reduce the Au cations in the solution according to the equation:

$$3\ H_{ads} + Au^{3+} \longrightarrow Au_{ads} + 3\ H^{+} \qquad \text{Eq. 1.2.1}$$

Au reduction proceeds with the reduction potential values: $AuCl_4^-/Au$ (E_0 = 1.002 V/SHE) or Au^{3+}/Au (E_0 = 1.498 V/SHE). A similar "Electroless Deposition" method was reported by using a reducing agent instead of the adsorbed hydrogen such as dimethylamine borane or hydrazine, activated by the metal of the parent catalyst [99][100].

2.1.2.4. Co-Deposition Precipitation (Co-DP)

Co-DPNaOH was performed for the preparation of Au-Pd/TiO_2 [101] as a one pot synthesis. The maximum achievable metal loadings were 1 and 0.8 wt. % for Au and Pd, respectively. High Au loadings could be achieved using co-DPU [93]. Co-DPU is useful for the preparation of bimetallic Au-Pd particles with very low Pd loadings. Calcination is needed to remove the residual urea.

2.1.2.5. Colloidal synthesis

Colloidal synthesis usually leads to the formation of nicely alloyed and homogeneous bimetallic nanoparticles. It requires the use of a stabilizer such as PEG or a citrate salt, which adds a final calcination step. Au-Pd/silica-coated magnetite nanoparticles (Au:Pd = 1:4) were prepared. The samples were then calcined at 500°C in air and then reduced in H_2 flow at 500°C [102]. XRD profiles were recorded after each step (Fig. 1.2.5). The figure indicated the presence of an alloyed phase ($Au_1Pd_{1.3}$) initially as calculated using Vegard's law. The calcination step lead to oxidation of most Pd and its surface segregation. A residual Au_4Pd_1 alloy composition was also observed. Similar observations were also reported [103][5]. Reduction lead to the appearance of two peaks with bulk compositions of $Au_{1.7}Pd_1$ and $Au_1Pd_{7.3}$. The alloy formation was at least partially restored after reduction. Fig. 1.2.6 shows a schematic representation of the catalyst structure after each step.

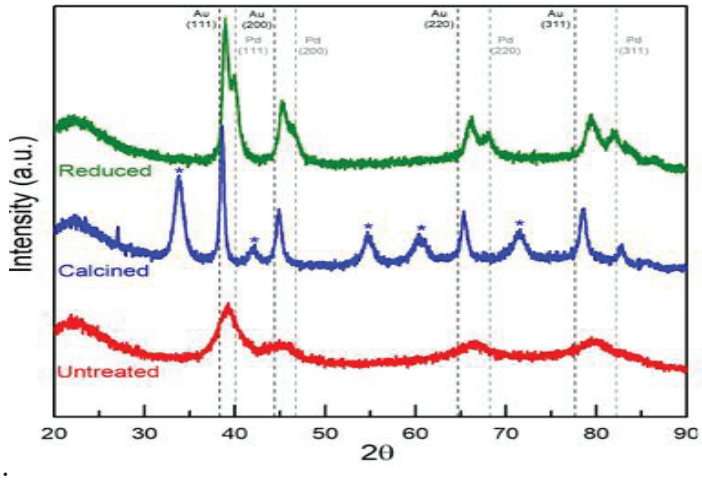

Figure 1.2.5 : XRD pattern of the AuPd 1:4 catalysts: untreated, calcined and reduced after calcination. PdO phase is indicated by star markers. [102]

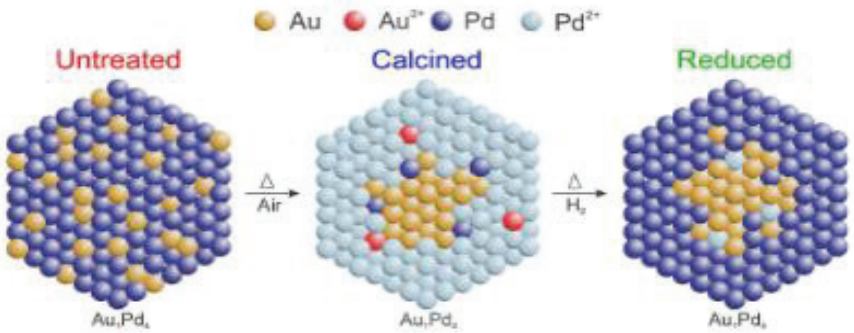

Figure 1.2.6 : Schematic cross-sectional representation of freshly prepared alloyed $AuPd_4$ NPs, and proposed structures after calcination in air and after reduction with molecular hydrogen. [102]

Atomic level alloying Pd–Au nanoparticles was also achieved where H_2 bubbling was used for the reduction without heating [104]. Fig. 1.2.7 shows the XRD analysis recorded for the monometallic and bimetallic samples indicating the alloying between Au and Pd.

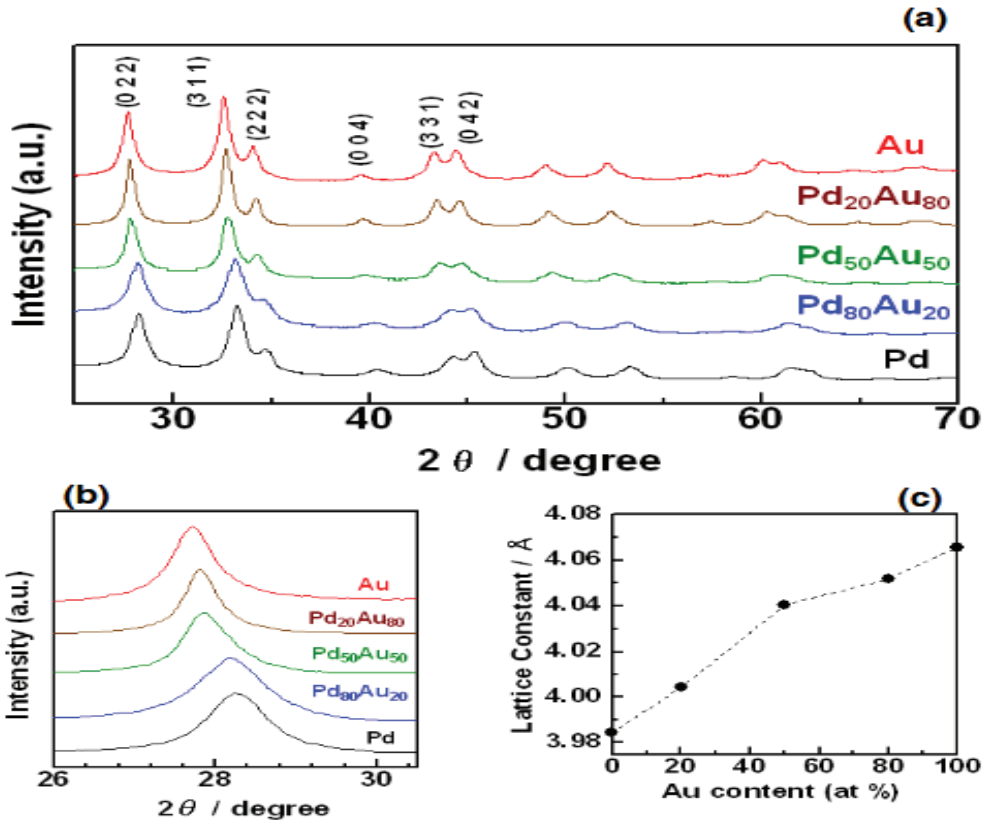

Figure 1.2.7 : PXRD patterns of Pd/Au nanoparticles. The 2θ ranges from 25.0° to 70.0° (a) and 26.0° to 30.5° (b). The lattice constants were estimated by Le Bail fitting to the diffraction patterns (c). [104]

Similarly, supported AuPd nanoparticles were also prepared using the colloidal synthesis and $NaBH_4$ as a reductant [105]. The alloy formation was evidenced by the XPS analysis (Fig. 1.2.8) by the shifts in the binding energies of (Au $4f_{7/2}$) and (Pd $3d_{5/2}$).

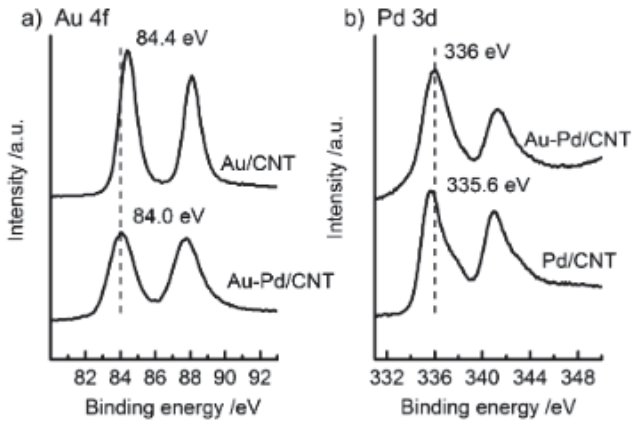

Figure 1.2.8 : XPS spectra of (a) Au 4f and (b) Pd 3d in the Au−Pd/CNT (Au/Pd = 1/1) and Au/CNT or Pd/CNT catalysts. CNT: carbon nanotubes. [105]

2.2. Nanoparticles encapsulated in zeolites

Zeolites are aluminosilicate materials with the general formula of $M_{X/n}Al_XSi_{1-X}O_2 \cdot yH_2O$ (M is H or metal ions; and n is the valence of the metal). Because of their peculiar pores and channels, zeolites exhibit interesting adsorption and catalytic properties. The classification of zeolite framework types was proposed by Meier and Olson [106]. There are numerous framework types such as the LTA (Linde Type A), FAU (Faujasite), MFI (Zeolite Socony Mobil-five) shown in Fig. 1.2.9 Zeolites are also classified based on their Si/Al atomic ratio into low (1-2), medium (3-10) and high (>10) silica zeolites [107]. This ratio plays a major role in determining the properties of zeolites [108].

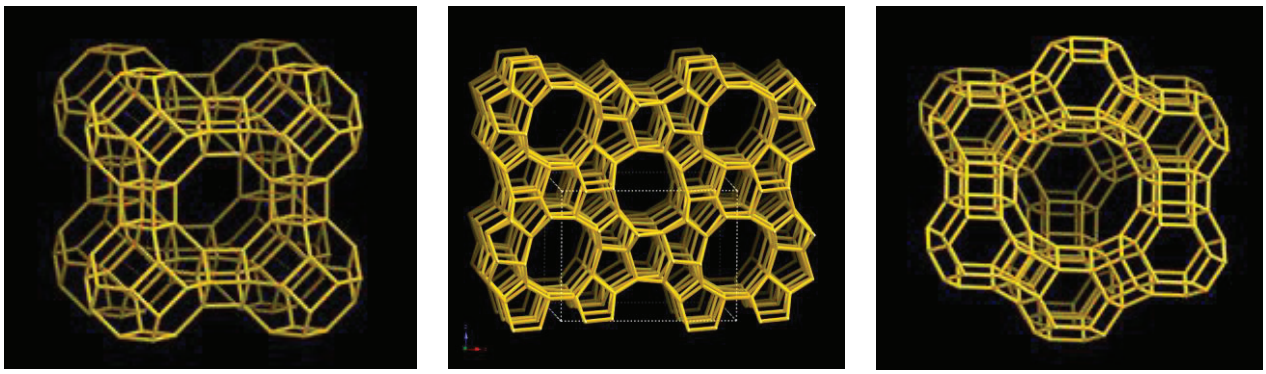

Figure 1.2.9 : Zeolite Framework Type LTA (left), MFI (middle), and FAU (right). [109]

It was reported by the work of Meier et al. [110] that the LTA structure has a general formula of $Na_{12}Al_{12}Si_{12}O_{48}.27H_2O$ with a Si/Al molar ratio of 1. Its 3-D structure consists of secondary building units (SBUs) and its cubic unit cell has a lattice constant 24.61 Å. The structure displays a very small pore diameter (0.4 nm) corresponding to an eight-member oxygen ring and a larger cavity of at least a 1.14 nm diameter [111].

2.2.1. Metal encapsulation in zeolites

Various methods were reported for the preparation of zeolites and zeolite-based catalysts. Monometallic and bimetallic nanoparticles are prepared in a one-pot synthesis. Iglesia et al. [112][113][114] reported the method of the simultaneous encapsulation of metals (Pt, Pd, Rh and Ag) during the preparation of zeolite structures including the LTA zeolite.

Nanoparticles of the order of 1-2 nm were obtained. Fig. 1.2.10 shows the TEM and XRD analyses of some LTA-based samples [113].

Our group earlier reported the encapsulation of metal nanoparticles into hollow Silicalite-1 structure with well-defined edges [115][116]. Fig. 1.2.11 shows the HRTEM analysis and Fig. 1.2.12 shows the operando CO adsorption analysis over Au, Ag and Au-Ag@Silicalite-1 [116]. The bimetallic sample displayed an adsorption spectrum in between the monometallic samples since the adsorption band at 2134 cm^{-1} associated with positively charged Au was significantly suppressed in the presence of Ag. This indicates that the Ag possibly occupied some surface sites replacing Au atoms.

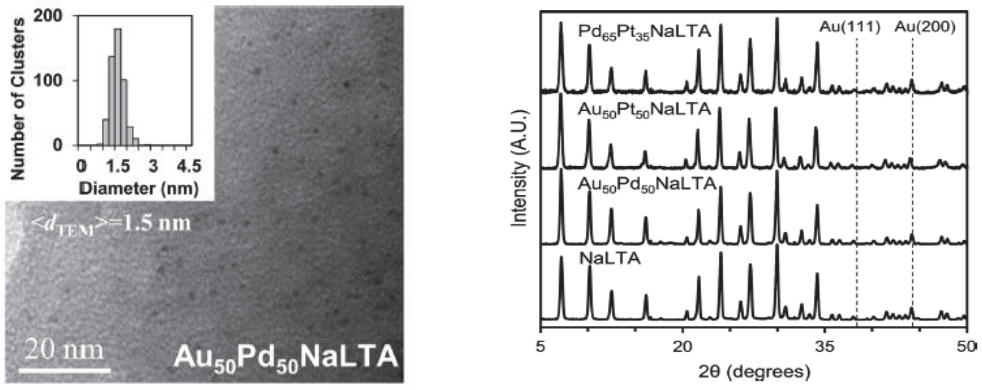

Figure 1.2.10 : TEM analysis of AuPd-LTA (left) and XRD patterns of LTA-based samples (right). [113]

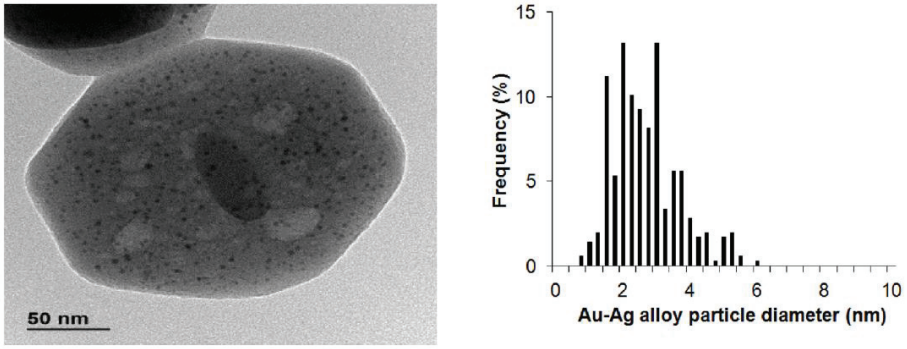

Figure 1.2.11 : HRTEM images of Au-Ag@Silicalite-1 and particle size distribution. [116]

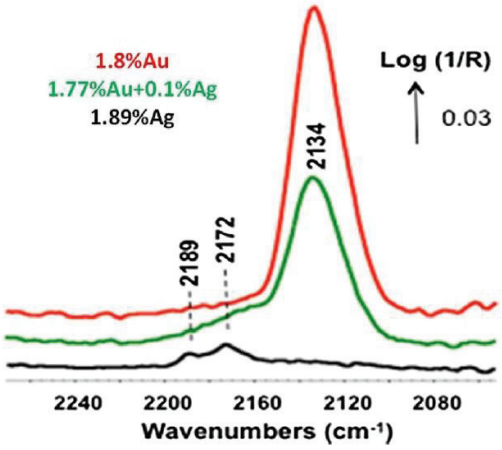

Figure 1.2.12 : Operando DRIFTS spectra collected over Au, Au-Au and Ag@silicalite-1. Feed: 2.8% CO + 8% O_2/He, 50 mL/min, 100 °C, 10 mg of catalyst. [116]

2.2.2. Impregnation

Metal impregnation on zeolites was also reported. Ag, Sn and Zn were impregnated on Y zeolite [117]. After the preparation, the catalysts were calcined and XPS analysis showed the presence of the metal oxide at the outer surface of the zeolite. Also, Ag was impregnated on activated zeolite [118]. The surface of the zeolite decreased after the impregnation due to partial pore blockage by Ag since Ag may not be well dispersed on the zeolite surface and in the pores.

2.2.3. Post-synthesis ion exchange

Post synthesis cation exchange is performed to zeolites to increase the pore size by replacing Na^+ or K^+ ions with Ca^{2+} or Mg^{2+}. For instance, the Ca-LTA form has a pore diameter of 0.5 nm higher than 0.4 nm for Na-LTA form [111]. Moreover, Iwamoto et al. [30][18] reported the remarkable catalytic activity of Cu-ZSM5 towards direct NO decomposition.

2.3. Treatment conditions

2.3.1. Calcination:

As reported [103], heating $Pd_{0.6}Au_{0.4}$ and $Pd_{0.22}Au_{0.78}$ alloy films in O_2 atmosphere at 300-500°C lead to the surface segregation of Pd but no bulk Pd oxidation. At 500-600°C, Pd oxidation started to take place. The authors suggest that at a Pd/Au atomic ratio lower than ~0.18 ($Pd_{0.18}Au = Pd_{0.15}Au_{0.85}$), Pd surface segregation and oxidation are extremely limited or may not even be possible. In another work [119], a $Pd_{0.7}Au_{0.3}$(110) alloy displayed the Pd surface segregation under O_2 pressure even at RT.

2.3.2. Reduction:

$Pd_{shell}Au_{core}/SiO_2$ was prepared with a 10% total metal loading where the precursor metal ions were reduced by sonication under Ar atmosphere [120]. A random alloy structure was obtained by heating at 300°C in H_2. PdAu/C alloy nanoparticles were prepared and treated with a 10% nitric acid solution for the selective removal of unalloyed Pd [70]. After that, a reduction treatment in H_2 similarly at 300°C was carried out for the reformation of the alloy. Heating under H_2 at 800°C lead to the full reduction of Pd/SiO_2 and resulted in the sintering of the nanoparticles [35]. However, heating under He at 800°C lead to the partial reduction of Pd and a lower average particle size.

2.4. Main characterization techniques

2.4.1. Electron microscopy

Various electron microscopy techniques are used according to the nature of the material to be investigated and the information required such as TEM, HRTEM, ETEM and SEM. These techniques can provide information about the shape and size of the nanoparticles. Moreover, EDX analysis allows the detection of the elements present and investigating alloying.

2.4.2. Powder X-ray diffraction (PXRD)

PXRD technique is useful to detect the crystalline phases of the active metals or the supports. Crystalline phases display XRD peaks corresponding the various crystallographic planes, and the peak intensity depends on the degree of crystallinity. Bragg's law is used to correlate the peak positions to the lattice parameters and crystallographic planes. Moreover, alloyed phases could also be detected where the peaks of alloyed phases fall in positions in between those of the monometallic phases [96][102][104]. Vegard's law [121] is then used to determine the approximate alloy composition. In general, XRD detects relatively large particles. For the identification of the phases, the observed XRD patterns are compared to the ICDD star-marked XRD reference files.

2.4.3. CO adsorption by DRIFTS

CO is used as a probe molecule for the DRIFTS technique since it adsorbs mostly molecularly on metal surfaces due to its high binding energy of ~1070 kJ/mol [122]. The stretching frequency of the adsorbed CO depends on the metal(s) present, the oxidation state of the metal(s), the adsorption mode (linear, bridged, or multi-bridged), the presence of co-adsorbates, the size of the particles, and also CO coverage. The coverage depends on the heats of adsorption, the adsorption temperature, and CO

pressure. Temkin's model [123][124] correlates the coverage to the heats of adsorption, the adsorption temperature and the applied CO pressure. In situ and operando measurements enable the characterization under conditions as relevant as possible to the actual catalytic conditions.

CO adsorption is useful for the characterization of the structure, particle size, and surface properties of metal nanoparticles and supports. The technique may also help investigate the formation of alloyed phases (random alloys [125] or single atom alloys [64][65][66]). The measurement is sensitive to the surface modifications under CO such as the surface segregation in bimetallic nanoparticles [126][127], the reduction of oxidized metals [128], or the sintering of the metal nanoparticles.

The limitation of the technique is that it is not directly quantitative [129]. The reason could be an inhomogeneous material composition, a temperature gradient that may exist in the DRIFTS cell [130], or a variation in the IR beam path length. Moreover, the presence of several adsorption sites and/or co-adsorbates may lead to the misinterpretation of the bands. More complexities may arise due to the surface segregation in alloyed nanoparticles [4]**(a review by our group)** or CO reactivity [131][132].

Fig. 1.2.13 shows the CO adsorption spectra over Au, Pd and AuPd/SiO_2 samples prepared by the successive wet impregnation where Au then Pd were impregnated. [66]. The authors observed three adsorption bands at: (i) 2127 cm^{-1} and the shoulder at 2108 cm^{-1} assigned to the CO linearly adsorbed over slightly positively charged Au and low coordinated Au, respectively; (ii) 2069 cm^{-1} assigned to the CO linearly adsorbed over Pd; and (iii) 1950 cm^{-1} assigned to the CO bridge adsorbed over Pd. Adding Pd resulted in the loss of the band at 2108 cm^{-1} indicating that Pd preferred the low coordination sites. Bridge CO adsorption on Pd was no longer observed at the Au/Pd atomic ratio of 40, indicating the presence of single Pd atoms in the Au matrix.

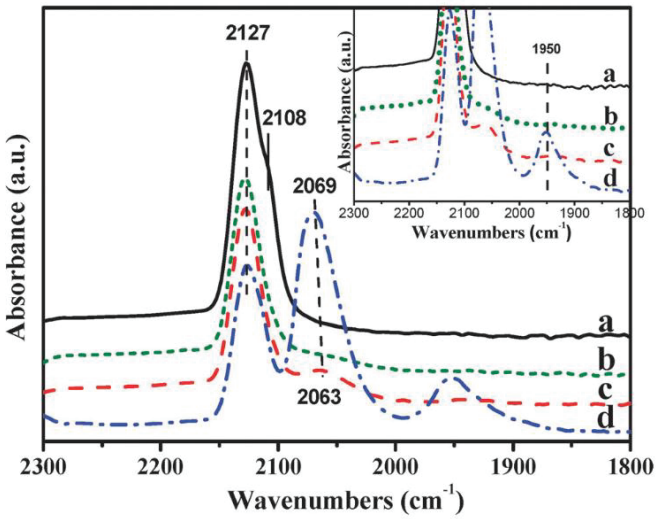

Figure 1.2.13 : CO adsorption of SiO_2-supported (a) Au, (b) $AuPd_{0.01}$, (c) $AuPd_{0.025}$ and (d) $AuPd_{0.1}$. [66]

3. NO_X removal processes

Nitric oxide (NO) is considered dangerous to life and health as it contributes to acid rains, reacts with ozone, and is also oxidized in air forming NO_2 which is dangerous for the respiratory system. NO is a major exhaust gas in combustion engines and several industrial processes. The following processes have been reported for the elimination of the NO_X emissions.

3.1. NO_X Storage Reduction (NSR)

NSR is used with lean-burn engines and works in two successive steps. First, in lean conditions, the NO_X species are oxidized and/or stored over the catalyst. Then, in combustion conditions, the stored species are reduced by HCs to N_2 and NH_3. Noble metals and zeolites can be used as catalysts. The process works at a λ (Air/Fuel) ratio higher than the TWC but is limited to a narrow temperature range for high conversions [133]. SiO_2 poisoning is also a major limitation [13]. It is also considered toxic due to the NH_3 emissions.

3.2. Selective Catalytic Reduction (SCR)

SCR [16] involves the conversion of NO to N_2 via reduction with NH_3, Urea or HCs. The reaction can be catalyzed using metal oxides, zeolites, or noble metals. SCR is a costly and hazardous process due to the high toxicity of the involved materials.

Selective Non-catalytic Reduction (SNCR) does not involve the use of a catalyst. The process is less practical than SCR due to the high temperature and reagents amounts required [17].

3.3. Three-Way Catalyst (TWC)

TWC [14][15] is based on the ability of noble metals (Pd, Pt or Rh) to perform three tasks simultaneously: the oxidation of CO to CO_2, the oxidation of HCs to CO_2 and H_2O, and the reduction of NO to N_2. At a stoichiometric λ (Air/Fuel) ratio, the catalyst works efficiently in all three tasks. In lean (O_2-rich) conditions such as diesel engines exhaust, the oxidation reactions are favored. The reduction of NO is favored with excess fuel i.e. a controlled O_2 level.

3.4. NO Direct Decomposition

As mentioned, direct NO decomposition to N_2 and O_2 is thermodynamically favored below 500°C and has a $\Delta H°$ of −90.2 kJ/mol at 25°C and a Gibbs free energy $\Delta G°$ of −86.6 kJ/mol [10]. Nonetheless, NO decomposition displays a very large kinetic barrier of ~335 kJ/mol [1][2] [134]. Several catalytic substances have been reported in literature.

3.4.1. Metal Oxides

Various metal oxides, doped metal oxides and mixed oxides were reported for the NO decomposition activity. Winters [19] studied NO decomposition over several metal oxides and reported an inhibition effect due to the presence of O_2. Table 1.3.1 also shows the reaction conditions and NO conversions reported over some metal oxides. The Ag-doped Co_3O_4 showed a superior activity compared to the non-doped catalyst where NO conversion increased from 9.3% to 45% [20]. Iwamoto et al. [18] studied the activity of several metal oxides and Co_3O_4 displayed the highest activity. However, O_2 had a detrimental effect on the activity. Mixing CeO_2 and CuO_X or NiO_X increased the conversion close to 100% compared to 4% while using CeO_2 in the absence of O_2 at 550°C [21]. Fig. 1.3.1 shows a proposed NO decomposition mechanism over rare earth oxides.

Table 1.3.1 : Reported NO decomposition data over some metal oxide catalysts.

Catalyst	NO conversion (%)	Reaction conditions					Ref.
		NO (%)	O_2 (%)	T (°C)	W/F ($g.s.cm^{-3}$)	GHSV (h^{-1})	
Co_3O_4	9.3	2	----	500	2		[20]
Ag-doped Co_3O_4	45	2	----	500	2		
Co_3O_4	25	2	----	500	0.5		[18]
Co_3O_4	2	2	5	500	0.5		
CeO_2	4	1	----	550		2100	[21]
CeO_2-CuO_X	98	1	----	550		2100	
CeO_2-NiO_X	97	1	----	550		2100	

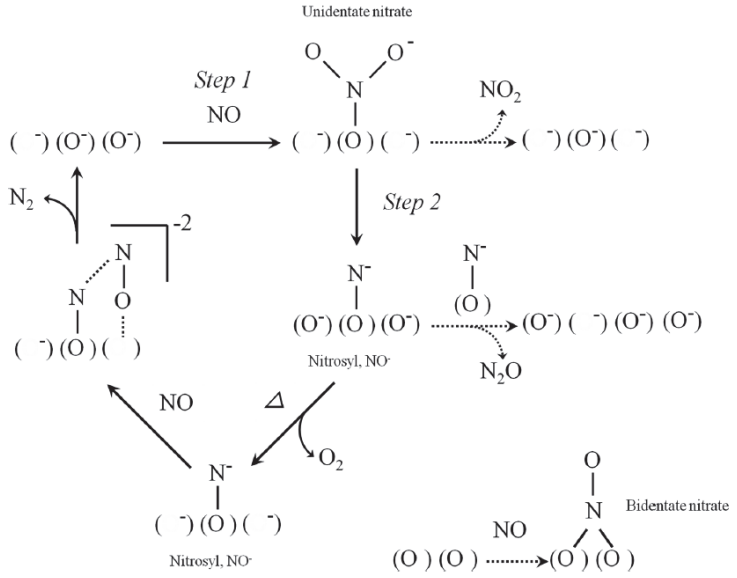

Figure 1.3.1 : Proposed NO decomposition mechanism over rare earth oxides catalyst. [22]

3.4.2. Perovskites

Ishihara et al. showed the promotional effect of metals such as Mg [23] or La and In [24] on the activity of $BaMnO_3$ in the absence of O_2 at high temperatures. Adding Mg enhanced the conversion from 30.3% to 88.5% at 850°C while La and In enhanced the conversion to 96.8% at 800°C. Table 1.3.2 shows the reaction conditions and NO conversions reported Fig. 1.3.2 shows a proposed NO decomposition mechanism over perovskites [25].

Table 1.3.2 : Reported NO decomposition data over some perovskite type catalysts.

Catalyst	NO conversion (%)	Reaction conditions					Ref.
		NO (%)	O_2 (%)	T (°C)	W/F ($g.s.cm^{-3}$)	GHSV (h^{-1})	
$BaMnO_3$	30.3	1	----	850	3		[23]
$BaMn_{0.8}Mg_{0.2}O_3$	88.5	1	----	850	3		
$La_{0.7}Ba_{0.3}Mn_{0.8}In_{0.2}O_3$	96.8	1	----	800	3		[24]

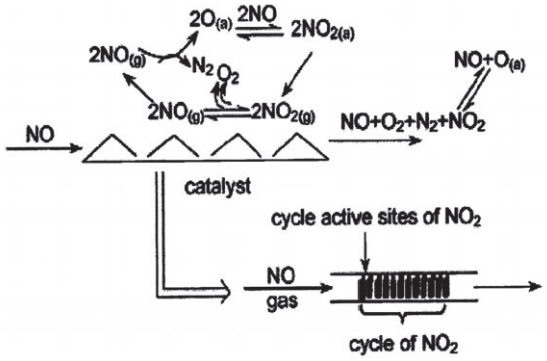

Figure 1.3.2 : Proposed NO decomposition mechanism over perovskite-type catalysts. [25]

3.4.3. Heteropoly acids

Ralph et al. [26] studied NO decomposition over phosphotungstic acid (HPW) and proposed an adsorption-decomposition mechanism as shown in the equations below:

$$H_3PW_{12}O_{40}.6H_2O + NO/O_2 \xrightarrow{\Delta} H_3PW_{12}O_{40}.3NO \qquad \text{Eq. 1.3.1}$$

$$H_3PW_{12}O_{40}.3NO + H_2O \xrightarrow{\Delta} H_3PW_{12}O_{40}.6H_2O + N_2 \qquad \text{Eq. 1.3.2}$$

Further works obtained NO conversions as high as 90% over titania-supported heteropoly acids [27] and 50% over silica-supported heteropoly acids [28]. It was also demonstrated that the presence of O_2 lead to a limited activity over heteropoly acids [29].

3.4.4. Cu-ZSM5 catalysts

The leading work of Iwamoto et. al [30] demonstrated the remarkable NO decomposition activity over Cu-exchanged zeolite. The catalytic activity was affected by the degree of the ion exchange and a high NO conversion to N_2 of 80-85% was achieved at 100% ion exchange. High conversions were also obtained with other groups [31] even in the presence of 5% O_2 in the feed [33] where also the addition of Ce and Zr induced a promotional effect to the activity of Cu-ZSM5. Table 1.3.3 shows the reaction conditions and NO conversions reported.

Table 1.3.3 : Reported NO decomposition data over some Cu-ZSM5 catalysts.

Catalyst	N_2 yield (%)	Reaction conditions					Ref.
		NO (%)	O_2 (%)	T (°C)	W/F ($g.s.cm^{-3}$)	GHSV (h^{-1})	
100% ion exchanged Cu-ZSM5	80-85	1	----	450	4		[30]
2.5-4% Cu-ZSM5	65	0.512	----	450	2		[31]
Cu-ZSM5	40	0.4	5	450		3000	[33]
Zr-Cu-Ce-ZSM5	75	0.4	5	450		3000	

A decomposition mechanism is proposed by Spoto et al [32] as shown in Fig. 1.3.3 involving a Cu^{+}-Cu^{2+} mechanism cycle. Oxygen was shown to result in an inhibition effect as reported by Valyon et al. using the equation below [135]. Iwamoto et al. reported the deactivation due to SO_2 [34].

$$r = \frac{k \times P_{NO}}{1 + K \times \sqrt{P_{O_2}}} \qquad \text{Eq. 1.3.3}$$

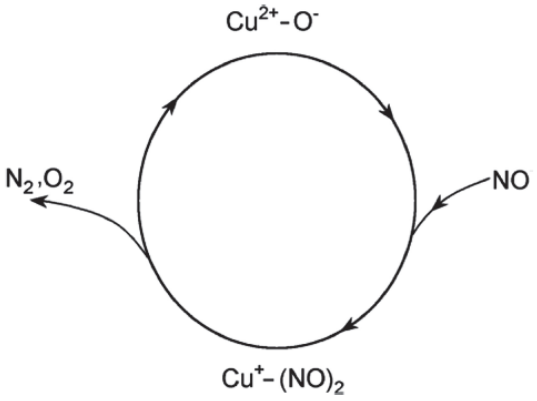

Figure 1.3.3 : Proposed NO decomposition mechanism over Cu-ZSM5. [32]

3.4.5. Supported noble Metals

Besides the remarkable results over ZSM5 catalysts, Iwamoto et al. [18] also studied NO decomposition over alumina supported noble metals (Pt, Pd, Rh, Ru). A high temperature was generally observed to enhance the activity of the metals. For instance, 0.5% Pt/Al2O3 showed a NO conversion to N_2 of only 2.1% at 400°C. Increasing the temperature to 700°C lead to a conversion increase to 47%. The presence of oxygen lead to a detrimental effect on the activity. Other works [35][36][37] also reported high activities (40-88%) at high temperatures (800-900°C). Table 1.3.4 shows the reaction conditions and NO conversions reported over noble metals.

Table 1.3.4 : Reported NO decomposition data over some supported noble metals.

Catalyst	NO conversion to N_2 (%)	Reaction conditions					Ref.
		NO (%)	O_2 (%)	T (°C)	W/F ($g.s.cm^{-3}$)	GHSV (h^{-1})	
0.5% Pt/Al_2O_3	2.1	2	----	400	0.5		[18]
0.5% Pt/Al_2O_3	10	2	----	500	0.5		
0.5% Pt/Al_2O_3	28	2	----	600	0.5		
0.5% Pt/Al_2O_3	47	2	----	700	0.5		
0.5% Pt/Al_2O_3	8	2	5	700	0.5		
0.5% Pt/Al_2O_3	62	0.1	----	700	0.5		
0.5% Pt/Al_2O_3	40	0.1	0.05	700	0.5		
5% Pd/SiO_2	20	~1	----	650		2100	[35]
	60	~1	----	800		2100	
5% Pd/Al_2O_3	88	0.1	----	900	1		[36]
$Pt_8Ir_1Au_1/Al_2O_3$	40	1	----	900	0.8		[37]

3.4.5.1. NO decomposition mechanism over noble metals

NO decomposition over metal surfaces possibly generally proceeds via the widely accepted reaction steps listed below including: (Eq. 1.3.4)-(Eq. 1.3.8) [136][137][138], (Eq. 1.3.9)-(Eq. 1.3.11) [139] and (Eq. 1.3.12)-(Eq. 1.3.13) [140].

$$NO + Pt \longleftrightarrow NO\text{-}Pt \qquad \text{Eq. 1.3.4}$$

$$NO\text{-}Pt + Pt \longleftrightarrow N\text{-}Pt + O\text{-}Pt \qquad \text{Eq. 1.3.5}$$

$$N\text{-}Pt + N\text{-}Pt \longrightarrow N_2 + 2\ Pt \qquad \text{Eq. 1.3.6}$$

$$N\text{-}Pt + NO\text{-}Pt \longleftrightarrow N_2O + 2\ Pt \qquad \text{Eq. 1.3.7}$$

$$NO\text{-}Pt + NO\text{-}Pt \longleftrightarrow N_2O + O\text{-}Pt + Pt \quad \text{Eq. 1.3.8}$$

$$NO\text{-}Pt + O\text{-}Pt \longleftrightarrow NO_2\text{-}Pt + Pt \quad \text{Eq. 1.3.9}$$

$$NO_2\text{-}Pt \longleftrightarrow NO_2 + Pt \quad \text{Eq. 1.3.10}$$

$$N_2O \longleftrightarrow N_2 + O_{ads} \quad \text{Eq. 1.3.11}$$

$$O_{ads} + O_{ads} \longleftrightarrow (O_2)_{ads} \quad \text{Eq. 1.3.12}$$

$$(O_2)_{ads} \longleftrightarrow O_2 \quad \text{Eq. 1.3.13}$$

The NO dimer formation (Eq. 1.3.8) was also suggested to be the path for NO decomposition over Pt [141] and La(Ba)Mn(In)O_3 [24]. The formation and further decomposition of N_2O (Eq. 1.3.7, Eq. 1.3.8 and Eq. 1.3.11) are also consistent with the lower kinetic barrier of N_2O decomposition (240-260 kJ/mol) [142][143] than that of NO decomposition (~335 kJ/mol) [1][2].

The activity is inhibited by oxygen as reported by Amirnazmi et al. using the equation below [38].

$$r = \frac{N \times k \times P_{NO}}{1 + \alpha \times K \times P_{O_2}} \quad \text{Eq. 1.3.14}$$

3.4.5.2. Challenges accompanying using noble metals as deNOx catalysts

The major challenges are:

(i) **The electronegativity (EN) of noble metals.** It was suggested [144] that the electronegativity of the metals could be a factor that governs the catalytic activity towards NO decomposition. The decomposition could proceed via a charge transfer from the metal into the unoccupied anti-bonding molecular orbitals of NO. Therefore, the metals to the left of the periodic table with low electronegativities are expected to be more active than the metals to the right. Fig. 1.3.4 shows the observed performance of the transition metals in the periods 4, 5 and 6 of the periodic table regarding the molecular (M) vs. the dissociative (D) adsorption of NO. The shown thick line represents the borderline between molecular and dissociative adsorption of NO at room temperature. The data indicate the relatively limited NO decomposition activity on noble metals.

4	Sc 1.36	Ti 1.54	V 1.63	Cr 1.66	Mn 1.55	Fe 1.83	Co 1.88	Ni (D+M) 1.91	Cu 1.9
5	Y 1.22	Zr 1.33	Nb	Mo 2.16	Tc	Ru	Rh 2.28	Pd (M) 2.2	Ag 1.93
6	La 1.1	Hf	Ta	W 2.36	Re	Os	Ir (D+M) 2.2	Pt (M) 2.28	Au 2.45

Figure 1.3.4 : Sections of the Periodic Table showing the room temperature adsorption behavior of NO. M denotes molecular adsorption and D dissociative adsorption on at least one surface, single crystal, or a polycrystalline surface. The thick line in the Periodic Table gives the borderline between molecular and dissociative adsorption at room temperature. The table is adapted from reference [144]. The values in red are the corresponding values of electronegativity on Pauling scale [145].

(ii) The adsorption behavior of the main species involved in the NOx decomposition reaction (NO, N and O) over noble metals. A previous study [146] showed by experimental and calculated data that the NO decomposition activity of noble metals (Fig. 1.3.5) falls in the order: Pd > Pt > Rh > Ru >> Ag > Au; where Ag and Au displayed extremely lower activities. The authors associated the observed superior activity of Pd with the fact that the Pd-O/Pd-N bond strength ratio is the lowest compared to the other metals investigated.

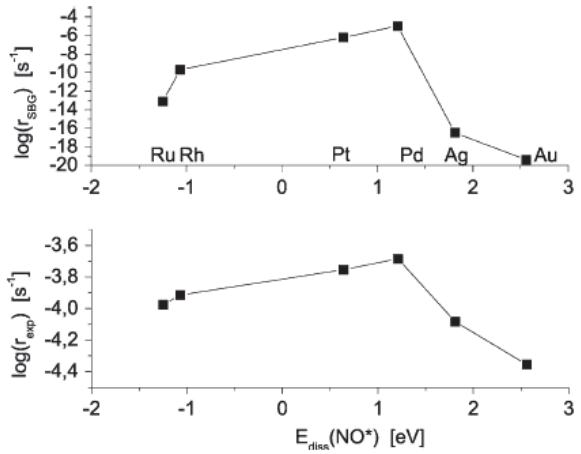

Figure 1.3.5 : The Sabatier–Gibbs microkinetic model (top) compared to the experimental activities (bottom) versus the dissociation energy of adsorbed NO. Reaction conditions: 1 vol.% NO/He, 25 mL/min, 600-650°C. Typically, 300 mg of each catalyst is used. The catalyst is the metal supported on $MgAl_2O_4$ by incipient wetness impregnation with a metal loading of 92 µmol/g. [146]

(iii)Cohesive energy of the metals. Another study [147] suggested another approach in order to understand the difference in the performance of transition metals towards NO decomposition activity. Fig. 1.3.6 shows a relation between the metal melting point (which is a direct measure of cohesive energy) and the tendency for NO dissociation. A higher melting point is associated

with a higher cohesive energy, and hence, a stronger NO-metal bond which in turn leads to a higher tendency for NO dissociation rather than molecular adsorption.

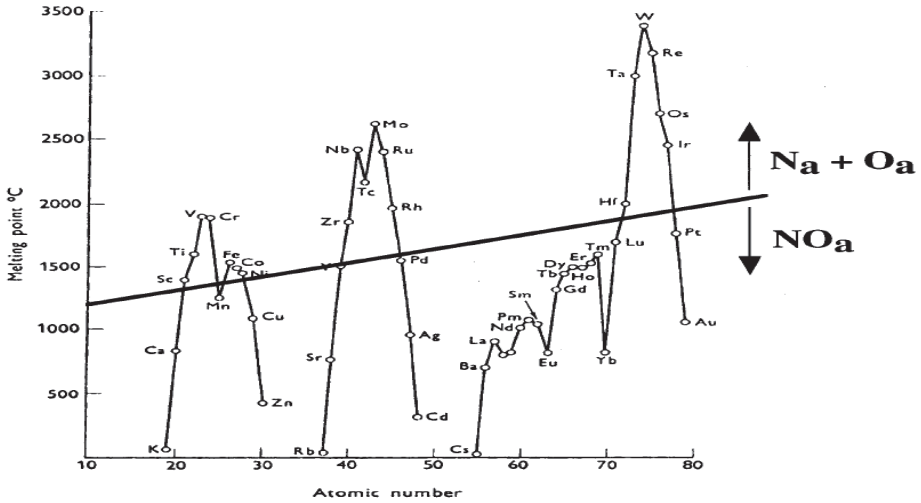

Figure 1.3.6 : The melting points of the transition metals, and rare earths, versus atomic number [147]. On this diagram we also show a suggested correlation between the propensity for a metal to dissociate NO, and its melting point.

(iv) The poisoning of the metal surface by oxygen (formed and/or introduced in the feed).

Oxygen is more strongly bound than NO to most noble metal surfaces [148]. At low temperatures, the strongly adsorbed oxygen adatoms could poison the metal surface since those can compete with NO for adsorption sites. At moderate temperatures (200-500°C), oxygen can lead to formation of the metal oxide (as observed with Pd [149]) which is inactive for NO decomposition. In such case, a mere redox reaction would take place between the metal and NO (Fig. 1.3.7) [35]. It is only at high temperatures that the metal oxide can be decomposed, and oxygen can be liberated off the metal surface and bulk restoring the metallic state. This explains the high activities achieved over noble metals at high temperatures.

From the above arguments, it can be concluded that noble metals adsorb NO molecularly rather than dissociatively at low temperatures. Moreover, at moderate temperatures, the active metals merely undergo a redox reaction with NO where the metal oxide is formed, that leads to deactivation. A high temperature is then required to restore the metallic state and enhance the catalytic activity. The presence of oxygen in the feed inhibits the catalytic activity since oxygen can oxidize the metal and can also compete with NO for adsorption sites.

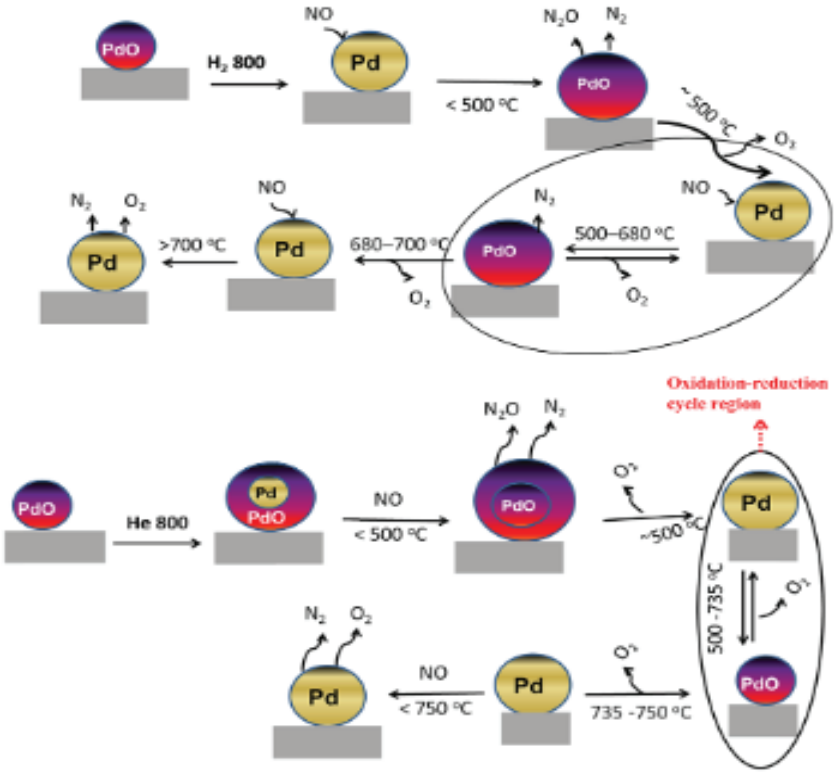

Figure 1.3.7 : Mechanism of the direct NO decomposition over PdO/SiO_2 catalysts in low, medium and high temperature regions over hydrogen and helium pretreated catalysts. [35]

Conclusions

This chapter introduced a few features of heterogeneous catalysis carried out on monometallic and bimetallic nanoparticles. Au features an excellent oxidation resistance and was reported to display catalytic activity such as in CO oxidation. Au can also form alloys with several metals. Alloying Au with Pd was reported to enhance the catalytic activity and oxidation resistance of Pd in several catalytic reactions. Various synthetic routes were reported for the preparation of numerous monometallic and Au-based bimetallic nanoparticles supported on oxide supports or encapsulated in zeolites. Several characterization techniques were also used to investigate the properties of the nanoparticles. The NO_X emissions represent a serious health hazard. Several processes were developed for the removal of these emissions such as NSR, SCR, SNCR, TWC and direct decomposition. Direct NO decomposition to N_2 and O_2 is a highly favorable green process since it does not require a fuel or reductants. Several catalysts were reported to show activity. Perovskites require high temperatures which is not practical. Metal oxides and heteropoly acids are active but the activity is inhibited by oxygen. Cu-ZSM5 was reported to display the highest activity at 300-600°C but is poisoned by SO_X and water. Noble metals are active but are poisoned by oxygen at moderate temperatures low than 500°C. The need for an active catalyst that resists deactivation is still present. The principle of the project is to combine the catalytic activity of noble metals at moderate temperatures and the oxidation resistance of Au. Au-based bimetallic alloy nanoparticles are expected to facilitate the desorption of O_2 and enhance the oxidation resistance of the active metal.

References

[1] F. Garin, "Mechanism of NOx decomposition," *Appl. Catal. A Gen.*, vol. 222, no. 1–2, pp. 183–219, 2001, doi: 10.1016/S0926-860X(01)00827-4.

[2] H. Wise and M. F. Frech, "Kinetics of decomposition of nitric oxide at elevated temperatures. I. Rate measurements in a quartz vessel," *J. Chem. Phys.*, vol. 20, no. 1, pp. 22–24, 1952, doi: 10.1063/1.1700189.

[3] R. A. (PhD Dissertation), "NO direct decomposition in the presence of excess oxygen over gold-based catalysts," 2021.

[4] T. Elgayyar, R. Atwi, A. Tuel, and F. C. Meunier, "Contributions and limitations of IR spectroscopy of CO adsorption to the characterization of bimetallic and nanoalloy catalysts," *Catal. Today*, vol. 373, pp. 59–68, 2021, doi: 10.1016/j.cattod.2021.01.009.

[5] T. Elgayyar *et al.*, "Au-Modified Pd catalyst exhibits improved activity and stability for NO direct decomposition," *Catal. Sci. Technol.*, vol. 11, no. 8, pp. 2908–2914, 2021, doi: 10.1039/d1cy00301a.

[6] R. Atwi, T. Elgayyar, F. J. Cadete Santos Aires, A. Tuel, and F. C. Meunier, "Revisiting the Evolution of IR Spectra of CO Adsorbed on Au Nanoparticles Supported on Non-reducible Supports," *Top. Catal.*, vol. 63, no. 15–18, pp. 1596–1605, 2020, doi: 10.1007/s11244-020-01372-2.

[7] Y. Yao, L. Chen, X. Mao, Y. Yang, J. Chen, and L. Zhou, "In Situ PM-IRRAS Study of CO Adsorption on Au Surfaces: Solving the Puzzle," *J. Phys. Chem. C*, vol. 125, no. 16, pp. 8606–8619, 2021, doi: 10.1021/acs.jpcc.1c01638.

[8] R. Atwi, T. Elgayyar, F. J. Cadete Santos Aires, A. Tuel, and F. C. Meunier, "Retraction Note to: Revisiting the Evolution of IR Spectra of CO Adsorbed on Au Nanoparticles Supported on Non-reducible Supports," *Top. Catal.*, vol. 64, no. 17–20, pp. 1054–1055, 2021, doi: 10.1007/s11244-021-01467-4.

[9] Y. B. Zeldovich, "The Oxidation of Nitrogen in Combustion and Explosions," *Acta Physicochim.*, vol. 21, pp. 577–628, 1946.

[10] H. S. Click, J. J. Klein, and W. Squire, "Single-pulse shock tube studies of the kinetics of the reaction N 2+O2⇄2NO between 2000-3000°K," *J. Chem. Phys.*, vol. 27, no. 4, pp. 850–857, 1957, doi: 10.1063/1.1743864.

[11] EEA, "https://www.eea.europa.eu/data-and-maps/indicators/eea-32-nitrogen-oxides-nox-emissions-1/assessment.2010-08-19.0140149032-3."

[12] EC, "https://ec.europa.eu/environment/air/sources/road.htm."

[13] N. Miyoshi and S. N. I. Mastumoto, "NOx storage-reduction catalyst (NSR catalyst) for automotive engines: Sulfur poisoning mechanism and improvement of catalyst performance," *Stud. Surf. Sci. Catal.*, vol. 121, pp. 245–250, 1999, doi: 10.1016/s0167-2991(99)80074-3.

[14] R. J. Farrauto and R. M. Heck, "Catalytic converters : state of the art and perspectives," *Catal. Today*, vol. 51, no. 3–4, pp. 351–360, 1999.

[15] S. Nandi *et al.*, "Relationship between design strategies of commercial three-way monolithic catalysts and their performances in realistic conditions," *Catal. Today*, vol. 384–386, no. April 2021, pp. 122–132, 2022, doi: 10.1016/j.cattod.2021.05.005.

[16] H. Kim *et al.*, "Current Catalyst Technology of Selective Catalytic Reduction (SCR) for NO x Removal in South Korea," *Catalysts*, vol. 10, no. 1, p. 52, 2020.

[17] E. S. P. B. V, "Formation and control of nitrogen oxides," *Catal. Today*, vol. 2, no. 4, pp. 369–379, 1988, doi: 10.1016/0920-5861(88)80002-6.

[18] M. Iwamoto and H. Hamada, "Catalysis Today, 10 (1991) 67-71," *Catal. Today*, vol. 10, p. 57, 1991.

[19] E. R. S. Winter, "The catalytic decomposition of nitric oxide by metallic oxides," *J. Catal.*, vol. 22, no. 2, pp. 158–170, 1971, doi: 10.1016/0021-9517(71)90182-5.

[20] H. Hamada, Y. Kintaichi, M. Sasaki, and T. Ito, "Silver-promoted Cobalt Oxide Catalysts for Direct Decomposition of Nitrogen Monoxide," *Chemistry Letters*, vol. 19, no. 7. pp. 1069–1070, 1990, doi: 10.1246/cl.1990.1069.

[21] G. K. Reddy, T. C. Peck, and C. A. Roberts, "CeO2-M xO y (M = Fe, Co, Ni, and Cu)-Based Oxides for Direct NO Decomposition," *J. Phys. Chem. C*, vol. 123, no. 47, pp. 28695–28706, 2019, doi: 10.1021/acs.jpcc.9b07736.

[22] S. Tsujimoto, K. Yasuda, T. Masui, and N. Imanaka, "Effects of Tb and Ba introduction on the reaction mechanism of direct NO decomposition over C-type cubic rare earth oxides based on Y2O 3," *Catal. Sci. Technol.*, vol. 3, no. 8, pp. 1928–1936, 2013, doi: 10.1039/c3cy20746c.

[23] H. Iwakuni, Y. Shinmyou, H. Yano, H. Matsumoto, and T. Ishihara, "Direct decomposition of NO into N2 and O2 on BaMnO3-based perovskite oxides," *Appl. Catal. B Environ.*, vol. 74, no. 3–4, pp. 299–306, 2007, doi: 10.1016/j.apcatb.2007.02.020.

[24] T. Ishihara *et al.*, "Direct decomposition of NO into N2 and O2 over La(Ba)Mn(In)O3 perovskite oxide," *J. Catal.*, vol. 220, no. 1, pp. 104–114, 2003, doi: 10.1016/S0021-9517(03)00265-3.

[25] J. Zhu, D. Xiao, J. Li, X. Xie, X. Yang, and Y. Wu, "Recycle - New possible mechanism of NO decomposition over perovskite(-like) oxides," *J. Mol. Catal. A Chem.*, vol. 233, no. 1–2, pp. 29–34, 2005, doi: 10.1016/j.molcata.2005.02.011.

[26] R. T. Yang and N. Chen, "A New Approach to Decomposition of Nitric Oxide Using Sorbent/Catalyst without Reducing Gas: Use of Heteropoly Compounds," *Ind. Eng. Chem. Res.*, vol. 33, no. 4, pp. 825–831, 1994, doi: 10.1021/ie00028a007.

[27] Z. Zhang, L. Zhu, J. Ma, S. Ren, and X. Yang, "Temperature programmed desorption-mass spectrometry study of no desorption and decomposition by Titania supported 12-tungstophosphoric acid," *React. Kinet. Catal. Lett.*, vol. 76, no. 1, pp. 93–101, 2002, doi: 10.1023/A:1015669529142.

[28] R. L. McCormick, S. K. Boonrueng, and A. M. Herring, "In situ IR and temperature programmed desorption-mass spectrometry study of NO absorption and decomposition by silica supported 12-tungstophosphoric acid," *Catal. Today*, vol. 42, no. 1–2, pp. 145–157, 1998, doi: 10.1016/S0920-5861(98)00085-6.

[29] J. Schnee, L. Delannoy, G. Costentin, and C. Thomas, "Unraveling the Direct Decomposition of NO xover Keggin Heteropolyacids and Their Deactivation Using a Combination of Gas-IR/MS and in Situ DRIFT Spectroscopy," *J. Phys. Chem. C*, vol. 124, no. 41, pp. 22459–22470, 2020, doi: 10.1021/acs.jpcc.0c05945.

[30] M. Iwamoto, H. Yahiro, K. Tanda, N. Mizuno, Y. Mine, and S. Kagawa, "Removal of nitrogen monoxide through a novel catalytic process. 1. Decomposition on excessively copper ion exchanged ZSM-5 zeolites," *J. Phys. Chem.*, vol. 95, no. 9, pp. 3727–3730, 1991, doi: 10.1021/j100162a053.

[31] T. Curtin, P. Grange, and B. Delmon, "The direct decomposition of nitrogen monoxide," *Catal. Today*, vol. 35, no. 1–2, pp. 121–127, 1997, doi: 10.1016/S0920-5861(96)00138-1.

[32] G. Spoto *et al.*, "Cu(I)-ZSM-5 zeolites prepared by reaction of H-ZSM-5 with gaseous CuCl: Spectroscopic characterization and reactivity towards carbon monoxide and nitric oxide," *Appl. Catal. B, Environ.*, vol. 3, no. 2–3, pp. 151–172, 1994, doi: 10.1016/0926-3373(93)E0032-7.

[33] P. Yang, J. Zhou, and Z. Wang, "Direct decomposition of NO into N2 and O2 over Cu /ZSM-5 containing Ce and Zr as promoter," *Adv. Mater. Res.*, vol. 113–116, pp. 1735–1739, 2010, doi: 10.4028/www.scientific.net/AMR.113-116.1735.

[34] M. Iwamoto, H. Yahiro, S. Shundo, Y. Yu-u, and N. Mizuno, "Influence of sulfur dioxide on catalytic removal of nitric oxide over copper ion-exchanged ZSM-5 zeolite," *Appl. Catal.*, vol. 69, no. 1, pp. 0–4, 1991, doi: 10.1016/S0166-9834(00)83286-8.

[35] G. K. Reddy, C. Ling, T. C. Peck, and H. Jia, "Understanding the chemical state of palladium during the direct NO decomposition-influence of pretreatment environment and reaction temperature," *RSC Adv.*, vol. 7, no. 32, pp. 19645–19655, 2017, doi: 10.1039/c7ra00836h.

[36] M. Haneda, Y. Kintaichi, I. Nakamura, T. Fujitani, and H. Hamada, "Comprehensive study combining surface science and real catalyst for NO direct decomposition," *Chem. Commun.*, vol. 2, no. 23, pp. 2816–2817, 2002, doi: 10.1039/b207619e.

[37] A. Morikawa, K. Okumura, M. Ishii, K. Kikuta, A. Suda, and H. Shinjo, "Characterization of termetallic Pt-Ir-Au catalysts for NO decomposition," *Rare Met.*, vol. 30, no. 1, pp. 53–57, Feb. 2011, doi: 10.1007/s12598-011-0196-6.

[38] A. Amirnazmi, J. E. Benson, and M. Boudart, "Oxygen inhibition in the decomposition of NO on metal oxides and platinum," *J. Catal.*, vol. 30, no. 1, pp. 55–65, 1973, doi: 10.1016/0021-9517(73)90051-1.

[39] B. J. Keene, "Review of data for the surface tension of pure metals," *Int. Mater. Rev.*, vol. 38, no. 4, pp. 157–192, 1993, doi: 10.1179/imr.1993.38.4.157.

[40] J. Emsley, "The Elements," *3rd Ed. Oxford Clarendon Press*, 1998.

[41] H. Okamoto and TB. Massalski, "Phase Diagrams of Binary Gold Alloys," *ASM Int.*, 1987.

[42] H. Okamoto, D. J. Chakrabarti, D. E. Laughlin, and T. B. Massalski, "The Au- Cu (gold-copper) system," *J. Phase Equilibria*, vol. 8, no. 5, pp. 454–474, 1987.

[43] T. Elgayyar, R. Atwi, A. Tuel, L. Burel, Y. Schuurman, and F. C. Meunier, "Evidencing Pt-Au alloyed domains on supported bimetallic nanoparticles using CO desorption kinetics," *Appl. Catal. A Gen.*, vol. 639, no. April, p. 118643, 2022, doi: 10.1016/j.apcata.2022.118643.

[44] F. C. Meunier, T. Elgayyar, K. Dembélé, and H. Kaper, “Stability of Pt-Adsorbed CO on Catalysts for Room Temperature-Oxidation of CO,” *Catalysts*, vol. 12, no. 5, pp. 1–12, 2022, doi: 10.3390/catal12050532.

[45] P. Unnikrishnan and D. Srinivas, *Heterogeneous Catalysis*. Elsevier Inc., 2016.

[46] C. H. Bartholomew, “Mechanisms of catalyst deactivation,” *Appl. Catal. A Gen.*, vol. 212, no. 1–2, pp. 17–60, 2001, doi: 10.1016/S0926-860X(00)00843-7.

[47] R. F. Marzke, “Quantum Size Effects in Small Metallic Particles,” *Catal. Rev.*, vol. 19, no. 1, pp. 43–65, 1979, doi: 10.1080/03602457908065100.

[48] Ryogo Kubo, “Electronic Properties of Metallic Fine Particles. I.,” *J. Phys. Soc. Jpn.*, vol. 17, pp. 975–986, 1962, doi: 10.1143/JPSJ.17.975.

[49] H. Hirai, Y. Nakao, and N. Toshima, “Colloidal Rhodium in Poly(Vinylpyrrolidone) As Hydrogenation Catalyst for Internal Olefins,” *Chem. Lett.*, vol. 7, no. 5, pp. 545–548, 1978, doi: 10.1246/cl.1978.545.

[50] H. Hirai, Y. Nakao, and N. Toshima, “Preparation of Colloidal Transition Metals in Polymers by Reduction with Alcohols or Ethers,” *J. Macromol. Sci. Part A - Chem.*, vol. 13, no. 6, pp. 727–750, 1979, doi: 10.1080/00222337908056685.

[51] H. Hirai, Y. Nakao, and N. Toshima, “Journal of Macromolecular Science : Part A - Chemistry : Pure and Applied Chemistry Preparation of Colloidal Transition Metals in Polymers by Reduction with Alcohols or Ethers,” *J. Macromol. Sci. Part A - Chem.*, vol. 12, no. 8, pp. 1117–1141, 1978.

[52] G. J. Hutchings, “Vapor phase hydrochlorination of acetylene: Correlation of catalytic activity of supported metal chloride catalysts,” *J. Catal.*, vol. 96, no. 1, pp. 292–295, 1985.

[53] O. G. Ellert, M. V Tsodikov, S. A. Nikolaev, and V. M. Novotortsev, “Bimetallic nanoalloys in heterogeneous catalysis of industrially important reactions: synergistic effects and structural organization of active components,” *Russ. Chem. Rev.*, vol. 83, no. 8, pp. 718–732, 2014, doi: 10.1070/rc2014v083n08abeh004432.

[54] R. Ferrando, J. Jellinek, and R. L. Johnston, “Nanoalloys : From Theory to Applications of Alloy Clusters and Nanoparticles,” *Chem. Rev.*, vol. 108, no. 3, pp. 845--910, 2008, doi: 10.1021/cr040090g.

[55] Z. Peng and H. Yang, “Designer platinum nanoparticles: Control of shape, composition in alloy, nanostructure and electrocatalytic property,” *Nano Today*, vol. 4, no. 2, pp. 143–164, 2009, doi: 10.1016/j.nantod.2008.10.010.

[56] M. Chi *et al.*, “Surface faceting and elemental diffusion behaviour at atomic scale for alloy nanoparticles during in situ annealing,” *Nat. Commun.*, vol. 6, pp. 1–9, 2015, doi: 10.1038/ncomms9925.

[57] S. J. Oldenburg, R. D. Averitt, S. L. Westcott, and N. J. Halas, “Nanoengineering of optical resonances,” *Chem. Phys. Lett.*, vol. 288, no. 2–4, pp. 243–247, 1998, doi: 10.1016/S0009-2614(98)00277-2.

[58] Y.-H. Tee, L. Bachas, and D. Bhattacharyya, “Degradation of Trichloroethylene by Iron-Based Bimetallic Nanoparticles,” *J. Phys. Chem. C*, vol. 113, no. 28, pp. 12616–12616, 2009, doi: 10.1021/jp905273a.

[59] K. J. Carroll *et al.*, “One-pot aqueous synthesis of Fe and Ag core/shell nanoparticles,” *Chem. Mater.*, vol. 22, no. 23, pp. 6291–6296, 2010, doi: 10.1021/cm101996u.

[60] L. Gan, R. Yu, J. Luo, Z. Cheng, and J. Zhu, “Lattice strain distributions in individual dealloyed Pt-Fe catalyst nanoparticles,” *J. Phys. Chem. Lett.*, vol. 3, no. 7, pp. 934–938, 2012, doi: 10.1021/jz300192b.

[61] R. K. Rai *et al.*, “Access to highly active Ni-Pd bimetallic nanoparticle catalysts for C-C coupling reactions,” *Catal. Sci. Technol.*, vol. 6, no. 14, pp. 5567–5579, 2016, doi: 10.1039/c6cy00037a.

[62] J. He *et al.*, “Pt–Pd bimetallic nanoparticles anchored on uniform mesoporous MnO2 sphere as an advanced nanocatalyst for highly efficient toluene oxidation,” *Green Energy Environ.*, no. xxxx, 2021, doi: 10.1016/j.gee.2021.03.002.

[63] R. Wang *et al.*, “Graphene-supported Au–Pd bimetallic nanoparticles with excellent catalytic performance in selective oxidation of methanol to methyl formate,” *Chem. Commun.*, vol. 49, no. 74, pp. 8250–8252, 2013, doi: 10.1039/c3cc43948h.

[64] A. V. Rassolov *et al.*, “Formation of Isolated Single-Atom Pd1 Sites on the Surface of Pd–Ag/Al2O3 Bimetallic Catalysts,” *Kinet. Catal.*, vol. 61, no. 5, pp. 758–767, 2020, doi: 10.1134/S0023158420050080.

[65] A. V. Rassolov, G. O. Bragina, G. N. Baeva, I. S. Mashkovsky, and A. Y. Stakheev, “Alumina-Supported Palladium–Silver Bimetallic Catalysts with Single-Atom Pd1 Sites in the Liquid-Phase Hydrogenation of Substituted Alkynes,” *Kinet. Catal.*, vol. 61, no. 6, pp. 869–878, 2020, doi: 10.1134/S0023158420060129.

[66] G. X. Pei *et al.*, “Promotional effect of Pd single atoms on Au nanoparticles supported on silica for the selective hydrogenation of acetylene in excess ethylene,” *New J. Chem.*, vol. 38, no. 5, pp. 2043–2051, 2014, doi: 10.1039/c3nj01136d.

[67] G. C. Bond, P. A. Sermon, G. Webb, D. A. Buchanan, and P. B. Wells, “Hydrogenation over supported gold catalysts,” *J. Chem. Soc. Chem. Commun.*, no. 13, pp. 444–445, 1973, doi: 10.1039/C3973000444b.

[68] N. Haruta, Masatake and Kobayashi, Tetsuhiko and Sano, Hiroshi and Yamada, "Novel gold catalysts for the oxidation of carbon monoxide at a temperature far below 0 C," *Chem. Lett.*, vol. 16, no. 2, pp. 405–408, 1987.

[69] S. Karanjit *et al.*, "Significant stabilization of palladium by gold in the bimetallic nanocatalyst leading to an enhanced activity in the hydrodechlorination of aryl chlorides," *Chem. Commun.*, vol. 51, no. 64, pp. 12724–12727, 2015, doi: 10.1039/c5cc04432d.

[70] M. Bonarowska, Z. Kaszkur, D. Łomot, M. Rawski, and Z. Karpiński, "Effect of gold on catalytic behavior of palladium catalysts in hydrodechlorination of tetrachloromethane," *Appl. Catal. B Environ.*, vol. 162, pp. 45–56, 2015, doi: 10.1016/j.apcatb.2014.06.007.

[71] F. Ksar, L. Ramos, B. Keita, L. Nadjo, P. Beaunier, and H. Remita, "Bimetallic palladium-gold nanostructures: application in ethanol oxidation," *Chem. Mater.*, vol. 21, no. 15, pp. 3677–3683, 2009, doi: 10.1021/cm901364w.

[72] L. D. Zhu, T. S. Zhao, J. B. Xu, and Z. X. Liang, "Preparation and characterization of carbon-supported sub-monolayer palladium decorated gold nanoparticles for the electro-oxidation of ethanol in alkaline media," *J. Power Sources*, vol. 187, no. 1, pp. 80–84, 2009, doi: 10.1016/j.jpowsour.2008.10.089.

[73] T. A. G. Silva, E. Teixeira-Neto, N. López, and L. M. Rossi, "Volcano-like behavior of Au-Pd core-shell nanoparticles in the selective oxidation of alcohols," *Sci. Rep.*, vol. 4, pp. 1–5, 2014, doi: 10.1038/srep05766.

[74] X. Zhu *et al.*, "Optimising surface d charge of AuPd nanoalloy catalysts for enhanced catalytic activity," *Nat. Commun.*, vol. 10, no. 1, pp. 1–11, 2019, doi: 10.1038/s41467-019-09421-5.

[75] A. M. Venezia, V. La Parola, V. Nicolì, and G. Deganello, "Effect of gold on the HDS activity of supported palladium catalysts," *J. Catal.*, vol. 212, no. 1, pp. 56–62, 2002, doi: 10.1006/jcat.2002.3778.

[76] D. Zhao and B. Q. Xu, "Enhancement of Pt utilization in electrocatalysts by using gold nanoparticles," *Angew. Chemie - Int. Ed.*, vol. 45, no. 30, pp. 4955–4959, 2006, doi: 10.1002/anie.200600155.

[77] J. P. Sim, B. J. Lee, G. H. Han, D. H. Kim, and K. Y. Lee, "Promotional effect of Au on Fe/HZSM-5 catalyst for methane dehydroaromatization," *Fuel*, vol. 274, no. April, p. 117852, 2020, doi: 10.1016/j.fuel.2020.117852.

[78] C. Especel, D. Duprez, and F. Epron, "Bimetallic catalysts for hydrogenation in liquid phase," *Comptes Rendus Chim.*, vol. 17, no. 7, pp. 790–800, 2014, doi: 10.1016/j.crci.2013.12.009.

[79] A. G. Boudjahem, T. Mokrane, A. Redjel, and M. M. Bettahar, "Silica supported nanopalladium prepared by hydrazine reduction," *Comptes Rendus Chim.*, vol. 13, no. 12, pp. 1433–1439, 2010, doi: 10.1016/j.crci.2010.06.022.

[80] A. Garron, K. Lázár, and F. Epron, "Effect of the support on tin distribution in Pd-Sn/Al2O 3 and Pd-Sn/SiO2 catalysts for application in water denitration," *Appl. Catal. B Environ.*, vol. 59, no. 1–2, pp. 57–69, 2005, doi: 10.1016/j.apcatb.2005.01.002.

[81] A. Dasgupta, E. K. Zimmerer, R. J. Meyer, and R. M. Rioux, "Generalized approach for the synthesis of silica supported Pd-Zn, Cu-Zn and Ni-Zn gamma brass phase nanoparticles," *Catal. Today*, vol. 334, no. July 2018, pp. 231–242, 2019, doi: 10.1016/j.cattod.2018.10.050.

[82] Y. T. Tsu and Y. W. Chen, "Preparation of gold-containing binary metal clusters by co-deposition-precipitation method and for hydrogenation of chloronitrobenzene," *AIMS Mater. Sci.*, vol. 4, no. 3, pp. 738–754, 2017, doi: 10.3934/matersci.2017.3.738.

[83] W. Zou and R. D. Gonzalez, "The preparation of silica supported Pd catalysts: the effect of pretreatment variables on particle size," *Catal. Letters*, vol. 12, no. 1–3, pp. 73–86, 1992, doi: 10.1007/BF00767190.

[84] Y. K. Leong, "Yield stress and zeta potential of nanoparticulate silica dispersions under the influence of adsorbed hydrolysis products of metal ions - Cu(II), Al(III) and Th(IV)," *J. Colloid Interface Sci.*, vol. 292, no. 2, pp. 557–566, 2005, doi: 10.1016/j.jcis.2005.06.004.

[85] F. Gauthard, F. Epron, and J. Barbier, "Palladium and platinum-based catalysts in the catalytic reduction of nitrate in water: Effect of copper, silver, or gold addition," *J. Catal.*, vol. 220, no. 1, pp. 182–191, 2003, doi: 10.1016/S0021-9517(03)00252-5.

[86] X. Liu *et al.*, "Synthesis of thermally stable and highly active bimetallic Au-Ag nanoparticles on inert supports," *Chem. Mater.*, vol. 21, no. 2, pp. 410–418, 2009, doi: 10.1021/cm8027725.

[87] J. C. Bauer *et al.*, "Synthesis of silica supported AuCu nanoparticle catalysts and the effects of pretreatment conditions for the CO oxidation reaction," *Phys. Chem. Chem. Phys.*, vol. 13, no. 7, pp. 2571–2581, 2011, doi: 10.1039/c0cp01859g.

[88] R. J. Davis and M. Boudart, "Structure of supported PdAu clusters determined by X-ray absorption spectroscopy," *J. Phys. Chem.*, vol. 98, no. 21, pp. 5471–5477, 1994, doi: 10.1021/j100072a012.

[89] H. Kusama, K. Okabe, K. Sayama, and H. Arakawa, "Alcohol synthesis by catalytic hydrogenation of CO2 over Rh-Co/SiO2," *Appl. Organomet. Chem.*, vol. 14, no. 12, pp. 836–840, 2000, doi: 10.1002/1099-

0739(200012)14:12<836::AID-AOC97>3.0.CO;2-C.

[90] W. M. Chen, Y. J. Ding, D. H. Jiang, Z. D. Pan, and H. Y. Luo, "An effective method of controlling metal particle size on impregnated Rh-Mn-Li/SiO2 catalyst," *Catal. Letters*, vol. 104, no. 3–4, pp. 177–180, 2005, doi: 10.1007/s10562-005-7948-6.

[91] J. Scalbert, C. Daniel, Y. Schuurman, C. Thomas, and F. C. Meunier, "Rational design of a CO2-resistant toluene hydrogenation catalyst based on FT-IR spectroscopy studies," *J. Catal.*, vol. 318, pp. 61–66, 2014, doi: 10.1016/j.jcat.2014.07.013.

[92] L. Jiao and J. R. Regalbuto, "The synthesis of highly dispersed noble and base metals on silica via strong electrostatic adsorption: I. Amorphous silica," *J. Catal.*, vol. 260, no. 2, pp. 329–341, 2008, doi: 10.1016/j.jcat.2008.09.022.

[93] A. Hugon, L. Delannoy, J. M. Krafft, and C. Louis, "Selectivehydrogenation of 1,3-butadiene in the presence of an excess of alkenes over supported bimetallic gold-palladium catalysts," *J. Phys. Chem. C*, vol. 114, no. 24, pp. 10823–10835, 2010, doi: 10.1021/jp100479b.

[94] T. Akita, P. Lu, S. Ichikawa, K. Tanaka, and M. Haruta, "Analytical TEM study on the dispersion of Au nanoparticles in Au / TiO 2 catalyst prepared under various temperatures," *Surf. Interface Anal.*, vol. 31, no. 2, pp. 73–78, 2001.

[95] K. P. De Jong, J. H. E. Glezer, H. P. C. E. Kuipers, A. Knoester, and C. A. Emeis, "Highly dispersed Rh/SiO2 and Rh/MnO/SiO2 catalysts. 1. Synthesis, Characterization, and CO Hydrogenation Activity," *J. Catal.*, vol. 124, no. 2, pp. 520–529, 1990, doi: 10.1016/0021-9517(90)90198-S.

[96] X. Yang *et al.*, "An effective Pd-promoted gold catalyst supported on mesoporous silica particles for the oxidation of benzyl alcohol," *Appl. Catal. B Environ.*, vol. 140–141, pp. 419–425, 2013, doi: 10.1016/j.apcatb.2013.04.029.

[97] C. Resch, H. F. Berger, K. D. Rendulic, and E. Bertel, "Adsorption dynamics for the system hydrogen/palladium and its relation to the surface electronic structure," *Surf. Sci.*, vol. 316, no. 3, 1994, doi: 10.1016/0039-6028(94)91213-0.

[98] G. L. Holleck, "Diffusion and solubility of hydrogen in palladium and palladium-silver alloys," *J. Phys. Chem.*, vol. 74, no. 3, pp. 503–511, 1970, doi: 10.1021/j100698a005.

[99] K. D. Beard, M. T. Schaal, J. W. Van Zee, and J. R. Monnier, "Preparation of highly dispersed PEM fuel cell catalysts using electroless deposition methods," *Appl. Catal. B Environ.*, vol. 72, no. 3–4, pp. 262–271, 2007, doi: 10.1016/j.apcatb.2006.11.006.

[100] J. Rebelli, A. A. Rodriguez, S. Ma, C. T. Williams, and J. R. Monnier, "Preparation and characterization of silica-supported, group IB-Pd bimetallic catalysts prepared by electroless deposition methods," *Catal. Today*, vol. 160, no. 1, pp. 170–178, 2011, doi: 10.1016/j.cattod.2010.06.011.

[101] N. Mimura, N. Hiyoshi, M. Date, T. Fujitani, and F. Dumeignil, "Microscope Analysis of Au – Pd / TiO 2 Glycerol Oxidation Catalysts Prepared by Deposition – Precipitation Method," *Catal. Letters*, vol. 144, no. 12, pp. 2167–2175, 2014, doi: 10.1007/s10562-014-1382-6.

[102] T. A. G. Silva, C. P. Ferraz, R. V. Gonçalves, E. Teixeira-Neto, R. Wojcieszak, and L. M. Rossi, "Restructuring of Gold-Palladium Alloyed Nanoparticles: A Step towards More Active Catalysts for Oxidation of Alcohols," *ChemCatChem*, vol. 11, no. 16, pp. 4021–4027, 2019, doi: 10.1002/cctc.201900553.

[103] L. Hilaire, P. Légaré, Y. Holl, and G. Maire, "Interaction of oxygen and hydrogen with Pd-Au alloys: An AES and XPS study," *Surf. Sci.*, vol. 103, no. 1, pp. 125–140, 1981, doi: 10.1016/0039-6028(81)90103-5.

[104] H. Kobayashi, M. Yamauchi, R. Ikeda, and H. Kitagawa, "Atomic-level Pd-Au alloying and controllable hydrogen-absorption properties in size-controlled nanoparticles synthesized by hydrogen reduction," *Chem. Commun.*, no. 32, pp. 4806–4808, 2009, doi: 10.1039/b907875d.

[105] X. Wan *et al.*, "Base-free aerobic oxidation of 5-hydroxymethyl-furfural to 2,5-furandicarboxylic acid in water catalyzed by functionalized carbon nanotube-supported au-pd alloy nanoparticles," *ACS Catal.*, vol. 4, no. 7, pp. 2175–2185, 2014, doi: 10.1021/cs5003096.

[106] W. M. MEIER and D. H. OLSON, "Zeolite Frameworks," *Adv. Chem.*, vol. 1, pp. 155–170, 1971, doi: 10.1021/ba-1971-0101.ch014.

[107] S. M. Csicsery, "Catalysis by shape selective zeolites - science and technology," *Pure Appl. Chem.*, vol. 58, no. 6, pp. 841–856, 1986, doi: 10.1351/pac198658060841.

[108] Y. Li, L. Li, and J. Yu, "Applications of Zeolites in Sustainable Chemistry," *Chem*, vol. 3, no. 6, pp. 928–949, 2017, doi: 10.1016/j.chempr.2017.10.009.

[109] "http://www.iza-structure.org/databases/."

[110] V. Gramlich and W. M. Meier, "The crystal structure of hydrated NaA: A detailed refinement of a

pseudosymmetric zeolite structure," *Zeitschrift fur Krist. - New Cryst. Struct.*, vol. 133, no. 133, pp. 134–149, 1971, doi: 10.1524/zkri.1971.133.133.134.

[111] Y. Wang, F. F. Ren, D. H. Pan, and J. H. Ma, "A hierarchically micro-meso-macroporous zeolite caa for methanol conversion to dimethyl ether," *Crystals*, vol. 6, no. 11, pp. 1–10, 2016, doi: 10.3390/cryst6110155.

[112] S. Goel, Z. Wu, S. I. Zones, and E. Iglesia, "Synthesis and catalytic properties of metal clusters encapsulated within small-pore (SOD, GIS, ANA) zeolites," *J. Am. Chem. Soc.*, vol. 134, no. 42, pp. 17688--17695, 2012, doi: 10.1021/ja307370z.

[113] T. Otto, J. M. Ramallo-López, L. J. Giovanetti, F. G. Requejo, S. I. Zones, and E. Iglesia, "Synthesis of stable monodisperse AuPd, AuPt, and PdPt bimetallic clusters encapsulated within LTA-zeolites," *J. Catal.*, vol. 342, pp. 125–137, 2016, doi: 10.1016/j.jcat.2016.07.017.

[114] Z. Wu, S. Goel, M. Choi, and E. Iglesia, "Hydrothermal synthesis of LTA-encapsulated metal clusters and consequences for catalyst stability, reactivity and selectivity," *J. Catal.*, vol. 311, pp. 458–468, 2014, doi: 10.1016/j.jcat.2013.12.021.

[115] S. Li *et al.*, "Hollow Zeolite Single-Crystals Encapsulated Alloy Nanoparticles with Controlled Size and Composition," *ChemNanoMat*, vol. 2, no. 6, pp. 534–539, 2016, doi: 10.1002/cnma.201600058.

[116] R. Atwi, A. Tuel, M. Maffre, L. Burel, J. L. Rousset, and F. Meunier, "Highly dispersed Au, Ag and Au-Ag alloy nanoparticles encapsulated in single crystal multi-hollow silicalite-1," *Appl. Catal. A Gen.*, vol. 569, no. October 2018, pp. 86–92, 2019, doi: 10.1016/j.apcata.2018.10.028.

[117] L. P. Ozorio *et al.*, "Metal-impregnated zeolite y as efficient catalyst for the direct carbonation of glycerol with CO2," *Appl. Catal. A Gen.*, vol. 504, pp. 187–191, 2015, doi: 10.1016/j.apcata.2014.12.010.

[118] S. Sumari, F. Fajaroh, I. Bagus Suryadharma, A. Santoso, and A. Budianto, "Zeolite Impregnated with Ag as Catalysts for Glycerol Conversion to Ethanol Assisted by Ultrasonic," *IOP Conf. Ser. Mater. Sci. Eng.*, vol. 515, no. 1, pp. 0–10, 2019, doi: 10.1088/1757-899X/515/1/012075.

[119] M. C. Saint-Lager *et al.*, "Oxygen-Induced Changes of the Au30Pd70(110) Surface Structure and Composition under Increasing O2 Pressure," *J. Phys. Chem. C*, vol. 122, no. 39, pp. 22588–22596, 2018, doi: 10.1021/acs.jpcc.8b07068.

[120] T. Nakagawa *et al.*, "Structural analysis of sonochemically prepared Au/Pd nanoparticles dispersed in porous silica matrix," *Ultrason. Sonochem.*, vol. 12, no. 4, pp. 249–254, 2005, doi: 10.1016/j.ultsonch.2004.02.002.

[121] A. R. Denton and N. W. Ashcroft, "Vegard's law," *Phys. Rev. A*, vol. 43, no. 6, pp. 3161–3164, 1991.

[122] S. W. Benson, "Resource papers - III bond energies," *J. Chem. Educ.*, vol. 42, no. 9, pp. 502–515, 1965, doi: 10.1021/ed042p502.

[123] O. Dulaurent and D. Bianchi, "Adsorption isobars for CO on a Pt/Al2O3 catalyst at high temperatures using FTIR spectroscopy: Isosteric heat of adsorption and adsorption model," *Appl. Catal. A Gen.*, vol. 196, no. 2, pp. 271–280, 2000, doi: 10.1016/S0926-860X(99)00472-X.

[124] O. Dulaurent, M. Nawdali, A. Bourane, and D. Bianchi, "Heat of adsorption of carbon monoxide on a Ru/Al2O3 catalyst using adsorption equilibrium conditions at high temperatures," *Appl. Catal. A Gen.*, vol. 201, no. 2, pp. 271–279, 2000, doi: 10.1016/S0926-860X(00)00447-6.

[125] L. Zhang *et al.*, "Efficient and durable Au alloyed Pd single-atom catalyst for the Ullmann reaction of aryl chlorides in water," *ACS Catal.*, vol. 4, no. 5, pp. 1546–1553, 2014, doi: 10.1021/cs500071c.

[126] H. Liao, A. Fisher, and Z. J. Xu, "Surface Segregation in Bimetallic Nanoparticles : A Critical Issue in Electrocatalyst Engineering," pp. 1–26, 2015, doi: 10.1002/smll.201403380.

[127] H. An, H. Ha, M. Yoo, and H. Y. Kim, "Understanding the atomic-level process of CO-adsorption-driven surface segregation of Pd in (AuPd)147 bimetallic nanoparticles," *Nanoscale*, vol. 9, no. 33, pp. 12077–12086, 2017, doi: 10.1039/c7nr04435f.

[128] G. Spezzati *et al.*, "Atomically dispersed Pd-O species on CeO2(111) as highly active sites for low-temperature CO oxidation," *ACS Catal.*, vol. 7, no. 10, pp. 6887–6891, 2017, doi: 10.1021/acscatal.7b02001.

[129] J. Sirita, S. Phanichphant, and F. C. Meunier, "Quantitative Analysis of Adsorbate Concentrations by Diffuse Reflectance FT-IR," vol. 79, no. 10, pp. 3912–3918, 2007, doi: 10.1021/ac0702802.

[130] H. Li, M. Rivallan, F. Thibault-Starzyk, A. Travert, and F. C. Meunier, "Effective bulk and surface temperatures of the catalyst bed of FT-IR cells used for in situ and operando studies," *Phys. Chem. Chem. Phys.*, vol. 15, no. 19, pp. 7321–7327, 2013.

[131] F. J. Cadete Santos Aires, C. Deranlot, Y. Jugnet, L. Piccolo, and J.-C. Bertolini, "METALLIC SURFACES UNDER ELEVATED GAS PRESSURE STUDIED IN SITU BY SCANNING TUNNELING MICROSCOPY: O 2 , H 2 /Au(111); CO/Au(110)," *B. N. Dev (Ed.), Proc. Int. Conf. Phys. Surfaces Interfaces, World Sci. Publ.*

Singapore, no. lll, pp. 13–21, 2003, doi: 10.1142/9789812704221_0002.

[132] Y. Iwasawa, R. Mason, M. Textor, and G. A. Somorjai, "The reactions of carbon monoxide at coordinatively unsaturated sites on a platinum surface," *Chem. Phys. Lett.*, vol. 44, no. 3, pp. 468–470, 1976, doi: 10.1016/0009-2614(76)80706-3.

[133] S. Matsumoto, K. Yokota, H. Doi, M. Kimura, K. Sekizawa, and S. Kasahara, "Research on new DeNOx catalysts for automotive engines," *Catal. Today*, vol. 22, no. 1, pp. 127–146, 1994, doi: 10.1016/0920-5861(94)80097-9.

[134] Y. Zhang, G. Cao, and X. Yang, "Advances in De-NOxMethods and Catalysts for Direct Catalytic Decomposition of NO: A Review," *Energy and Fuels*, vol. 35, no. 8, pp. 6443–6464, 2021, doi: 10.1021/acs.energyfuels.1c00330.

[135] J. Valyon and W. K. Hall, "Studies of the surface species formed from NO on copper zeolites," *J. Phys. Chem.*, vol. 97, no. 6, pp. 1204–1212, 1993, doi: 10.1021/j100108a016.

[136] V. Medhekar, V. Balakotaiah, and M. P. Harold, "TAP study of NOx storage and reduction on Pt/Al2O3 and Pt/Ba/Al2O3," *Catal. Today*, vol. 121, no. 3–4, pp. 226–236, 2007, doi: 10.1016/j.cattod.2006.08.063.

[137] R. Burch, P. J. Millington, and A. P. Walker, "Mechanism of the selective reduction of nitrogen monoxide on platinum-based catalysts in the presence of excess oxygen," *Appl. Catal. B, Environ.*, vol. 4, no. 1, pp. 65–94, 1994, doi: 10.1016/0926-3373(94)00014-X.

[138] G. P. Ansell, S. E. Golunski, J. W. Hayes, A. P. Walker, R. Burch, and P. J. Millington, "The mechanism of the lean Nox reaction over Pt-based catalysts," *Stud. Surf. Sci. Catal.*, vol. 96, no. C, pp. 577–590, 1995, doi: 10.1016/S0167-2991(06)81459-X.

[139] A. Kumar, V. Medhekar, M. P. Harold, and V. Balakotaiah, "NO decomposition and reduction on Pt/Al2O3 powder and monolith catalysts using the TAP reactor," *Appl. Catal. B Environ.*, vol. 90, no. 3–4, pp. 642–651, 2009, doi: 10.1016/j.apcatb.2009.04.027.

[140] X. Wei *et al.*, "Bimetallic Au-Pd alloy catalysts for N 2O decomposition: Effects of surface structures on catalytic activity," *J. Phys. Chem. C*, vol. 116, no. 10, pp. 6222–6232, 2012, doi: 10.1021/jp210555s.

[141] Q. Ge, W. A. Brown, R. K. Sharma, and D. A. King, "NO monomer and (NO)x polymeric chain chemisorption on Pt{110}: Structure and energetics," *J. Chem. Phys.*, vol. 110, no. 24, pp. 12082–12088, 1999, doi: 10.1063/1.479143.

[142] H. Nakamura and S. Kato, "Theoretical study on the spin-forbidden predissociation reaction of N2O: Ab initio potential energy surfaces and quantum dynamics calculations," *J. Chem. Phys.*, vol. 110, no. 20, pp. 9937–9947, 1999, doi: 10.1063/1.478954.

[143] E. Hunter, "The thermal decomposition of nitrous oxide at pressures up to forty atmospheres," *Proc. R. Soc. London. Ser. A, Contain. Pap. a Math. Phys. Character*, vol. 144, no. 852, pp. 386–412, 1934, doi: 10.1098/rspa.1934.0057.

[144] G. BrodÉn, T. N. Rhodin, C. Brucker, R. Benbow, and Z. Hurych, "Synchrotron radiation study of chemisorptive bonding of CO on transition metals - Polarization effect on Ir(100)," *Surf. Sci.*, vol. 59, no. 2, pp. 593–611, 1976, doi: 10.1016/0039-6028(76)90038-8.

[145] A. Louis Allred, "Electronegativity values from thermochemical data," *J. Inorg. Nucl. Chem.*, vol. 17, no. 1949, pp. 215–221, 1961, [Online]. Available: https://pdf.sciencedirectassets.com/272894/1-s2.0-S0022190200X00565/1-s2.0-0022190261801425/main.pdf?x-amz-security-token=AgoJb3JpZ2luX2VjEMX%2F%2F%2F%2F%2F%2F%2F%2F%2F%2FwEaCXVzLWVhc3QtMSJGMEQCIAT2WU8Mm0qIfFkuYVOF2x1UWUFOJcYm6HeujgPqcPQjAiAWS2aHoZ%2FUbWb.

[146] H. Falsig, T. Bligaard, J. Rass-Hansen, A. L. Kustov, C. H. Christensen, and J. K. Nørskov, "Trends in catalytic NO decomposition over transition metal surfaces," *Top. Catal.*, vol. 45, no. 1–4, pp. 117–120, 2007, doi: 10.1007/s11244-007-0250-7.

[147] W. A. Brown and D. A. King, "NO Chemisorption and Reactions on Metal Surfaces: A New Perspective," *J. Phys. Chem. B*, vol. 104, no. 12, pp. 2578–2595, 2000, doi: 10.1021/jp9930907.

[148] J. K. Nørskov *et al.*, "Universality in heterogeneous catalysis," *J. Catal.*, vol. 209, no. 2, pp. 275–278, 2002, doi: 10.1006/jcat.2002.3615.

[149] A. N. Salanov and E. A. Suprun, "Interaction between oxygen and polycrystalline palladium at O2 pressures of 10-6-10 Pa," *Kinet. Catal.*, vol. 50, no. 1, pp. 31–39, 2009, doi: 10.1134/S0023158409010054.

Chapter 2. Experimental

This chapter discusses the chemicals and methods used for preparation of the catalysts as well as the experimental set-ups, conditions and procedures for the various characterization techniques and the NO decomposition catalytic test.

1. Chemicals

Table 2.1.1 lists all chemical substances used.

Table 2.1.1 : Chemical substances used for this thesis and their characteristics. For the liquid and solid substances, the purities are expressed in wt.% while for the gases, the purities are expressed in vol.%.

Substance	Formula	Usage	Purity	Phase	Supplier
colloidal silica (Ludox AS-40)	SiO_2	Si source	40%	Liquid	Sigma Aldrich
Sodium aluminum oxide	$NaAlO_2$	Al source	76%	Solid	Riedel de Häen
MPTMS: 3-mercaptopropyltrimethoxysilane	$(H_3CO)_3$-Si-$(CH_2)3$-SH	Stabilizer for metals	95%	Liquid	Sigma Aldrich
Sodium hydroxide	NaOH	Base	97%	Solid pellets	Carlo Erba reagents
APTMS: 3-aminopropyltrimethoxysilane	$(H_3CO)_3$-Si-$(CH_2)3$-NH_2	Stabilizer for metals	97%	Liquid	Sigma Aldrich
Chloroauric acid trihydrate	$HAuCl_4.3H_2O$	Au source	99.999%	Solid	Sigma Aldrich
Silver nitrate	$AgNO_3$	Ag source	>99.5%	Solid	Fluka
Chloroplatinic acid	H_2PtCl_6	Pt source	25.05% Pt assay	Liquid	Specialty Products
Rhodium (III) chloride	$RhCl_3$	Rh source	98%	Solid	Sigma Aldrich
Palladium nitrate hydrate Palladiumtetramminenitrate	$Pd(NO_3)_2.xH_2O$ $Pd(NH_3)_4(NO_3)_2$	Pd source Pd source	Varies 10%	Solid Liquid	Sigma Aldrich
Hydrogen hexachloroiridate hydrate	$H_2IrCl_6.xH_2O$	Ir source	99.9%	Solid	Sigma Aldrich
Copper nitrate trihydrate	$Cu(NO_3)_2.3H_2O$	Cu source	99%	Solid	Sigma Aldrich
Silica (B) : Commercial silica (BET = 275 m^2/g)	SiO_2	Support		Powder (<300 µm)	----

Substance	Formula	Usage	Purity	Phase	Supplier
Sodium borohydride	$NaBH_4$	Reducing agent	99.99%	Solid	Sigma Aldrich
Distilled water	H_2O	Solvent		Liquid	----
Ethanol	C_2H_5OH	Solvent		Liquid	
Helium gas	He	Inert gas		Gas	Air Liquide
Hydrogen gas cylinder	H_2	reduction		Gas	Messer
Synthetic air cylinder	-----	calcination	20% O_2/N_2	Gas	Messer
Oxygen cylinder	O_2	calcination	20% O_2/He	Gas	Air Liquide
Carbon monoxide gas	CO	adsorption	5% CO/He	Gas	Air Liquide
Nitric oxide cylinder	NO	Catalytic test	1% NO/Ar	Gas	Nippon Gases
Liquid Nitrogen	N_2	Trap		Liquid	Air Liquide

2. Material synthesis

Two types of supports (commercial silica and laboratory-prepared LTA zeolite) were used for the synthesis of monometallic and Au-based bimetallic nanoparticles. Over the silica support, Au, Pd, Pt, Pd-Au and Pt-Au nanoparticles were synthesized. Over the LTA zeolite support, monometallic Au, Pd, Pt, Ag, Rh, Cu and Ir nanoparticles and their Au-based bimetallic counterparts were synthesized.

2.1. Silica-supported metal nanoparticles

Table 2.2.1 lists the samples prepared using silica as support.

Table 2.2.1 : List of all the silica-supported samples prepared. Metal loadings are in wt.%.

Sample	Au/M
0.55% Au/SiO_2	**----**
4.25% Pd/SiO_2	**0**
4.72% Pd + 1.03% Au/SiO_2	**0.12**
3.96% Pd + 4.02% Au/SiO_2	**0.55**

2.1.1. The monometallic nanoparticles

First, silica was functionalized with APTMS (3-aminopropyltrimethoxysilane) as adapted from a previous work **[1]**. Silica was suspended in a solution of 2 g of APTMS in 50 mL of ethanol per gm of silica in a round bottom flask. The suspension was refluxed in an oil bath for 24 h at 70°C under vigorous stirring. Then, the suspension was filtered and washed several times with ethanol and kept in an oven over night at 90°C. This step was crucial to promote the interaction of anionic precursors with silica such as the precursor of Au ($HAuCl_4$) or Pt (H_2PtCl_6) and to prevent the aggregation of the formed nanoparticles **[2]**. Silica has a PZC (point of zero charge) of ~2 [3] and therefore, displays a negatively charged surface in water [4]. Therefore, a repulsion could take place between the metal precursor anions and non-functionalized silica. The APTMS molecules attach to the surface of silica through an ether bond (Si-O-Si) while the amino groups act as cationic anchors for the precursor anions [2][5] as illustrated in Fig. 2.2.1.

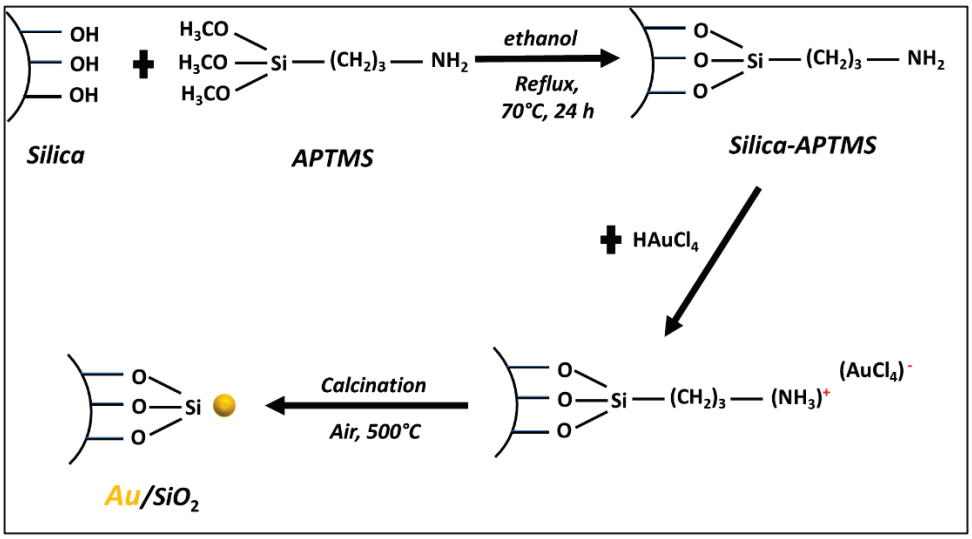

Figure 2.2.1 : General mechanism of the formation of Au/SiO_2 nanoparticles using APTMS.

Then, the monometallic samples were prepared at room temperature using a wet impregnation method [6]. The metal precursors used were $HAuCl_4.3H_2O$ for Au, $Pd(NO_3)_2.xH_2O$ for Pd. The metal precursor solution was added to a suspension of silica-APTMS in 20 mL of distilled water per gm of silica-APTMS. After vigorous stirring for 30 min, the suspension was filtered and washed several times with distilled water. Then, the collected solid was re-dispersed in distilled water and a freshly prepared $NaBH_4$ solution was added drop wise with a 10:1 molar excess with respect to the metal and stirring was kept for 30 min more. The suspension was then filtered and washed several times with distilled water and then kept in an oven over night at 90°C.

Typically, 2 g of the Au/SiO_2-APTMS samples were prepared while 5 g of the Pd/SiO_2-APTMS was prepared since this was used as the parent catalyst for the preparation of the Au-based bimetallic samples.

After the preparation, a calcination treatment was necessary in order to get rid of the organic moiety prior to the catalytic test. The Pd/SiO_2 parent catalyst was not calcined before the preparation of the Pd-Au bimetallic samples. Therefore, an *in situ* calcination was performed just before the catalytic test under the flow of 50 mL/min of (500 ppm NO + 5% O_2/He) at 200-450°C. This lead to the formation of N_2, N_2O and CO_2 due to the reaction of NO with APTMS. The calcination treatment was kept until CO_2 formation ceased. Then the samples were *in situ* reduced under a flow of 40 mL/min of 50% H_2/He at 450°C for 1 h.

Prior to the characterization of all the silica-based (monometallic and bimetallic) samples, an *ex situ* calcination treatment was performed in a flow of 100 mL/min of synthetic air. Then, the samples were reduced under a flow of 40 mL/min of 50% H_2/He at 450°C for 1 h.

Fig. 2.2.2 shows the Carbolite tubular furnace equipped with a quartz tube used for the *ex situ* calcination. The air source is a synthetic air cylinder, and its flow was controlled using a ball flowmeter (from Brooks).

Figure 2.2.2 : The Carbolite tubular furnace used for calcination.

2.1.2. The Au-based bimetallic nanoparticles

The bimetallic samples were prepared using a surface redox method adapted from a previous work [7]. For each sample, 1 g of the dried parent catalyst was suspended in 20 mL of water with gentle stirring in a three-neck round bottom flask (Fig. 2.2.3). One neck was used for the entry of the gases (H_2 and N_2), one neck as a vent and one neck for introducing the Au precursor solution.

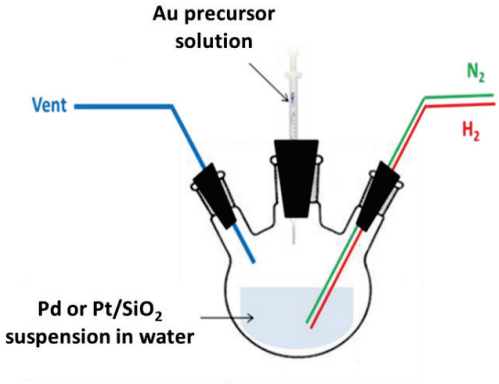

Figure 2.2.3: A representation of the Surface Redox set-up. The syringe containing the Au precursor solution is maintained covered with Al foil to protect the solution against sunlight.

Nitrogen was bubbled into the suspension for 15 min in order to degas the oxygen in the water and to expel all air inside the flask. Then, nitrogen was stopped and hydrogen is bubbled into the

suspension for 30 min at a flow of 50 mL/min. The H_2 flow was controlled using a ball flowmeter (from Brooks). Then, the Au precursor solution was added drop wise using a plastic syringe while maintaining the hydrogen flow and the stirring. For each sample, the amount of the Au precursor was adjusted so as to achieve the target loading. Then, the hydrogen flow is stopped and nitrogen is purged again for 15 min to expel the hydrogen before opening the flask. Finally, the suspension was filtered and washed several times with distilled water and then kept in an oven over night at 90°C. Fig. 2.2.4 shows a schematic representation of the surface redox process chemical steps.

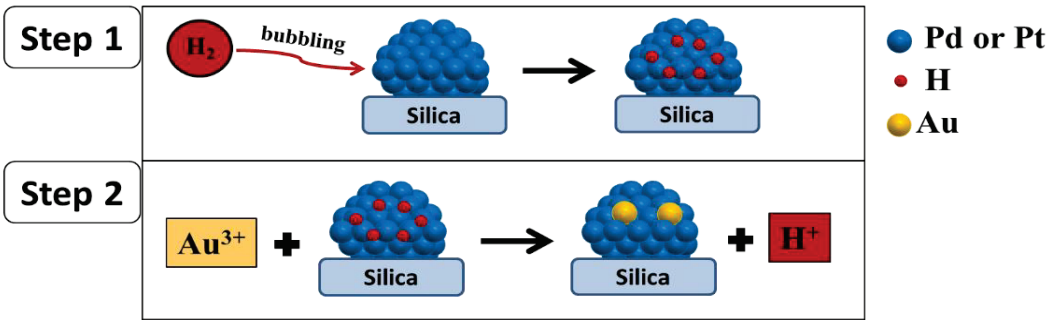

Figure 2.2.4: Schematic representation of the preparation of the bimetallic samples via the surface redox method using H_2 bubbling. $Au3^+$ cations are in the form of $AuCl4^-$.

The basic idea of the surface redox method is that hydrogen adsorbs dissociatively on Pd at room temperature due to the very low activation energy of adsorption on Pd of 4.8 kJ/mol [8] and the low activation energy of dissociation on Pd of 23.4 kJ/mol [9]. The adsorbed H atoms can then reduce the cationic Au from the precursor solution according to the equation below.

$$3\,H_{ads} + Au^{3+} \longrightarrow Au_{ads} + 3\,H^{+}$$

2.2. LTA-encapsulated metal nanoparticles

The preparation procedure was adapted from a previous work [10]. The procedure was applied to both the monometallic and bimetallic samples since the metals were encapsulated into the LTA structure simultaneously during the preparation. The target total metal loading was 1 wt. %. Monometallic Au and Pt nanoparticles and were prepared as well as Pt-Au bimetallic samples were prepared with a Au/Pt atomic ratios of (0.25, 0.5, 1, 2 and 3). Table 2.2.2 lists the LTA-based samples.

Table 2.2.2 : List of the LTA-based samples and the corresponding Au/metal atomic ratio. Metal loadings are in wt.%. The values correspond to the nominal loadings.

Sample	Au/M
1% Au@Ca-LTA	**----**
0.33% Pt@Ca-LTA	**0**
0.8% Pt + 0.2% Au@Ca-LTA	**0.25**
0.67% Pt + 0.33% Au@Ca-LTA	**0.5**
0.5% Pt + 0.5% Au@Ca-LTA	**1**
0.33% Pt + 0.67% Au@Ca-LTA	**2**

The typical preparation procedure is as follows to obtain 4.5 g of the catalyst:

1- 0.5 g of MPTMS and a solution of 2.5 g of NaOH dissolved in 9 mL of distilled water were mixed under stirring in PP bottle at room temperature for 8 h, and the stirring was set at 400 rpm during the whole course of the experiment.

2- The precursor solution was dissolved in 9 mL of distilled water and added dropwise into the PP bottle. In the case of the bimetallic samples, the two precursors' solutions were dissolved separately in 4.5 mL of distilled water each and were then added concurrently dropwise into the bottle. An Al foil was used to cover the bottle. The stirring was kept for 30 min more. The metal precursors used were: $HAuCl_4.3H_2O$, $Pd(NH_3)_4(NO_3)_2$, H_2PtCl_6, $RhCl_3$, $AgNO_3$ and $Cu(NO_3)_2.3H_2O$.

3- 4 g of Ludox colloidal silica AS-40 (40 wt% silica) was added dropwise into the bottle. Then, the bottle was capped and heated in an oil bath at 80°C while stirring for 30 min. Then, the heating was stopped and the bottle was let to cool down to room temperature.

4- 4 g $NaAlO_2$ (76% purity) was dissolved in 9 mL of distilled water and added dropwise into the PP bottle, and the stirring was maintained for 2 h at room temperature.

5- The bottle was heated in an oil bath at 100°C while stirring for 12 h.

6- The resulting suspension was filtered and washed with distilled water till pH = 7. The collected solid was then dried in an oven at 90°C for 8 h.

7- After the preparation, a calcination treatment was applied in order to remove the organic and nitrogen-containing residues. The samples were calcined in the Carbolite furnace shown before (Fig. 2.2.2) in a flow of 100 mL/min of air for 4 h at 350°C (the bimetallic samples) or 500°C (the monometallic samples) at a heating ramp of 2°C/min.

8- A Ca^{2+} ion exchange process was carried out with the goal of increasing the pore size of the LTA structure. 1 g of the LTA sample was mixed with 100 mL of a 1 M solution of

$CaCl_2.2H_2O$ and stirring was maintained for 8 h at 70°C. The suspension is then filtered and washed with distilled water and the collected solid is dried in an oven at 90°C for 8 h.

9- Then, the resulting catalyst fine powder (<100 µm) was resized in the range of 300-400 µm prior to the catalytic test.

10- Prior to the catalyst test and the characterizations, the catalysts were reduced in a flow of 55 mL/min of 18% H_2/He at 350°C.

2.3. Alumina-supported metal nanoparticles [11]

The monometallic Au and Pt samples were prepared using a wet impregnation method [12]. The aqueous solutions of the precursor of Au or Pt were added to a suspension of 1 g of alumina support in 35 mL of distilled water, and the stirring for 45 min at room temperature. A freshly prepared solution of $NaBH_4$ in 10 mL distilled water was added dropwise, and the stirring was kept for 25 min. The $NaBH_4$/metal ratio was 20 for Pt and 10 for Au. Finally, the suspension was filtered and washed several times with distilled water, and finally dried in an oven overnight at 90 °C. The Pt-Au bimetallic sample was prepared using a co-wet impregnation method i.e. the impregnation of the two metals was performed simultaneously in a one-pot synthesis. Table 2.2.3 lists the alumina-based samples. Prior to the characterization of the samples using CO adsorption by DRIFTS, the catalysts were reduced in a flow of 50 mL/min of 60% H_2/He at 350°C.

Table 2.2.3 : List of the prepared alumina-based samples and the corresponding Au/metal atomic ratio. Metal loadings are in wt.%. The values correspond to the actual loadings measured by ICP.

Sample	Au/M
2.13% Au/Al_2O_3	**----**
1.3% Pt/Al_2O_3	**0**
2.1% Pt + 0.3% Au/Al_2O_3	**0.14**

2.4. Sample storage

Supported gold nanoparticles may undergo sintering due to the exposure to light or moisture [13][14]. It was therefore recommended to store the samples without reduction in dry conditions and away from light and to perform the reduction just before characterization or the catalytic test [13]. Otherwise, since the silica-based samples were typically reduced during the preparation, all the samples were stored in a refrigerator as recommended in such case [13][14].

3. Characterization techniques

Several characterization techniques were used to characterize the metal loading, dispersion, average particle size and accessibility. Moreover, the alloy formation was investigated in the bimetallic samples as well as the formation of the LTA structure. The structure of the catalyst was monitored at each stage: after the preparation, pre-treatments and catalytic test.

3.1. Inductively coupled plasma-Optical emission spectroscopy (ICP-OES)

The technique was used to measure the metal loading. The measurement was performed using an ACTIVA spectrophotometer (from Horiba JOBIN YVON). The samples (solid powder) were solubilized in a mixture of HF, H_2SO_4 and aqua regia solutions. After that, the solution was then introduced into the core of an inductively coupled Ar plasma (Ar ICP) at a temperature of ~9000 K. At this temperature, the solution evaporates, and the analyte is atomized, ionized and thermally excited. An optical emission spectrometer (OES) was used to measure the intensity of the emitted radiation at a specific wavelength characteristic of each metal. The measured intensity was converted to a concentration (using a standard calibration curve) and further to a wt.% metal loading.

3.2. Transmission Electronic Microscopy (TEM)

TEM provides information about the metal particle size distribution and dispersion. TEM images were obtained using a JEOL 2010 microscope (resolution of 0.19 nm) operating at 200 kV.

3.1.1. Sample preparation for the TEM measurement

The sample was prepared by grinding in ethanol (LTA samples) or water (silica samples) in a mortar, since ethanol could affect the (Au/oxide support) particles size [15]. A drop of the resulting suspension was then deposited on a Cu TEM holey carbon grid and dried under an IR lamp. This way, a very thin layer of the sample was deposited on the carbon grid. This prevents the overlap between the catalyst particles and allows an easier imaging of the metal particles.

3.1.2. TEM instrument

Fig. 2.3.1 shows the TEM instrument and a schematic representation of its parts. An electron beam is emitted by an electron gun containing an emission source (LaB_6 single crystal) connected to a high voltage source (200 kV) under vacuum. The condenser lenses are responsible for the primary electron beam and its focus on the sample. When electrons pass through the sample, they are scattered due to

collisions with the sample atoms. The resulting beam is then focused by the objective lenses to form the images of the sample. The projector lenses magnify the images and project them on the instrument imaging device (a CCD camera). The images are then recorded using Digital Micrograph software. The resolution of the TEM is governed by the speed and wavelength of the electrons. The magnification power is determined by the distance between the specimen and the imaging plane of the objective lens. The contrast is due to the absorption of electrons by the solid depending on the thickness and composition of the material.

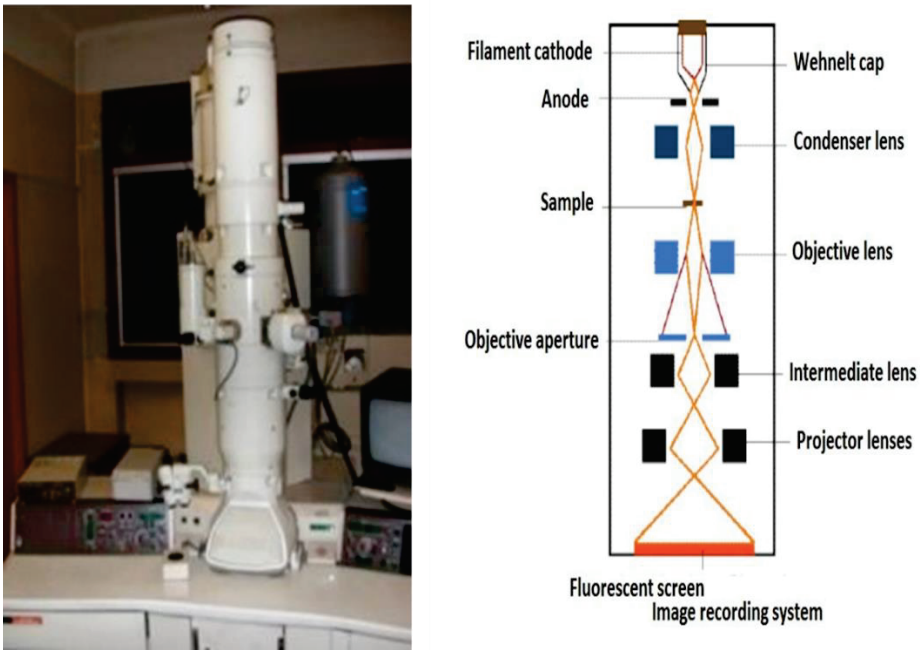

Figure 2.3.1: The JEOL-2010 TEM instrument (left) and a schematic representation (right).

3.1.3. Statistical study of nanoparticles based on TEM images

The particle diameters (d_i) were measured using Image J software. The average particle diameter (or number weighted diameter) was calculated as ($d_{NW} = \sum n_i d_i / \sum n_i$); where n_i is the number of the particles with diameter d_i). The surface weighted diameter was calculated as ($d_{SW} = \sum n_i d_i^3 / \sum n_i d_i^2$). The dispersion and the specific surface area of the nanoparticles were calculated depending on the d_{SW} using the calculation methodology reported by Van Hardeveld and Hartog [16] considering a cuboctahedral model [17][18][19].

3.1.4. Energy Dispersive X-Ray Spectroscopy (EDX) measurement

The JEOL 2010 microscope is equipped with an EDX Link ISIS analyzer (Oxford Instruments). That can identify the elements present in the sample. When the electron beam passes through the sample,

X-rays are also emitted with a spectrum characteristic of each element present. In addition, the number of the emitted photons due to an element is proportional to its atomic (and mass) concentration. Hence, EDX can provide a precise composition at the nanometer scale but is limited only to some selected regions of the sample.

3.3. Powder X-Ray Diffraction (PXRD)

Powder X-ray diffraction (PXRD) is used to identify the crystalline phases present in a solid and to determine the mean crystallite size of each phase. The measurement consists of introducing X-ray beams (λ=1.54184 Å) at a range of angle (θ) values onto the sample. At certain θ values characteristic of a certain phase and its crystallographic planes, these rays are diffracted by these lattice planes at the corresponding 2θ angle values. The diffracted rays interfere constructively, and they are detected in the form of intensity peaks. This technique is based on the Bragg's law:

$$n.\lambda = 2d_{hkl}.\sin\theta$$

Where

- λ: Wavelength of the incident light (1.54184 Å)
- d_{hkl}: Lattice interplanar spacing of the crystal (Å)
- θ: Diffraction angle (°)
- n: Order of diffraction line

The mean crystallite sizes (d_M) are estimated using the Scherrer equation from the half width of the XRD broadening peak as follows:

$$d_M = \frac{0.9\lambda}{\beta\cos\theta}$$

where

- λ: X-ray wavelength (1.54184 Å)
- θ: Bragg angle (°)
- β: Full width at half-maximum intensity (FWHM) of the diffraction peak (in radians)

In the case of an alloyed phase formation, the diffraction peaks are observed in between the positions of the diffraction peaks of each of the monometallic phase. Using the 2θ value, the lattice constant of the alloyed phase is determined. This value is used to calculate the approximate alloy composition according to Vegard's law, which holds a linear relation at constant temperature between the alloy composition and the lattice spacing [20] as explained below. This is valid for bulk binary alloys assuming a perfect random distribution of the phases.

$$a_{AB} = a_A (1 - X) + a_B (X)$$

where

- X is the mole fraction of the phase B
- a_A and a_B and a_{AB} are the lattice parameters of the phase A, the phase B, and the alloyed phase respectively (Å)

3.1.5. In situ PXRD analysis

The measurement was performed using a Bruker D8 Advance XRD diffractometer with a CuKα radiation source (λ = 1.54184 Å), an Anton Paar XRK-900 reactor chamber (Fig. 2.3.2) for the *in situ* treatments, and a LYNXEYE XE-T detector. Diffractograms were collected over the range of 2θ = 25-90° at a rate of 0.01°s^{-1} (0.02° step measurement were carried out and the step time is 2 s). The mean crystallite size was calculated by Scherrer equation using DIFFRAC.EVA software.

3.1.5.1. Procedure

1- A few mg of the sample was placed into the reaction chamber.
3- Synthetic air flow was introduced into the XRD chamber at a flow of 25 mL/min at 25°C, and the XRD pattern was collected.
4- The temperature was raised to 500°c with a heating ramp of 5°C/min and kept for 7 h for calcination. The XRD pattern was collected after 1 and 7 h.
5- The temperature was cooled down to 25°C with a cooling ramp of 5°C/min. The XRD pattern was then collected at 25°C under air flow.
6- Air flow was purged off the chamber using N_2 flow for 30 min.
7- H_2 was introduced into the chamber at a flow of 25 mL/min and the XRD pattern was collected at 25°C.
8- The temperature was raised to 450°C at a heating ramp of 2°C/min and kept for 1 h under H_2 flow. The XRD pattern was then collected at 450°C.
9- The temperature was cooled down to 25°C under H_2 flow at a cooling ramp of 2°C/min and the XRD pattern was then collected.
10- H_2 was purged off the chamber using N_2 for 30 min.
11- N_2 flow was stopped and ambient air is introduced into the chamber at 25°C and the XRD pattern was collected.
12- Finally, the sample was recovered.

Figure 2.3.2 : The Anton Paar XRK-900 reactor chamber.

3.1.6. Ex situ PXRD analysis

The measurement was performed at ambient atmosphere using a Bruker D8 advance A25 X-ray diffractometer (Fig. 2.3.3) with a CuKα radiation source (λ = 1.54184 Å), a Ni filter and a multi-channel LYNXEYE detector. Diffractograms were collected at 2θ = 30-50° at a rate of 0.64°s^{-1}.

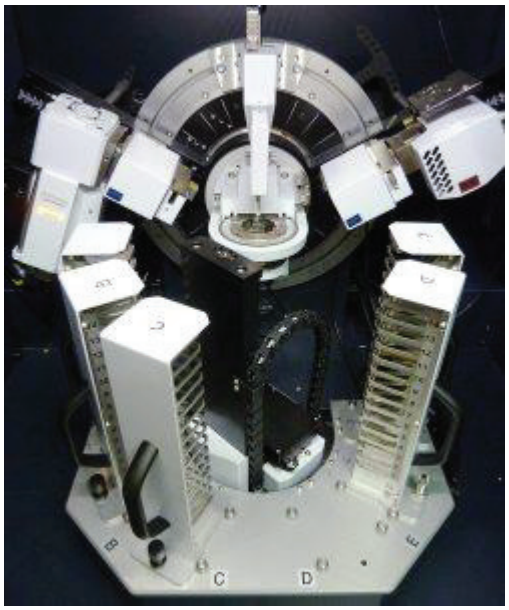

Figure 2.3.3 : The D8 advance A25 X-ray diffractometer.

3.4. Diffuse Reflectance Infrared Fourier Transform Spectroscopy (DRIFTS)

Molecules exhibit vibrational and rotational modes corresponding to discrete energy levels which correspond to specific wavelengths. To establish an IR spectrum of a sample, an IR beam is passed through the sample and the absorption is measured at each wavelength of a chosen range of wavelengths. The (IR) measurements can depend on measuring the transmission or reflection of the light where there are several FTIR techniques such as DRIFTS, TIR, ATR and RAIRS. The DRIFTS technique, as the name implies, depends on the diffuse reflection of the beam after the interaction with the surface of the sample as explained below in Fig. 2.3.4.

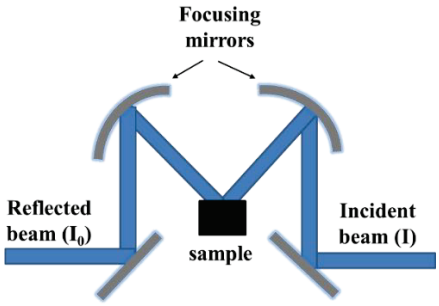

Figure 2.3.4 : The principle of the DRIFTS technique.

Where I_0 and I are the intensities of the incident and diffuse reflected IR beams, respectively. The reflectance (R) equals the ratio of (I/I_0) and is converted into the absorbance (A) as follows:

$$A = -\log(R) = -\log\left(\frac{I}{I_0}\right)$$

3.4.1. Fourier transform infrared spectroscopy (FT-IR)

An FT-IR spectrometer consists of five main compartments:

1- The incident light source: an incandescent black body.
2- Interferometer: to generate the constructive interferences of the incident beam
3- The sample compartment: when the incident beam enters the sample compartment, it is transmitted through or is reflected by the surface of the sample, depending on the IR technique used. The DRIFTS technique depends on the measuring the reflectance.
4- Detector: it converts the reflected photon beam into an electrical signal.
5- Computer: the measured signal is sent to the computer and processed by Fourier transform and the final infrared spectrum is presented.

3.4.2. Advantages of the DRIFTS technique

The technique allows the direct measurement of the powder samples without a special preparation. It may give information about the catalyst structure, the nature of the metal sites and oxidation state, and the alloy formation. In situ and operando measurements are possible, that enables the characterization under conditions relevant to the catalytic test conditions.

3.4.3. Limitations of the DRIFTS technique

The technique is not very reliable when it comes to quantitative measurements [21]. The reason could be an inhomogeneous material composition, or a temperature gradient that may exist in the DRIFTS cell [22]. Moreover, the observed adsorption bands are usually associated with various adsorption modes that may feature different molar extinction coefficients. These different adsorption modes could be associated with different metals present or different adsorption sites and/or adsorbates of the same metal. Furthermore, some adsorption bands may be overlapping and may not be possible to decompose. An even more challenging spectrum interpretation may arise due to a surface segregation in alloyed nanoparticles [23] or a possible reactivity of CO [24][25].

3.4.4. Set-up description

Figure 2.3.5 : The Nicolet 8700 instrument (left) and the Harrick cell ™ (right).

The experiments were carried in a Flying Mantis DRIFTS reaction cell from Harrick (Fig. 2.3.5 right). The cell was placed in a collector assembly and fitted in a Nicolet 8700 FTIR spectrometer (from Thermo Fischer Scientific) (Fig. 2.3.5 left) equipped with a mercury cadmium telluride (MCT) detector cooled with liquid nitrogen. The spectra were collected using OMNIC software (with a resolution of 4 cm^{-1}) and analyzed using OPUS software. The gas flows were controlled by independent mass flow controllers (from Brooks). The effluent gases were also analyzed using a

Nicolet FTIR analyzer with a gas cell heated at 80°C and a DTGS detector. Fig. 2.3.6 shows a schematic representation of the setup.

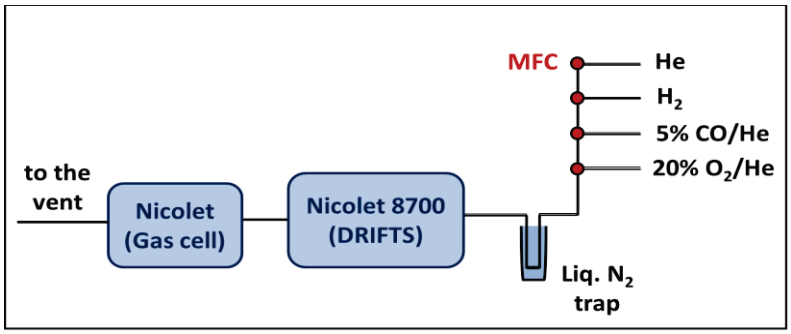

Figure 2.3.6 : Schematic representation of the CO adsorption setup at IRCELYON.

3.4.5. CO adsorption test

CO is used as a probe molecule for the DRIFTS technique since it adsorbs mostly molecularly on metal surfaces due to its high binding energy of ~1070 kJ/mol [26]. The stretching frequency of the adsorbed CO depends on the metal(s) present, the oxidation state of the metal present, the adsorption mode (linear, bridge or multi-bridged) and the presence of co-adsorbates.

The test procedure was as follows:

1- A few milligrams of the sample was loaded into a Harrick cell on top of SiC.
2- A liquid N_2 trap was connected at the common inlet line of the gases.
3- An in situ calcination pre-treatment was performed only over the LTA-based samples in a flow of 5% O_2 /He with a total flow of 50 mL/min at 350°C for 60 min. Then, the O_2 flow was stopped and the system was flushed with a He flow for 10 min. During calcination, the system was heated from room temperature to 350°C at a heating ramp of 10°C/min.
4- An in situ reduction pre-treatment was then performed (i) over the LTA-based samples in a flow of 18% H_2 /He with a total flow of 55 mL/min at 350°C for 30 min, and (ii) over the alumina-based samples in a flow of 60% H_2 /He with a total flow of 50 mL/min at 300°C for 30 min. Then, H_2 was stopped and the system was cooled down to 50°C in a He flow. During the reduction of the alumina-based samples, the system was heated from room temperature to 350°C at a heating ramp of 10°C/min.
5- During the pre-treatment and cooling down, spectra were collected at various temperatures using a background spectrum collected over KBr.
6- After cooling down to 50°C, a new background was collected over the sample.
7- Then, the CO adsorption test was carried out under a flow of 1% CO/He at a total flow of 50 mL/min.

8- Finally, CO was stopped and the CO desorption was monitored (i) over the LTA-based samples in a flow of He with a total flow of 40 mL/min at 50°C for 4-5 h, and (ii) over the alumina-based samples in a flow of He with a total flow of 100 mL/min at 50°C for 4-5 h.

3.4.6. Band area integration

The absorption bands of the gas-phase CO in the collected spectra were subtracted using a $CO_{(g)}$ spectrum file collected under the same test conditions over a KBr powder. The method E in OPUS software was used for the integration of all band areas. The method required a baseline point (2200 cm^{-1}), a left edge point and a right edge point for each band (Table 2.3.1). The edge points of each band were not exactly the same over the monometallic and bimetallic samples, considering to the overlapping of the bands in the bimetallic samples. Similarly, the band edges' points needed to be edited for the desorption spectra, considering the red shifts observed.

Table 2.3.1 : The integration ranges of the CO adsorption bands. The numbers are expressed in cm^{-1}.

Band	Monometallic samples		Bimetallic samples	
	Left edge	Right edge	Left edge	Right edge
Au L-CO	2200	2000	2200	2100
Pt L-CO	2200	1930	2100	1930
Pt B-CO	1930	1700	1930	1700

4. Catalytic NO decomposition reaction

Two setups were used for measuring the catalytic activities of the samples presented in the thesis. The performances of the LTA-based samples were measured at IRCELYON and the performances of the silica-based samples were measured at LRS laboratory (Sorbonne University) in Paris. The two setups will be explained in sections 4.2 and 4.3, respectively. The Transmission FTIR technique was mainly used to measure the products of the catalytic NO decomposition.

4.1. Transmission FT-IR spectroscopy (TIR)

In this technique, the sample is placed in the path of the IR beam. The sample exhibits absorption at certain wavelength and the intensity of the transmitted light is measured (Fig. 2.4.1). The Fourier transform is also used to generate the final spectrum is presented using a computer.

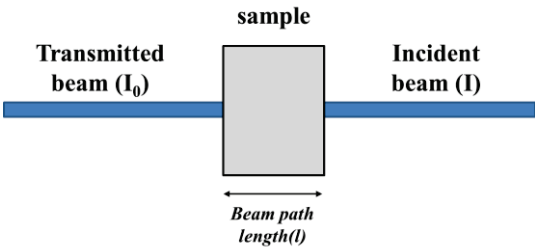

Figure 2.4.1 : The principle of the TIR technique.

Where I_0 and I are the intensities of the incident and transmitted IR beams, respectively. The transmittance (T) equals the ratio of (I/I_0) and is converted into the absorbance (A) as follows:

$$A = -\log(T) = -\log\left(\frac{I}{I_0}\right)$$

The calculated absorbance (A) is directly proportional to the concentration (c) of the analyte according to the Beer-Lambert law:

$$A = \varepsilon l c$$

Where

- ε is the molar absorption ($cm^2.mol^{-1}$)
- l is the beam path length (cm).

4.1.1. IR active molecules

The IR active vibration modes are those accompanied with a change in the dipole moment. Examples are the vibration modes of NO, NO_2, N_2O and the asymmetric vibration modes of CO_2. Symmetric

stretching modes do not exhibit a dipole moment change and are therefore IR inactive. These include the vibration modes of N_2 and O_2 as well as the symmetric vibration mode of CO_2.

4.2. IRCELYON setup

4.2.1. Setup Description

The NO direct decomposition activity of the LTA-based samples was investigated using the setup at IRCELYON. The flow of each gas was controlled using a separate mass flow controller (MFC) (from Brooks). The catalytic activity was monitored using a tubular quartz reactor (4 mm i.d.) placed into a tubular furnace (Fig. 2.4.2) and the temperature was controlled using a temperature controller (from Delta Elektronika). The effluent gases were analyzed using a Bruker (Tensor 27) FTIR analyzer (Fig. 2.4.3) equipped with a transmission gas cell (with an optical path of 2 m and heated at 60 °C) and a DTGS detector. A schematic representation is shown in Fig. 2.4.4.

Figure 2.4.2 : The tubular furnace with a quartz reactor connected.

Figure 2.4.3 : The Bruker Tensor-27 instrument (left) and its gas cell (right).

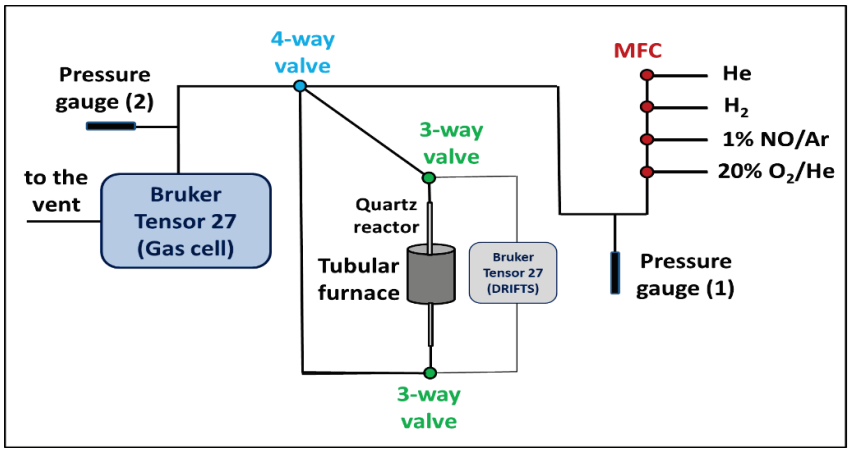

Figure 2.4.4 : Schematic representation of the catalytic test setup at IRCELYON.

4.2.2. Procedure

1- Prior to the test, the catalyst fine powder was resized as 300-400 µm grains so as to avoid pressure drops.

2- 50 mg of the sample was loaded into a quartz reactor and hold using quartz wool.

3- A reduction pre-treatment was performed in a flow of 18% H_2 /He with a total flow of 55 mL/min at 350°C for 30 min.

4- Then, H_2 was stopped and the system was flushed with a flow of 45 mL/min of He for 10 min.

5- Then, the He flow was switched into the bypass line and a new background was collected.

6- A flow of 5 mL/min of 1% NO/Ar was introduced into the system. The overall feed composition monitored through the bypass line was 1000 ppm NO/ArHe with a total flow rate of 50 mL/min.

7- After one min through the bypass, the feed was switched into the reactor and the catalytic test was typically monitored for 60 min.

8- Then, the feed was switched into the bypass line and a few spectra were collected.

9- The pressure readings before and after the reactor were collected as well as the gas cell temperature along the experiment.

4.2.3. Methodology of calculation

NO, N_2O, NO_2 and CO_2 can be detected by IR (Fig. 2.4.5), while N_2 and O_2 cannot be detected since those are symmetrical diatomic molecules and are IR inactive. Therefore, the activity was expressed as the disappearance of NO and NO_2 as will be explained (eq. 2.4.1).

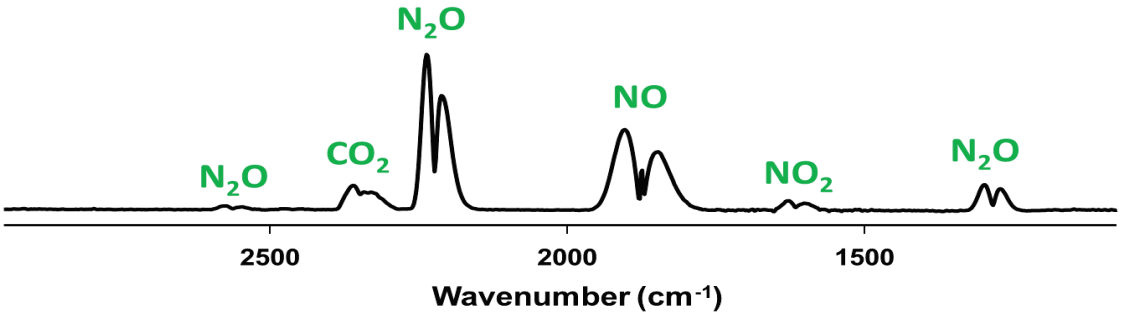

Figure 2.4.5 : IR active molecules.

The catalytic spectra were collected and treated using OPUS software. The quantification of the effluent gases was performed by the integration of the peak areas of the various gases (NO, NO_2 and N_2O and CO_2). Table 2.4.1 shows the integration method and range for each species.

Table 2.4.1 : Table of the species detected by FT-IR Bruker-Tensor 27 gas cell and their corresponding integration methods in OPUS software.

Compound	Integration method	Integration range (cm^{-1})		1st Baseline range (cm^{-1})		2nd Baseline range (cm^{-1})	
NO	E	1980	1840	2100	2020	1480	1400
NO_2	E	1680	1540	2100	2020	1480	1400
N_2O	B	2273	2125	----	----	----	----
CO_2	B	2400	2274	----	----	----	----

The measured NO_X (= NO + NO_2) conversion is calculated as follows:

The measured NO_X conversion(t) is calculated as follows:

$$\mathbf{NO_X\ conversion(t)} = \frac{[(NO_X)_{feed}] - [NO_X(t)]}{[(NO_X)_{feed}]} \qquad \textbf{Eq. 2.4.1}$$

4.3. LRS setup

4.3.1. Setup description [27]

The NO direct decomposition activity of the silica-based samples [28] was investigated using the setup at LRS (Fig. 2.4.6). The experiments were carried out in a U-shape quartz reactor (15 mm i.d.) at atmospheric pressure and the catalyst bed was held using quartz wool. The reactor was connected into a tubular furnace and the temperature was controlled using a temperature controller (Eurotherm 2408) using a K-type thermocouple. The gases (gas cylinders supplied from Air Liquide) were introduced into the system and their flows were controlled using mass flow controllers (Brooks 5850TR). The reactor inlet and outlet gases were analyzed using a FT-IR analyzer (MKS MultiGas 2030) with 1 record every s with an internal calibration to quantify NO, NO_2, CO_2 and H_2O. In addition, a Pfeiffer Vacuum OmniStar mass spectrometer (MS) was used to detect the formed N_2 using Ar as an internal standard (with 1 record every 6−6.5 s). Simultaneously, an Agilent CP490 micro-gas chromatograph (μ-GC) was used to quantify N_2 and O_2 (with 1 injection every 3.5 min).

Figure 2.4.6 : The LRS set-up with its U-shape quartz reactor.

4.3.2. Procedure

1- Prior to the test, the catalyst fine powder was resized as 300-400 μm grains so as to avoid pressure drops.
2- 100 mg of the sample was loaded into the U-shape quartz reactor and held using quartz wool.

3- A reduction pre-treatment was performed in a flow of 50% H_2 /He with a total flow of 40 mL/min at 200°C for 60 min.
4- Then, H_2 was stopped and the system is flushed with He for 20 min.
5- A flow of 50 mL/min of 500 ppm NO + 5% O_2/ArHe was introduced into the bypass line for few min.
6- After the NO feed stabilized through the bypass, the feed was switched into the reactor and the catalytic performance was monitored at a temperature range of 200-450°C with a 50°C stepwise increase and the reaction was monitored for 30 min at each temperature. This step generated a lot of CO_2 (SCR reaction) and was kept till the production of CO_2 ceased.
7- Then, a reduction treatment was performed at 450°C for 60 min in a flow of 50% H_2 /He with a total flow of 40 mL/min.
8- The catalytic performance was then monitored in a flow of 50 mL/min of 500 ppm NO/ArHe at 450°C i.e. in the absence of O_2 for 1000 min.

4.3.3. Methodology of calculation

The real NO catalytic decomposition activity was only calculated after the production of CO_2 ceased. NO_2 is not a decomposition product since it is formed by the reaction of NO from the feed with the produced oxygen. Hence, NO conversion to (N_2 + N_2O) as the decomposition products is calculated according to Eq. 2.4.2, where (NO_X = NO + NO_2). The selectivity to N_2 production is calculated according to Eq. 2.4.3. N and O balances are calculated according to equations 2.4.4 and 2.4.5.

$$\mathbf{NO\ conversion(t)} = \frac{\mathbf{[N_2(t)] \times 2 + [N_2O(t)] \times 2}}{\mathbf{[(NO_X)_{feed}]}} \qquad \textbf{Eq. 2.4.2}$$

$$\mathbf{Selectivity\ to\ N_2(t)} = \frac{\mathbf{[N_2(t)]}}{\mathbf{[N_2(t)] + [N_2O(t)]}} \qquad \textbf{Eq. 2.4.3}$$

The total N- and O-equivalents were calculated as follows:

$$\mathbf{Total\ N-equivalents(t)} = \mathbf{[N_2(t)] \times 2 + [N_2O(t)] \times 2\ +\ [NO(t)] + [NO_2(t)]} \qquad \textbf{Eq. 2.4.4}$$

$$\mathbf{Total\ O-equivalents(t)} = \mathbf{[O_2(t)] \times 2 + [NO_2(t)] \times 2\ +\ [NO(t)] + [N_2O(t)]} \qquad \textbf{Eq. 2.4.5}$$

References

[1] C. H. Tu, A. Q. Wang, M. Y. Zheng, X. D. Wang, and T. Zhang, "Factors influencing the catalytic activity of SBA-15-supported copper nanoparticles in CO oxidation," Appl. Catal. A Gen., vol. 297, no. 1, pp. 40–47, 2006, doi: 10.1016/j.apcata.2005.08.035.

[2] L. F. Gutiérrez, S. Hamoudi, and K. Belkacemi, Synthesis of gold catalysts supported on mesoporous silica materials: Recent developments, vol. 1, no. 1. 2011.

[3] Y. K. Leong, "Yield stress and zeta potential of nanoparticulate silica dispersions under the influence of adsorbed hydrolysis products of metal ions - Cu(II), Al(III) and Th(IV)," J. Colloid Interface Sci., vol. 292, no. 2, pp. 557–566, 2005, doi: 10.1016/j.jcis.2005.06.004.

[4] L. Jiao and J. R. Regalbuto, "The synthesis of highly dispersed noble and base metals on silica via strong electrostatic adsorption: I. Amorphous silica," J. Catal., vol. 260, no. 2, pp. 329–341, 2008, doi: 10.1016/j.jcat.2008.09.022.

[5] K. Stawicka and M. Ziolek, Silica Hosts for Acid and Basic Organosilanes: Preparation, Characterization, and Application in Catalysis. Elsevier Inc., 2019.

[6] G. X. Pei et al., "Promotional effect of Pd single atoms on Au nanoparticles supported on silica for the selective hydrogenation of acetylene in excess ethylene," New J. Chem., vol. 38, no. 5, pp. 2043–2051, 2014, doi: 10.1039/c3nj01136d.

[7] F. Gauthard, F. Epron, and J. Barbier, "Palladium and platinum-based catalysts in the catalytic reduction of nitrate in water: Effect of copper, silver, or gold addition," J. Catal., vol. 220, no. 1, pp. 182–191, 2003, doi: 10.1016/S0021-9517(03)00252-5.

[8] C. Resch, H. F. Berger, K. D. Rendulic, and E. Bertel, "Adsorption dynamics for the system hydrogen/palladium and its relation to the surface electronic structure," Surf. Sci., vol. 316, no. 3, 1994, doi: 10.1016/0039-6028(94)91213-0.

[9] G. L. Holleck, "Diffusion and solubility of hydrogen in palladium and palladium-silver alloys," J. Phys. Chem., vol. 74, no. 3, pp. 503–511, 1970, doi: 10.1021/j100698a005.

[10] T. Otto, J. M. Ramallo-López, L. J. Giovanetti, F. G. Requejo, S. I. Zones, and E. Iglesia, "Synthesis of stable monodisperse AuPd, AuPt, and PdPt bimetallic clusters encapsulated within LTA-zeolites," J. Catal., vol. 342, pp. 125–137, 2016, doi: 10.1016/j.jcat.2016.07.017.

[11] R. A. (PhD Dissertation), "NO direct decomposition in the presence of excess oxygen over gold-based catalysts," 2021.

[12] K. Heidkamp, M. Aytemir, and K. Vorlop, "Ceria supported gold--platinum catalysts for the selective oxidation of alkyl ethoxylates," Catal. Sci. Technol., vol. 3, no. 11, pp. 2984–2992, 2013, doi: 10.1039/c3cy00252g.

[13] R. Zanella and C. Louis, "Influence of the conditions of thermal treatments and of storage on the size of the gold particles in Au / TiO 2 samples," Catal. Today, vol. 107, pp. 768–777, 2005, doi: 10.1016/j.cattod.2005.07.008.

[14] B. Schumacher, V. Plzak, M. Kinne, and R. J. Behm, "Highly active Au/TiO2 catalysts for low-temperature CO oxidation : preparation , conditioning and stability," Catal. Letters, vol. 89, no. 1–2, pp. 109–114, 2003.

[15] R. Zanella and C. Louis, "Influence of the conditions of thermal treatments and of storage on the size of the gold particles in Au / TiO 2 samples," Catal. today, vol. 107, pp. 768–777, 2005, doi: 10.1016/j.cattod.2005.07.008.

[16] R. Van Hardeveld and F. Hartog, “The statistics of surface atoms and surface sites on metal crystals,” Surf. Sci., vol. 15, no. 2, pp. 189–230, 1969, doi: 10.1016/0039-6028(69)90148-4.

[17] F. J. Owens and C. P. Poole Jr., Introduction to Nanotechnology. Wiley-VCH.

[18] R. Atwi, A. Tuel, M. Maffre, L. Burel, J. L. Rousset, and F. Meunier, “Highly dispersed Au, Ag and Au-Ag alloy nanoparticles encapsulated in single crystal multi-hollow silicalite-1,” Appl. Catal. A Gen., vol. 569, no. October 2018, pp. 86–92, 2019, doi: 10.1016/j.apcata.2018.10.028.

[19] L. J. De Jongh, “Metal-cluster Compounds: Model Systems for Nanosized Metal Particles,” Appl. Organomet. Chem., vol. 12, no. 6, pp. 393–399, 1998, doi: 10.1002/(SICI)1099-0739(199806)12:6<393::AID-AOC744>3.0.CO;2-W.

[20] A. R. Denton and N. W. Ashcroft, “Vegard’s law,” Phys. Rev. A, vol. 43, no. 6, pp. 3161–3164, 1991.

[21] J. Sirita, S. Phanichphant, and F. C. Meunier, “Quantitative Analysis of Adsorbate Concentrations by Diffuse Reflectance FT-IR,” vol. 79, no. 10, pp. 3912–3918, 2007, doi: 10.1021/ac0702802.

[22] H. Li, M. Rivallan, F. Thibault-Starzyk, A. Travert, and F. C. Meunier, “Effective bulk and surface temperatures of the catalyst bed of FT-IR cells used for in situ and operando studies,” Phys. Chem. Chem. Phys., vol. 15, no. 19, pp. 7321–7327, 2013.

[23] T. Elgayyar, R. Atwi, A. Tuel, and F. C. Meunier, “Contributions and limitations of IR spectroscopy of CO adsorption to the characterization of bimetallic and nanoalloy catalysts,” Catal. Today, vol. 373, pp. 59–68, 2021, doi: 10.1016/j.cattod.2021.01.009.

[24] F. J. CADETE SANTOS AIRES, C. DERANLOT, Y. JUGNET, L. PICCOLO, and J.-C. BERTOLINI, “ METALLIC SURFACES UNDER ELEVATED GAS PRESSURE STUDIED IN SITU BY SCANNING TUNNELING MICROSCOPY: O 2 , H 2 /Au(111); CO/Au(110) ,” B. N. Dev (Ed.), Proc. Int. Conf. Phys. Surfaces Interfaces, World Sci. Publ. Singapore, no. lll, pp. 13–21, 2003, doi: 10.1142/9789812704221_0002.

[25] Y. Iwasawa, R. Mason, M. Textor, and G. A. Somorjai, “The reactions of carbon monoxide at coordinatively unsaturated sites on a platinum surface,” Chem. Phys. Lett., vol. 44, no. 3, pp. 468–470, 1976, doi: 10.1016/0009-2614(76)80706-3.

[26] S. W. Benson, “Resource papers - III bond energies,” J. Chem. Educ., vol. 42, no. 9, pp. 502–515, 1965, doi: 10.1021/ed042p502.

[27] J. Schnee, L. Delannoy, G. Costentin, and C. Thomas, “Unraveling the Direct Decomposition of NO xover Keggin Heteropolyacids and Their Deactivation Using a Combination of Gas-IR/MS and in Situ DRIFT Spectroscopy,” J. Phys. Chem. C, vol. 124, no. 41, pp. 22459–22470, 2020, doi: 10.1021/acs.jpcc.0c05945.

[28] T. Elgayyar et al., “Au-Modified Pd catalyst exhibits improved activity and stability for NO direct decomposition,” Catal. Sci. Technol., vol. 11, no. 8, pp. 2908–2914, 2021, doi: 10.1039/d1cy00301a.

Chapter 3. Silica-supported Pd-Au nanoparticles

1. Introduction

One of the major applications of supported catalysts is the elimination of gaseous contaminations and toxic gases such as the NO_X. Supported bimetallic nanoparticles may combine the advantages of both metals used, where a monometallic catalyst would display a limited activity or undergo deactivation. The formation of alloyed PdAu nanoparticles is feasible due to the excellent miscibility of both metals. The reported preparation methods of supported monometallic nanoparticles include wet impregnation [1] and ion exchange [2], and of bimetallic nanoparticles include co-impregnation [3], successive wet impregnation [1] and the surface redox method [4].

Noble metals, such as Pd, show activity for NO direct decomposition at high temperatures (> 500°C) [5][6]. At lower temperatures, these metals are unable to desorb O_2, that leads to the poisoning and deactivation of the metals. Au is inactive for NO direct decomposition but shows excellent oxidation resistance. Combining Pd and Au is a promising idea to obtain a catalyst that is active for NO decomposition by being able to desorb O_2 preferably at low temperatures.

This chapter aims at characterizing the prepared SiO_2-supported Au, Pd and Pd-Au nanoparticles using techniques such as ICP-OES, TEM-EDX and PXRD which are useful for monitoring the structure and phases of the catalyst at each stage: after the preparation, after the different treatments and after the catalytic test. The chapter also discusses the catalytic activity of the catalysts for NO direct decomposition in the presence/absence of O_2 in the feed at 450°C. The effect of alloying Pd with Au is to be investigated at different Au/Pd ratios. The results are compared to those reported in literature so as to evaluate the efficiency of this Pd-Au/SiO_2 system.

Four SiO_2-supported samples were prepared. The monometallic Au and Pd samples were prepared via a wet impregnation method. Then, two bimetallic samples were prepared using the same batch of the monometallic Pd/SiO_2 sample as a parent catalyst and Au was introduced via a surface redox method. The preparation methods are explained in detail in Chapter 2 (Experimental chapter).

2. ICP-OES elemental analysis

Table 3.2.1 shows the elemental analysis of the four samples. The bimetallic samples were all prepared using the same batch of the Pd(4) parent catalyst. The loading of Pd in all the Pd-containing samples is 4.3 ± 0.3 wt.% which is lower than the target loading of 5 wt.%. The reason could be the hydration water in the Pd precursor [$Pd(NO_3)_2.xH_2O$] that could vary during manufacturing or storage and handling. The actual loadings of Au match with nominal loadings.

Table 3.2.1 : ICP-OES elemental analysis results of the SiO_2-supported Au, Pd and Pd-Au samples. The two bimetallic samples were all prepared from the same batch of the monometallic Pd sample.

Sample code	Nominal loading (wt.%)		Actual loading (wt.%)		Au/Pd atomic ratio
	Pd	Au	Pd	Au	
Au(1)	---	1	---	0.55	---
Pd(4)	5	---	4.25	---	---
Pd(4)Au(1)	5	1	4.72	1.03	0.12
Pd(4)Au(4)	5	4	3.96	4.02	0.55

3. TEM-EDX analysis

Prior to the TEM analysis, the samples Au(1), Pd(4) and Pd(4)Au(1) were calcined in air at 500°C for 7 h followed by reduction under H_2 at 450°C for 1 h. The sample Pd(4)Au(1) was also tested for TEM-EDX after reduction with $NaBH_4$ and displayed similar (metal composition) result to that obtained after reduction with H_2 at 450°C. The sample Pd(4)Au(4) was calcined in air at 500°C for 6 h followed by reduction with $NaBH_4$ at room temperature. The measurement was not repeated after reduction with H_2 for Pd(4)Au(4), since similar result was expected as the case of Pd(4)Au(1).

3.1. TEM analysis of Au(1)

Fig. 3.3.1 shows the TEM images and particle size distribution of the monometallic Au sample. The average particle diameter is 3.6 nm and the SWD is 4.7 nm. The sample shows a reasonable dispersion (24.6%) and a narrow range of particle size (2-9 nm).

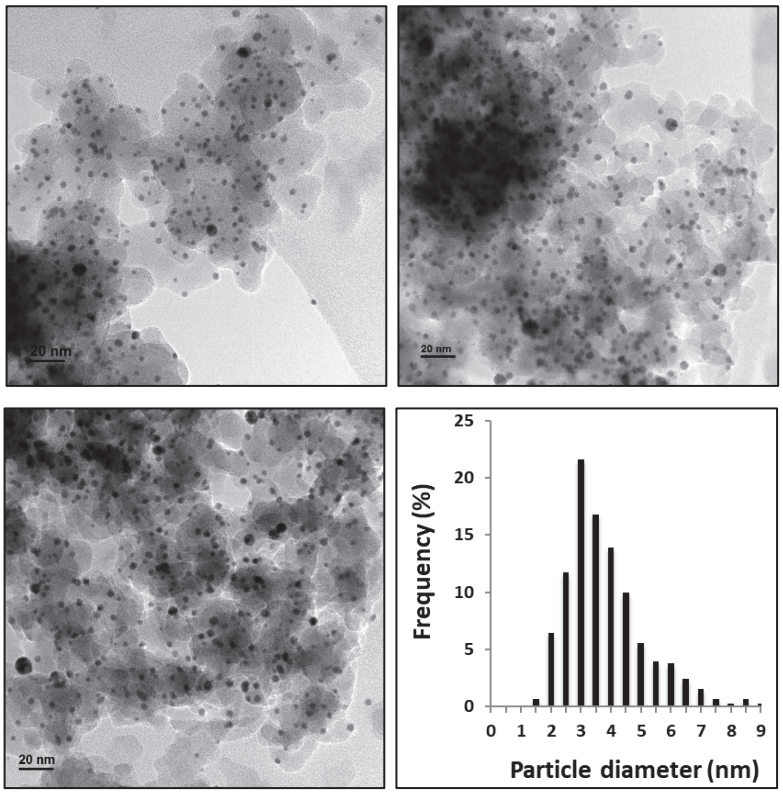

Figure 3.3.1 : TEM images of Au(1), and the corresponding particle size distribution where 453 particles were measured. Average particle size is 3.6 nm and SWD is 4.7 nm. Pre-treatment : calcination in air at 500°C for 7 h followed reduction with H_2 at 450°C for 1 h.

3.2. TEM analysis of Pd(4)

Fig. 3.3.2 shows the TEM images and particle size distribution of the monometallic Pd sample. The average particle diameter equals 3.7 nm. The SWD is relatively high (9.1 nm) due to the presence of large particles up to 15 nm. The presence of such large particles could be due to the high loading of the metal (4.25 wt.%). The sample shows a low dispersion (12.2%).

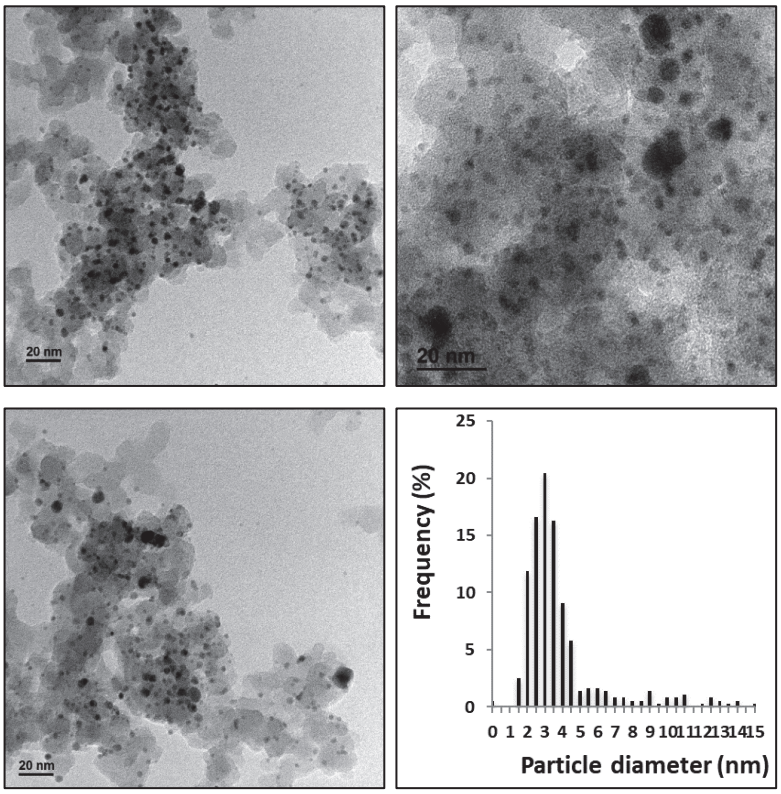

Figure 3.3.2 : TEM images of Pd(4), and the corresponding particle size distribution where 362 particles were measured. Average particle size is 3.7 nm and SWD is 9.1 nm. Pre-treatment: calcination in air at 500°C for 7 h followed reduction with H_2 at 450°C for 1 h.

The fraction of the large particles (> 9 nm) accounts for 48% of the overall surface area of the nanoparticles. Therefore, these large particles are expected to display a significant contribution to the catalytic performance and other characterization techniques such as PXRD.

3.3. TEM-EDX analysis of Pd(4)Au(1)

Fig. 3.3.3 shows the particle size distribution and TEM images of the bimetallic Pd(4)Au(1) sample. The average particle diameter is small (4.4 nm) and the SWD is higher (10.4 nm) due to the presence of large particles. The sample shows a low dispersion (10.8%). The presence of the large particles could be due to the addition of the Au atoms onto the surface of Pd using the surface redox method

simply leading to the formation larger particles. The large particles (> 9 nm) account for a significant fraction of 39% of the overall surface area of the nanoparticles.

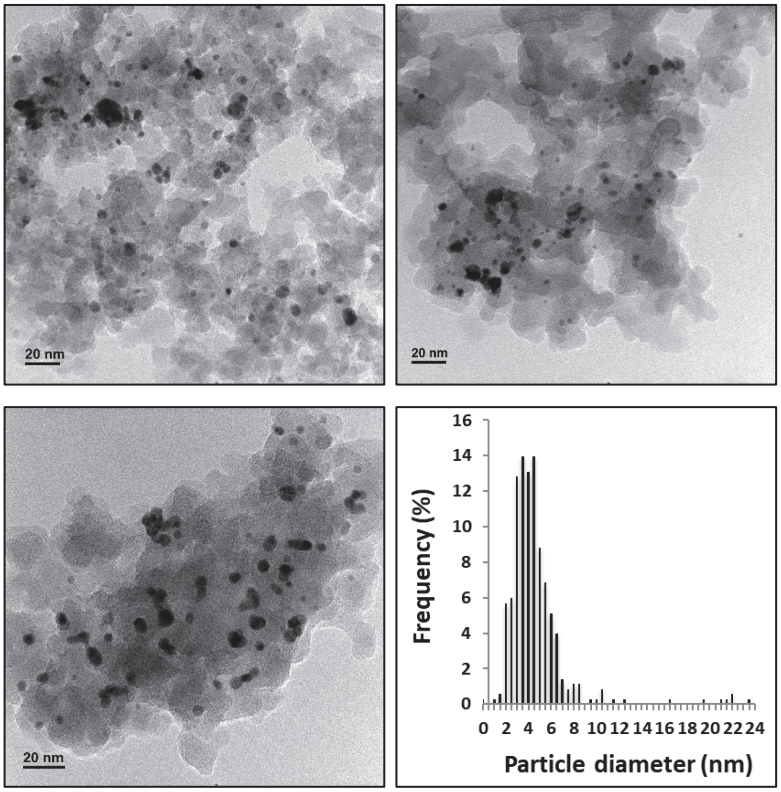

Figure 3.3.3 : TEM images of Pd(4)Au(1), and the corresponding particle size distribution where 351 particles were measured. Average particle size is 4.4 nm and SWD is 10.4 nm. Pre-treatment: calcination in air at 500°C for 7 h followed reduction with H_2 at 450°C for 1 h.

Fig. 3.3.4 shows the TEM-EDX analysis data over selected separate particles isolated from one another. Most particles displayed alloyed regions with varying proportions of Au and Pd after reduction with H_2 at 450°C.

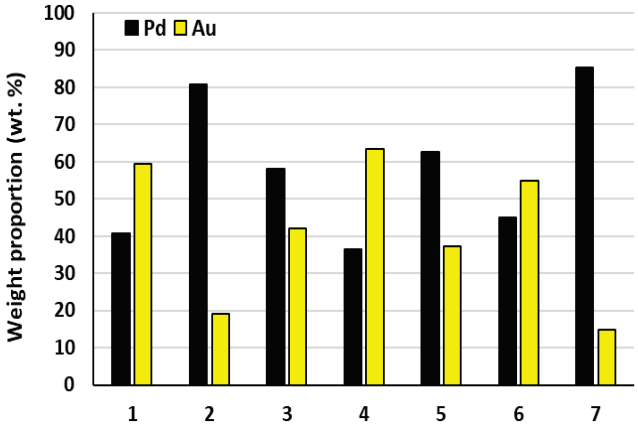

Figure 3.3.4 : Proportion (in wt. %) of Pd and Au measured by TEM-EDX over Pd(4)Au(1) in various particles.

According to TEM-EDX, the average Au/Pd atomic ratio is 0.6 which is higher than the actual value of 0.12 based on the ICP analysis. The reason could be the limited number of regions investigated by TEM-EDX. Another reason could be the fact that the TEM-EDX analysis has a limited beam penetration depth and is only able to measure the near-surface regions where most Au is expected to be located following the preparation method. Nonetheless, this measurement is rather relevant to the catalytic activity that depends on the surface properties.

3.4. TEM-EDX analysis of Pd(4)Au(4)

Fig. 3.3.5 shows the TEM images and the particle size distribution of the bimetallic Pd(4)Au(4) sample. The sample showed the presence of a lot of large particles which resulted in a wide range of particle size distribution of 4-24 nm. The average particle size is 7.6 nm and the SWD is 13.6 nm. The sample displays a low dispersion of 8.3%. The fraction of the large particles (> 9 nm) accounts for 71% of the overall surface area of the nanoparticles.

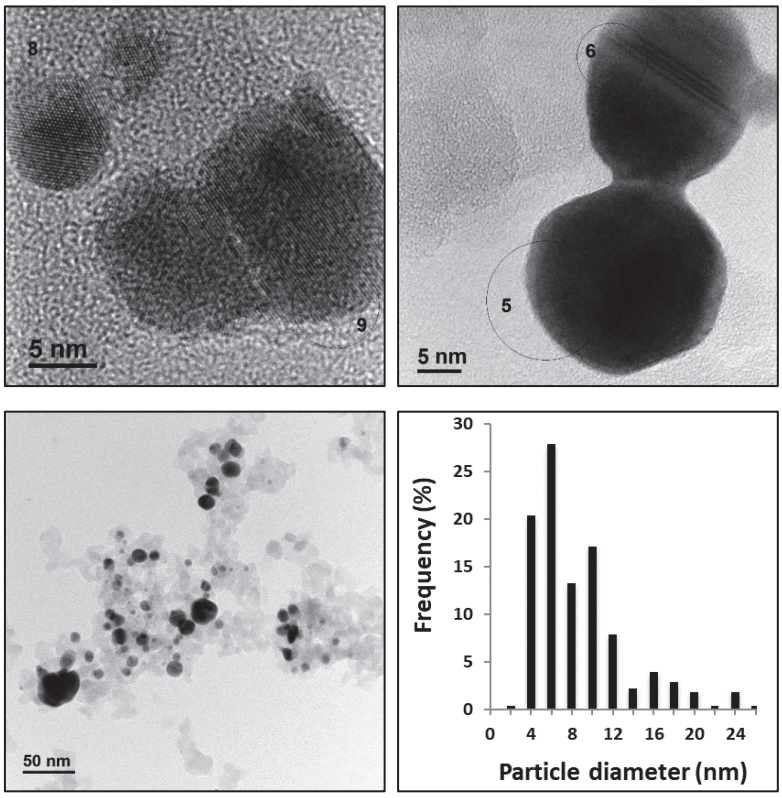

Figure 3.3.5 : TEM images of Pd(4)Au(4), and the corresponding particle size distribution where 280 particles were measured. Average particle size is 7.6 nm and SWD is 13.6 nm. Pre-treatment: calcination in air at 500°C for 6 h followed by reduction with $NaBH_4$ at RT.

Fig. 3.3.6 shows the TEM-EDX analysis data over selected separate particles. Several alloyed regions were identified with varying proportions of Au and Pd. The average Au/Pd atomic ratio is 1.35 (from

TEM-EDX data) which is higher than the actual value of 0.55 based on the ICP analysis, similar to what was observed with the other bimetallic samples.

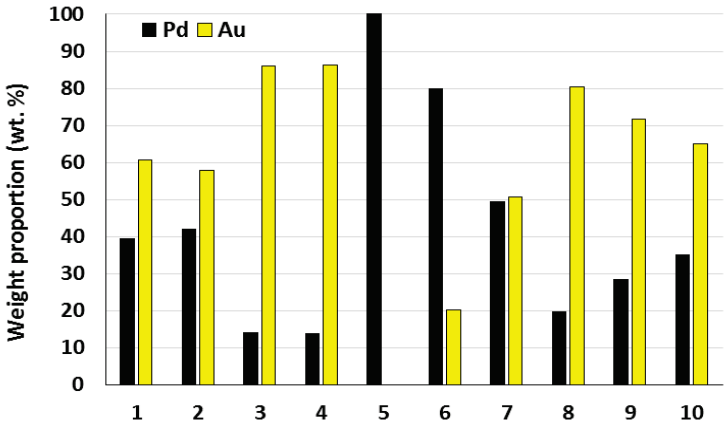

Figure 3.3.6 : Proportion (in wt. %) of Pd and Au measured by TEM-EDX over the Pd(4)Au(4) sample in various particles.

3.5. Comparison

Table 3.3.1 compares the parameters of the four samples. For all samples, the SWD is higher than the average particle diameter, which is associated with the presence of large particles. The monometallic Au sample showed small particles. The Pd-containing samples showed larger values due to the presence of large particles (>9 nm). Increasing the loading of Au lead to an increasing tendency to the formation of larger particles probably because of using the surface redox method. The fraction of the surface area of those large particles was significant i.e. those are expected to play a major role regarding the catalytic activity.

Table 3.3.1 : Parameters calculated from TEM analysis for all the silica-based samples.

Sample	Average particle diameter (nm)	SWD (nm)	Dispersion (%)	Surface area fraction at (d > 9 nm)
Au(1)	3.6	4.7	24.6	0%
Pd(4)	3.7	9.1	12.2	48%
Pd(4)Au(1)	4.4	10.4	10.8	39%
Pd(4)Au(4)	7.6	13.6	8.3	71%

4. PXRD analysis

The PXRD analysis is generally useful for detecting the various phases (and thereby oxidation states) of the metals after different treatments. The analysis is performed to characterize the catalysts after calcination in air and after reduction with H_2.

4.1. *In situ* PXRD analysis

The in situ PXRD experiment is useful for characterizing the catalysts under conditions relevant to the pre-treatments prior to the catalytic test. It is also important to avoid the exposure to ambient air during storage or between the treatments. The measurement was performed on the three samples listed in Table 3.4.1.

Table 3.4.1 : The samples characterized by the *in situ* PXRD analysis.

Sample	Au/Pd at. ratio
Au(1)	0
Pd(4)	----
Pd(4)Au(1)	0.12

4.1.1. Baseline correction

The signal of the silica support contributes significantly to the overall XRD signal recorded over the samples. Therefore, baseline correction is crucial in order to accurately identify the peak position and lattice constants as well as the peak area and the mean crystallite size.

As an example, Fig. 3.4.1 compares the XRD pattern of silica to the final XRD pattern collected over Pd(4) in air at 25°C. The figure shows the agreement of the signal of silica in both patterns. Fig. 3.4.2 shows the baseline corrected final XRD pattern of Pd(4) obtained by subtracting that of silica. The figure indicates the good quality of the baseline correction.

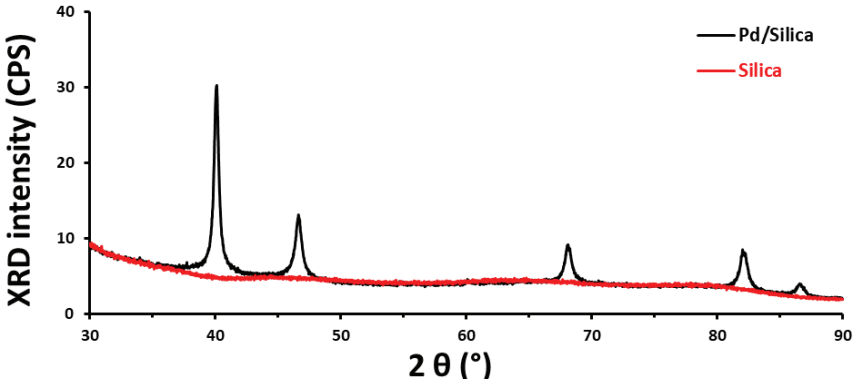

Figure 3.4.1 : Final XRD pattern of Pd(4) vs. XRD pattern of silica.

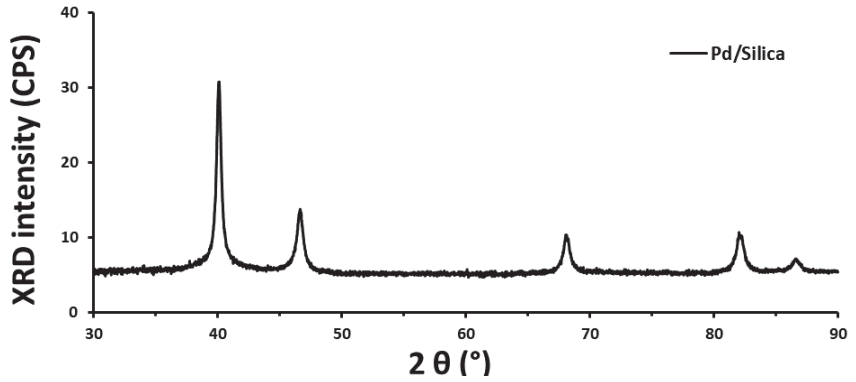

Figure 3.4.2 : Baseline corrected final PXRD pattern of Pd(4).

4.1.2. PXRD analysis of Au(1)

Fig. 3.4.3 and 3.4.4 show the XRD patterns collected over the Au(1) sample after the various treatments. Fig. 3.4.3 shows a wider range (2θ = 30-90°) while Fig. 3.4.4 focuses on a smaller range (2θ = 32-43°) where the highest intensity peaks are located. Beneath all the subsequent XRD plots, the ICDD reference files are shown corresponding to the observed phases.

No apparent change was observed for the XRD pattern after the different treatments. All patterns display the peaks perfectly matching with fcc Au structure (PDF 00-004-0784). The XRD signal is very poor possibly due to the small Au particle sizes (2-9 nm) as measured by the TEM analysis. This could indicate that the XRD measurement is only able to measure relatively large particles and crystalline phases. The lattice constant (a_{Au}) is found to be 4.075 (Å). The mean crystallite size is ~1.5 nm. This value is quite smaller than both the average particle diameter of 3.6 nm and the SWD of 4.7 nm obtained from the TEM images. This may indicate that most Au is amorphous and cannot detected by XRD.

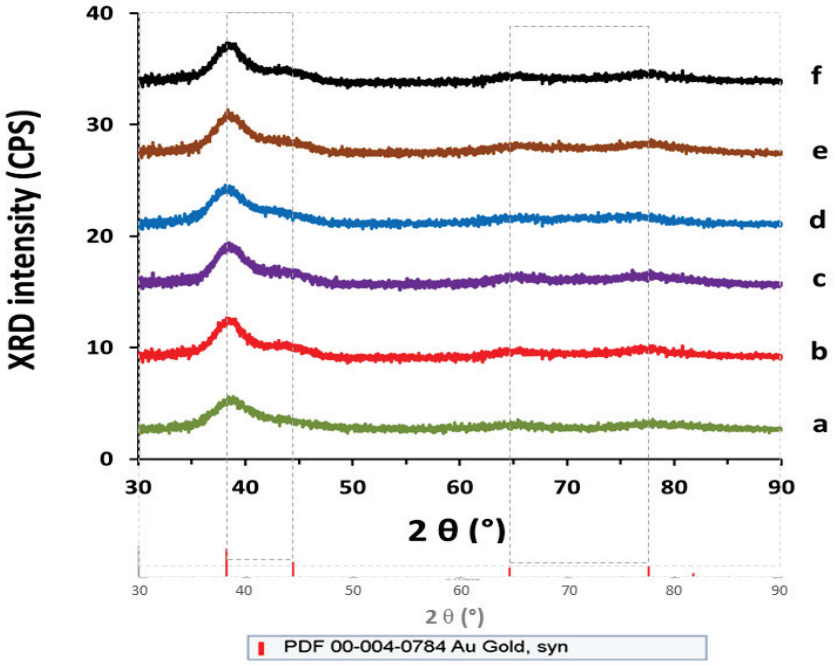

Figure 3.4.3 : XRD patterns (2θ = 30-90°) of Au(1) at (a) 25 °C in air after synthesis, (b) 25 °C in air after oxidation at 500 °C, (c) 25 °C in H_2, (d) 450 °C in H_2, (e) 25 °C in H_2 and (f) 25 °C in air. The peaks correspond to fcc Au structure (PDF 00-004-0784).

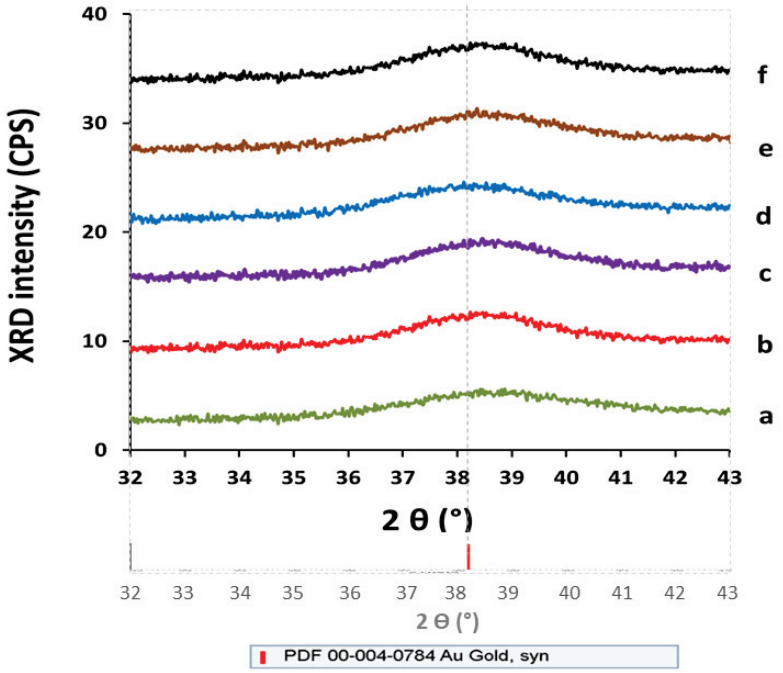

Figure 3.4.4 : XRD patterns (2θ = 32-43°) of Au(1) at (a) 25 °C in air after synthesis, (b) 25 °C in air after oxidation at 500 °C, (c) 25 °C in H_2, (d) 450 °C in H_2, (e) 25 °C in H_2 and (f) 25 °C in air. The peaks correspond to fcc Au structure (PDF 00-004-0784).

4.1.3. PXRD analysis of Pd(4)

Fig. 3.4.5 and Fig. 3.4.6 show the XRD patterns collected over the Pd(4) sample after the various treatments. Fig. 3.4.5 shows a wider range (2θ = 30-90°) while Fig. 3.4.6 focuses on the range of the highest intensity peaks (2θ = 32-43°) for a better and clearer identification of the phases.

Initially, the XRD pattern shows the presence of poorly crystalline metallic Pd. The peaks of Pd are observed at slightly lower angles compared to the reference (PDF 00-046-1043). This could indicate the presence of a residual amount of PdH_X phase initially present due to the reduction with $NaBH_4$ during the preparation. No XRD peaks corresponding to crystalline PdO were observed initially despite the fact that the sample was in contact with air after the preparation; yet, the presence of amorphous PdO cannot be excluded. The mean crystallite size is ~2 nm.

After the calcination treatment, only a tetragonal PdO phase is observed. The mean size of the crystalline domains increased from ~2 nm for the metallic Pd to ~6 nm for the PdO phase. This does not necessarily refer to a sintering process up on calcination. It may also be due to the oxidation and crystallization of some amorphous Pd initially present.

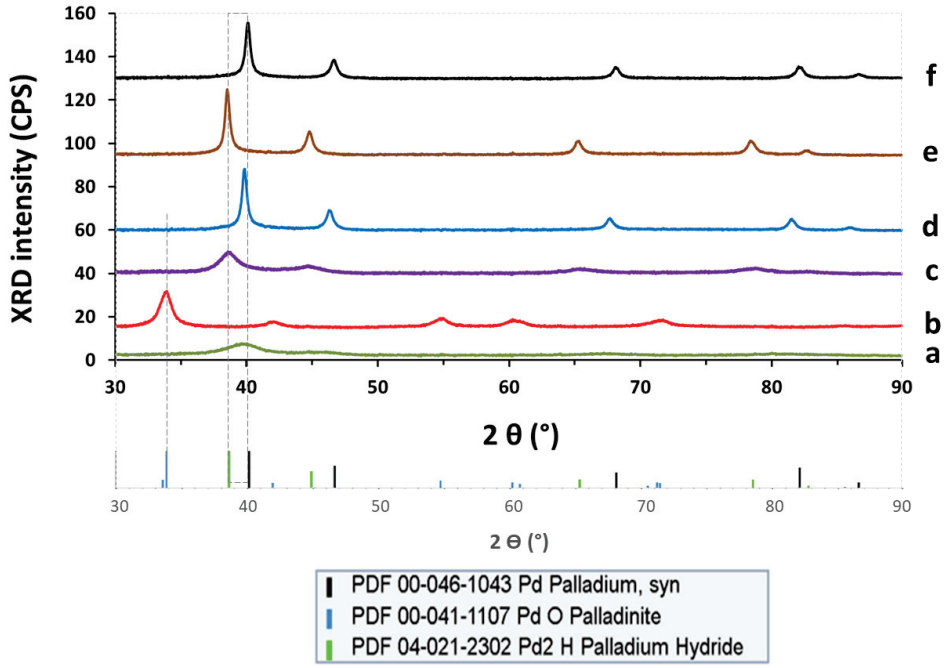

Figure 3.4.5 : XRD patterns (2θ = 30-90°) of Pd(4) at (a) 25 °C in air after synthesis, (b) 25 °C in air after oxidation at 500 °C, (c) 25 °C in H_2, (d) 450 °C in H_2, (e) 25 °C in H_2 and (f) 25 °C in air. The peaks correspond to fcc Pd structure (PDF 00-046-1043), PdO tetragonal phase (PDF 00-041-1107) and Pd_2H cubic phase (PDF 04-021-2302).

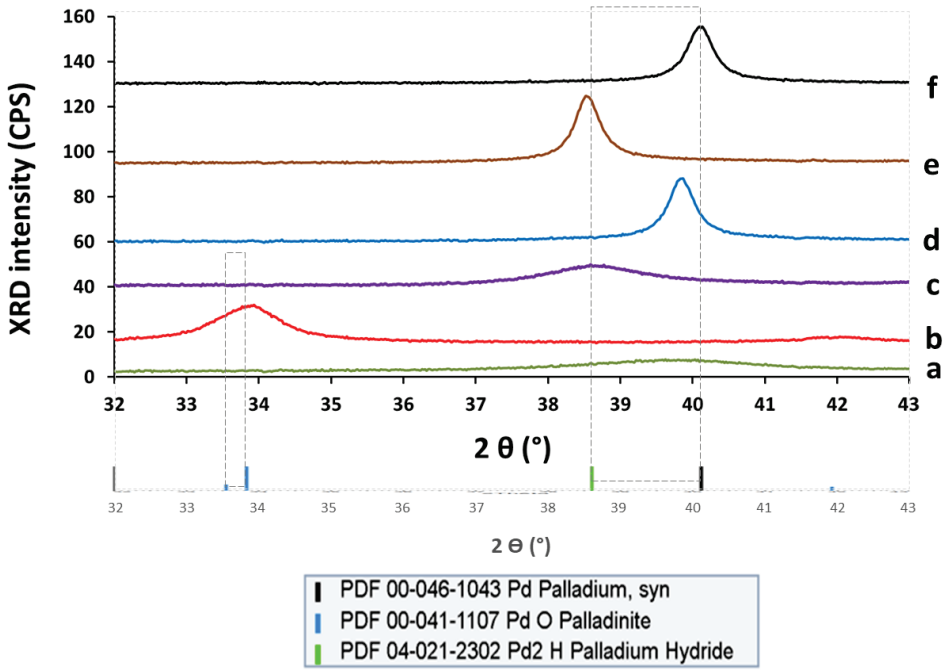

Figure 3.4.6 : PXRD patterns (2θ = 32-43°) of Pd(4) at (a) 25 °C in air after synthesis, (b) 25 °C in air after oxidation at 500 °C, (c) 25 °C in H_2, (d) 450 °C in H_2, (e) 25 °C in H_2 and (f) 25 °C in air. The peaks correspond to fcc Pd structure (PDF 00-046-1043), PdO tetragonal phase (PDF 00-041-1107) and Pd_2H cubic phase (PDF 04-021-2302).

Introducing H_2 flow at 25°C resulted in the immediate disappearance of the PdO peaks and the appearance of a PdH_X (β-palladium hydride) phase as indicated, for instance, by the PdH_X(111) peak at 2θ = 38.5° with a mean crystallite size of ~3 nm. This change in the crystallite size refers to a decreased degree of crystallinity since the diffusion of hydrogen disturbs the lattice of PdO and converts it into PdH_X. The formation of PdH_X (X~0.65) was also reported on deposited Pd films below 40°C in a flow of 5% H_2/Ar [7].

However, heating to 450°C resulted in restoring all the XRD peaks related to metallic Pd with an increased mean crystallite size of ~11 nm. Heating under H_2 has been already reported to increase the crystallinity of Pd/SiO_2 nanoparticles [6]. However, the peaks are slightly shifted towards lower 2θ values compared to the reference (PDF 00-046-1043). For instance, the Pd(111) peak is observed at 2θ = 39.9° compared to 40.1° for the reference. This could be due to the lattice expansion up on heating of Pd [8], Pt [9] and Au [10]. The thermal linear expansion coefficient of Pd is (11.8×10^{-6} K) and would result in a shift of the Pd(111) diffraction angle to 2θ = 39.95° which is very close to the observed value of 39.9°. The presence of a PdH_X (with a very small X) is also possible and is consistent with the fact that at 450°C, most hydrogen is expelled from the Pd bulk and surface. Using thermal desorption spectroscopy [11], it was reported that hydrogen diffused into the Pd bulk and desorbed as one broad peak with a maximum at ~650 K (377°C).

Cooling down to 25°C under H_2 flow lead to the re-formation of the hydride phase with a similar mean crystallite size of 12-13 nm.

After stopping H_2 flow and introducing N_2 flow for 30 min at 25°C followed by air resulted in the removal of the H stored in the metal either by the desorption from the bulk or combustion on the surface, restoring the metallic Pd phase. As reported earlier [7], stopping the H_2 flow and introducing N_2 flow was also sufficient to decompose the PdH_X (X~0.65) phase into metallic Pd below 40°C. The activation energy of desorption of hydrogen absorbed in the Pd bulk is as low as 30 kJ/mol [12] or 35.5 kJ/mol [11]. The mean crystallite size of the Pd phase measured by XRD is ~13 nm size which is higher than the average particle diameter measured by TEM of 3.7 nm but is close to the SWD of 9.1 nm. This reenforces that only relatively large particles are detected by the XRD measurement. Table 3.4.2 shows the lattice constants and mean crystallite sizes observed over the Pd(4) sample.

Table 3.4.2 : The lattice constants and mean crystallite sizes of the Pd(4) sample.

Conditions (T°C, flow, treatment)	Lattice parameters (Å)			Mean crystallite size (nm)		
	a_{Pd}	a-c_{PdO}	a_{PdHx}	Pd	PdO	PdH_X
25°C, air, before calcination	3.945			2		
25°C, air, after calcintion		3.037-5.339			6	
25°C, H_2, after calcintion			4.041			3
450°C, H_2, during reduction	3.916			11		
25°C, H_2, after reduction			4.044			12-13
25°C, air, after reduction	3.891			13		

Two important observations are to be highlighted: (i) the lack of an evidence of the ability of air to oxidize Pd to PdO at room temperature and (ii) the immediate conversion of PdO into PdH_X by H_2 at room temperature.

On the one hand, oxygen strongly adsorbs on Pd with a heat of adsorption of 230 kJ/mol at $\theta \leq 0.3$ [13] where the Pd-O bond energy is 324-364 kJ/mol at $\theta = 0.5$-0 [14]. The dissociative adsorption of O_2 on Pd has a very low activation energy (<10 kJ/mol) [14] and it takes place at room temperature [15]. However, oxygen diffuses into the Pd subsurface layers preferably at high temperatures due to the high activation energy of diffusion of 150-200 kJ/mol [14]. At a temperature of 300-500 K, Pd exposure to an O_2 pressure of 10 Pa leads to the formation of a Pd surface oxide film. However, the diffusion of O atoms into the Pd bulk at 300-500 K is extremely low and is enhanced only at a high

temperature (> 500 K) [13][14]. In conclusion, at room temperature, oxygen strongly adsorbs to the Pd surface and can form a surface oxide film but does not necessarily form a bulk oxide.

On the other hand, the reduction of PdO by H_2 to metallic Pd forming water is a thermodynamically favored reaction at room temperature and has a $\Delta G°$ of ~-28 kJ/mol [16]. The minimum temperature required for the reduction of oxidized Pd is below 230 K for oxygen chemisorbed on Pd and 290 K for oxygen in the PdO structure [16] . Moreover, H_2 has a very low activation energy of adsorption on Pd of 4.8 kJ/mol [17], a low activation energy of dissociation on Pd of 23.4 kJ/mol [18] and a low activation energy of diffusion into the Pd bulk of 23.4 kJ/mol [19]. Hence, the adsorption and dissociation of H_2 molecules followed by the diffusion of the H adatoms into the Pd bulk forming a PdH_X phase is rather favored at room temperature under H_2 pressure. At 25°C, the equilibrium H_2 pressure for the formation of the PdH_X phase was reported as low as ~16.5 mm Hg (0.022 atm) up to a H/Pd atomic ratio of 0.5 [20].

4.1.4. PXRD analysis of Pd(4)Au(1)

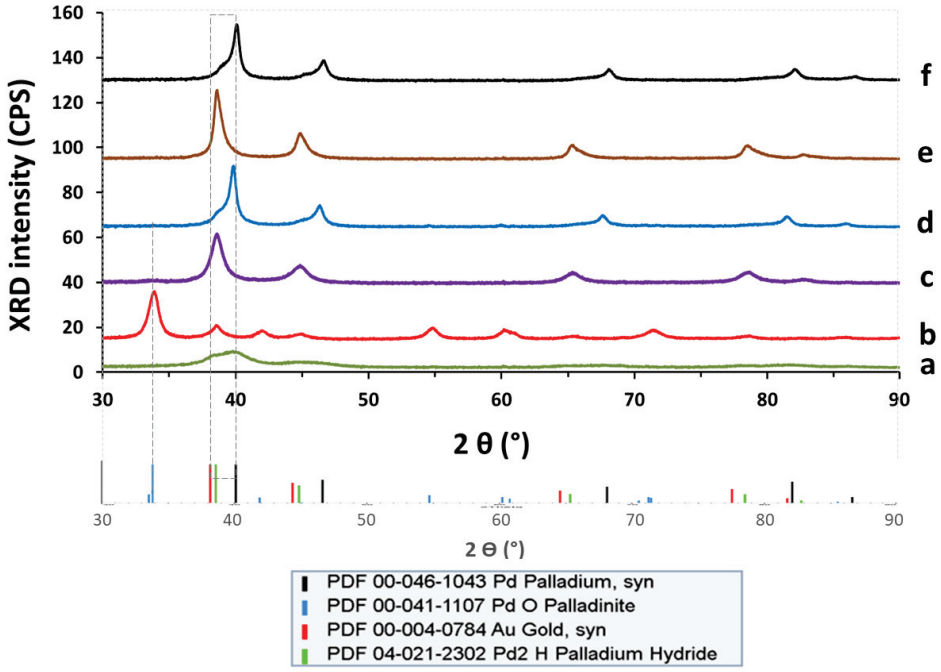

Figure 3.4.7 : XRD patterns (2θ = 30-90°) of Pd(4)Au(1) at (a) 25 °C in air after synthesis, (b) 25 °C in air after oxidation at 500 °C, (c) 25 °C in H_2, (d) 450 °C in H_2, (e) 25 °C in H_2 and (f) 25 °C in air. The peaks correspond to fcc Pd structure (PDF 00-046-1043), PdO tetragonal phase (PDF 00-041-1107) and Pd_2H cubic phase (PDF 04-021-2302) and fcc Au phase (PDF 00-004-0784).

Fig. 3.4.7 and Fig. 3.4.8 show the XRD patterns collected over the Pd(4) sample after the various treatments. Fig. 3.4.7 shows a wider range (2θ = 30-90°) while Fig. 3.4.8 focuses on the range of the

highest intensity peaks (2θ = 32-43°). The XRD peaks due to the presence of Pd dominate the XRD pattern due to its high loading (4.72 wt. %) compared to Au (1.03 wt. %).

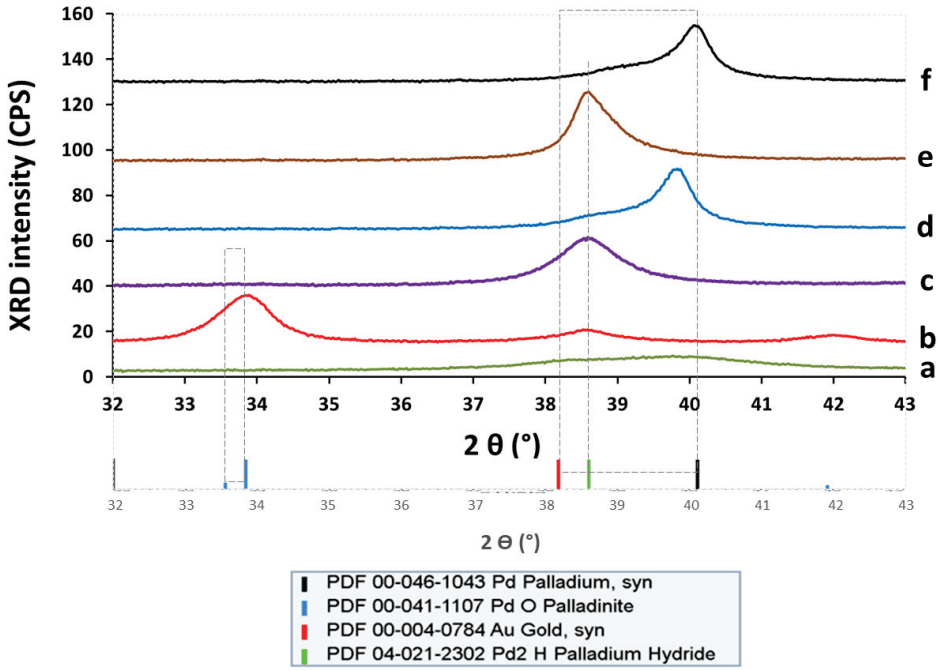

Figure 3.4.8 : XRD patterns (2θ = 32-43°) of Pd(4)Au(1) at (a) 25 °C in air after synthesis, (b) 25 °C in air after oxidation at 500 °C, (c) 25 °C in H_2, (d) 450 °C in H_2, (e) 25 °C in H_2 and (f) 25 °C in air. The peaks correspond to fcc Pd structure (PDF 00-046-1043), PdO tetragonal phase (PDF 00-041-1107) and Pd_2H cubic phase (PDF 04-021-2302) and fcc Au phase (PDF 00-004-0784).

Initially, overlapping peaks of metallic Au and Pd phases are observed with no conclusive evidence of alloying. The low intensities could indicate the presence mostly amorphous phases or very small nanoparticles. The observed mean crystallite sizes are 2 and 3 nm for Pd and Au, respectively.

After calcination, most metallic Pd was oxidized to PdO. In addition, a Au-rich PdAu alloy phase is also observed. According to the peak position, the phase displays an approximate composition of $Pd_{0.2}Au_{0.8}$ as calculated by Vegard's law. This composition is apparently a limiting composition that displays a full oxidation resistance under our calcination conditions. The oxidation resistance of the PdAu alloy was also reported [21][22][23]. There could be a residual amount of free Au whose peak would be completely overlapping with those of the alloy phase. The mean crystallite size for PdO phase is 7-8 nm and for the PdAu alloy phase is ~5 nm assuming no free Au.

Introducing H_2 at 25°C, immediately resulted in the formation of PdH_X phase, whose XRD peaks fall at similar positions as those for Au and PdAu alloy phase. Therefore, it is not possible to clearly differentiate the contribution of each phase in these peaks. Assuming that there is only PdH_X, the

mean crystallite size would be of the order of ~5 nm. There is a residual amount left of PdO that amounts for 5% of the total mass of the observed phases.

Heating to 450°C under H_2, resulted in the desorption of most H_2 and the appearance of the peaks of Pd featuring peak shoulders at positions in between the typical positions of the peaks of Au and Pd. These peak shoulders are ascribed to the presence of alloyed PdAu regions. The alloy formation is actually aided by heating due to the fast Pd diffusion into Au lattice as reported over a $\mathbf{Pd_{core}Au_{shell}}$ structure when heated to 500°C or higher [24]. The authors also reported that the alloy formation while heating a $\mathbf{Pd_{core}Au_{shell}}$ structure is faster than heating $\mathbf{Au_{core}Pd_{shell}}$ structure due to the lower activation energy of Pd diffusion into Au of 1.0 ± 0.6 eV vs. 1.6 ± 0.2 eV for Au diffusion into Pd. No clearly resolved peaks were observed in the typical positions of Au peaks.

The reduction treatment resulted in increasing the crystallinity of the Pd particles in the bimetallic sample with a mean crystallite size of 11-13 nm. The presence of monometallic Au phase cannot be ruled out; yet, a significant amount of Au is probably present in the form of PdAu alloy phase. Moreover, the peaks of the metallic Pd phase are slightly shifted to lower 2θ values due to the crystal expansion at this high temperature as explained before with the monometallic Pd sample.

Cooling down to 25°C in H_2 lead to the re-appearance of the PdH_X phase. The PdH_X peaks are of higher intensities (increased crystallinity) and display peak shoulders as compared to the peaks observed before heating to 450°C in H_2. Similarly, the peak shoulders could be to the formation of alloyed Au-Pd regions. The apparent mean crystallite size of PdH_X is ~13 nm.

Introducing N_2 flow for 30 min followed by air at 25°C after the reduction treatment resulted in the removal/combustion of H_2. The resulting pattern shows the formation of the PdAu alloy regions besides metallic Pd regions. The mean crystallite size of the Pd phase measured by XRD is 13-14 nm size which is higher than the average diameter of 4.4 nm measured by TEM but is close to the SWD of 10.4 nm. This indicates that only relatively large particles are detected by the XRD measurement. The alloy phase displays a lower crystallinity; yet, it is not possible to accurately calculate the mean crystallite size. Applying Vegard's law for the final XRD pattern collected in air at 25°C yields an approximate average alloy phases' composition of $Pd_{0.63}Au_{0.37}$.

Table 3.4.3 shows the lattice constants and mean crystallite sizes observed over the bimetallic Pd(4)Au(1) sample after each step of the treatment.

Table 3.4.3 : The lattice constant (a, c), mean crystallite size and the phase mass fraction for the Pd(4)Au(1) sample at (1) 25 °C in air after synthesis, (2) 25 °C in air after oxidation at 500 °C, (3) 25 °C in H_2, (4) 450 °C in H_2, (5) 25 °C in H_2 and (6) 25 °C in air.

Treatment	Lattice parameters (Å)					Mean crystallite size (nm) and wt. %				
	a_{Pd}	a_{Au}	a_{Pd-Au}	$a\text{-}c_{PdO}$	a_{PdH_x}	Pd	Au	PdAu	PdO	PdH_X
1	3.912	4.061				2 80%	3 20%			
2		4.042		3.043- 5.338				5 17%	7-8 83%	
3					4.040				5 5%	5 95%
4	3.917		3.981			11-13 60%		40%		
5			4.010		4.044			5 50%		13 50%
6	3.893		3.960			13-14 60%		40%		

4.1.5. Comparison between Au(1), Pd(4) and Pd(4)Au(1):

The following figures compare between the patterns of each of the three samples after calcination and after reduction. The patterns collected under H_2 at 25°C are not useful for the comparison since the PdH_X peaks overlap with the peaks of free Au and the PdAu alloy. Also, the patterns collected under H_2 at 450°C are similar to the final pattern except for the thermal expansion effect.

Fig. 3.4.9 shows the XRD patterns of the three sample after calcination. The figure shows the formation of PdO in both samples and the $Pd_{0.2}Au_{0.8}$ alloy in the bimetallic sample. The mean crystallite sizes of the bimetallic samples are slightly higher than those of the monometallic Au and Pd samples. PdO mean crystallite size is ~7 nm for the Pd-Au sample and ~5 nm for the monometallic Pd sample. The mean crystallite size of the PdAu alloy phase is ~3 nm in the Pd-Au sample while the mean crystallite size in Au sample is ~1.5 nm. This could indicate that depositing Au on the surface of Pd using the surface redox method increases the tendency of the formation of larger crystallites as also concluded from the TEM analysis.

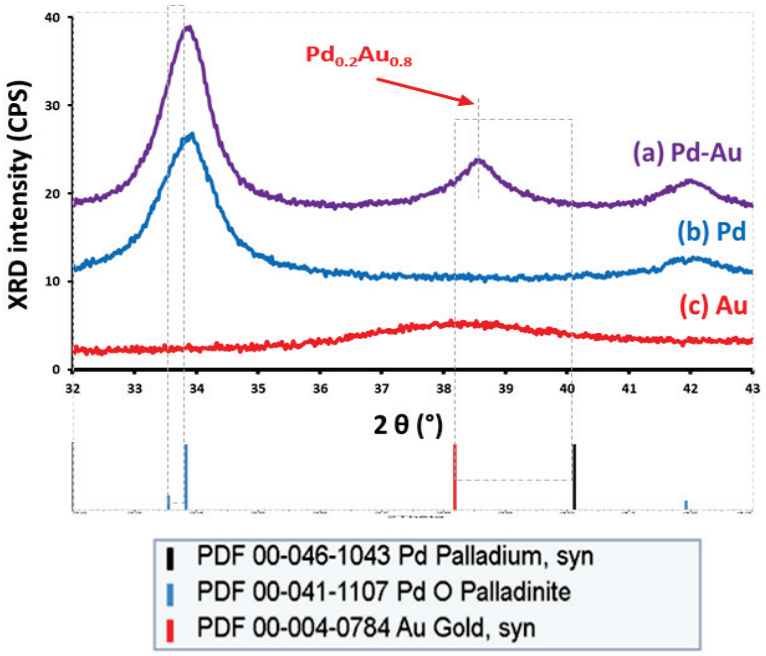

Figure 3.4.9 : XRD patterns of Au(1) vs. Pd(4) vs. Pd(4)Au(1) collected at 25°C in air after calcination in air at 500°C for 7 h. The peaks correspond to PdO tetragonal phase (PDF 00-041-1107), fcc Au phase (PDF 00-004-0784) and fcc PdAu alloy phase.

Fig. 3.4.10 shows the final patterns collected over the three samples after removing H_2 pressure and introducing air. In the Pd-containing samples, the position and intensity of the Pd(111) peak are essentially the same. The presence of Au in the bimetallic sample lead to the formation of the alloy phase and there is no clear evidence if there is free Au.

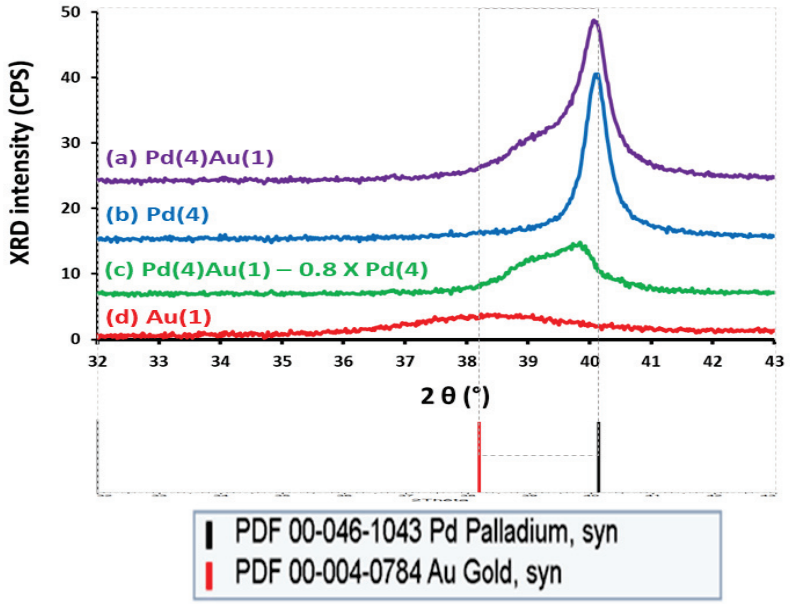

Figure 3.4.10 : XRD patterns of Au(1) vs. Pd(4) vs. Pd(4)Au(1) after cooling down to 25°C in air flow after the reduction treatment. Pattern (c) is obtained by subtracting a fraction (0.8) of the Pd(4) pattern from the Pd(4)Au(1) pattern. The peaks correspond to fcc Pd structure (PDF 00-046-1043), fcc Au structure (PDF 00-004-0784) and fcc PdAu phase.

The peak of the alloy phase alone (Fig. 3.4.10 c) was obtained by subtracting a fraction of the XRD pattern of the Pd sample from that of the Pd-Au sample. The peak shows the presence of a distribution of alloy compositions and corresponds to an average alloy composition of $Pd_{0.63}Au_{0.37}$.

Fig. 3.4.11 shows the alloy phase formed after calcination and reduction. The figure demonstrates the significance of the reduction treatment. After reduction, the alloy phase shows a higher degree of alloying as it is richer in Pd besides the fact that almost all Au is consumed for alloying. The peak area is also higher after reduction and is 1.6 times that observed after calcination.

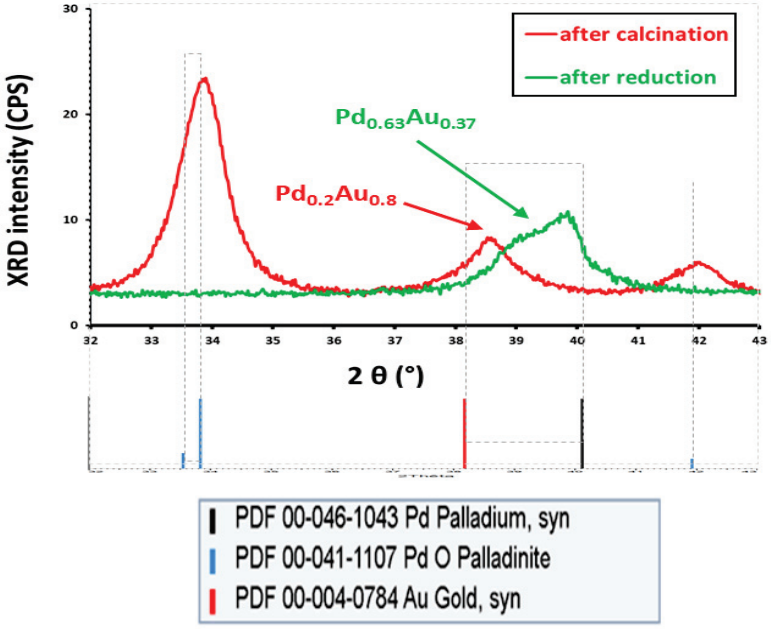

Figure 3.4.11 : XRD patterns of Pd(4)Au(1) at 25 °C in air after calcination (red line) and after reduction (green line). The pattern collected after reduction shows only the alloy phase (same as in Fig. 3.4.10 c). The peaks correspond to fcc PdAu phases and PdO tetragonal phase (PDF 00-041-1107).

Table 3.4.4 summarizes the particle diameter and mean crystallite sizes for all samples.

Table 3.4.4 : Comparison between the average particle diameter, the SWD and the mean crystallite sizes of all SiO_2-based samples.

Sample	Average particle diameter (nm)	SWD (nm)	*In situ* XRD mean crystallite size (nm)
Au(1)	3.6	4.7	1.5
Pd(4)	3.7	9.1	Pd : 13
Pd(4)Au(1)	4.4	10.4	Pd : 13-14
Pd(4)Au(4)	7.6	13.6	n.d.

4.2. *Ex situ* PXRD analysis

The measurement was performed on the three Pd-containing samples listed in Table 3.4.5.

Table 3.4.5 : The samples characterized by the *ex situ* PXRD analysis.

Sample	Au/Pd at. ratio
Pd(4)	----
Pd(4)Au(1)	0.12
Pd(4)Au(4)	0.55

The *in situ* PXRD experiment was useful for monitoring the effect of one (calcination + reduction) treatment cycle. Therefore, two cycles of (calcination + reduction) treatments were applied before the *ex situ* PXRD measurement in order to investigate the PdAu alloy formed after one (calcination + reduction) cycle. After re-calcination, the oxidation resistance of the PdAu alloy is to be checked. After re-reduction, the effect of the Au/Pd atomic ratio on the degree of alloying is to be monitored.

Before the *ex situ* XRD measurement, the samples were *ex situ* calcined in air at 450°C for 6 h, *ex situ* reduced in a flow of 50% H_2/He at 450°C for 30 min and then, *ex situ* re-calcined in air at 450°C for 6 h. The same amounts of the samples were collected after the XRD measurement, *ex situ* reduced in a flow of 50% H_2/He at 450°C for 30 min and finally, re-measured by XRD.

4.2.1. After the re-calcination treatment

Fig. 3.4.12 shows the XRD patterns collected over the three samples after the (calcination + reduction + re-calcination). The patterns of the re-calcined samples are normalized so that the PdO(101) peaks at 33.8° in all patterns have the same peak intensity (and also peak area). The purpose of this normalization is to follow the change in the intensity of the alloy phase for the bimetallic samples with changing the loading of Au.

The monometallic Pd sample displays full oxidation whereas the bimetallic sample shows the presence of both PdO and PdAu alloy phases. This indicates the (partial) oxidation resistance of Pd induced by alloying with Au. The peak positions of the alloy phase of the three bimetallic sample are fairly the same and correspond to an approximate alloy composition of $\mathbf{Pd_{0.2}Au_{0.8}}$ as calculated by Vegard's law. This composition represents a threshold alloy composition at which Pd displays full

oxidation resistance under air at 450°C. A similar value of **$Pd_{0.15}Au_{0.85}$** was reported [23] at which the interaction of a PdAu alloy with O_2 is extremely limited up to 600°C.

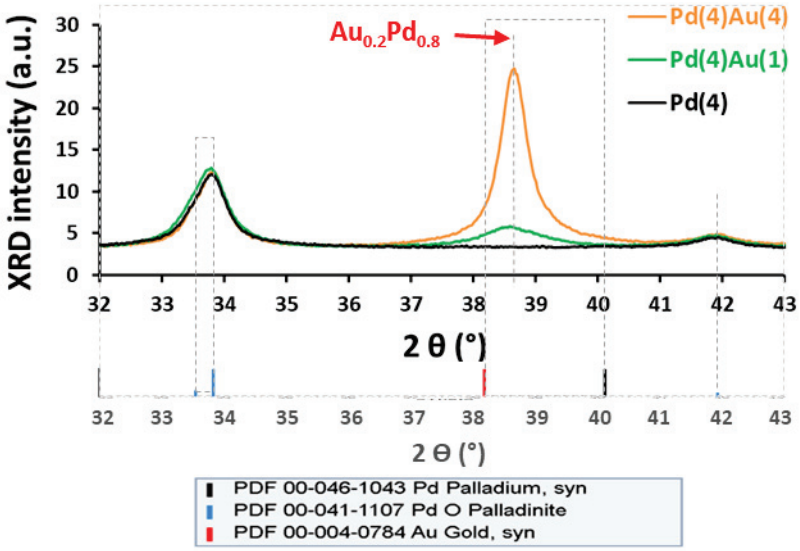

Figure 3.4.12 : PXRD patterns of the three samples after the *ex situ* calcination treatment. all patterns are normalized so that the PdO(101) peaks at 33.8° have the same peak intensity (and peak area).

It is not clear if there is free Au in the bimetallic samples since its peak could be overlapping with that of the alloy phase. This could indicating that all or most Au is consumed for alloying with Pd which is in large excess already.

Fig. 3.4.13 follows the evolution of PXRD patterns of the Pd(4)Au(1) sample after the *in situ* calcination, the *in situ* reduction and the *ex situ* calcination.

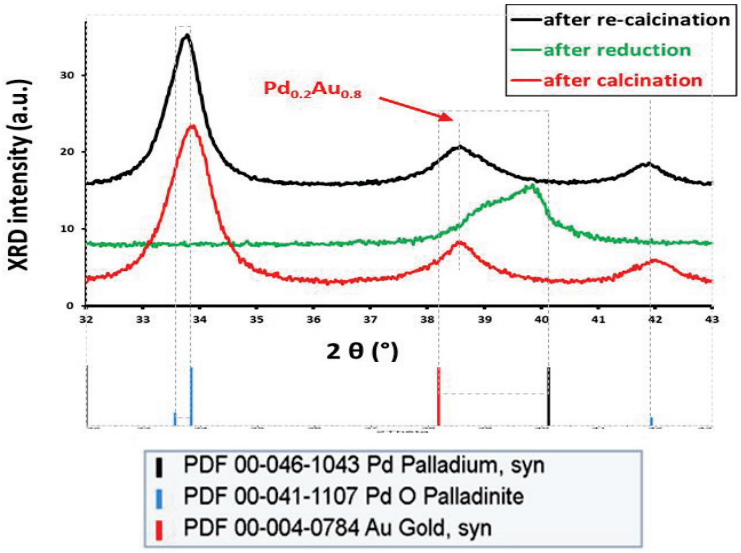

Figure 3.4.13 : PXRD patterns of Pd(4)Au(1) after the *in situ* calcination (red line), the in situ reduction (green line) and the *ex situ* re-calcination (black line).

The pattern recorded after the *ex situ* re-calcination is normalized so that the PdO(101) peak (at 2θ = 33.8°) has the same peak area as the pattern recorded after the in situ calcination. The patterns after both calcination treatments are almost identical. This reenforces the conclusion that the $Pd_{0.2}Au_{0.8}$ is a limiting composition which is resistant to oxidation.

4.2.2. After the re-reduction treatment

Fig. 3.4.14 shows the XRD patterns after the final re-reduction treatment. The monometallic Pd sample displays peaks corresponding to metallic Pd phase. The bimetallic sample display peaks corresponding to metallic Pd as well as PdAu alloy phases. With increasing the loading of Au, the alloy phase peaks display a linear increase relative to the metallic Pd peak areas (see Fig. 3.4.18 in section 4.2.3), indicating that all Au is consumed for the alloying in the presence of an excess Pd, similar to what is observed with the XRD patterns after re-calcination. Moreover, the peak positions of the alloy phase are shifted to lower angles with increasing the loading of Au. Table 3.4.6 in section 4.2.3 shows the approximate alloy compositions of the alloy phase for the three bimetallic samples after calcination and after reduction.

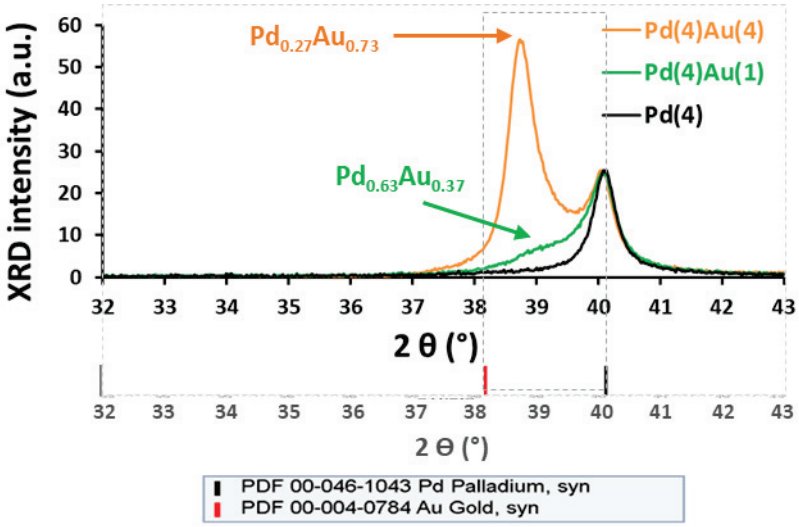

Figure 3.4.14 : PXRD patterns of the three samples after the *ex situ* (calcination in air at 500°C + reduction with H_2 at 450°C) treatment. all patterns are normalized so that the Pd(111) peaks at 40.1° have the same peak intensity.

All samples display very low intensities at the position of the reference file of Au. This indicates that almost all Au is essentially alloyed which is expected considering the surface redox preparation method. However, a free metallic Pd and Au-rich alloy phases were observed with Pd(4)Au(4). The alloy phases were expected to be richer in Pd which is already in excess in all the samples as the case

of Pd(4)Au(1). This could indicate that the reduction conditions may not be sufficient for a higher degree of alloying at Au loading of 4.02 wt.%.

As reported [24], the alloying of Au and Pd is aided by heating a $\mathbf{Pd_{core}Au_{shell}}$ structure at 500°C or higher. Another work [23] reported that after the oxidation of a $\mathbf{Au_{0.4}Pd_{0.6}}$ alloy, heating under H_2 at 300°C was enough for the reduction of Pd while heating to 600°C was necessary for the re-alloying of Au and Pd. Therefore, a higher reduction temperature is expected to enhance alloying. Effect of the Au/Pd atomic ratio

Table 3.4.6 shows the calculated approximate alloy compositions of the observed alloy phases after the two steps of the *ex situ* PXRD measurement of the two bimetallic samples. With increasing the loading of Au, the calculated alloy composition after the *ex situ* re-calcination treatment is almost the same. All the bimetallic samples display the approximate limiting alloy composition of $Pd_{0.2}Au_{0.8}$ resistant to oxidation.

Table 3.4.6 : Approximate compositions of the alloy phase calculated by Vegard's law for the bimetallic samples after the *ex situ* re-calcination and re-reduction.

Sample	Au/Pd at. ratio	Alloy phase composition	
		Re-calcined	Re-reduced
Pd(4)Au(1)	0.12	$Pd_{0.18}Au_{0.82}$	$Pd_{0.63}Au_{0.37}$
Pd(4)Au(4)	0.55	$Pd_{0.23}Au_{0.77}$	$Pd_{0.27}Au_{0.73}$

After the re-reduction, the formed alloy phases are generally richer in Pd than after the re-calcination. This reenforces the importance of the reduction in increasing the degree of alloying. Moreover, the fraction of Pd in the alloy phases increases with decreasing the loadings of Au (decreasing the Au/Pd atomic ratios). However, at Au/Pd atomic ratios of 0.55, the alloy phase is richer in Au than Pd. This is not what would be expected at such Au/Pd atomic ratios (<1) where Pd is in excess in all samples. This may indicate that the alloying is limited, possibly only to surface sites where all/most Au is expected to be located.

5. Conclusion on the characterizations performed

The TEM images were collected after calcination in air at 500°C followed by reduction in H_2 at 450°C. The analysis showed the formation of small Au/SiO_2 nanoparticles. The Pd-containing samples displayed the presence of larger particles. With increasing the loading of Au in the bimetallic samples, a higher tendency was observed towards the formation of larger particles. The large nanoparticles (> 9 nm) in the Pd-containing samples display a significant fraction of the overall surface area of the nanoparticles. The TEM-EDX analysis has shown the presence of both Pd and Au in most nanoparticles investigated. The limitation of the TEM-EDX analysis is that it is probably only limited to measuring the surface composition.

The *in situ* PXRD analysis showed that the Au sample displayed an initial poor crystallinity and was not affected by any treatment applied. The Pd-containing samples displayed an initial poor crystallinity and immediate changes upon changing the feed even at room temperature. The calcination treatment lead to the oxidation of Pd. The bimetallic sample with the Au/Pd atomic ratio of 0.12 displayed a $Pd_{0.2}Au_{0.8}$ alloy resistant to oxidation. Exposure to H_2 at room temperature immediately forms a PdH_X phase which decomposes to metallic Pd while heating or once H_2 pressure is removed. The reduction treatment at 450°C in H_2 resulted in increasing the crystallinity of Pd and the degree of Au and Pd alloying. The major limitation of the XRD analysis is that only relatively large particles and crystalline phase are detected.

The *ex situ* PXRD analysis showed that all Au is consumed for alloying with Pd at Au/Pd atomic ratios of 0.12 and 0.55. The re-calcination of the initially calcined then reduced bimetallic samples lead to the formation of PdO and a $Pd_{0.2}Au_{0.8}$ alloy resistant to oxidation at all the Au/Pd ratios tested. The final re-reduction lead to the formation of alloy phases richer in Pd than $Pd_{0.2}Au_{0.8}$ with the Pd fraction increasing with decreasing the Au/Pd ratio.

6. Catalytic activity for NO_X decomposition

The catalytic test was performed using the four samples listed in Table 3.6.1.

Table 3.6.1 : The samples tested for NO direct decomposition.

Sample	Au/Pd at. ratio
Au(1)	----
Pd(4)	0
Pd(4)Au(1)	0.12
Pd(4)Au(4)	0.55

6.1. NO feed through the empty reactor

The feed signal is collected for a few minutes through the by-pass until the NO signal stabilizes. The flow is then switched into the quartz reactor. Fig. 3.6.1 shows the FTIR profile of NO initially through the by-pass line before switching the flow into the empty quartz reactor. For the subsequent figures, the starting point of the reaction is chosen to be the point at which the signal of NO starts to change after switching the flow from the by-pass to the reactor.

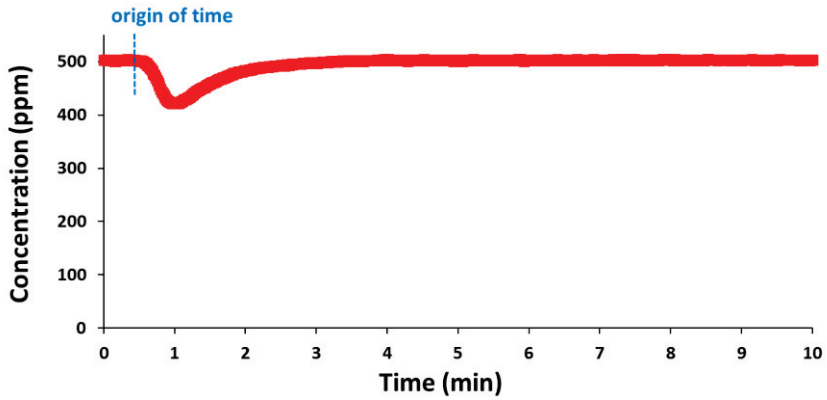

Figure 3.6.1 : FTIR data of the NO profile through the empty reactor. NO steady state concentration is 503 ppm. The point at which the feed is switched from the by-pass line to the reactor is chosen to be the origin of time for the subsequent figures.

In Fig. 3.6.1, the concentration of NO through the empty reactor is 503 ppm before the purge of the dead-volume of the reactor observed between 0.5 and 4 min. The NO profile through the empty reactor thus takes about three minutes to stabilize back to 503 ppm. Assuming that NO does not react and its temporary disappearance is merely due to the purge of the dead-volume initially filled with pure He, we can use the NO signal as that of an inert tracer. The NO curve can be used to calculate

the reactor line dead-volume, by integrating the "missing NO" area following the switch given by Eq. 3.6.1:

$$\textbf{Reactor line dead volume} = \frac{\mathbf{F}}{\mathbf{503}} \int_0^{TOS} \{\, \mathbf{503} - [\mathbf{NO(t)}] \,\}\, dt \qquad \textbf{Eq. 3.6.1}$$

where F is the flow rate (50 mL/min) and TOS is the time on stream (10 min for instance). This results in a dead-volume of 7.9 mL.

The missing amount of NO can then be calculated according to Eq. 3.6.2:

$$[\textbf{Missing NO(t)}] = [\mathbf{NO_{feed}}] - [\mathbf{NO(t)}] - [\mathbf{NO_2(t)}] - \mathbf{2} \times [\mathbf{N_2O(t)}] \qquad \textbf{Eq. 3.6.2}$$

Fig. 3.6.2 shows the FTIR profiles of N_2O, NO_2 and the calculated missing NO through the empty reactor. Negligible amounts of NO_2 and N_2O are observed. In addition, the missing NO profile falls to zero after ~4 min i.e. after the purge of the dead-volume of the reactor line. As reported, NO decomposition displays a very large kinetic barrier of ~335 kJ/mol [25][26] and a very low equilibrium constant up to 1500 K [27]. This essentially reenforces that NO does not react inside the empty reactor and the change in its concentration after switching the flow to the reactor is only due to the purge of the dead-volume as discussed before.

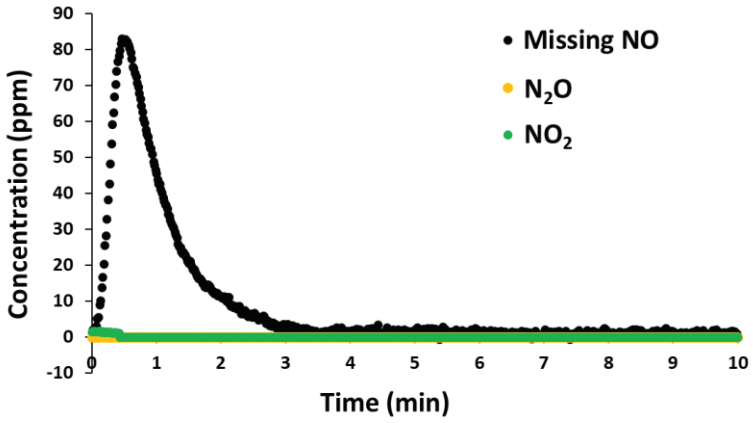

Figure 3.6.2 : FTIR data of the NO_2, N_2O and the missing NO through the empty reactor. The starting point is the chosen origin of time. NO steady state concentration is 503 ppm.

6.2. Methodology of calculation

FTIR can only detect NO, NO_2 and N_2O but not N_2 or O_2. Therefore, a micro-GC is used to quantify N_2 and O_2. NO_2 is not a decomposition product since it is formed by the reaction of NO from the feed with the produced oxygen. Hence, NO conversion to (N_2 + N_2O) as the decomposition products is

calculated according to Eq. 3.6.3, where (NO_X = NO + NO_2). The selectivity to N_2 production is calculated according to Eq. 3.6.4.

$$\textbf{NO conversion}(t) = \frac{[N_2(t)] \times 2 + [N_2O(t)] \times 2}{[(NO_X)_{feed}]} \qquad \textbf{Eq. 3.6.3}$$

$$\textbf{Selectivity to } N_2(t) = \frac{[N_2(t)]}{[N_2(t)] + [N_2O(t)]} \qquad \textbf{Eq. 3.6.4}$$

The total N- and O-equivalents are calculated as follows:

$$\textbf{Total N} - \textbf{equivalents}(t) = [N_2(t)] \times 2 + [N_2O(t)] \times 2 \; + \; [NO(t)] + [NO_2(t)] \qquad \textbf{Eq. 3.6.5}$$

$$\textbf{Total O} - \textbf{equivalents}(t) = [O_2(t)] \times 2 + [NO_2(t)] \times 2 \; + \; [NO(t)] + [N_2O(t)] \qquad \textbf{Eq. 3.6.6}$$

6.3. Experimental conditions

All the samples were exposed to a flow of 500 ppm NO + 5% O_2 at a temperature range of 200-450°C. Fig. 3.6.3 and 3.6.4 show two examples monitoring the effluent gases observed during the pretreatment of the Pd(4) and Pd(4)Au(1) samples, respectively.

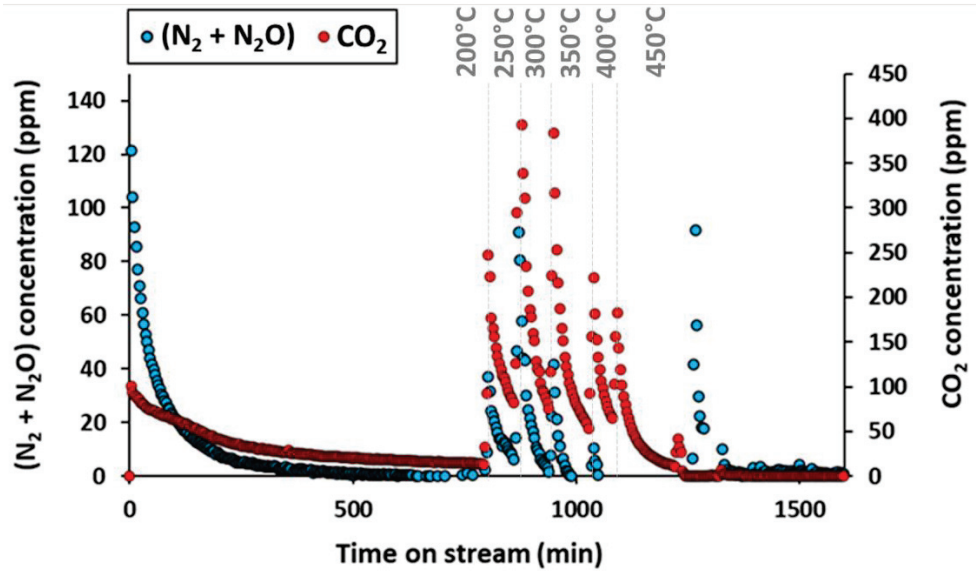

Figure 3.6.3 : Effluent gases detected during the pre-treatment of Pd(4). Feed: 500 ppm NO + 5% O_2/He, 50 mL/min, 200-450°C.

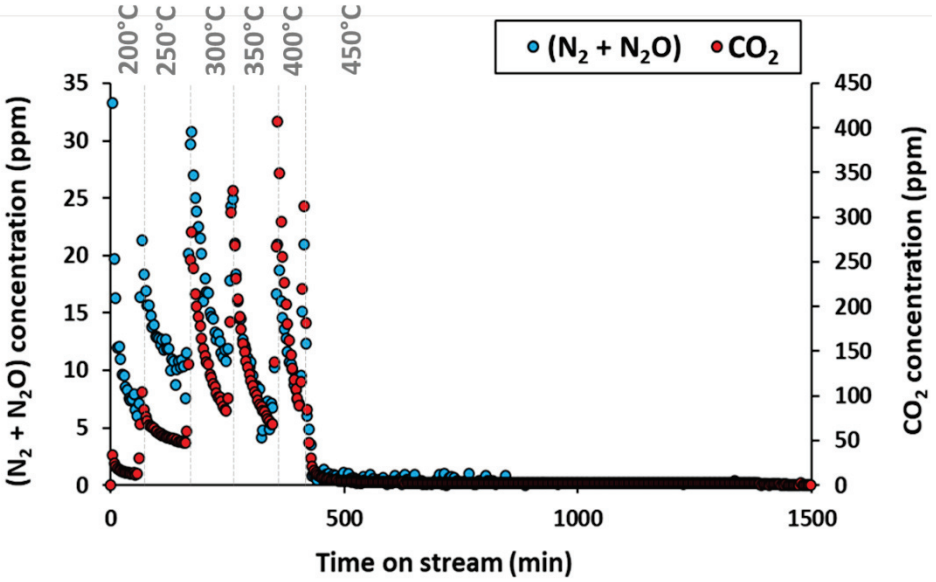

Figure 3.6.4 : Effluent gases detected during the pre-treatment of the bimetallic sample Pd(4)Au(1). Feed: 500 ppm NO + 5% O_2/He, 50 mL/min, 200-450°C.

Significant N_2 and N_2O production was observed which was associated with the evolution of CO_2. This indicates that APTMS present at the surface of the silica support can lead to NO_X reduction. This stresses that the catalysts should be calcined in order to avoid such unwanted reactions. The pretreatment was kept until the NO_X reduction ceased and the signal of CO_2 was no longer observed indicating the removal of the organic residues.

The production to (N_2 + N_2O) over the samples dropped to zero once CO_2 production ceased, indicating that the catalysts are not active for NO decomposition in the presence of 5% O_2. A similar observation was observed over supported noble metals [5].

Eq. 3.6.7 was reported by Valyon *et al.* [28] for the catalytic NO decomposition activity of Cu−ZSM5, where the rate of the reaction is 1st order in NO pressure and is inhibited by the presence of O_2. A similar conclusion was reported by Amirnazmi *et al.* over supported Pt [29].

$$\mathbf{r} = \frac{\boldsymbol{k} \times \mathbf{P_{NO}}}{\mathbf{1} + \mathbf{K} \times \sqrt{\mathbf{P_{O_2}}}} \qquad \textbf{Eq. 3.6.7}$$

Also, as reported [30][31], heating PdAu alloys in O_2 above 450 °C can lead to the formation and surface segregation of PdO. Therefore, the catalysts were then reduced in a flow of 40 mL/min of 50% H_2/He at 450 °C for 1 h so as to reduce the formed PdO and to ensure the re-alloying of Pd and Au. The NO decomposition activity was then measured at 450 °C in a flow of 500 ppm NO/He over

1000 min with a total flowrate of 50 mL/min. in the absence of O_2. The following sections show the catalytic performance of the silica-based samples under NO in the absence of O_2 [32].

6.4. Performance of Au(1)

Fig. 3.6.5 shows the N_2 production over the Au(1) catalyst. The sample is essentially not active for NO decomposition reaction under these conditions, as the level of (N_2 + N_2O) formed (~3 ppm) was close to the precision of the measure.

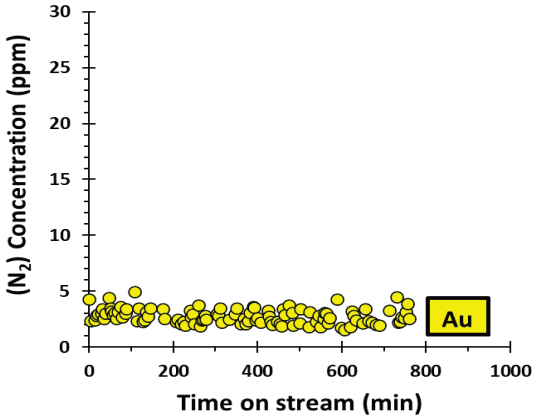

Figure 3.6.5 : The evolution of the concentration of N_2 produced over 100 mg of Au(1) during the catalytic test. Feed: 500 ppm NO/ArHe, 50 mL/min, 450°C.

6.5. Performance of Pd(4)

Fig. 3.6.6 shows the gases produced over the Pd(4) sample under NO in the absence of O_2. The catalyst shows measurable amounts of all gases. The catalyst favors the production of O_2 and N_2 rather than N_2O or NO_2.

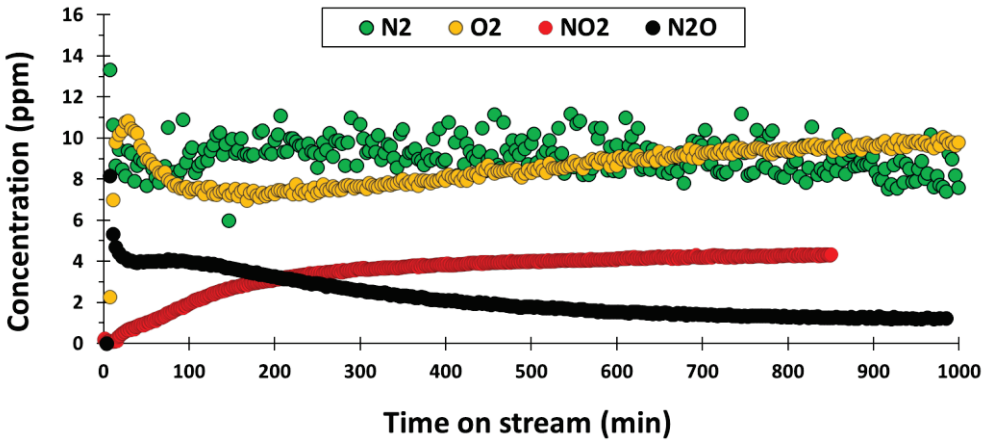

Figure 3.6.6 : The evolution of the concentrations of the NO decomposition products detected over 100 mg of Pd(4) during the catalytic test. Feed: 519 ppm NO/ArHe, 50 mL/min, 450°C.

After the NO feed stabilizes, the profiles of N_2 and N_2O show an uprubt deactivation initially for 50 min before a slower deactivation is observed. This could indicate the presence of two different types of active sites. The different crystallites of Pd interact diffrently with NO. It was reported that the stepped Pd(112) surface is more active towards NO decomposition than the Pd(111) plane [33].

The catalyst favors the formation of N_2 rather than N_2O possibly due to the more faesible desorption of the N_{ads} rather than the O_{ads} atoms. The Pd-N_2 bond is very weak and has a bond energy ~25 kJ/mol on Pd(110) surface [34]. Also, N_2 desorbs off the Pd(111) surface at 70 K [35]. However, the Pd-O bond displays a high bond energy of 324-364 kJ/mol at θ = 0.5-0 [14]. The formation of the two gases (N_2 and N_2O) could be due to a real NO direct decomposition or due to a redox reaction between metallic Pd and NO leading to the formation of PdO. A redox reaction could explain the initial rapid deactivation since PdO is not active for NO decomposition.

The production of O_2 indicates that the catalyst exhibits some catalytic activity. The initial rapid decrease in the O_2 profile for ~200 min is associated with the rapid increase in the formation of NO_2 and does not neceassarily refer to the deactivation of the catalyst. However, the catalyst displays a higher tendency to the formation of O_2 rather than NO_2. After 200 min, the production of NO_2 slows down and the formation of O_2 increases.

The reason could be that after ~200 min of NO exposure, the catalyst surface would reach a high coverage with O adatoms which would lead to an increased probability of the formation and desorption of O_2. This is also consistent with the slower formation of NO_2, since the adsorbed oxygen would poison the catalyst's surface and compete with NO for adsorption sites. Expectedly, this would lead to a lower probability of NO to react with the adsorbed oxygen or even undergo decomposition. This could explain the slow deactivation behavior in the formation of N_2 and N_2O at 50-1000 min. Moreover, the nanoparticles may undergo sintering under NO which could also contribute to the deactivation behavior.

Fig. 3.6.7 shows the evolution of the NO profile as well as the calculated total N- and O-equivalents. The total N-equivalents correspond to 519 ppm and the total O-equivalents correspond to 518 ppm in average. This perfectly matches with the measured concentration of NO in the feed of 519 ppm, with no missing N- or O-equivalents. This shows the accuracy of the measure despite the observed fluctuation of the NO signal. Moreover, this indicates that the catalyst efficiently desorbs the produced gases and possibly does not favor NO_X storage.

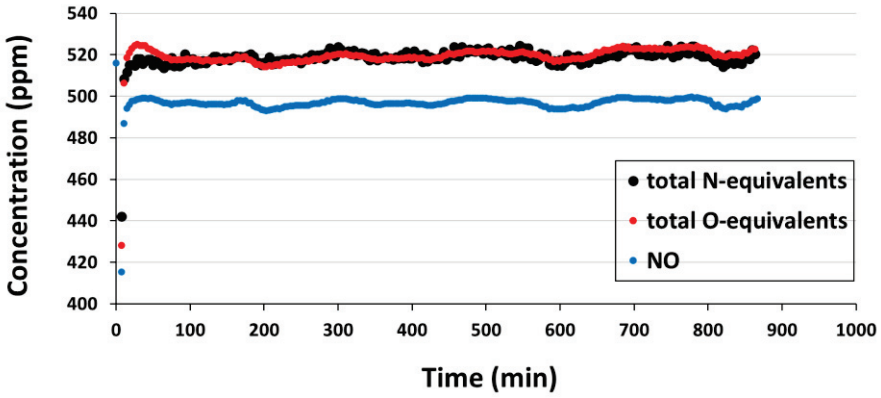

Figure 3.6.7 : The evolution of the concentration of NO and the calculated total N- and O-equivalents over 100 mg of Pd(4) during the catalytic test. Feed: 519 ppm NO/ArHe, 50 mL/min, 450°C.

Fig. 3.6.8 shows the calculated NO conversion into ($N_2 + N_2O$). The plot clearly shows the continuous deactivation behavior of the catalyst under NO.

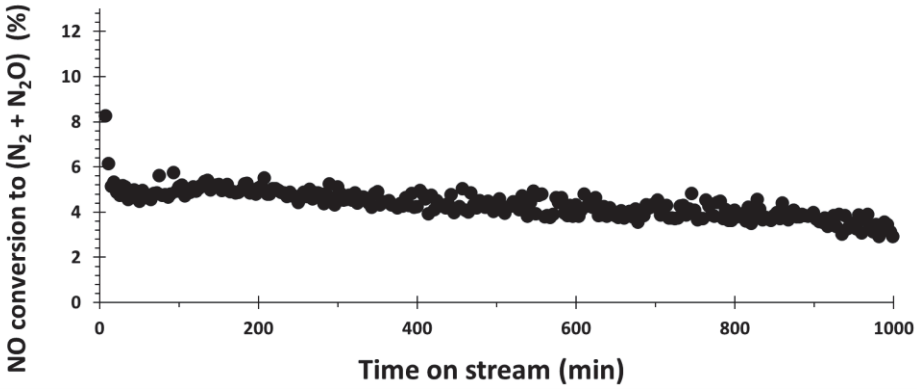

Figure 3.6.8 : The evolution of the NO conversion to ($N_2 + N_2O$) over 100 mg of Pd(4) during the catalytic test. Feed: 519 ppm NO/ArHe, 50 mL/min, 450°C.

6.5.1. Calculation of the number of moles of Pd in the bed:

Catalyst mass = 100 mg

Actual weight fraction of Pd in the catalyst = 4.25 %

m_{Pd} = 100 /1000 x 4.25 /100 = 4.25 mg

MW Pd = 106.4 g/mol

Mol Pd = 4.25/1E3 / 106.4 = 0.04 mmol

6.5.2. Calculation of the converted NO (in mol) over 1000 min:

Total volumetric flow = 50 mL / min

NO mole or volume fraction in the feed = $[NO_{feed}]$ = 519 ppm = 0.0519 %

The number of moles of converted NO over 1000 min is:

$$\mathbf{NO}_{converted}\ (mol) = \int_0^{1000} \textit{Molar flow of NO reacted}\ dt \qquad \textbf{Eq. 3.6.8}$$

$$= \int_0^{1000} \frac{\textit{Volumic flow of NO converted}}{V_M}\ dt \qquad \textbf{Eq. 3.6.9}$$

where V_M is the perfect gas molar volume (24.465 L/mol at 25°C and a pressure of 1 atm),

$$\mathbf{NO}_{converted}\ (mol) = \int_0^{1000} \frac{\textit{Total volumetric flow} \times [\mathrm{NO}_{feed}] \times \textit{NO conversion}}{V_M}\ dt \qquad \textbf{Eq. 3.6.10}$$

$$= \frac{\text{Total volumetric flow} \times [\mathrm{NO}_{feed}]}{V_M} \times \int_0^{1000} \text{NO conversion}\ dt \qquad \textbf{Eq. 3.6.11}$$

The integral of NO conversion(t) over 1000 min is:

$$\int_0^{1000} \text{NO conversion}\ dt \quad = \quad 47.02 \text{ min}$$

$$\mathrm{NO}_{converted} = \frac{50\ /1000 \text{ x } 0.0519/100}{24.465} \times 47.02 \quad = \quad 0.05 \text{ mmol}$$

6.5.3. Discussion on the comparison Pd moles and total NO converted:

The sample lead to the conversion of only 1.25 moles of NO per mole of Pd during 1000 min Along with the continous deactivation behavior observed under NO, this indicates that the sample only undergoes a redox reaction under NO.

6.6. Performance of Pd(4)Au(1)

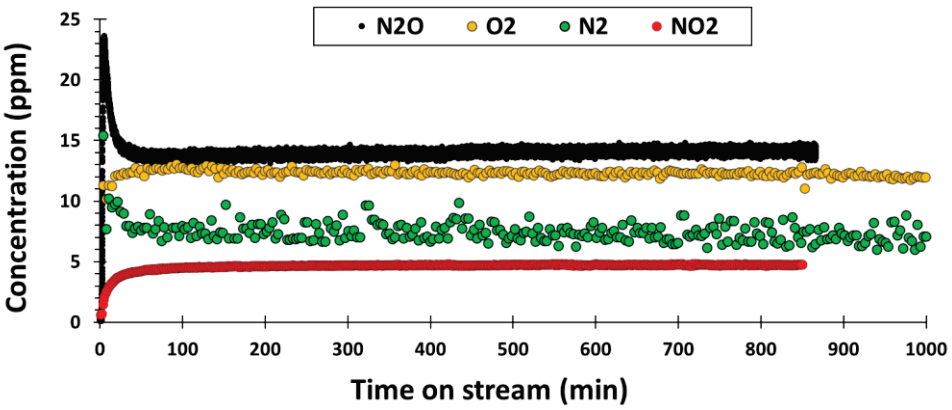

Figure 3.6.9 : The evolution of the concentrations of the NO decomposition products detected over 100 mg of Pd(4)Au(1) during the catalytic test. Feed: 516 ppm NO/ArHe, 50 mL/min, 450°C.

Fig. 3.6.9 shows the gases produced over the Pd(4)Au(1) sample with the Au/Pd atomic ratio of 0.12 under NO in the absence of O_2. The catalyst generally favors the formation of N_2O and O_2 rather than N_2 and NO_2. An initial rapid deactivation for only ~30 min is observed in the production of N_2O and N_2 possibly due to an initial redox reaction between NO and unalloyed metallic Pd. The profiles of the two gases are similar possibly due to a similar formation mechanism. The catalyst also generates measurable amounts of NO_2 with the level of O_2 being three times that of NO_2. The evolution of NO_2 formation is similar to that of O_2 since NO_2 is formed via the reaction of NO and oxygen. At the steady state, after 30 min, the catalyst shows steady levels of all gases.

Fig. 3.6.10 also shows the evolution of the NO profile as well as the calculated total N- and O-equivalents. The total N-equivalents is almost identical to the total O-equivalents, and both show slightly (~2%) overestimated total equivalents compared to the level of NO in the feed. However, this level is in the normal experimental accuracy range.

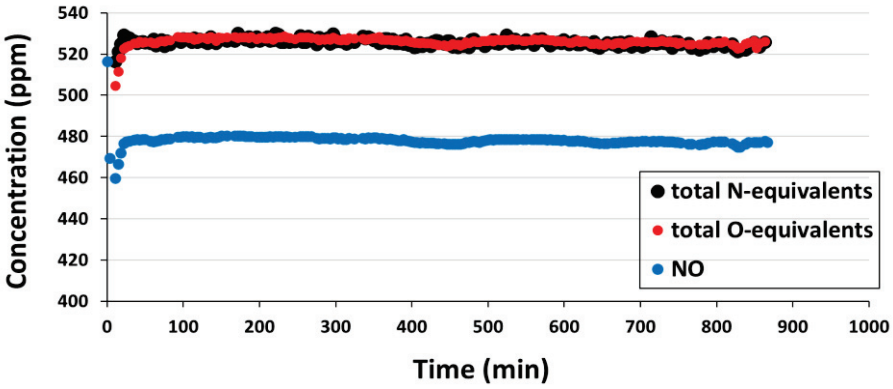

Figure 3.6.10 : The evolution of the concentration of NO and the calculated total N- and O-equivalents over 100 mg of Pd(4)Au(1) during the catalytic test. Feed: 516 ppm NO/ArHe, 50 mL/min, 450°C.

Fig. 3.6.11 shows the calculated NO conversion into (N_2 + N_2O). The plot clearly shows the steady activity of the catalyst of ~9% under NO.

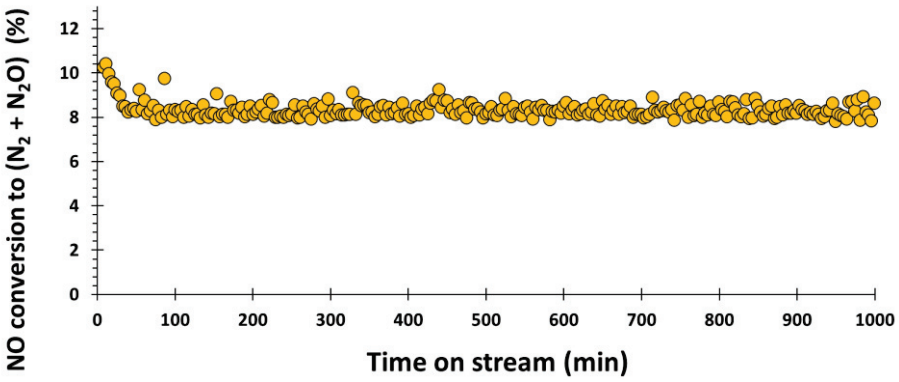

Figure 3.6.11 : The evolution of the NO conversion to (N_2 + N_2O) over 100 mg of Pd(4)Au(1) during the catalytic test. Feed: 516 ppm NO/ArHe, 50 mL/min, 450°C.

6.6.1. Calculation of the number of moles of Pd in the bed:

Catalyst mass = 100 mg

Actual weight fraction of Pd in the catalyst = 4.72 %

m_{Pd} = 100 /1000 x 4.72 /100 = 4.72 mg

MW Pd = 106.4 g/mol

Mol Pd = 4.72/1E3 / 106.4 = 0.044 mmol

6.6.2. Calculation of the converted NO (in mol) over 1000 min (using Eq. 3.6.8 – 3.6.11):

Total volumetric flow = 50 mL / min

NO mole or volume fraction in the feed = $[NO_{feed}]$ = 516 ppm = 0.0516 %

The integral of NO conversion(t) over 1000 min is:

$$\int_0^{1000} \text{NO conversion } dt \;=\; 83.8 \text{ min}$$

The number of moles of converted NO over 1000 min is:

$$NO_{converted} = \frac{50\ /1000 \text{ x } 0.0516/100}{24.465} \times 83.8 \;=\; 0.0884 \text{ mmol}$$

6.6.3. Discussion on the comparison Pd moles and total NO converted:

The sample lead to the conversion of two moles of NO per mole of Pd during 1000 min. However, the stable activity indicates a real catalytic activity.

6.7. Performance of Pd(4)Au(4)

Fig. 3.6.12 shows the gases produced over the Pd(4)Au(4) sample with the Au/Pd atomic ratio of 0.55 under NO in the absence of O_2 for 1000 min. An initial rapid deactivation for only ~100 min is observed in the production of N_2O and N_2 possibly due to a redox reaction between NO and unalloyed metallic Pd. At the steady state after ~100 min, the catalyst produces steady and equal levels of N_2 and N_2O. The catalyst also produces steady levels of O_2 and NO_2. The catalyst favors the formation O_2 more than the other gases. The profile of NO_2 is similar to that of O_2 with level of O_2 being three times that of NO_2.

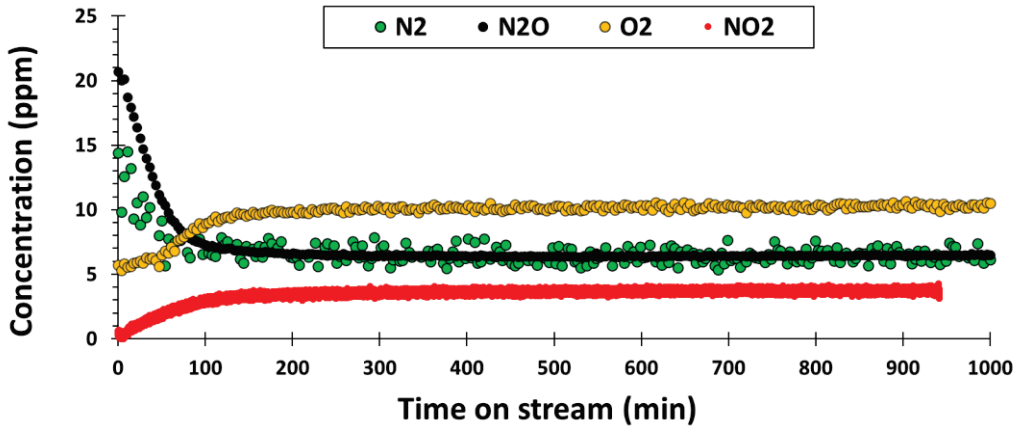

Figure 3.6.12 : The evolution of the concentrations of the NO decomposition products detected over 100 mg of Pd(4)Au(4) during the catalytic test. Feed: 494 ppm NO/ArHe, 50 mL/min, 450°C.

Fig. 3.6.13 shows the evolution of the NO profile as well as the calculated total N- and O-equivalents. The total O-equivalents is initially lower than the total O-equivalents possibly due a redox reaction leading to the formation of some PdO or due to some nitrate formation. During the steady state, both plots are almost identical. Both profiles show (~3%) overestimated total equivalents compared to the level of NO in the feed, which is in the experimental accuracy range.

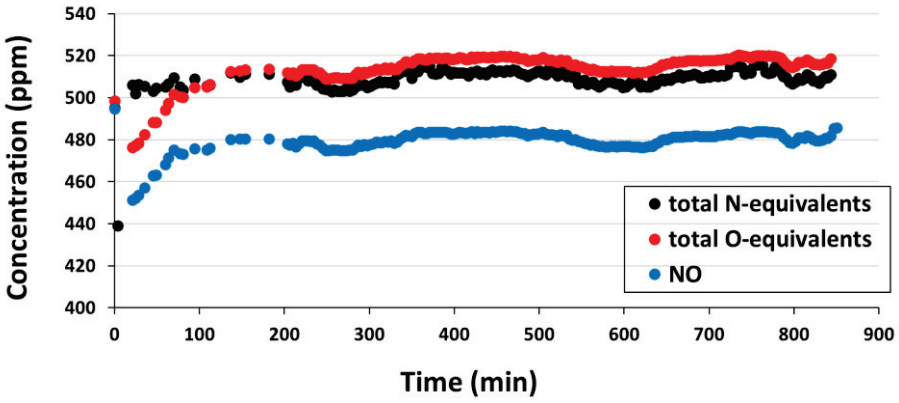

Figure 3.6.13 : The evolution of the concentration of NO and the total N- and O-equivalents over 100 mg of Pd(4)Au(4) during the catalytic test. Feed: 494 ppm NO/ArHe, 50 mL/min, 450°C.

Fig. 3.6.14 shows the calculated NO conversion into (N_2 + N_2O). The plot shows the steady NO conversion of ~6% under over the Pd(4)Au(4) catalyst.

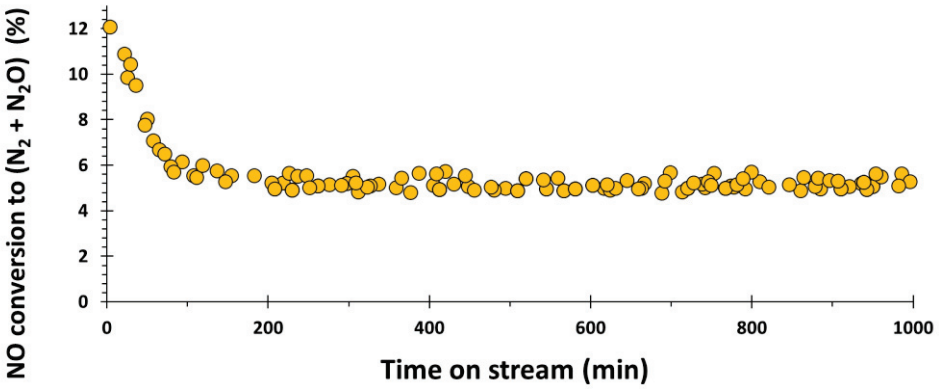

Figure 3.6.14 : The evolution of the NO conversion to (N_2 + N_2O) over 100 mg of Pd(4)Au(4) during the catalytic test. Feed: 494 ppm NO/ArHe, 50 mL/min, 450°C.

6.7.1. Calculation of the number of moles of Pd in the bed:

Catalyst mass = 100 mg

Actual weight fraction of Pd in the catalyst = 3.96 %

m_{Pd} = 100 /1000 x 3.96 /100 = 3.96 mg

MW Pd = 106.4 g/mol

Mol Pd = 3.96/1E3 / 106.4 = 0.037 mmol

6.7.2. Calculation of the converted NO (in mol) over 1000 min (using Eq. 3.6.8 – 3.6.11):

Total volumetric flow = 50 mL / min

NO mole or volume fraction in the feed = $[NO_{feed}]$ = 494 ppm = 0.0494 %

The integral of NO conversion(t) over 1000 min is:

$$\int_0^{1000} \text{NO conversion } dt \;=\; 58.5 \text{ min}$$

The number of moles of converted NO over 1000 min is:

$$NO_{converted} = \frac{50\ /1000 \text{ x } 0.0494/100}{24.465} \times 58.5 \;=\; 0.059 \text{ mmol}$$

6.7.3. Discussion on the comparison Pd moles and total NO converted:

The sample lead to the conversion of 1.6 moles of NO per mole of Pd during 1000 min. However, the stable activity indicates a real catalytic activity.

6.8. Synergy between Pd and Au

Fig. 3.6.15 compares the NO conversions over the four samples in terms of the formed (N_2 + N_2O).

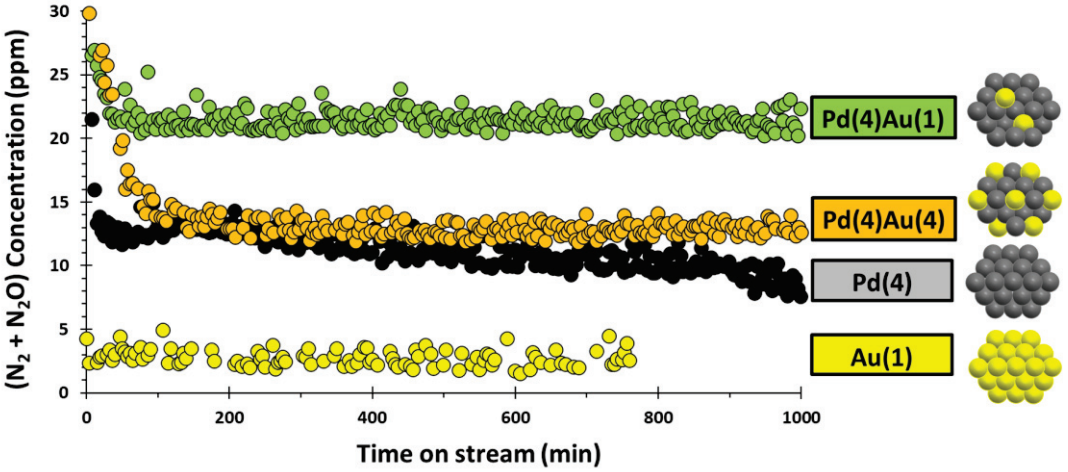

Figure 3.6.15 : The evolution of the NO conversion to (N_2 + N_2O) over 100 mg of the four samples during the catalytic test. Feed: 500 ppm NO/ArHe, 50 mL/min, 450°C.

We have already published the data of Au(1), Pd(4) and Pd(4)Au(1) in a recent publication [32]. Both the bimetallic samples show stable activity for at least 1000 min while the Pd sample shows a continuous deactivation. This indicates the enhanced oxidation resistance of Pd by alloying with Au.

However, the activity of Pd(4)Au(1) with the Au/Pd atomic ratio of 0.12 is 1.6 times that of the Pd(4)Au(4) sample with the Au/Pd atomic ratio of 0.55. This could be due to the larger SWD of the Pd(4)Au(4) as measured by the TEM analysis and hence, a lower dispersion of the metals. The Pd(4)Au(4) sample displayed a SWD of 13.6 nm which is 1.3 times that of the Pd(4)Au(1) of 10.4 nm (see Table 3.3.1). However, the increase in the SWD may not entirely account for the loss of the catalytic activity. There is also a possibility that the alloying of Au and Pd features an optimum Au/Pd ratio for enhancing the activity of Pd for NO direct decomposition. At a ratio as high as 0.55, Au possibly covers a significant fraction of the surface of the nanoparticles leading to a decreased dispersion of Pd as compared to the bimetallic sample with the lower Au loading.

Fig. 3.6.16 shows the selectivity to N_2 production over the four catalysts. It must be noted that this comparison is not established at the same level of activity over the four catalysts.

The Pd(4) sample shows the highest selectivity to N_2 production. The presence of a small amount of Au in the Pd(4)Au(1) sample enhances the overall activity but decreases the selectivity to ~35%. The presence of more Au in the Pd(4)Au(4) sample enhances the N_2 selectivity to 50%. This could refer to an enhanced ability of the Pd(4)Au(4) catalyst towards N_2 formation or the decomposition of the

formed N_2O into N_2 and O_2. This could also explain the preferential O_2 production over Pd(4)Au(4). The activity and N_2 selectivity over the bimetallic samples are generally different from those of the Pd(4) sample, which indicates the modification of the metal sites induced by the presence of Au.

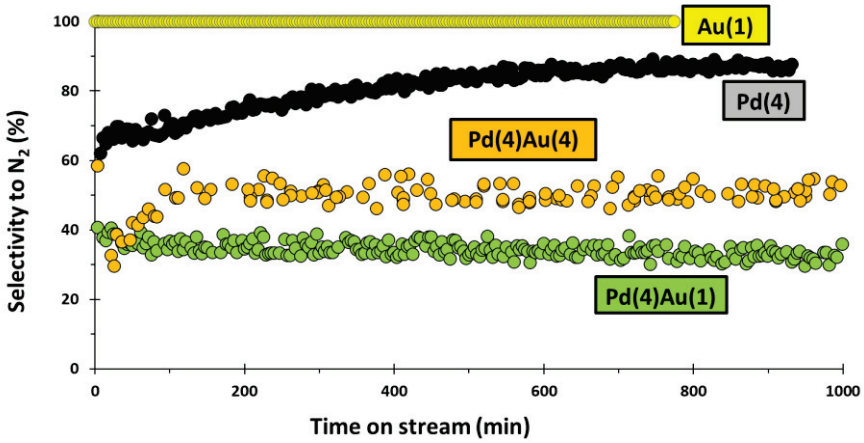

Figure 3.6.16 : The evolution of the selectivity for N_2 production over 100 mg of of Au(1), Pd(4), Pd(4)Au(1) and Pd(4)Au(4) during the catalytic test. Feed: 500 ppm NO/ArHe, 50 mL/min, 450°C.

Fig. 3.6.17 shows the evolution of the concentrations of O_2 over the Pd(4), Pd(4)Au(1) and Pd(4)Au(4) samples. The O_2 production generally higher over the bimetallic samples and is significantly greater in the case of the Pd(4)Au(1) sample. This supports the conclusion that Au facilitates the desorption of O_2 and induces a greater resistance of Pd against oxidation/poisoning by O_{ads} atoms. This could explain the stability of the bimetallic catalyst.

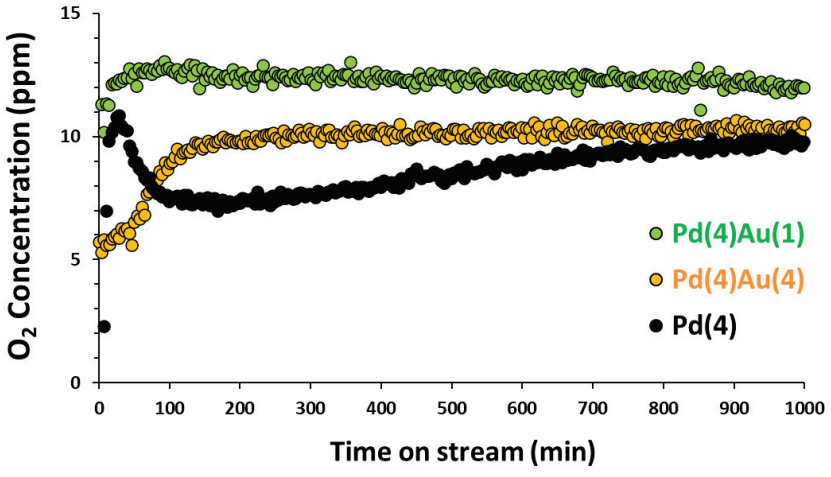

Figure 3.6.17 : The evolution of the concentration of O_2 produced over Pd(4) vs. Pd(4)Au(1) vs. Pd(4)Au(4) samples during the catalytic test. Feed: 500 ppm NO/ArHe, 50 mL/min, 450°C.

6.8.1. Characterization by PXRD

Fig. 3.6.18 shows the XRD patterns of the bimetallic sample recorded after calcination, after reduction and after the NO decomposition reaction. The post-reaction pattern of Pd(4)Au(1) exhibited

PdO, PdAu alloyed phases and free metallic Pd. This indicates that a fraction of the alloyed Pd may have eventually got segregated under NO. The pattern is intermediate between that obtained after calcination at 450°C showing PdO and $Pd_{0.2}Au_{0.8}$ (Fig. 3.6.18 a) and that obtained after reduction at 450°C showing a $Pd_{0.63}Au_{0.37}$ alloy phase and Pd (Fig. 3.6.18 b). Apparently, 500 ppm of NO in the feed has a lower oxidizing potential than air.

Surprisingly, the Pd(4) post-reaction pattern exhibited a negligible fraction of PdO (Fig. 3.6.18 d), in contrast to the bimetallic sample (Fig. 3.6.18 c). This observation can possibly be explained by an improved diffusion of O in the alloyed domains (presenting more defects), as O diffusion has been proposed as the limiting step during Pd oxidation [36][37]. This also could reenforce the conclusion that the deactivation of the Pd(4) sample is mostly due to the surface poisoning by the produced O_{ads} atoms and not necessarily due to oxidation. The steady NO decomposition activity observed over Pd(4)Au(1) indicates that under our conditions, most bimetallic nanoparticles exhibited a sufficient Au fraction at the surface to protect Pd against oxidation and prevent deactivation, in agreement with the TEM-EDX analysis (Fig. 3.3.4). This is also consistent with the lower surface tension of Au of (1145 mJ m^{-2}) than that of Pd (1482 mJ m^{-2}) [38].

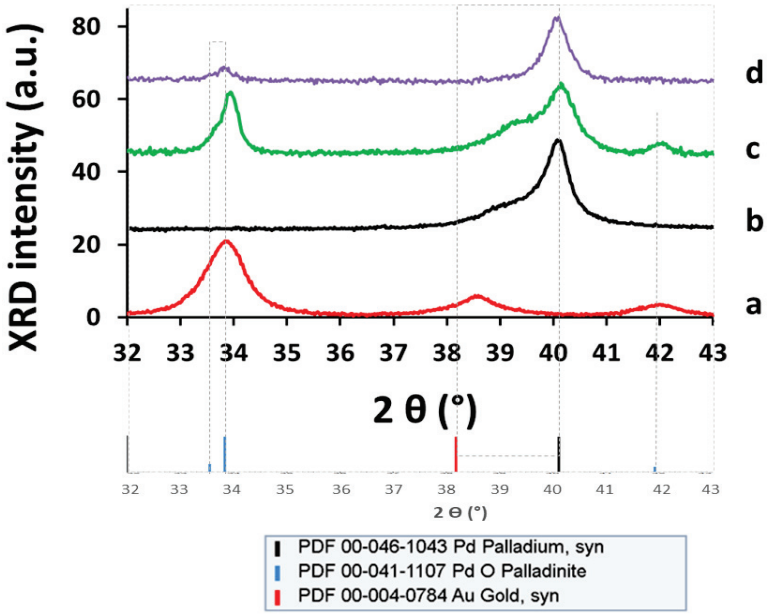

Figure 3.6.18: X-ray diffraction patterns of the Pd(4)Au(1) at room temperature in air after (a) reduction in H_2 at 450 °C, (b) oxidation at 500 °C and (c) use for NO decomposition at 450 °C. (d) X-ray diffraction patterns of the Pd(4) at room temperature in air after use for NO decomposition.

6.9. Mechanism

The similarity between the profiles of N_2 and N_2O formed over Pd(4)Au(1) and Pd(4)Au(4) (Fig. 3.6.9 and Fig. 3.6.12, respectively) could suggest that both gases share a similar formation

mechanism. The formation of NO dimers could account for this similarity. The two adjacent NO_{ads} molecules could further react forming N_2O (eqaution S5 below) that could eventually decompose into N_2 and O_2 (equations S6-S8 below). The NO dimer formation was suggested as the path for NO decomposition over Pt [39] and La(Ba)Mn(In)O_3 [40]. However, another possible pathway could be the decomposition of a single NO_{ads} molecule forming N_{ads} that could further react with other N_{ads} or NO_{ads} species giving N_2 and N_2O (equations S1-S4 below).

The equations below summarize the possible steps of NO decomposition (over metal surfaces) including: (S1)-(S5) [41][42][43], and (S6)-(S8) [44].

$$NO + Pt \longleftrightarrow NO\text{-}Pt \quad (S1)$$

$$NO\text{-}Pt + Pt \longleftrightarrow N\text{-}Pt + O\text{-}Pt \quad (S2)$$

$$N\text{-}Pt + N\text{-}Pt \longrightarrow N_2 + 2\ Pt \quad (S3)$$

$$N\text{-}Pt + NO\text{-}Pt \longleftrightarrow N_2O + 2\ Pt \quad (S4)$$

$$NO\text{-}Pt + NO\text{-}Pt \longleftrightarrow N_2O + O\text{-}Pt + Pt \quad (S5)$$

$$N_2O \longleftrightarrow N_2 + O\text{-}Pd \quad (S6)$$

$$O\text{-}Pd + O\text{-}Pd \longleftrightarrow (O_2)\text{-}Pd \quad (S7)$$

$$(O_2)\text{-}Pd \longleftrightarrow O_2 \quad (S8)$$

Moreover, the higher N_2 selectivity over Pd(4)Au(4) than over Pd(4)Au(1) could indicate a higher activity for N_2O decomposition. Pd-Au/SiO_2 were already reported to be active for N_2O decomposition [44]. This is not surprising considering the lower kinetic barrier of N_2O decomposition (240-260 kJ/mol) [45][46] than that of NO decomposition (~335 kJ/mol) [25][26]. This could be due to the higher Au/Pd atomic ratio of Pd(4)Au(4) and the corresponding Au-rich PdAu alloy phase detected by the *ex situ* PXRD analysis (Fig. 3.4.12).

As shown by TEM-EDX and PXRD, the catalysts contained significant amount of monometallic Pd phase in addition to the PdAu alloyed phase. We believe that the alloyed phase was responsible for the steady catalytic activity since only Pd alloyed with Au could resisted oxidation. Unalloyed Pd resulted in the initial deactivation in the bimetallic samples under NO.

6.10. Comparison with NO conversions reported in literature

Table 3.6.2 summarizes the conversions obtained over the four samples tested and the experimental conditions. The highest achieved activity corresponds to ~9% NO conversion which is quite low

compared to what was achieved using other catalytic substances. Moreover, the Pd-Au/SiO_2 system has shown to undergo full deactivation in the presence of O_2 in the feed.

Table 3.6.2 : NO decomposition activities over the four SiO_2 based samples tested.

Catalyst	NO conversion (%)	N_2 selectivity (%)	Reaction conditions			
			NO (%)	O_2 (%)	T (°C)	W/F ($g.s.cm^{-3}$)
Au(1)	inactive		0.05	----	450	0.12
Pd(4)	deactivates		0.05	----	450	0.12
Pd(4)Au(1)	9	35	0.05	----	450	0.12
Pd(4)Au(4)	6	50	0.05	----	450	0.12

Also, Table 3.6.3 lists some of the catalytic substances reported for NO direct decomposition below 500°C. The comparison with the catalytic data in this current work may not be straightforward due to the different conditions used. However, the significant difference in the conversion values may refer to a limited activity that can be achieved over the Pd-Au/SiO_2 system. As shown in the table, N_2 yields as high as 59-99% were achieved at or below 450°C even in the presence of 5-8% of O_2 in the feed. In the light of these remarkable activities reported, different formulations need to be considered for practical applications in the presence of excess O_2.

Table 3.6.3: NO decomposition activities reported over several catalytic substances below 500°C.

Catalyst	N_2 yield (%)	Reaction conditions					Ref.
		NO (%)	O_2 (%)	T (°C)	W/F ($g.s.cm^{-3}$)	GHSV (h^{-1})	
100% ion exchanged Cu-ZSM5	80-85	1	----	450	4		[5]
Cu-ZSM5	65	0.512	----	450	2		[47]
Rh/CNTs	100	1	----	300	0.06		[48]
Rh/C	100	1	----	400	0.3		[49]
Pd/C	21.6	1	----	400	0.3		[49]
CeO_2	14.7	0.1	----	400	0.1		[50]
Pr_6O_{11}	19.6	0.1	----	400	0.1		[50]
La_2CuO_4 nanofiber	100	1	----	300-450		60000	[51]
Zr-Cu-Ce-ZSM5	75	0.4	5	450		3000	[52]
$MgCo_2O_4$–40% $BaCO_3$	99	0.1	5	350	1		[53]
5% $AgLa_{0.6}Ce_{0.4}CoO_3$	59	0.1	8	400		30000	[54]

Conclusions

Silica-supported Au, Pd and Pd-Au nanoparticles were prepared. The monometallic samples were prepared via wet impregnation. The bimetallic samples were prepared using the parent Pd catalyst and Au was added via a surface redox method with different Au/Pd ratios (0.12 and 0.55). After the preparation, the catalysts were calcined in a flow of 500 ppm NO + 5% O_2/He to burn off the carbonaceous compounds used during the wet impregnation. Then, a reduction treatment was performed under H_2 at 450°C to ensure the re-alloying of the metals.

TEM analyses showed the formation of small Au nanoparticles of a narrow particle size distribution. The Pd-containing samples displayed a significant fraction of larger particles which added a significant contribution to the overall surface area of the particles. The presence of large particles in the bimetallic samples increased with increasing the loading of Au. The TEM-EDX analyses of the bimetallic samples showed the presence of both Au and Pd in most regions investigated. The TEM-EDX analysis is probably only relevant to the particles' surface composition.

PXRD analyses were performed to monitor the structure of the catalysts at different stages of the calcination or reduction treatments and after the catalytic test.

The *in situ* PXRD experiment was useful to determine the effect of the calcination and reduction treatments. It was also useful to show the immediate changes up on changing the feed. The Au sample displayed a poor crystallinity and did not undergo an apparent change after any of the treatments applied. A poorly crystalline metallic Pd was initially observed. The calcination treatment at 500°C in air lead to the oxidation of Pd to PdO. Introducing H_2 at 25°C immediately converted PdO into PdH_X. Heating to 450°C under H_2, decomposed PdH_X into Pd featuring an increased crystallinity and thermal lattice expansion. PdH_X was reformed while cooling down to 25°C under H_2. Removing H_2 at 25°C lead to the formation of metallic Pd.

The Pd(4)Au(1) sample displayed poorly crystalline metallic Pd and Au initially. The calcination treatment lead to the oxidation of most Pd. In addition, a $Pd_{0.2}Au_{0.8}$ alloy was observed which is resistant to oxidation. Introducing H_2 at 25°C immediately converted PdO into PdH_X, whose peaks overlap with those of the PdAu alloy. Heating to 450°C under H_2, decomposed PdH_X into Pd featuring an increased crystallinity and thermal lattice expansion. A Pd-rich $Pd_{0.63}Au_{0.37}$ was also observed with a distribution of alloy compositions. PdH_X was reformed while cooling down to 25°C under H_2. Removing H_2 at 25°C yielded metallic Pd and a Pd-rich PdAu phase.

The effect of the Au/Pd atomic ratio was investigated through the *ex situ* PXRD analysis. The samples were tested after two cycles of calcination and reduction treatments. After re-calcination, all the

bimetallic sample displayed PdO in addition to a $Pd_{0.2}Au_{0.8}$ alloy which is a threshold alloy composition resistant to oxidation. After re-reduction, metallic Pd and PdAu alloy phases were obtained. The alloy compositions became richer in Au while increasing the loading of Au. The Pd(4)Au(1) sample displayed Pd-rich alloy, whereas the Pd(4)Au(4) sample displayed Au-rich alloy. In all the bimetallic samples, all Au was alloyed with the excess Pd.

The catalytic test was performed over the non-calcined catalysts under a flow of (500 ppm NO + 5% O_2/He) at 450°C. A SCR reaction occurred and yielded CO_2, N_2 and NO_2. This indicates the necessity of calcination to clean the catalyst surface. After the SCR reaction ceased, the catalysts displayed full deactivation in the presence of 5% O_2.

Then, the catalysts were regenerated by reduction in H_2 at 450°C and tested in the absence of O_2. The Au sample was inactive. The Pd sample showed a measurable activity but continuously deactivated due to the oxidation and/or surface poisoning by the produced oxygen. The post reaction XRD patterns showed the presence of negligible PdO, indicating that the deactivation is possibly mostly due the poisoning by the O adatoms.

The Pd(4)Au(1) sample showed an enhanced and stabilized activity as compared to the Pd sample. The sample favored the formation of N_2O rather than N_2 and liberated more O_2 (and NO_2) than the Pd sample. The presence of Au facilitated the desorption of oxygen and protected Pd against oxidation which enhanced and stabilized the activity. However, the selectivity for N_2 was lower than that over the Pd sample indicating the modification of the Pd sites by Au. The post reaction XRD pattern showed the presence of significant PdO besides metallic Pd and a Pd-rich alloy phase. This indicates the lower oxidation potential of the NO feed than air. This also indicates the easier diffusion of O atoms and PdO formation in the bimetallic sample possibly due to the presence of more defects as compared to the Pd sample.

The Pd(4)Au(4) sample showed a stable activity; though the activity was comparable to that observed over the Pd sample. The sample displayed a higher average particle diameter as compared to the bimetallic sample. This possibly resulted in decreasing the dispersion of Pd, which did not assist in enhancing the overall activity. However, Au protected some Pd against oxidation and stabilized the activity. The sample favored the formation of O_2 and showed an enhanced N_2 selectivity compared to the Pd(4)Au(1) sample.

These data possibly indicated an enhanced N_2O decomposition activity due to the higher Au loading. Moreover, this also suggested that NO decomposition probably proceeded via a NO dimer formation mechanism over the Pt surface. Despite the promising results obtained, the activity achieved was limited compared to the values reported in the literature.

References

[1] G. X. Pei *et al.*, "Promotional effect of Pd single atoms on Au nanoparticles supported on silica for the selective hydrogenation of acetylene in excess ethylene," *New J. Chem.*, vol. 38, no. 5, pp. 2043–2051, 2014, doi: 10.1039/c3nj01136d.

[2] A. Dasgupta, E. K. Zimmerer, R. J. Meyer, and R. M. Rioux, "Generalized approach for the synthesis of silica supported Pd-Zn, Cu-Zn and Ni-Zn gamma brass phase nanoparticles," *Catal. Today*, vol. 334, no. July 2018, pp. 231–242, 2019, doi: 10.1016/j.cattod.2018.10.050.

[3] X. Yang *et al.*, "An effective Pd-promoted gold catalyst supported on mesoporous silica particles for the oxidation of benzyl alcohol," *Appl. Catal. B Environ.*, vol. 140–141, pp. 419–425, 2013, doi: 10.1016/j.apcatb.2013.04.029.

[4] F. Gauthard, F. Epron, and J. Barbier, "Palladium and platinum-based catalysts in the catalytic reduction of nitrate in water: Effect of copper, silver, or gold addition," *J. Catal.*, vol. 220, no. 1, pp. 182–191, 2003, doi: 10.1016/S0021-9517(03)00252-5.

[5] M. Iwamoto, H. Yahiro, K. Tanda, N. Mizuno, Y. Mine, and S. Kagawa, "Removal of nitrogen monoxide through a novel catalytic process. 1. Decomposition on excessively copper ion exchanged ZSM-5 zeolites," *J. Phys. Chem.*, vol. 95, no. 9, pp. 3727–3730, 1991, doi: 10.1021/j100162a053.

[6] G. K. Reddy, C. Ling, T. C. Peck, and H. Jia, "Understanding the chemical state of palladium during the direct NO decomposition-influence of pretreatment environment and reaction temperature," *RSC Adv.*, vol. 7, no. 32, pp. 19645–19655, 2017, doi: 10.1039/c7ra00836h.

[7] A. J. Corso, A. Martucci, M. Bazzan, P. Zuppella, D. Garoli, and M. G. Pelizzo, "In situ real-time investigation of hydrogen-induced structural and optical changes in palladium thin films," *J. Alloys Compd.*, vol. 704, pp. 303–310, 2017, doi: 10.1016/j.jallcom.2017.02.042.

[8] B. N. Dutta and B. Dayal, "Lattice Constants and Thermal Expansion of Palladium and Tungsten up to 878 °C by X-Ray Method," *Phys. Status Solidi*, vol. 3, no. 12, pp. 2253–2259, 1963, doi: 10.1002/pssb.19630031207.

[9] C. X. Hu, P. Liu, and Y. Liu, "High temperature X-ray diffraction studies of the sample heating units," *Procedia Eng.*, vol. 24, pp. 404–411, 2011, doi: 10.1016/j.proeng.2011.11.2666.

[10] B. N. Dutta and B. Dayal, "Lattice Constants and Thermal Expansion of Gold up to 878 °C by X-Ray Method," *Phys. Status Solidi*, vol. 3, no. 3, pp. 473–477, 1963, doi: 10.1002/pssb.19630030312.

[11] A. L. Cabrera, E. Morales, and J. N. Armor, "Kinetics of hydrogen desorption from palladium and ruthenium-palladium foils," *J. Mater. Res.*, vol. 10, no. 3, pp. 779–785, 1995, doi: 10.1557/JMR.1995.0779.

[12] M. Johansson, E. Skúlason, G. Nielsen, S. Murphy, R. M. Nielsen, and I. Chorkendorff, "Hydrogen adsorption on palladium and palladium hydride at 1 bar," *Surf. Sci.*, vol. 604, no. 7–8, pp. 718–729, 2010, doi: 10.1016/j.susc.2010.01.023.

[13] A. N. Salanov and E. A. Suprun, "Oxygen desorption from polycrystalline palladium: Thermal desorption of O2 from a chemisorbed layer of oads in the course of the decomposition of PdO surface oxide and in the release of oxygen from the bulk of palladium," *Kinet. Catal.*, vol. 51, no. 3, pp. 416–427, 2010, doi: 10.1134/S0023158410030158.

[14] A. N. Salanov and E. A. Suprun, "Interaction between oxygen and polycrystalline palladium at O2 pressures of 10-6-10 Pa," *Kinet. Catal.*, vol. 50, no. 1, pp. 31–39, 2009, doi: 10.1134/S0023158409010054.

[15] S. A. Singh, K. Vishwanath, and G. Madras, "Role of Hydrogen and Oxygen Activation over Pt and Pd-Doped

Composites for Catalytic Hydrogen Combustion," *ACS Appl. Mater. Interfaces*, vol. 9, no. 23, pp. 19380–19388, 2017, doi: 10.1021/acsami.6b08019.

[16] C. W. Chou *et al.*, "Temperature-programmed reduction study on calcination of nano-palladium," *J. Phys. Chem. B*, vol. 105, no. 38, pp. 9113–9117, 2001, doi: 10.1021/jp011170g.

[17] C. Resch, H. F. Berger, K. D. Rendulic, and E. Bertel, "Adsorption dynamics for the system hydrogen/palladium and its relation to the surface electronic structure," *Surf. Sci.*, vol. 316, no. 3, 1994, doi: 10.1016/0039-6028(94)91213-0.

[18] H. Nakatsuji and M. Hada, "Interaction of a Hydrogen Molecule with Palladium," *J. Am. Chem. Soc.*, vol. 107, no. 26, pp. 8264–8266, 1985, doi: 10.1021/ja00312a078.

[19] G. L. Holleck, "Diffusion and solubility of hydrogen in palladium and palladium-silver alloys," *J. Phys. Chem.*, vol. 74, no. 3, pp. 503–511, 1970, doi: 10.1021/j100698a005.

[20] F. A. Lewis, "The Hydrides of Palladium and Palladium Alloys," *Platin. Met. Rev.*, vol. 5, no. 1, pp. 21–25, 1961.

[21] T. A. G. Silva, C. P. Ferraz, R. V. Gonçalves, E. Teixeira-Neto, R. Wojcieszak, and L. M. Rossi, "Restructuring of Gold-Palladium Alloyed Nanoparticles: A Step towards More Active Catalysts for Oxidation of Alcohols," *ChemCatChem*, vol. 11, no. 16, pp. 4021–4027, 2019, doi: 10.1002/cctc.201900553.

[22] A. M. Venezia, V. La Parola, V. Nicolì, and G. Deganello, "Effect of gold on the HDS activity of supported palladium catalysts," *J. Catal.*, vol. 212, no. 1, pp. 56–62, 2002, doi: 10.1006/jcat.2002.3778.

[23] L. Hilaire, P. Légaré, Y. Holl, and G. Maire, "Interaction of oxygen and hydrogen with Pd-Au alloys: An AES and XPS study," *Surf. Sci.*, vol. 103, no. 1, pp. 125–140, 1981, doi: 10.1016/0039-6028(81)90103-5.

[24] S. W. Chee, Z. M. Wong, Z. Baraissov, S. F. Tan, T. L. Tan, and U. Mirsaidov, "Interface-mediated Kirkendall effect and nanoscale void migration in bimetallic nanoparticles during interdiffusion," *Nat. Commun.*, vol. 10, no. 1, pp. 1–8, 2019, doi: 10.1038/s41467-019-10623-0.

[25] F. Garin, "Mechanism of NOx decomposition," *Appl. Catal. A Gen.*, vol. 222, no. 1–2, pp. 183–219, 2001, doi: 10.1016/S0926-860X(01)00827-4.

[26] H. Wise and M. F. Frech, "Kinetics of decomposition of nitric oxide at elevated temperatures. I. Rate measurements in a quartz vessel," *J. Chem. Phys.*, vol. 20, no. 1, pp. 22–24, 1952, doi: 10.1063/1.1700189.

[27] Y. Zhang, G. Cao, and X. Yang, "Advances in De-NOxMethods and Catalysts for Direct Catalytic Decomposition of NO: A Review," *Energy and Fuels*, vol. 35, no. 8, pp. 6443–6464, 2021, doi: 10.1021/acs.energyfuels.1c00330.

[28] J. Valyon and W. K. Hall, "Studies of the surface species formed from NO on copper zeolites," *J. Phys. Chem.*, vol. 97, no. 6, pp. 1204–1212, 1993, doi: 10.1021/j100108a016.

[29] A. Amirnazmi, J. E. Benson, and M. Boudart, "Oxygen inhibition in the decomposition of NO on metal oxides and platinum," *J. Catal.*, vol. 30, no. 1, pp. 55–65, 1973, doi: 10.1016/0021-9517(73)90051-1.

[30] J. K. Edwards *et al.*, "Direct synthesis of hydrogen peroxide from H2 and O2 using TiO2-supported Au-Pd catalysts," *J. Catal.*, vol. 236, no. 1, pp. 69–79, 2005, doi: 10.1016/j.jcat.2005.09.015.

[31] R. Ferrando, J. Jellinek, and R. L. Johnston, "Nanoalloys : From Theory to Applications of Alloy Clusters and Nanoparticles," *Chem. Rev.*, vol. 108, no. 3, pp. 845--910, 2008, doi: 10.1021/cr040090g.

[32] T. Elgayyar *et al.*, "Au-Modified Pd catalyst exhibits improved activity and stability for NO direct decomposition," *Catal. Sci. Technol.*, vol. 11, no. 8, pp. 2908–2914, 2021, doi: 10.1039/d1cy00301a.

[33] R. D. Ramsier *et al.*, "NO adsorption and thermal behavior on Pd surfaces. A detailed comparative study," *Surf. Sci.*, vol. 320, no. 3, pp. 209–237, 1994, doi: 10.1016/0039-6028(94)90310-7.

[34] Y. Kuwahara, M. Jo, H. Tsuda, M. Onchi, and M. Nishijima, "Adsorbed state and vibrational excitation of N2 on Pd(110)," *Surf. Sci.*, vol. 180, no. 2–3, pp. 421–432, 1987, doi: 10.1016/0039-6028(87)90218-4.

[35] M. Bertolo and K. Jacobi, "Adsorption of N2 on the Pd(111) surface at 20 K," *Surf. Sci.*, vol. 265, no. 1–3, pp. 12–30, 1992, doi: 10.1016/0039-6028(92)90484-n.

[36] E. H. Voogt, A. J. M. Mens, O. L. J. Gijzeman, and J. W. Geus, "Adsorption of oxygen and surface oxide formation on Pd(111) and Pd foil studied with ellipsometry, LEED, AES and XPS," *Surf. Sci.*, vol. 373, no. 2–3, pp. 210–220, 1997, doi: 10.1016/S0039-6028(96)01180-6.

[37] R. Burch, "Low NOx options in catalytic combustion and emission control," *Catal. Today*, vol. 35, no. 1–2, pp. 27–36, 1997, doi: 10.1016/S0920-5861(96)00131-9.

[38] B. J. Keene, "Review of data for the surface tension of pure metals," *Int. Mater. Rev.*, vol. 38, no. 4, pp. 157–192, 1993, doi: 10.1179/imr.1993.38.4.157.

[39] Q. Ge, W. A. Brown, R. K. Sharma, and D. A. King, "NO monomer and (NO)x polymeric chain chemisorption on Pt{110}: Structure and energetics," *J. Chem. Phys.*, vol. 110, no. 24, pp. 12082–12088, 1999, doi: 10.1063/1.479143.

[40] T. Ishihara *et al.*, "Direct decomposition of NO into N2 and O2 over La(Ba)Mn(In)O3 perovskite oxide," *J. Catal.*, vol. 220, no. 1, pp. 104–114, 2003, doi: 10.1016/S0021-9517(03)00265-3.

[41] V. Medhekar, V. Balakotaiah, and M. P. Harold, "TAP study of NOx storage and reduction on Pt/Al2O3 and Pt/Ba/Al2O3," *Catal. Today*, vol. 121, no. 3–4, pp. 226–236, 2007, doi: 10.1016/j.cattod.2006.08.063.

[42] R. Burch, P. J. Millington, and A. P. Walker, "Mechanism of the selective reduction of nitrogen monoxide on platinum-based catalysts in the presence of excess oxygen," *Appl. Catal. B, Environ.*, vol. 4, no. 1, pp. 65–94, 1994, doi: 10.1016/0926-3373(94)00014-X.

[43] G. P. Ansell, S. E. Golunski, J. W. Hayes, A. P. Walker, R. Burch, and P. J. Millington, "The mechanism of the lean Nox reaction over Pt-based catalysts," *Stud. Surf. Sci. Catal.*, vol. 96, no. C, pp. 577–590, 1995, doi: 10.1016/S0167-2991(06)81459-X.

[44] X. Wei *et al.*, "Bimetallic Au-Pd alloy catalysts for N 2O decomposition: Effects of surface structures on catalytic activity," *J. Phys. Chem. C*, vol. 116, no. 10, pp. 6222–6232, 2012, doi: 10.1021/jp210555s.

[45] H. Nakamura and S. Kato, "Theoretical study on the spin-forbidden predissociation reaction of N2O: Ab initio potential energy surfaces and quantum dynamics calculations," *J. Chem. Phys.*, vol. 110, no. 20, pp. 9937–9947, 1999, doi: 10.1063/1.478954.

[46] E. Hunter, "The thermal decomposition of nitrous oxide at pressures up to forty atmospheres," *Proc. R. Soc. London. Ser. A, Contain. Pap. a Math. Phys. Character*, vol. 144, no. 852, pp. 386–412, 1934, doi: 10.1098/rspa.1934.0057.

[47] T. Curtin, P. Grange, and B. Delmon, "The direct decomposition of nitrogen monoxide," *Catal. Today*, vol. 35, no. 1–2, pp. 121–127, 1997, doi: 10.1016/S0920-5861(96)00138-1.

[48] J. Z. Luo, L. Z. Gao, Y. L. Leung, and C. T. Au, "The decomposition of NO on CNTs and 1 wt% Rh/CNTs," *Catal. Letters*, vol. 66, no. 1–2, pp. 91–97, 2000, doi: 10.1023/a:1019035220233.

[49] K. Almusaiteer, R. Krishnamurthy, and S. S. C. Chuang, "In situ infrared study of catalytic decomposition of NO on carbon-supported Rh and Pd catalysts," *Catal. Today*, vol. 55, no. 3, pp. 291–299, 2000, doi: 10.1016/S0920-5861(99)00242-4.

[50] M. Haneda, Y. Kintaichi, and H. Hamada, "Surface reactivity of prereduced rare earth oxides with nitric oxide:

New approach for NO decomposition," *Phys. Chem. Chem. Phys.*, vol. 4, no. 13, pp. 3146–3151, 2002, doi: 10.1039/b201340a.

[51] L. Gao, H. T. Chua, and S. Kawi, "The direct decomposition of NO over the la2CuO4 nanofiber catalyst," *J. Solid State Chem.*, vol. 181, no. 10, pp. 2804–2807, 2008, doi: 10.1016/j.jssc.2008.06.051.

[52] P. Yang, J. Zhou, and Z. Wang, "Direct decomposition of NO into N2 and O2 over Cu /ZSM-5 containing Ce and Zr as promoter," *Adv. Mater. Res.*, vol. 113–116, pp. 1735–1739, 2010, doi: 10.4028/www.scientific.net/AMR.113-116.1735.

[53] W. Xu *et al.*, "Development of MgCo2O4-BaCO3 composites as microwave catalysts for the highly effective direct decomposition of NO under excess O2 at a low temperature," *Catal. Sci. Technol.*, vol. 9, no. 16, pp. 4276–4285, 2019, doi: 10.1039/c9cy00797k.

[54] Z. Liu, J. Hao, L. Fu, and T. Zhu, "Study of Ag/La0.6Ce0.4CoO3 catalysts for direct decomposition and reduction of nitrogen oxides with propene in the presence of oxygen," *Appl. Catal. B Environ.*, vol. 44, no. 4, pp. 355–370, 2003, doi: 10.1016/S0926-3373(03)00103-6.

Chapter 4. LTA-encapsulated Pt-Au nanoparticles

1. Introduction

Zeolites are aluminosilicate materials with the general formula of $M_{X/n}Al_XSi_{1-X}O_2 \cdot yH_2O$ (M is H or metal ions; and n is the valence of the metal). Because of their peculiar pores and channels, zeolites exhibit interesting adsorption and catalytic properties. LTA zeolite has the formula of $Na_{12}Al_{12}Si_{12}O_{48}.27H_2O$ with a Si/Al molar ratio of 1. Zeolites (Cu-ZSM-5) have previously displayed activity for the direct decomposition of NO [1][2][3][4]. The LTA structure features a very small pore diameter of 0.4 nm corresponding to an eight-member oxygen ring and a larger cavity of at least a 1.14 nm diameter [5]. Such small pore sizes could host very small metal nanoparticles as well as small molecules such as NO or CO. This fact is tempting to test the catalytic activity of LTA-based metal nanoparticles for NO_X decomposition. In fact, other groups have also investigated the use of LTA-based metal nanoparticles for other processes [6][7][8][9].

The simultaneous encapsulation of the metals during the synthesis of the LTA structure [6] led to the presence of the nanoparticles inside the LTA pores and the alloying of the metals. Moreover, a post-synthesis Ca^{2+} ion exchange process was performed to increase the pore size [5], that could enhance the diffusion of the gases into the pores.

The studied catalysts include two monometallic LTA-encapsulated Au and Pt samples, in addition to four bimetallic Pt-Au samples with different Au/Pt atomic ratios (0.25, 0.5, 1 and 2). The monometallic samples are coded as M@Ca-LTA, where M is Au or Pt. The bimetallic samples are coded as Pt-Au(Au/Pt atomic ratio)@Ca-LTA. This chapter aims at characterizing the LTA-based Au, Pt and Pt-Au(2)@Ca-LTA nanoparticles by ICP, TEM and PXRD, and CO adsorption. The metal-free LTA zeolite sample is also characterized by PXRD and CO adsorption. The chapter also discusses the catalytic activity of all the prepared samples for NO direct decomposition in the absence of O_2 in the feed at 350°C.

It must be mentioned that several other metals (Pd, Rh, Ir, Ag and Cu) were used for the preparation and testing of monometallic nanoparticles and their Au-based bimetallic counterparts. Only the Pt-based samples showed measurable activities. Moreover, for the optimization of the catalytic activity, various reaction temperatures, NO concentrations, and reduction conditions were used. In this chapter, only the measurable activities over the Pt-based catalysts are presented.

2. ICP elemental analysis

Three LTA-based samples were analyzed by ICP (Table 4.2.1). The actual metal loadings are lower than the nominal loadings, indicating an incomplete encapsulation of the metal precursors.

Table 4.2.1 : Metal loadings of all the LTA-based samples measured by ICP-OES.

Sample code	Nominal metal loding (wt. %)		Nominal Au/Pt atomic ratio	Actual metal loading measured by ICP (wt. %)		Actual Au/Pt atomic ratio
	Pt	Au		Pt	Au	
Pt@Ca-LTA	0.33	----	0	0.25	----	0
Au@Ca-LTA	----	1	----	----	0.54	----
Pt-Au(2)@Ca-LTA	0.33	0.67	2	0.18	0.34	1.9
Pt-Au(1)@Ca-LTA	0.5	0.5	1	n.d.	n.d.	n.d.
Pt-Au(0.5)@Ca-LTA	0.67	0.33	0.5	n.d.	n.d.	n.d.
Pt-Au(0.25)@Ca-LTA	0.8	0.2	0.25	n.d.	n.d.	n.d.

3. TEM analysis

Prior to the analysis, thin slices (70 nm) of the samples were prepared. Without such a preparation step, no nanoparticles were detected, indicating that the nanoparticles are encapsulated.

3.1. Au@Ca-LTA

Fig. 4.3.1 shows TEM images of thin slices (70 nm) of the Au sample and the corresponding particle size distribution. The sample displayed a narrow particle size distribution, corresponding to an average particle size of 2.9 nm and a dispersion of 40.1%.

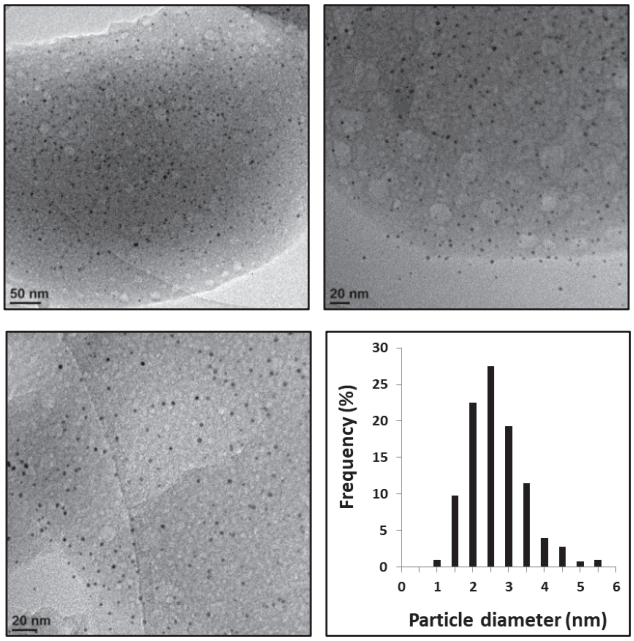

Figure 4.3.1 : TEM images of Au@Ca-LTA, and the corresponding particle size distribution where 400 particles were measured.

3.2. Pt@Ca-LTA

Fig. 4.3.3 shows TEM images of thin slices (70 nm) of the Pt sample. The sample displayed a very narrow particle size distribution corresponding to an average particle size of 1.7 nm and a dispersion of 66%. This is probably due to the very low metal loading (0.25 wt.%).

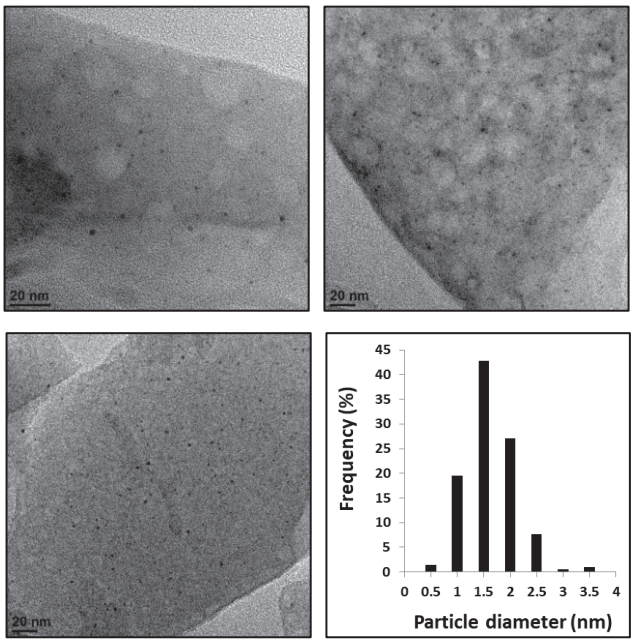

Figure 4.3.2 : TEM images of Pt@Ca-LTA, and the corresponding particle size distribution where 200 particles were measured.

3.3. Pt-Au(2)@Ca-LTA

Fig. 4.3.5 shows TEM images of the bimetallic sample. The sample displayed a narrow particle size distribution corresponding to an average particle size of 2 nm and a dispersion of 57.4%. The metals were not easily detected by the TEM-EDX analysis since the sample was too dense. However, TEM-EDX also showed the presence of some S and Cl residues used during the preparation.

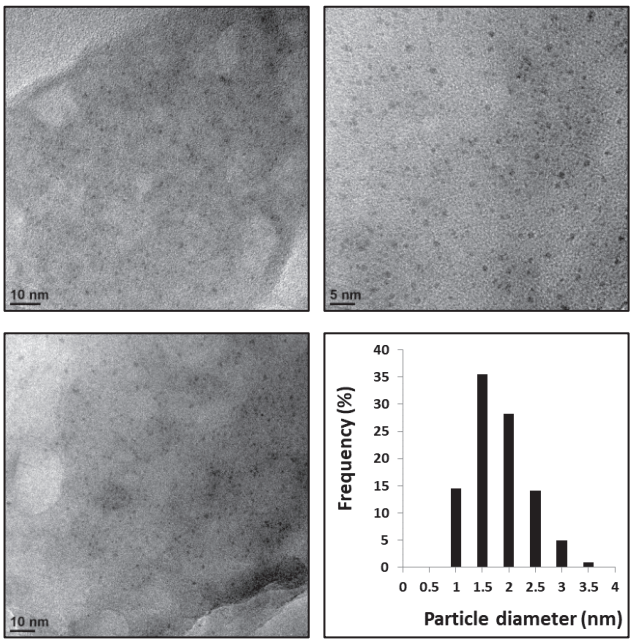

Figure 4.3.3 : TEM images of Pt-Au(2)@Ca-LTA, and the corresponding particle size distribution where 300 particles were measured.

4. PXRD analysis

The analysis was performed to characterize the catalysts after calcination in air at 350°C followed by the reduction with H_2 in 350°C. The measurement was performed on four samples, including the three samples analyzed by ICP (Table 4.2.1) in addition to a metal-free LTA zeolite sample. Fig. 4.4.1, 4.4.2, 4.4.2 and 4.4.3 show the PXRD patterns of the four samples.

Beneath each of the following patterns, the ICDD reference pattern of the LTA structure is shown (PDF 00-039-0222). In the metal-containing samples, the PXRD patterns did not display the peaks corresponding to the metal phases indicating low crystallinity, the presence of small particles, or even due to the very low metal loadings. The PXRD patterns of all the four samples corresponded perfectly to the LTA reference file.

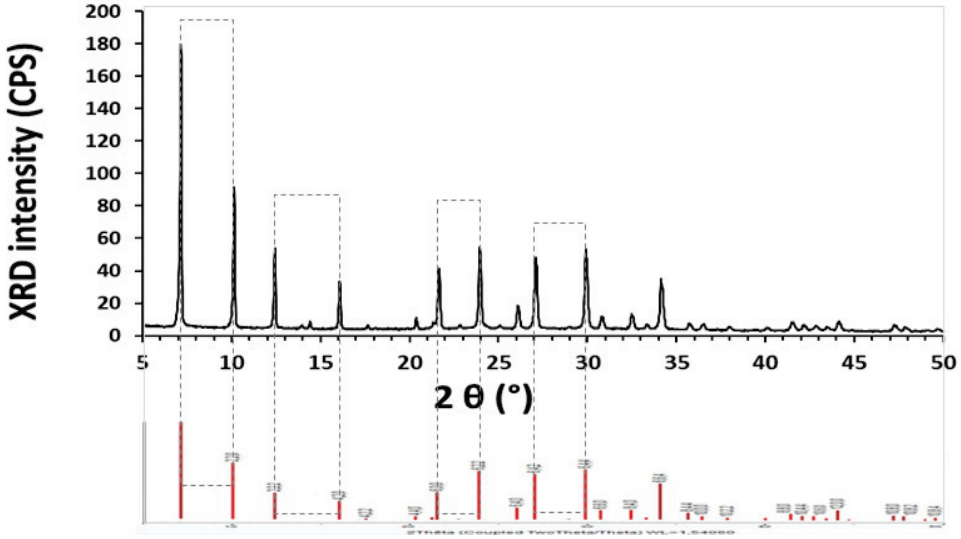

Figure 4.4.1 : PXRD pattern of the Ca-LTA zeolite support.

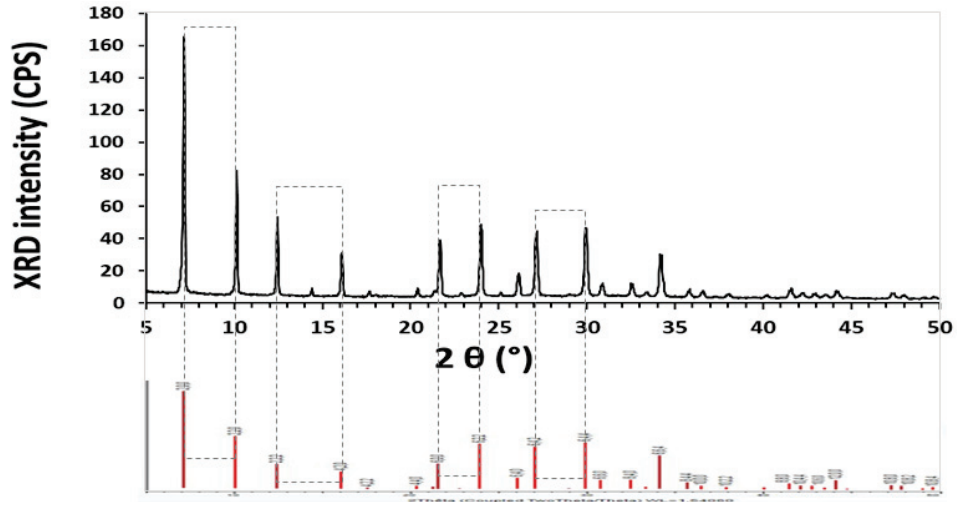

Figure 4.4.2 : PXRD pattern of Pt@Ca-LTA.

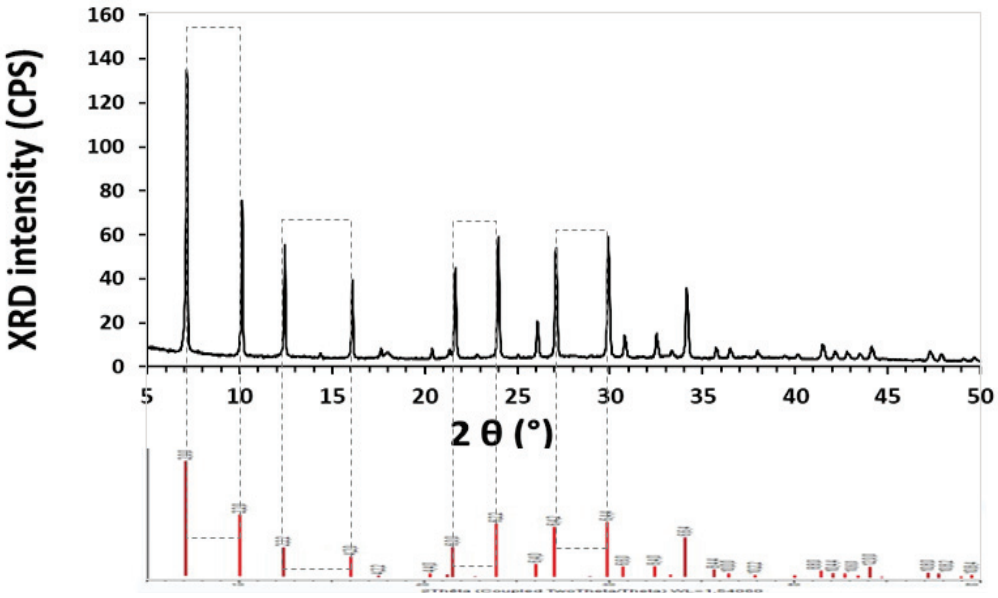

Figure 4.4.3 : PXRD pattern of Au@Ca-LTA.

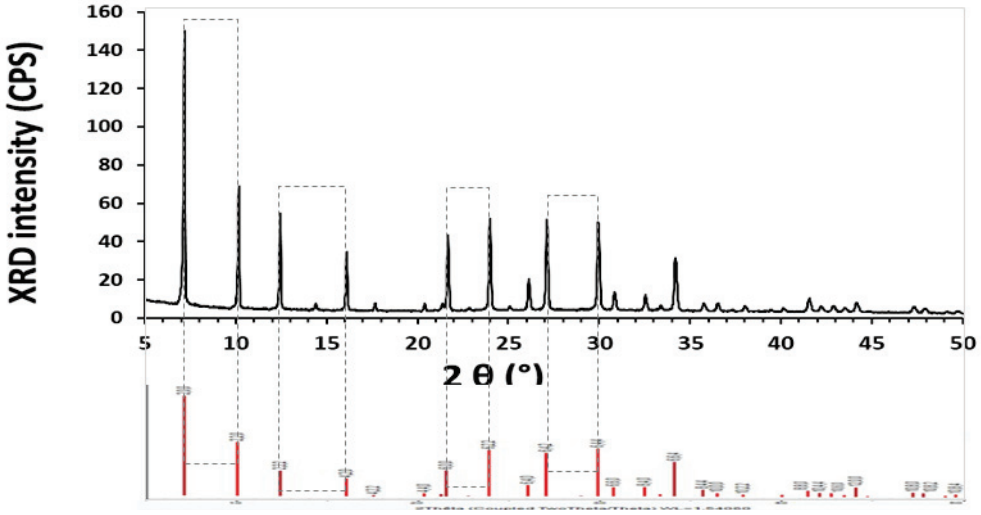

Figure 4.4.4 : PXRD pattern of Pt-Au(2)@Ca-LTA.

5. CO adsorption monitored by DRIFTS

5.1. Spectra collected before CO adsorption

5.1.1. Effect of the pre-treatments on the LTA spectra

Fig. 4.5.1 shows the effect of the calcination and reduction pre-treatments on the spectra collected over the Ca-LTA support. After both treatments, the spectra are similar. Both spectra show the disappaearance of the adsorbed water and the broad H-bonding band at 3400 cm^{-1} observed initially. Both spectra also display a low intensity terminal silanol band and a pronounced H-bonding band at 3566 cm^{-1}. Some bands assigned to calcium carbonte are also observed. Moreover, both show the presence of carbonaceous contaminants formed during the pre-treatments.

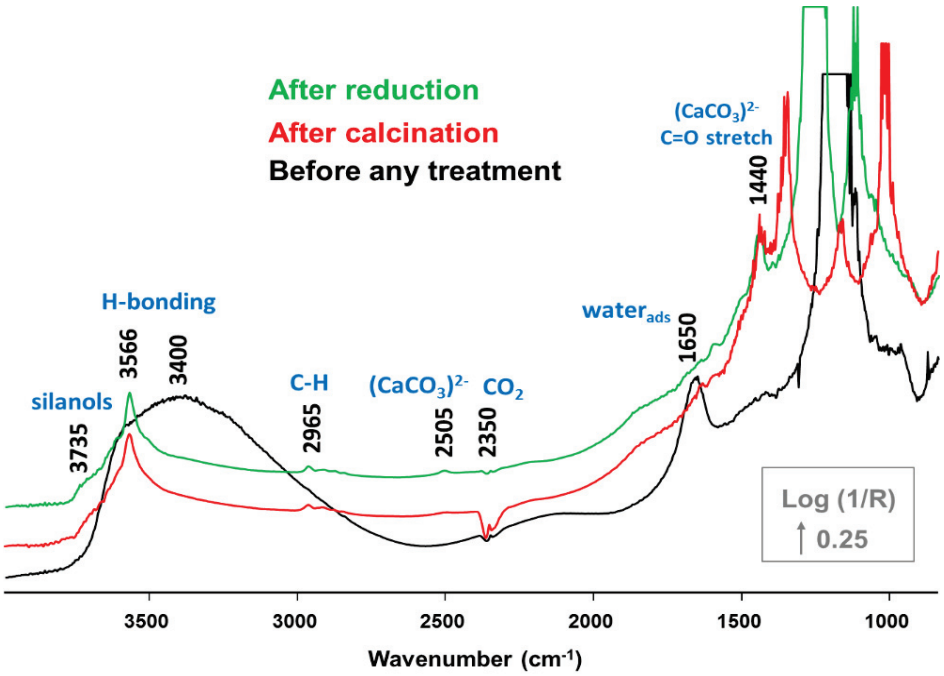

Figure 4.5.1: Spectra collected before CO adsorption over Ca-LTA with respect to KBr background before and after each pre-treatment.

5.1.2. Comparing the four samples

Fig. 4.5.2 and 4.5.3 show the spectra collected over the four LTA-based samples with respect to the KBr background before and after the pre-reatments, respectively. The spectra are similar to what was observed over the Ca-LTA zeolite support in both cases. The only difference is the absence of the C-H stretching band in the case of the Au-containing samples. This could indicate the easier removal of the formed organic compounds in the presence of Au.

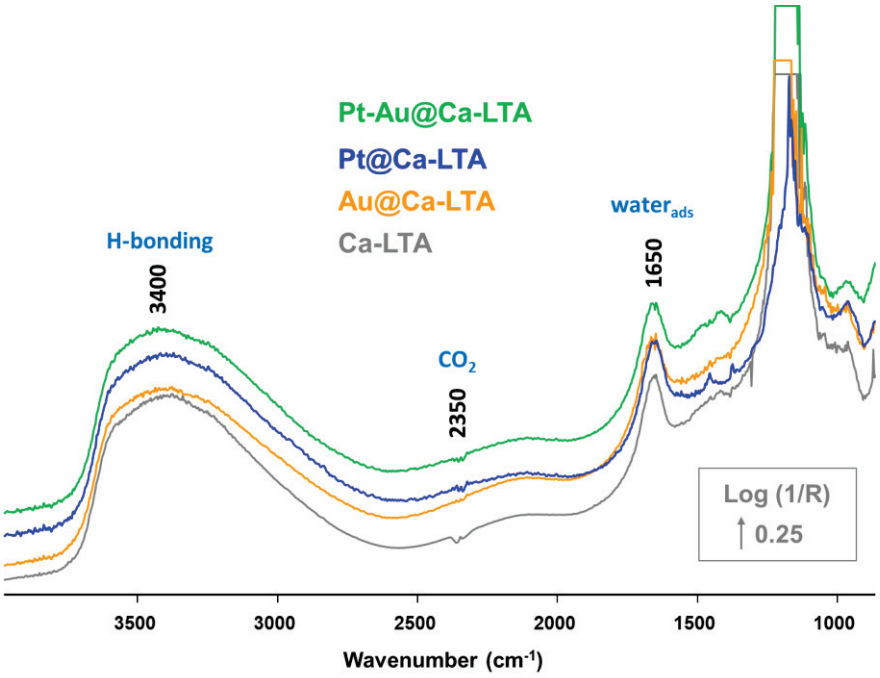

Figure 4.5.2 : Spectra collected at room temperature before any treatment over the four samples with respect to KBr background.

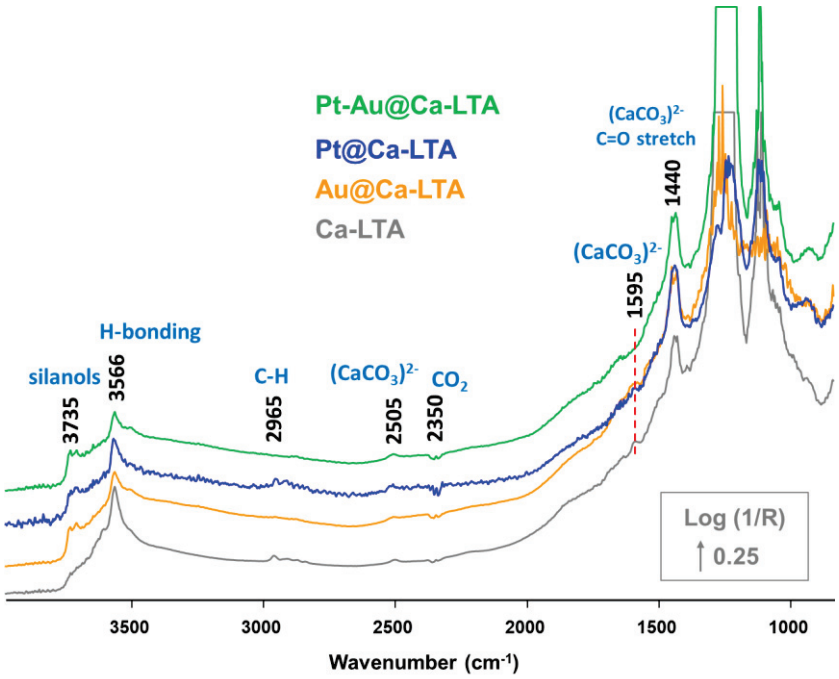

Figure 4.5.3 : Spectra collected after cooling to 50°C after the pre-treatments over the four samples with respect to KBr background.

5.2. CO adsorption/desorption spectra

5.2.1. Ca-LTA zeolite support

Fig. 4.5.4 shows the CO adsorption profile over the LTA sample. Two CO adsorption bands were observed at 2183 and 2112 cm^{-1}, and both stabilized rapidly within one min. The band at 2183 cm^{-1} possibly corresponding to CO adsorbed (through the C atom) on -OH groups as observed over basic zeolites [10], or mono- and poly-carbonyl species adsorbed on Ca^{2+} ions [11][12]. The band at 2112 cm^{-1} corresponding to CO adsorbed (through the O atom) on -OH groups or CO adsorbed on zeolite framework oxygen ions [10]. CO species adsorbed on Na^{+} ions were reported at 2175 cm^{-1} or lower [12]. Considering the absence of a distinct band at this position, Na^{+} ions probably were not of a significant abundance in the material following the Ca^{2+} ion exchange treatment.

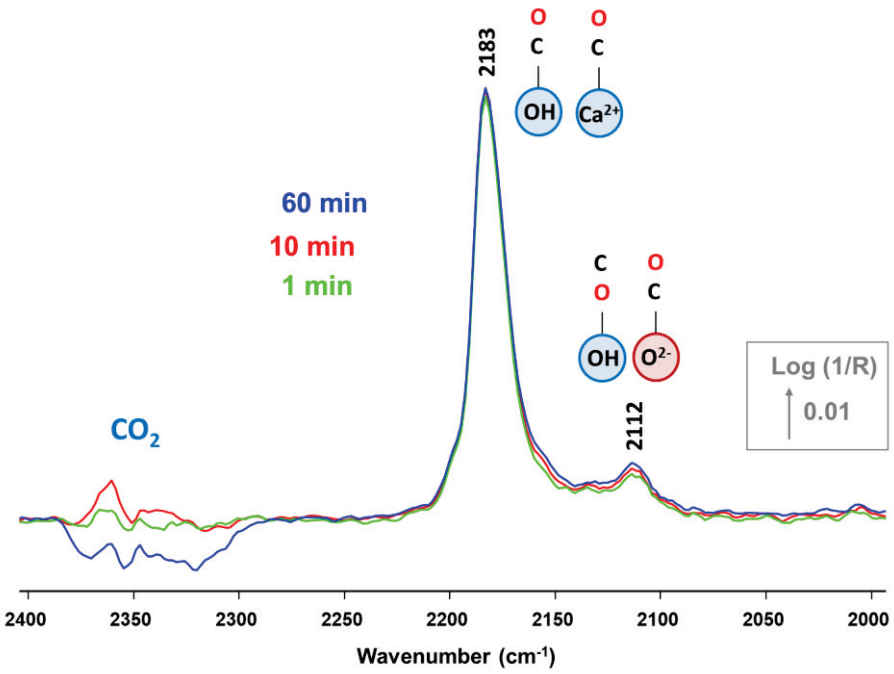

Figure 4.5.4 : The evolution with time under CO of the CO adsorption profile over Ca-LTA. Feed: 1% CO/He, 50°C, 50 mL/min.

After removing CO pressure Fig. 4.5.5, the minor adsorption band at 2112 cm^{-1} disappears in 1 min and the band at 2183 cm^{-1} disappears in 3 min. Both bands apparently relate to weak adsorption.

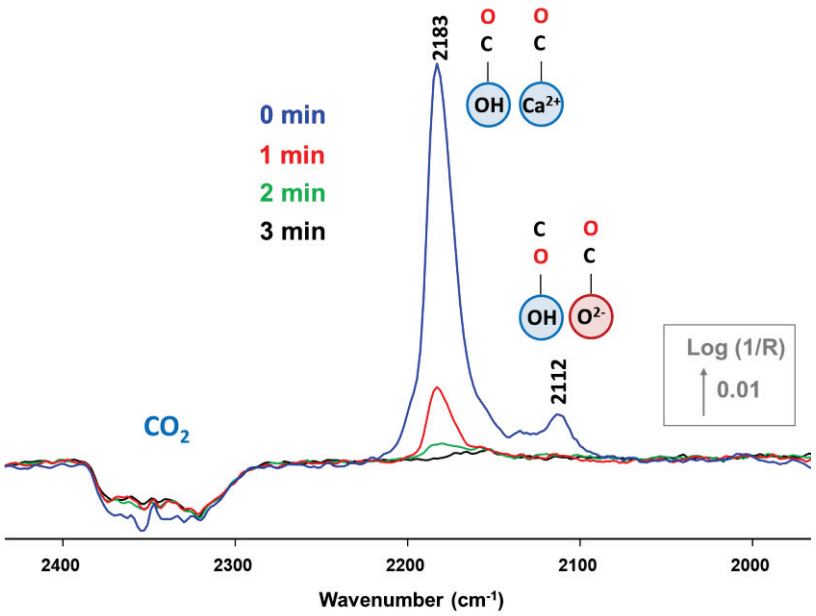

Figure 4.5.5 : CO desorption with time after stopping CO over Ca-LTA. Feed: He, 50°C, 40 mL/min. The sample was previously left under CO for 60 min.

5.2.2. Pt@Ca-LTA

Fig. 4.5.6 and 4.5.7 show the CO adsorption profile on the monometallic Pt sample.

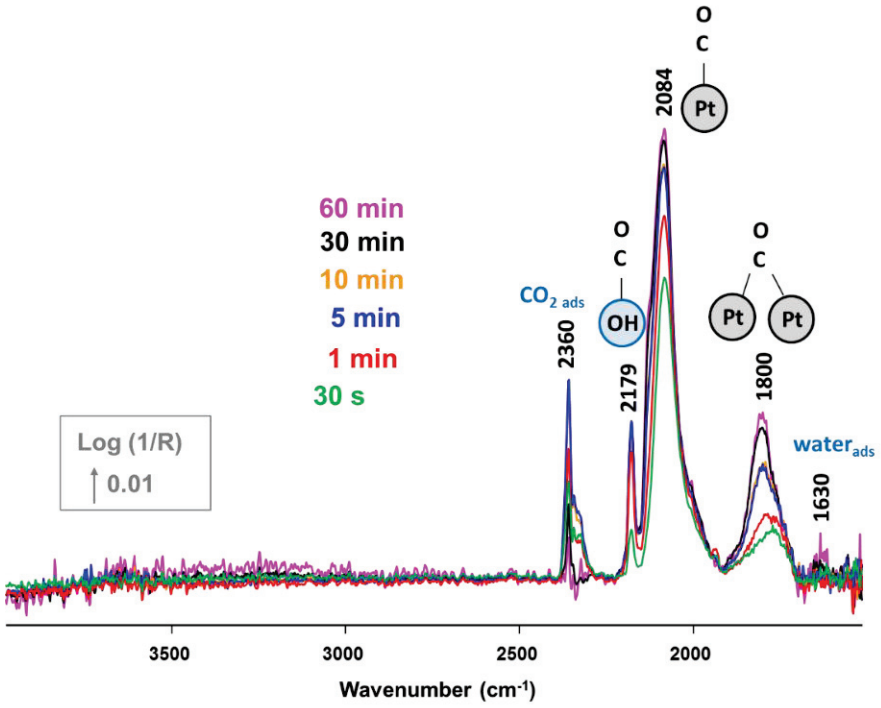

Figure 4.5.6 : The evolution with time under CO of the CO adsorption profile over Pt@Ca-LTA. Feed: 1% CO/He, 50°C, 50 mL/min.

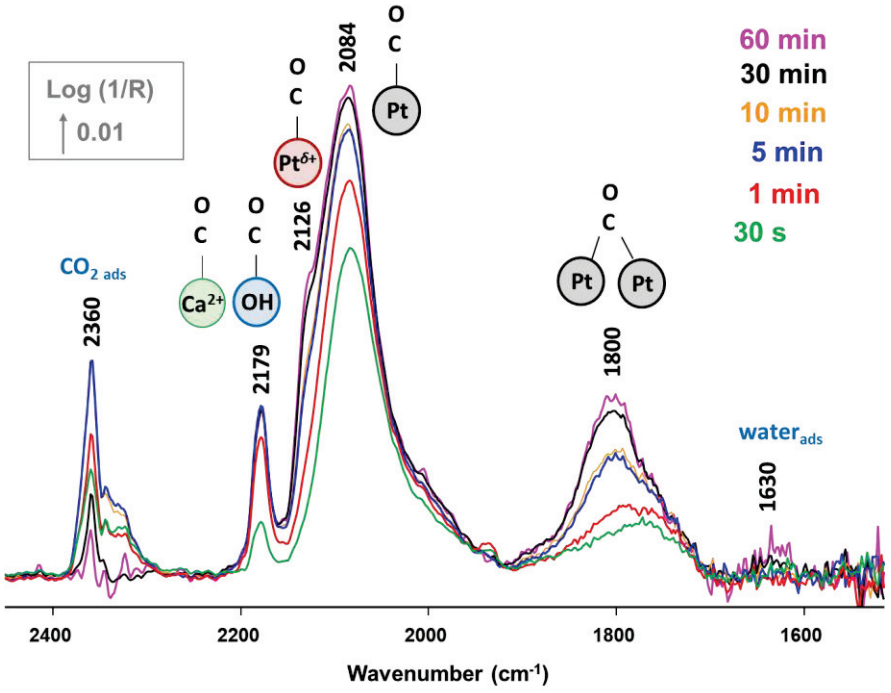

Figure 4.5.7 : The evolution with time under CO of the CO adsorption profile over Pt@Ca-LTA (1500-2400 cm^{-1}). Feed: 1% CO/He, 50°C, 50 mL/min.

Four adsorption bands are observed: (i) adsorbed CO_2 at 2360 cm^{-1}, (ii) CO adsorbed on -OH groups or Ca^{2+} ions of the LTA support at 2179 cm^{-1}, (iii) a band shoulder at 2126 cm^{-1} due to CO adsorption on $Pt^{\delta+}$ species [13], (iv) at 2084 cm^{-1} associated with the linear adsorption [14][15][16] on high coordination metallic Pt sites (referred to as Pt L-CO), and (v) at 1800 cm^{-1} associated with the bridge adsorption on metallic Pt [14][15][16] (referred to as Pt B-CO). The CO adsorption profile is mainly linear as also observed earlier [17] and could be due to the strong linear adsorption. The heat of the linear CO adsorption on Pt is 206-115 kJ/mol at θ = 0-1 [17][18] or 220-106 kJ/mol at θ = 0-1 [15] which is much higher than the heat of bridge CO adsorption on Pt of 94-45 kJ/mol at θ = 0-1[17][18].

The formation of $Pt^{\delta+}$ was also reported before over LTA support [19]. This is probably due to the oxidation of some Pt due to the Bronsted acid sites of the zeolite framework.

CO_2 could be formed due to a water-gas shift reaction ($CO + H_2O \rightarrow H_2 + CO_2$) or due to CO dissociation via Boudouard reaction ($2\ CO \rightarrow C + CO_2$) leading to the formation of elemental C that would be deposited on the surface of the catalyst.

Fig. 4.5.8 monitors the CO desorption spectra over the Pt sample after stopping CO. The OH-CO band desorbs in less than five min. The CO adsorption bands on Pt desorb slowly and reach ~0.8 of their initial band areas after 5 h (Fig. 4.5.9). However, the bridge adsorption band desorbs slightly faster due to its lower heat of adsorption as discussed. Both bands show a gradual red shift during the

desorption. The band due to the oxidized Pt fully disappeared within 3 h. The adsorbed water band increases possibly due some water to the He flow.

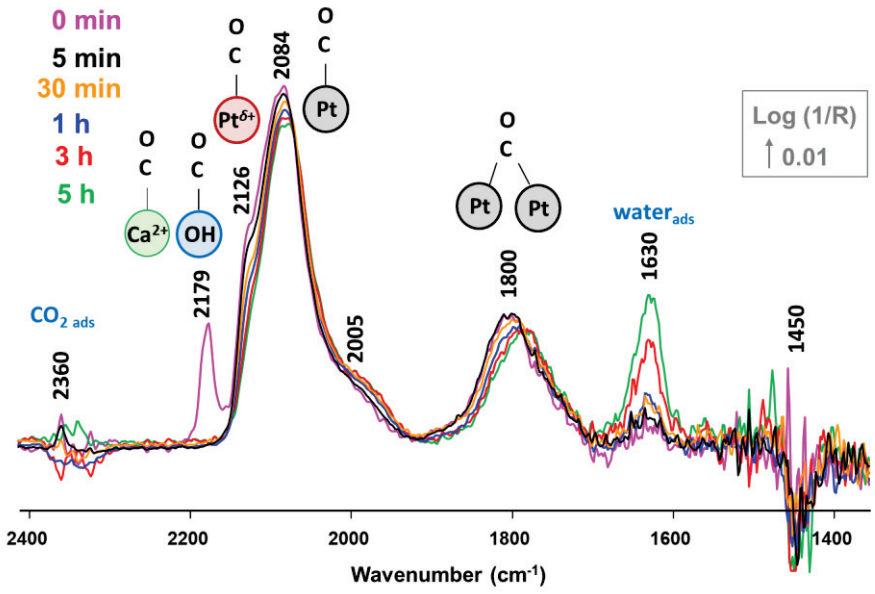

Figure 4.5.8 : CO desorption with time after stopping CO over Pt@Ca-LTA. Feed: He, 50°C, 40 mL/min. The sample was previously left under CO for 60 min.

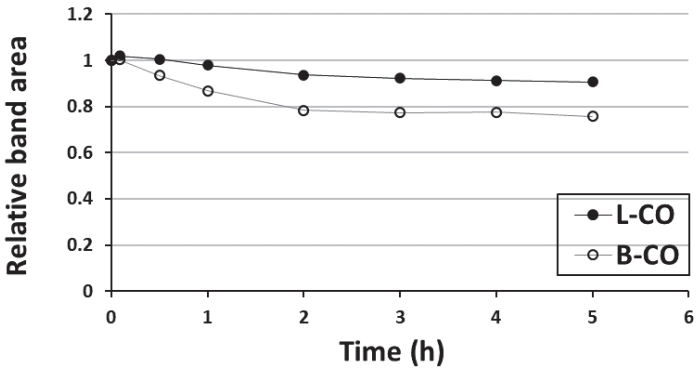

Figure 4.5.9 : The change in the relative band area of the two CO adsorption bands over Pt with the desorption time in Fig. 4.5.8: linear adsorption (L-CO) and bridge adsorption (B-CO).

5.2.3. Au@Ca-LTA

Fig. 4.5.10 and 4.5.11 monitor the evolution of the adsorption spectra over the Au sample. Three major adsorption bands were observed: (i) at 2360 cm^{-1} corresponding to adsorbed or trapped CO_2, (ii) at 2179 cm^{-1} possibly corresponding to CO adsorbed on -OH groups or Ca^{2+} ions of the LTA support [10], and (iii) at 2132 cm^{-1} corresponding to CO adsorbed linearly on partially oxidized Au (referred to as $Au^{\delta+}$-CO) [20][21]. The formation of such partially oxidized species cold be explained the same way as the formation of the oxidized Pt clusters in the Pt sample i.e. due to the Bronsted

acid sites. The low signal at 1630 cm^{-1} corresponds to adsorbed water possibly due to the CO feed. The CO adsorption bands stabilized rapidly within few min whereas the CO_2 adsorption band continued to increase for 60 min.

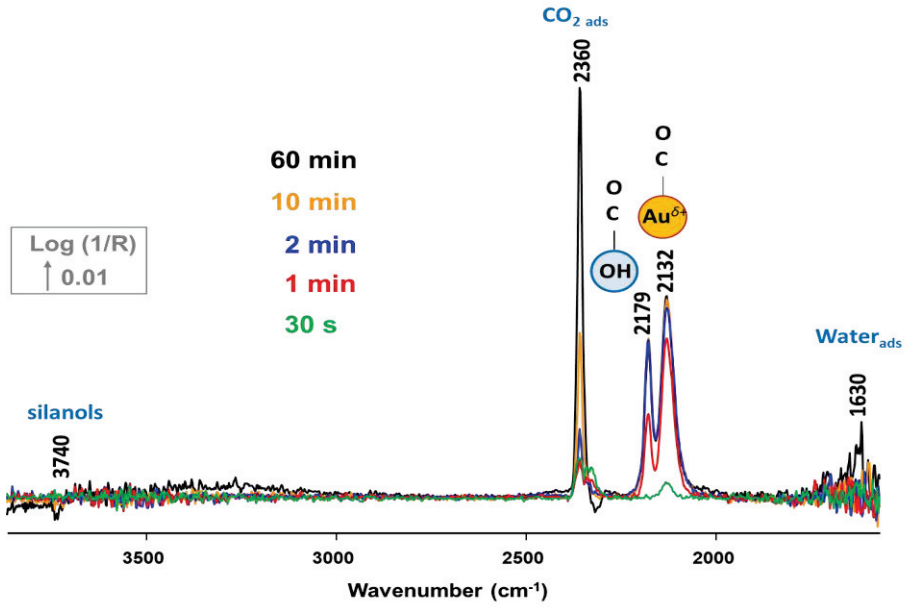

Figure 4.5.10 : The evolution with time under CO of the CO adsorption profile over Au@Ca-LTA. Feed: 1% CO/He, 50°C, 50 mL/min.

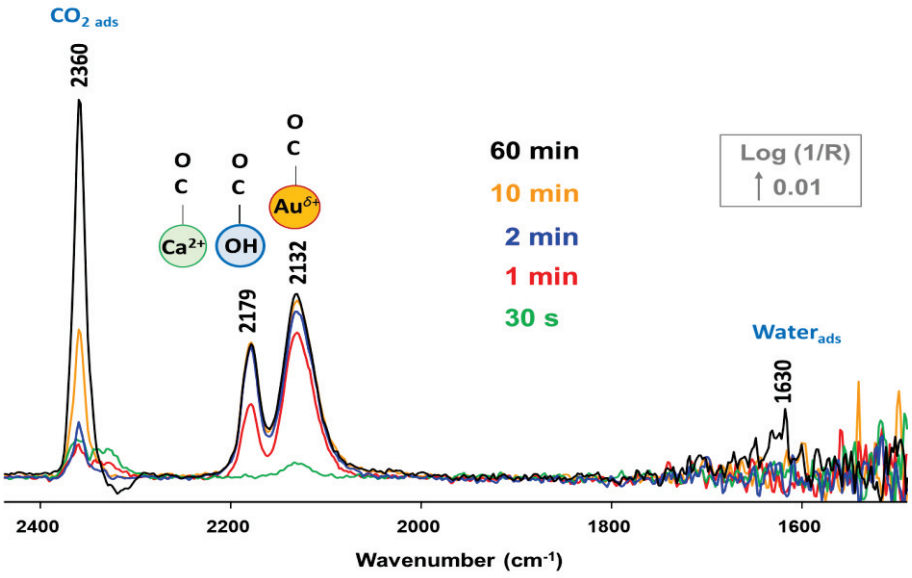

Figure 4.5.11 : The evolution with time under CO of the CO adsorption profile over Au@Ca-LTA (1500-2400 cm^{-1}). Feed: 1% CO/He, 50°C, 50 mL/min.

As discussed before, CO_2 could be formed due to a water-gas shift reaction or due to CO dissociation via Boudouard. Au was reported to promote Boudouard reaction [22][23].

Fig. 4.5.12 shows the CO desorption spectra over the Au sample after stopping CO. The OH-CO band desorbs rapidly in 3 min whereas $Au^{\delta+}$-CO takes ~7 min till full desorption. Adsorbed CO_2 continues to increase for five min after stopping CO flow before it starts to desorb.

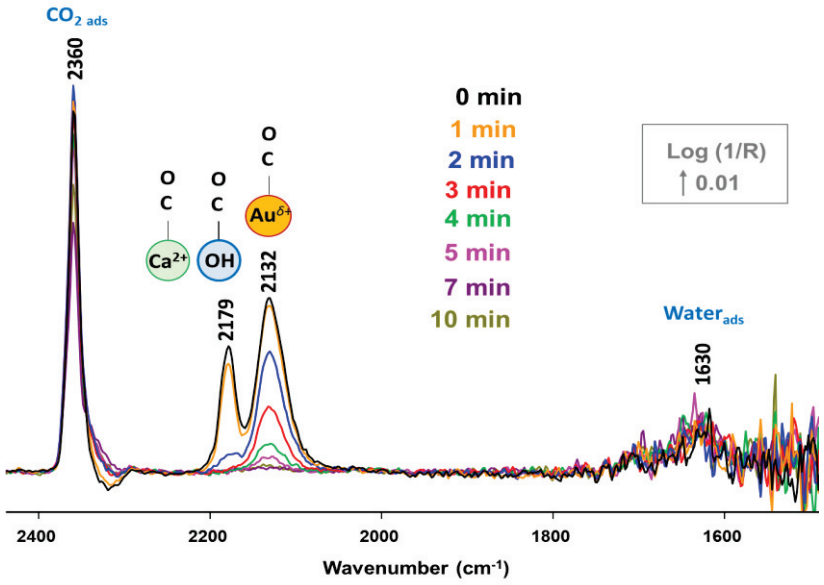

Figure 4.5.12 : CO desorption with time after stopping CO over Au@Ca-LTA. Feed: He, 50°C, 40 mL/min. The sample was previously left under CO for 60 min.

5.2.4. Pt-Au(2)@Ca-LTA

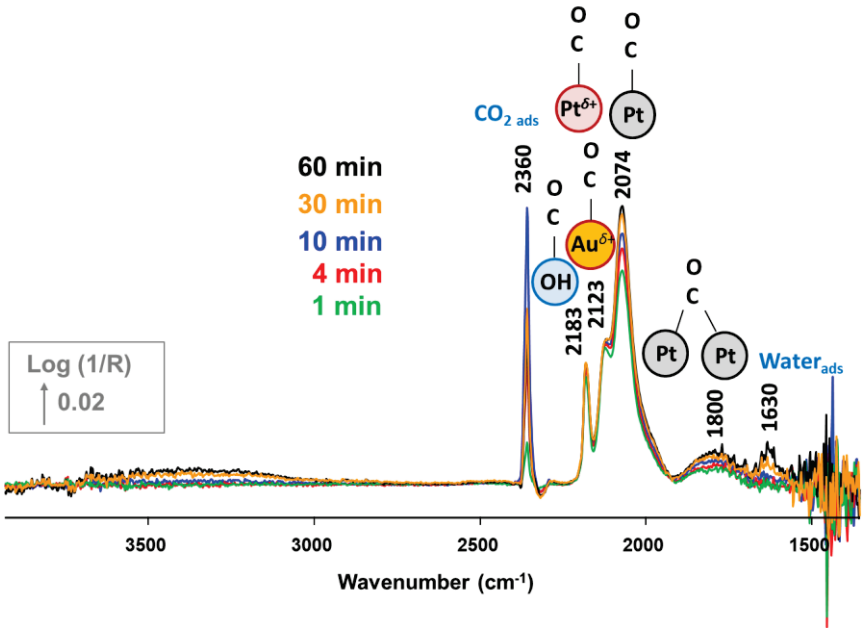

Figure 4.5.13 : The evolution with time under CO of the CO adsorption profile over Pt-Au(2)@Ca-LTA. Feed: 1% CO/He, 50°C, 50 mL/min.

Fig. 4.5.13 and 4.5.14 show the evolution of the adsorption profile over the bimetallic sample. The sample displayed all the adsorption bands observed with the monometallc samples and the metal-free LTA support.

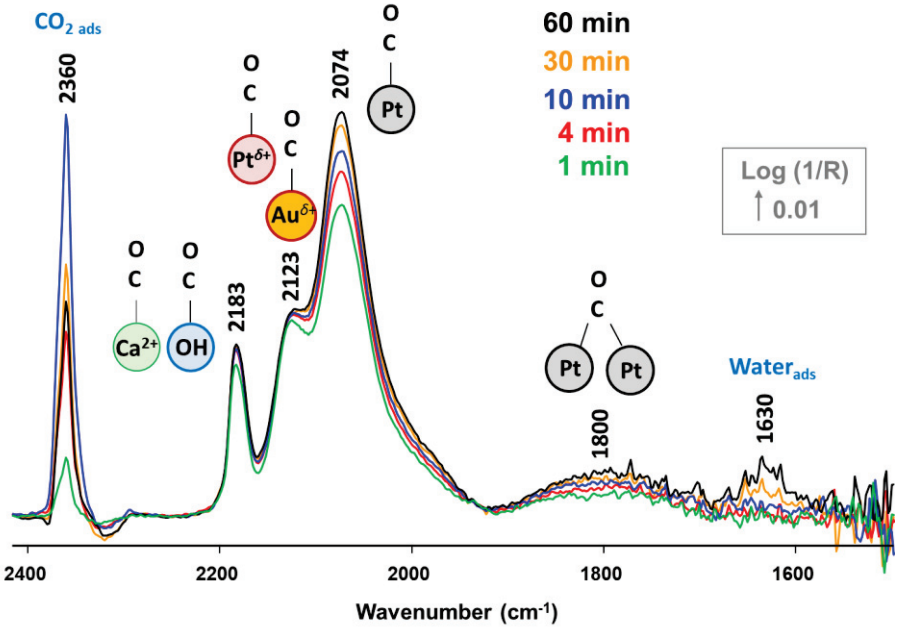

Figure 4.5.14 : The evolution with time under CO of the CO adsorption profile over Pt-Au(2)@Ca-LTA (1500-2400 cm^{-1}). Feed: 1% CO/He, 50°C, 50 mL/min.

The overlapping $Au^{\delta+}$-CO and Pt^{n+}-CO bands at 2123 cm^{-1} and the (OH-CO or Ca^{2+}-CO) band at 2183 cm^{-1} stabilized rapidly within 4 min under CO. However, The Pt L-CO band at 2074 cm^{-1} and the Pt B-CO band at 1800 cm^{-1} continued to increase for 60 min. This could be due to a significant surface segregation of Pt under CO. This would not necessarily significantly affect the intensity of CO adsorption on Au since Au terraces adsorb CO very weakly even at room temperature [24][25]. This could also indicate the presence of Au-rich regions where Au would preferably be located at surface sites due to its lower surface tension compared to Pt [26].

Some CO_2 was formed as indicated by the increase in the intensity of the adsrobed CO_2 band at 2360 cm-1 for 10 min before it continously dropped for 60 min. The adsorbed water band at 1630 cm^{-1} could be due to some water in the feed.

Fig. 4.5.15 and 4.5.16 show the desorption spectra after stopping CO. Fig. 4.5.15 presents the desorption during the first 16 min. The OH-CO (or Ca^{2+}-CO) band desorbs within 5 min and CO adsorbed on oxidized Au and Pt fully desorbs in 1 h (Fig. 4.5.16). There is no apparent change in the CO adsorption bands on metallic Pt for 16 min.

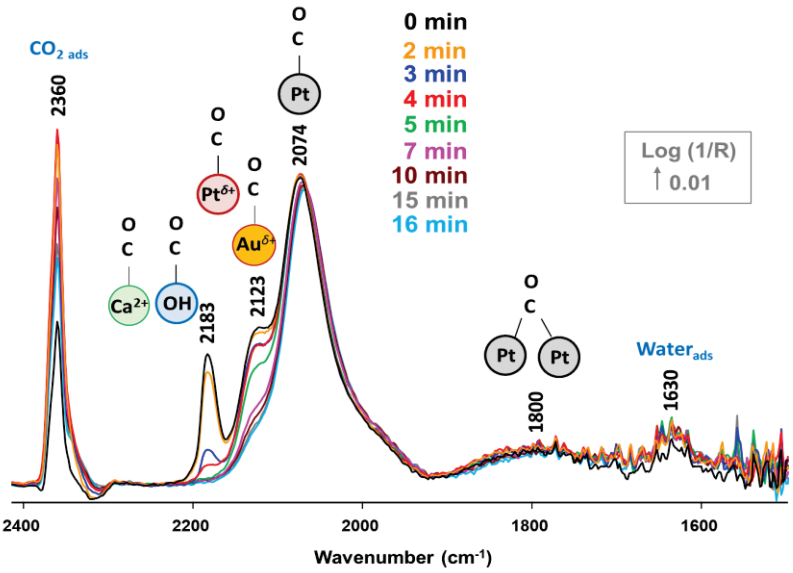

Figure 4.5.15 : CO desorption with time after stopping CO (during 16 min) over Pt-Au(2)@Ca-LTA. Feed: He, 50°C, 40 mL/min. The sample was previously left under CO for 60 min.

Fig. 4.5.16 shows the desorption spectra during 4 h. The intensity of the linear adsorption band decreases after 1 h; and then, remains almost the same. The band area remains almost unchanged (Fig. 4.5.17). The band also displays a red shift from 2074 to 2064 cm^{-1}. On the other hand, the bridge adsorption band does not display any apparent change in the band position and displays only a slight (10%) change in the band area after 4 h (Fig. 4.5.17). The stable band areas indicate a very strong adsorption of CO on Pt. During desorption, the adsorbed water continously increasesd possibly due to the He flow. The adsorbed CO_2 fully desorbs after two h.

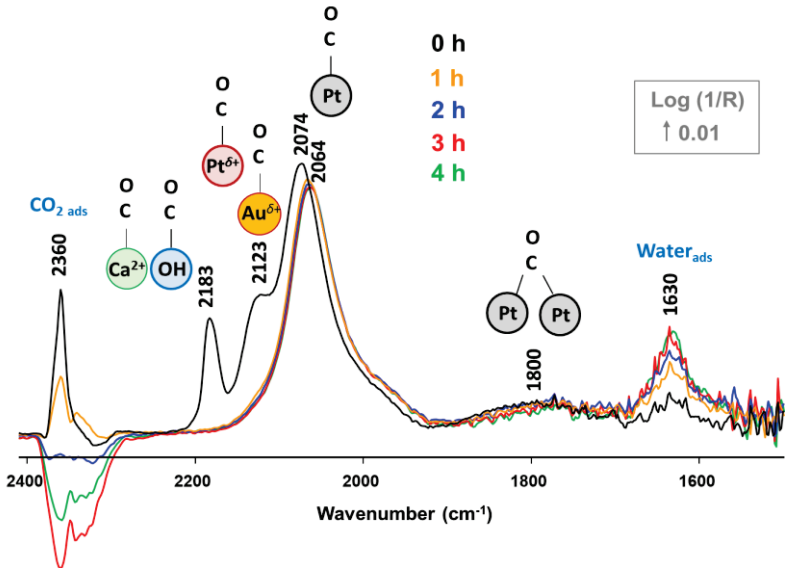

Figure 4.5.16 : CO desorption with time after stopping CO (during 4 h) over Pt-Au(2)@Ca-LTA. Feed: He, 50°C, 40 mL/min. The sample was previously left under CO for 60 min.

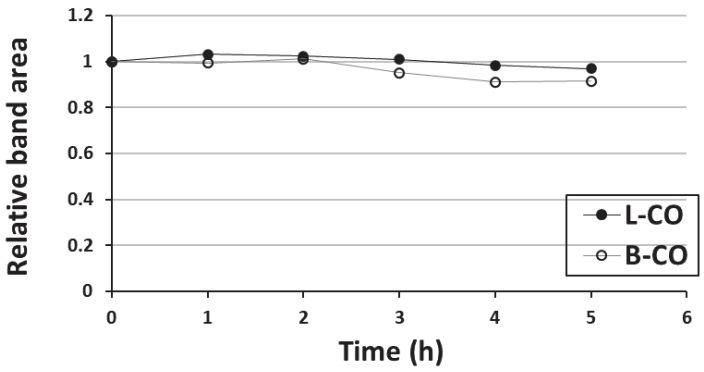

Figure 4.5.17 : The change in the relative band areas of CO adsorption bands on Pt over Pt-Au(2)@Ca-LTA with the desorption time in Fig. 4.5.16: (Pt L-CO: linear adsorption; Pt B-CO: bridge desorption).

5.2.5. Comparison between all the four samples

Fig. 4.5.18 compares the final adsorption spectra (60 min under CO) over the four samples.

The Pt L-CO band in the bimetallic sample is red shifted compared to the monometallic Pt sample. As reported [15][16], smaller Pt particles display a red shift in the linear adsorption band as compared to the larger particles. This could be explained based on the increased metal back bonding with the CO 2π* orbital for smaller particles [27]. This could indicate the presence of small Pt particles/clusters over the bimetallic sample. This could be also consistent with the possible dilution of Pt by the excess Au present (i.e. some degree of alloying), where Au atoms would prefereably occupy low coordination sites of the Pt surface (edges/corners) [28]. The two arguments were also supported by the apparently decreased tendency of the CO bridge adsorption on Pt in the bimetallic sample.

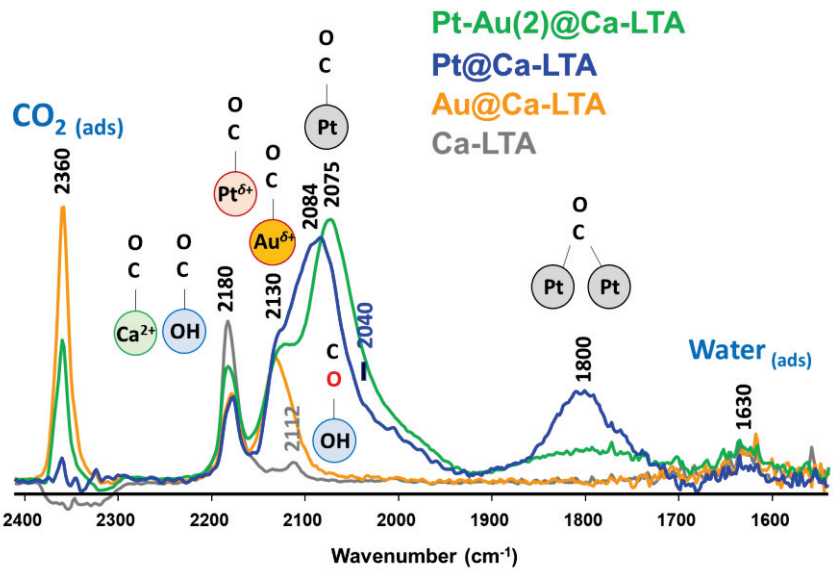

Figure 4.5.18 : Final adsorption profiles over the four samples (60 min under CO).

The adsorbed CO_2 band varied during the experiment over all the four samples. Similarly, the OH-CO (or Ca^{2+}-CO) band intensity could vary merely due to different catalyst amounts used in the DRIFTS cell. Therefore, the differences in their intensities are not meaningful to draw conclusions. Fig. 4.5.19 compares the relative band areas of the two Pt-CO adsorption bands during CO desorption over the two Pt-containing samples. Both bands desorb faster over the Pt sample. This could indicate a stronger Pt-CO adsorption over the bimetallic sample. This could be consistent with the conclusion of the formation of smaller Pt clusters.

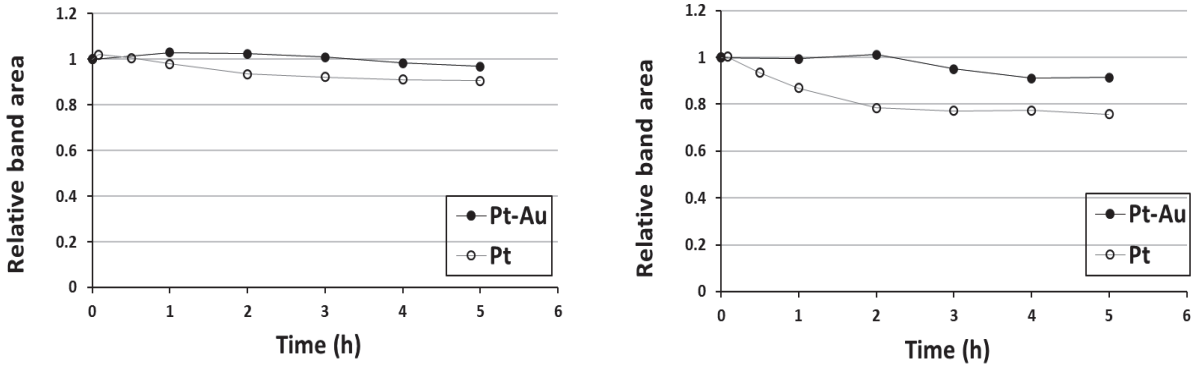

Figure 4.5.19 : The change in the relative band areas with the desorption time of the linear (left) and bridge (right) CO adsorption modes on Pt over Pt@Ca-LTA and Pt-Au(2)@Ca-LTA.

6. Conclusions on the characterizations performed

The LTA structure was evidenced by the PXRD analysis. TEM analysis showed the presence of nicely dispersed nanoparticles of the order of 2-3 nm (Table 4.6.1). As a matter of fact, the higher size of the Au nanoparticles is not surprising. As reported, the interaction between Au and the LTA zeolite framework is lower than that of Pt [29]. Therefore, Au displays a higher affinity to sintering.

Table 4.6.1 : TEM analysis results of the LTA-based samples.

Sample	d_{SW} (nm)	Dispersion (%)
Au@Ca-LTA	**2.9**	**40.1**
Pt@Ca-LTA	**1.7**	**56**
Pt-Au(2)@Ca-LTA	**2**	**57.4**

Moreover, the metals were successfully encapsulated in the pores of the LTA structure. However, this process did not prove to be very efficient since the actual metal loadings measured by ICP were almost half the nominal loadings. Moreover, S and Cl residues were observed by TEM-EDX after the preparation, indicating insufficient post-preparation treatments.

The calcination and reduction pretreatments resulted in the loss of the adsorbed water and the formation of carbonaceous contaminants in all samples as observed by DRIFTS. In all samples, the basic LTA support showed bands of CO adsorption on -OH groups. CO_2 was formed over the metal-containing samples possibly via Boudouard reaction or WGS. Pt adsorbed CO mostly linearly; and a significant bridge adsorption was also observed. The Au sample displayed a linear CO adsorption on Au atoms. The bimetallic sample displayed all adsorption bands observed with the two monometallic samples and the LTA support.

Compared to the Pt sample, the bimetallic sample possibly featured the dilution of Pt by the excess Au. This was concluded based on the decreased (bridge/linear adsorption) ratio compared to the Pt sample. Accordingly, the sample also possibly featured the formation of smaller Pt clusters and hence, a stronger CO adsorption on Pt. These observations supported the formation of some alloyed nanoparticles.

7. NO_X decomposition catalytic activity

The catalytic test was performed using the samples listed in Table 4.7.1. All the samples were pre-reduced in a flow of 18% H_2/He prior to the exposure to a flow of 1000 ppm NO/ArHe at 350°C. The following sections show the catalytic data of the samples under NO in the absence of O_2.

Table 4.7.1 : List of the LTA-based samples and the corresponding Au/metal atomic ratio.

Sample	Nominal Au/M ratio	Actual Au/M ratio
Au@Ca-LTA	----	----
Pt@Ca-LTA	0	0
Pt-Au(2)@Ca-LTA	2	1.9
Pt-Au(1)@Ca-LTA	1	n.d.
Pt-Au(0.5)@Ca-LTA	0.5	n.d.
Pt-Au(0.25)@Ca-LTA	0.25	n.d.

7.1. NO feed through the empty reactor

The feed signal is collected for a few minutes through the by-pass until the NO signal stabilizes. The flow is then switched into the quartz reactor. Fig. 4.7.1 shows the FTIR profile of NO initially through the by-pass line before switching the flow into the empty quartz reactor. For further figures, the starting point of the reaction is chosen to be the point at which the signal of NO starts to change after switching the flow from the by-pass to the reactor.

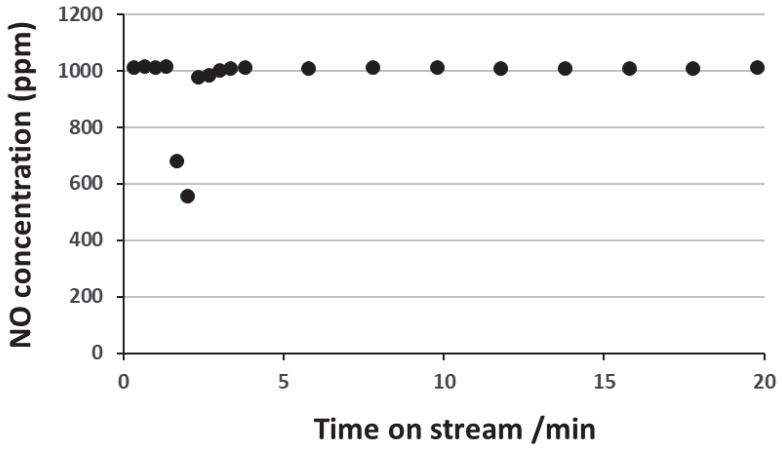

Figure 4.7.1 : FTIR data of the NO profile through the empty reactor. NO steady state concentration is 1000 ppm. The point at which the feed is switched from the by-pass line to the reactor is chosen to be the origin of time for the subsequent figures.

In Fig. 4.7.1, the concentration of NO through the empty reactor is 1000 ppm before the purge of the dead-volume of the reactor observed between 0.5 and 4 min. The NO profile through the empty reactor thus takes about three minutes to stabilize back to 1000 ppm. Assuming that NO does not react, and its temporary disappearance is merely due to the purge of the dead-volume initially filled with pure He, we can use the NO signal as that of an inert tracer. The NO curve can be used to calculate the reactor line dead-volume, by integrating the "missing NO" area following the switch given by Eq. 4.7.1:

$$\textbf{Reactor line dead volume} = \frac{\mathbf{F}}{\mathbf{1000}} \int_{\mathbf{0}}^{\mathbf{TOS}} \{\, \mathbf{1000} - [\mathbf{NO(t)}] \,\}\, \mathbf{dt} \qquad \textbf{Eq. 4.7.1}$$

where F is the flow rate (50 mL/min) and TOS is the time on stream (10 min for instance). This results in a dead-volume of 13.9 mL.

The missing amount of NO can then be calculated according to Eq. 4.7.2.

$$[\mathbf{Missing\ NO(t)}] = [\mathbf{NO_{feed}}] - [\mathbf{NO(t)}] - [\mathbf{NO_2(t)}] - \mathbf{2} \times [\mathbf{N_2O(t)}] \qquad \textbf{Eq. 4.7.2}$$

Fig. 4.7.2 shows the FTIR profiles of N_2O, NO_2 and the calculated missing NO through the empty reactor. Negligible amounts of NO_2 and N_2O are observed. In addition, the missing NO profile falls to zero after ~2 min i.e. after the purge of the dead-volume of the reactor line. As reported, NO decomposition displays a very large kinetic barrier of ~335 kJ/mol [30][31]. This essentially reenforces that NO does not react inside the empty reactor and the change in its concentration after switching the flow to the reactor is only due to the purge of the dead-volume as discussed before.

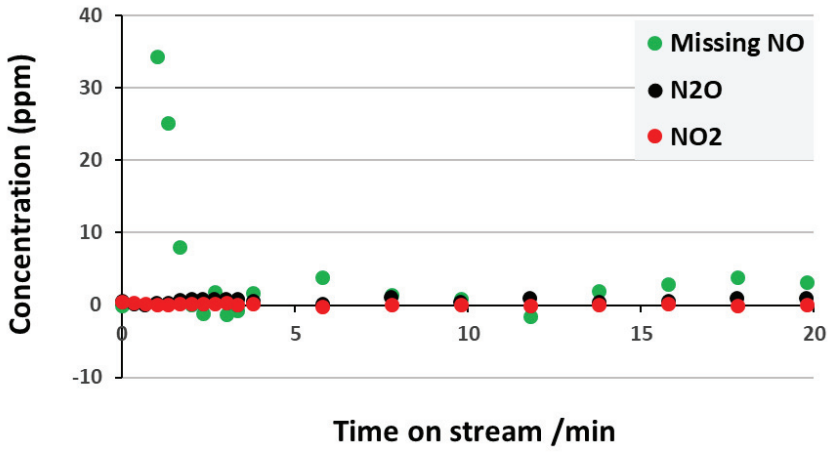

Figure 4.7.2 : FTIR data of the NO_2, N_2O and the missing NO through the empty reactor. The starting point is the chosen origin of time. NO steady state concentration is 1000 ppm.

7.2. Methodology of calculation

This section discusses the calculation of the NO_X conversion over the catalysts and the correlation between the converted NO moles to the number of the moles of the active metal in the catalyst.

7.2.1. NO_X conversion calculation

FTIR can only detect NO, NO_2 and N_2O but not N_2 or O_2. The quantification of the effluent gases was performed by the integration of the peak areas of the various gases (NO, NO_2 and N_2O) which are IR active molecules.

The measured NO_X (= NO + NO_2) conversion is calculated as follows:

The measured NO_X conversion(t) is calculated as follows:

$$\mathbf{NO_X\ conversion(t)} = \frac{[(\mathbf{NO_X})_{\mathbf{feed}}] - [\mathbf{NO_X(t)}]}{[(\mathbf{NO_X})_{\mathbf{feed}}]} \qquad \textbf{Eq. 4.7.3}$$

7.2.2. Calculation of the converted NO (in mol) over 1-60 min:

- The number of moles of reacted NO over 1-60 min is:

$$\mathbf{NO_{reacted}\ (mol)} = \int_1^{60} \mathbf{Molar\ flow\ of\ NO\ reacted\ dt}$$

$$= \int_1^{60} \frac{\mathbf{Volumetric\ flow\ of\ NO\ reacted}}{\mathbf{V_M}}\ \mathbf{dt}$$

where V_M is the perfect gas molar volume (24.465 L/mol at 25°C and a pressure of 1 atm),

$$\mathbf{NO_{reacted}\ (mol)} = \int_1^{60} \frac{\mathbf{Total\ volumetric\ flow} \times [\mathbf{NO_{feed}}] \times \mathbf{NO\ conversion}}{\mathbf{V_M}}\ \mathbf{dt}$$

$$= \frac{\mathbf{Total\ volumetric\ flow} \times [\mathbf{NO_{feed}}]}{\mathbf{V_M}} \int_1^{60} \mathbf{NO\ conversion\ dt} \qquad \textbf{Eq. 4.7.4}$$

where

- $[NO_{feed}]$ = NO mole or volume fraction in the feed = 1000 ppm = 0.1 %
- Total volumetric flow = 50 mL/min
- $\int$ **NO_X conversion dt** is calculated (in min.) for each metal using the corresponding NO_X conversion profile.

7.2.3. Calculation of the number of moles of Pt in the bed:

- Catalyst mass = 50 mg
- Weight fractions (wt.%) of each metal in the catalyst are given in table 4.2.1.
- M_{metal} (mg) = 100 /1000 x weight fraction /100
- The MW of Pt is 195.08 g/mol

$$\mathbf{Mol_{metal} = weight\ fraction\ (wt.\%)\ /1000\ /\ MW\ (g/mol)} \qquad \mathbf{Eq.\ 4.7.5}$$

7.3. Catalytic data

7.3.1. Performance of Au@Ca-LTA

The Au sample is inactive for NO decomposition reaction under these conditions (Fig. 4.7.3), similar to was observed over Au/SiO_2 (Chapter 3). This also indicates the inactivity of the LTA support itself.

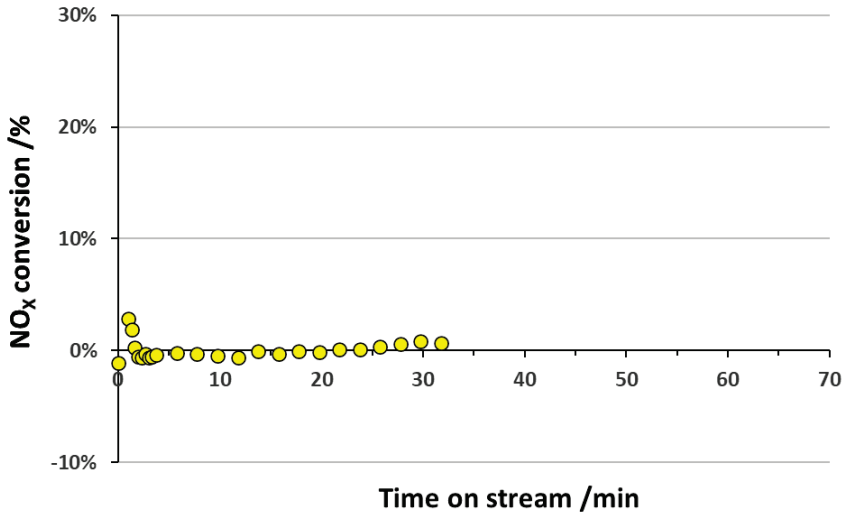

Figure 4.7.3 : The evolution of NO_X conversion over 50 mg of Au@Ca-LTA during the catalytic test. Pre-treatment: 18% H_2/He, 55 mL/min, 350°C. Feed: 1000 ppm NO/ArHe, 50 mL/min, 350°C.

7.3.2. Performance of Pt@Ca-LTA

The Pt sample showed a high initial NO conversion of 45% after the NO flow stabilized (Fig. 4.7.4). Then, the conversion dropped below 10% after 35 min after which, a slower deactivation was observed for additional 35 min. During NO exposure for 60 min, the number of moles of the Pt sample in the bed **(641 nmol)** resulted in the conversion of **26 times** higher amount of NO **(16541 nmol)**. This suggested that the observed NO conversion was at least partly due to true catalytic activity. However, the continuous deactivation suggested a redox reaction between NO and metallic Pt leading

to the formation of N_2, N_2O and PtO, which is not active at this temperature. The sample deactivates to a negligible activity after 10 min of NO exposure. The faster deactivation for the first 35 min could be due the poisoning of the surface by the produced oxygen, while the following slower deactivation could be due to the formation of bulk Pt oxide which is more kinetically hindered.

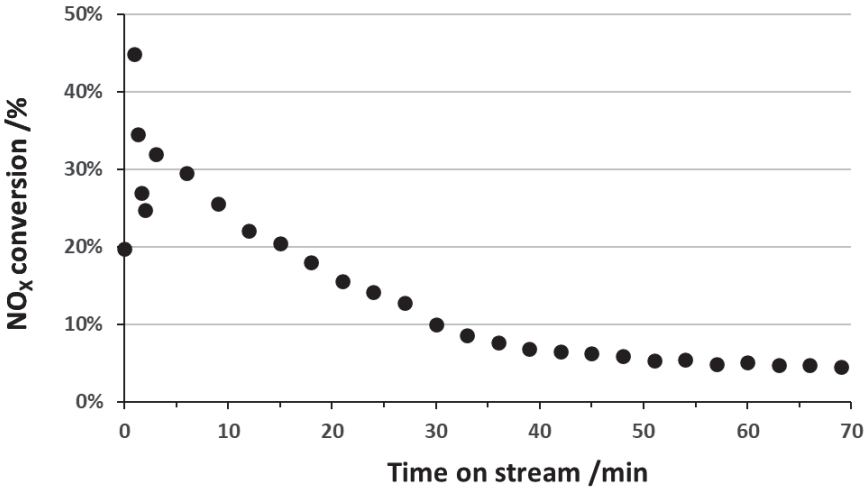

Figure 4.7.4 : The evolution of NO_X conversion over 50 mg of Pt@Ca-LTA during the catalytic test. Pre-treatment: 18% H_2/He, 55 mL/min, 350°C. Feed: 1000 ppm NO/ArHe, 50 mL/min, 350°C.

7.3.3. Performance of Pt-Au(2)@Ca-LTA

As shown in Fig. 4.7.5, the sample showed a high initial NO conversion of 45% after the NO flow stabilized. Then, the conversion rapidly dropped below to 4% within 5 min. After that, the conversion surprisingly increased and reached 8% after 25 min before a slow deactivation was observed till the end of the experiment.

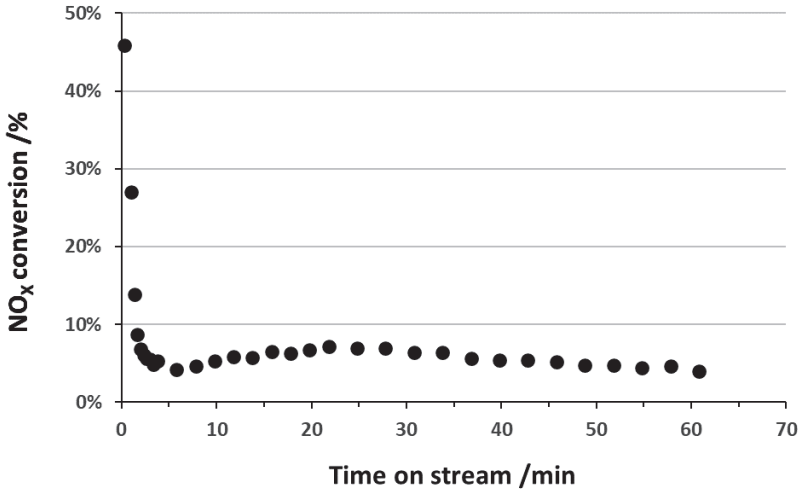

Figure 4.7.5 : The evolution of NO_X conversion over 50 mg of Pt-Au(2)@Ca-LTA during the catalytic test. Pre-treatment: 18% H_2/He, 55 mL/min, 350°C. Feed: 1000 ppm NO/ArHe, 50 mL/min, 350°C.

During NO exposure for 60 min, the number of moles of the Pt sample in the bed (461 nmol) resulted in the conversion of 14 times higher amount of NO (6607 nmol). This suggested that the observed NO conversion was at least partly due to true catalytic activity.

However, the initial rapid deactivation could suggest a major accessibility limitation of Pt. This could be due to the pore blockage possibly by some adsorbed nitrates formed up NO conversion, or merely due to a decreased Pt dispersion due to the excess Au of a lower surface tension. The intermediate activity rise could be due to the surface segregation of Pt under NO. The slow deactivation observed finally suggested a redox reaction between NO and metallic Pt.

7.3.4. Performance of Pt-Au(1)@Ca-LTA

As shown in Fig. 4.7.6, the sample showed a high initial NO conversion of 45% after the NO flow stabilized. Then, the conversion very rapidly dropped till full deactivation after 15 min. During the test, the sample resulted in the conversion of only (3583 nmol) of NO, while the nominal Pt content in the sample is 1302 nmol. The rapid deactivation suggested a redox reaction between NO and metallic Pt. Moreover, the very limited activity could indicate that the metals were not fully accessible and/or poisoned by S or Cl if present.

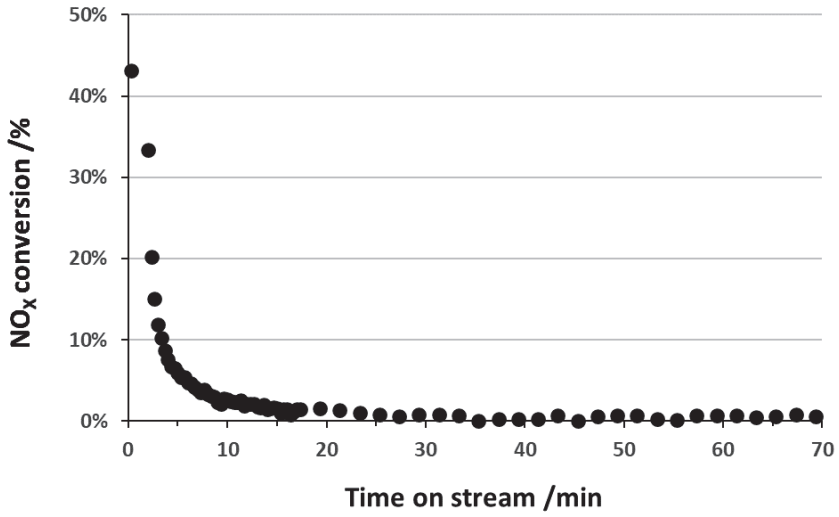

Figure 4.7.6 : The evolution of NO_X conversion over 50 mg of Pt-Au(1)@Ca-LTA during the catalytic test. Pre-treatment: 18% H_2/He, 55 mL/min, 350°C. Feed: 1000 ppm NO/ArHe, 50 mL/min, 350°C.

7.3.5. Performance of Pt-Au(0.5)@Ca-LTA

As shown in Fig. 4.7.7, the sample showed a high initial NO conversion of 35% after the NO flow stabilized. Then, the conversion dropped to 25% after only 1 min. The conversion then increased back to 35% after ~10 min before a continuous deactivation was observed till full deactivation after 50

min. During the test, the sample resulted in the conversion of a significant amount of NO (14197 nmol) while the nominal Pt content in the sample is only 1769 nmol. This could possibly refer to some true catalytic activity. The continuous deactivation mostly suggested also a redox reaction between NO and metallic Pt. The sudden activity rise after 2 min could indicate the surface segregation of Pt under NO.

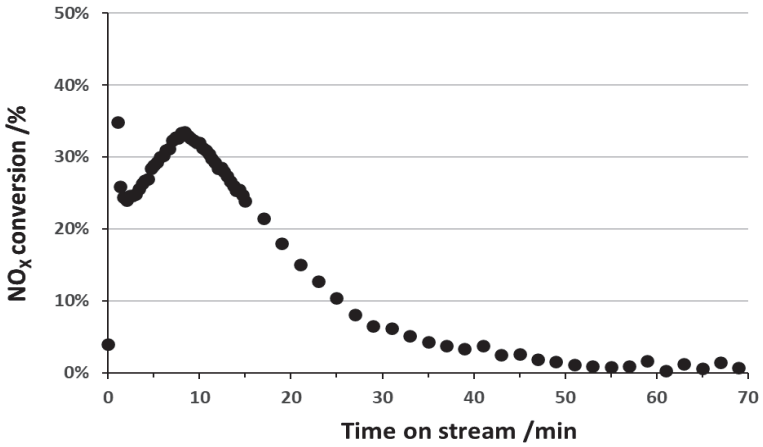

Figure 4.7.7 : The evolution of NO_X conversion over 50 mg of Pt-Au(0.5)@Ca-LTA during the catalytic test. Pre-treatment: 18% H_2/He, 55 mL/min, 350°C. Feed: 1000 ppm NO/ArHe, 50 mL/min, 350°C.

7.3.6. Performance of Pt-Au(0.25)@Ca-LTA

As shown in Fig. 4.7.8, the sample showed a high initial NO conversion of 45% after the NO flow stabilized. Then, the conversion continuously dropped till full deactivation after 45 min. During the test, the sample resulted in the conversion of (8951 nmol) of NO while the nominal Pt content in the sample is 2100 nmol. The low amount of the converted NO and the continuous deactivation suggested some true catalytic activity and redox reaction between NO and metallic Pt.

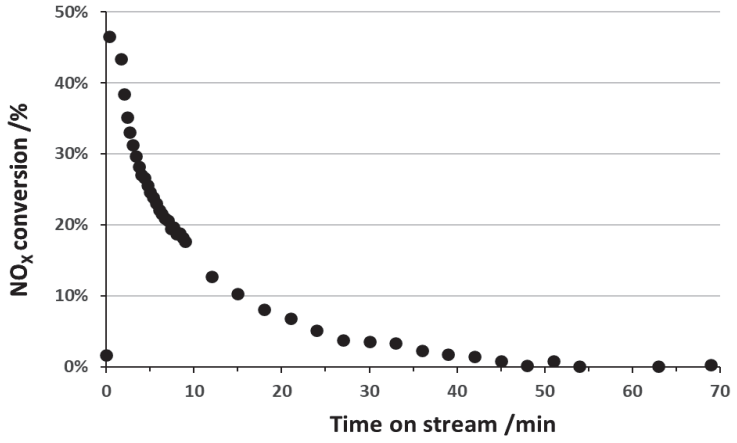

Figure 4.7.8 : The evolution of NO_X conversion over 50 mg of Pt-Au(0.25)/Ca-LTA during the catalytic test. Pre-treatment: 18% H_2/He, 55 mL/min, 350°C. Feed: 1000 ppm NO/ArHe, 50 mL/min, 350°C.

7.3.7. Comparison between all the samples

Fig. 4.7.9 shows the NO_X conversion measured over all the samples. Accordingly, Table 4.7.2 shows the total converted NO (in nmol) over all the samples. In general, the bimetallic samples displayed lower total NO conversions than the monometallic Pt sample in 60 min. Within 60 min, the samples displayed a full deactivation, except for Pt-Au(2)@Ca-LTA. The reason could be that the sample contained some alloyed regions as suggested by the CO adsorption data. The activity of the sample with the Au/Pt molar ratio of 0.5 could be due to several parameters. Among these parameters could be a higher accessibility of the metals or a less poisoning effect by the possible poisons present such as S or Cl. A higher degree of alloying of the metals might not be the reason considering the full deactivation of the sample.

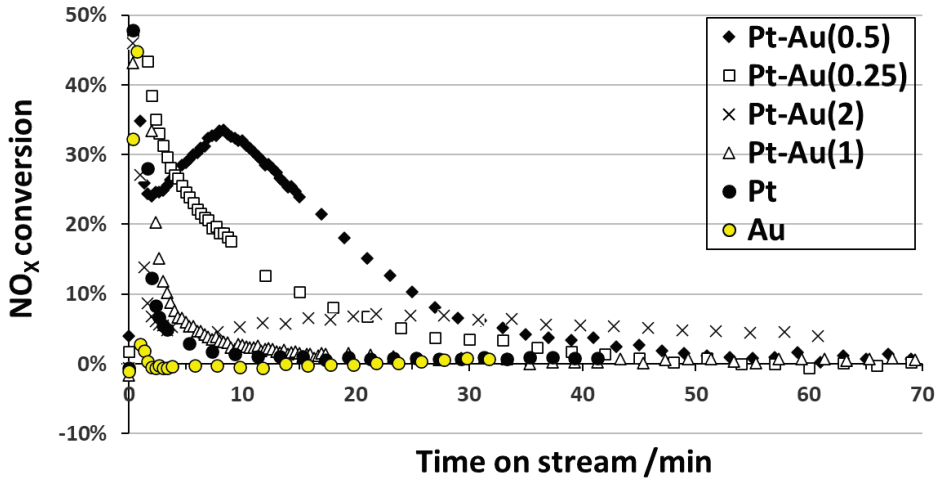

Figure 4.7.9 : The evolution of NO_X conversion all the LTA-based samples. Pre-treatment: 18% H_2/He, 55 mL/min, 350°C. Feed: 1000 ppm NO/ArHe, 50 mL/min, 350°C.

Table 4.7.2 : Total converted NO (in nmol) in 60 min over all the samples as compared to the Pt content and Au/Pt molar ratio in each sample.

Sample	Nominal Au/Pt molar ratio	Actual Au/Pt molar ratio	Pt (nmol)	Converted NO (nmol)	NO/Pt
Au@Ca-LTA	----	----	----	----	----
Pt@Ca-LTA	0	0	641	16541	26
Pt-Au(2)@Ca-LTA	1.9	1.9	461	6607	14
Pt-Au(1)@Ca-LTA	1	n.d.	n.d.	3583	n.d.
Pt-Au(0.5)@Ca-LTA	0.5	n.d.	n.d.	14197	n.d.
Pt-Au(0.25)@Ca-LTA	0.25	n.d.	n.d.	8951	n.d.

The Pt contents in the latter two samples were not significantly different and did not account for the difference in the observed NO conversion. This could suggest a possible inaccessibility of Pt in the bimetallic sample. Moreover, the dilution of Pt by the excess Au (according to the CO adsorption data) could also contribute to the activity loss, since NO decomposition could proceed via the NO dimer formation as reported [32][33]. However, the deactivation behavior observed over both samples could refer to a redox reaction between NO and metallic Pt, in addition to some true catalytic activity.

For the other bimetallic samples, the full deactivation could be due the poisoning of Pt. The poisoning could be due to the formed oxygen, which could compete with NO for adsorption sites or even lead to the oxidation of Pt i.e. a mere redox reaction between NO and metallic Pt. Another possibility could be S or Cl if present, that were used during the preparation. In the light of such inactivity, the use of such material is apparently challenging and requires extra precautions and/or treatments so as to avoid the deactivation observed.

Conclusions

The formation of the LTA structure was successful as evidenced by XRD. TEM showed the presence of well dispersed nanoparticles of the order of 2-3 nm in diameter. The samples displayed a successful encapsulation of the metals; yet, the encapsulation was incomplete. The post-preparation treatments were not successful at removing S and Cl used during the preparation.

All samples displayed the CO adsorption on -OH groups and/or Ca^{2+} ions of the basic LTA support. Pt adsorbed CO mostly linearly, in addition to some bridge adsorption. The Au sample displayed a linear CO adsorption on Au atoms. The bimetallic sample Pt-Au(2)@Ca-LTA displayed all adsorption bands observed with the two monometallic samples and the LTA support. Compared to the monometallic Pt sample, the bimetallic sample featured the dilution of Pt by the excess Au. Some CO_2 was formed over the metals possibly via Boudouard reaction or WGS.

All the samples displayed deactivation under NO at 350°C, possibly due to the oxidation of Pt by NO or due to the observed residual S and Cl. The bimetallic samples displayed lower total NO conversions than the monometallic Pt sample. Apparently, the presence of Au did not enhance the activity in the bimetallic samples. The catalysts may also undergo the inaccessibility of Pt, or the pore blockage due to the possible presence of adsorbed carbonates or nitrates.

References

[1] M. Iwamoto, H. Yahiro, K. Tanda, N. Mizuno, Y. Mine, and S. Kagawa, "Removal of nitrogen monoxide through a novel catalytic process. 1. Decomposition on excessively copper ion exchanged ZSM-5 zeolites," *J. Phys. Chem.*, vol. 95, no. 9, pp. 3727–3730, 1991, doi: 10.1021/j100162a053.

[2] T. Curtin, P. Grange, and B. Delmon, "The direct decomposition of nitrogen monoxide," *Catal. Today*, vol. 35, no. 1–2, pp. 121–127, 1997, doi: 10.1016/S0920-5861(96)00138-1.

[3] P. Yang, J. Zhou, and Z. Wang, "Direct decomposition of NO into N2 and O2 over Cu /ZSM-5 containing Ce and Zr as promoter," *Adv. Mater. Res.*, vol. 113–116, pp. 1735–1739, 2010, doi: 10.4028/www.scientific.net/AMR.113-116.1735.

[4] G. Spoto *et al.*, "Cu(I)-ZSM-5 zeolites prepared by reaction of H-ZSM-5 with gaseous CuCl: Spectroscopic characterization and reactivity towards carbon monoxide and nitric oxide," *Appl. Catal. B, Environ.*, vol. 3, no. 2–3, pp. 151–172, 1994, doi: 10.1016/0926-3373(93)E0032-7.

[5] Y. Wang, F. F. Ren, D. H. Pan, and J. H. Ma, "A hierarchically micro-meso-macroporous zeolite caa for methanol conversion to dimethyl ether," *Crystals*, vol. 6, no. 11, pp. 1–10, 2016, doi: 10.3390/cryst6110155.

[6] T. Otto, J. M. Ramallo-López, L. J. Giovanetti, F. G. Requejo, S. I. Zones, and E. Iglesia, "Synthesis of stable monodisperse AuPd, AuPt, and PdPt bimetallic clusters encapsulated within LTA-zeolites," *J. Catal.*, vol. 342, pp. 125–137, 2016, doi: 10.1016/j.jcat.2016.07.017.

[7] I. Friberg, A. Wang, and L. Olsson, "Hydrothermal aging of pd/LTA monolithic catalyst for complete CH4 oxidation," *Catalysts*, vol. 10, no. 5, 2020, doi: 10.3390/catal10050517.

[8] T. Ryu, Y. Kang, I. S. Nam, and S. B. Hong, "Iron-exchanged high-silica LTA zeolites as hydrothermally stable NH3-SCR catalysts," *React. Chem. Eng.*, vol. 4, no. 6, pp. 1050–1058, 2019, doi: 10.1039/c9re00007k.

[9] R. K. Parsapur and P. Selvam, "Rational design, synthesis, characterization and catalytic properties of high-quality low-silica hierarchical FAU- and LTA-type zeolites," *Sci. Rep.*, vol. 8, no. 1, pp. 1–13, 2018, doi: 10.1038/s41598-018-34479-4.

[10] A. A. Tsyganenko, E. V. Kondratieva, V. S. Yanko, and P. Y. Storozhev, "FTIR study of CO adsorption on basic zeolites," *J. Mater. Chem.*, vol. 16, no. 24, pp. 2358–2363, 2006, doi: 10.1039/b514752b.

[11] I. Voleská, P. Nachtigall, E. Ivanova, K. Hadjiivanov, and R. Bulánek, "Theoretical and experimental study of CO adsorption on Ca-FER zeolite," *Catal. Today*, vol. 243, no. C, pp. 53–61, 2015, doi: 10.1016/j.cattod.2014.07.029.

[12] K. Hadjiivanov and H. Knözinger, "Formation of Ca2+(CO)3 complexes during low-temperature CO adsorption on CaNaY zeolite," *J. Phys. Chem. B*, vol. 105, no. 20, pp. 4531–4534, 2001, doi: 10.1021/jp004248m.

[13] K. Ding *et al.*, "Identification of active sites in CO oxidation and water-gas shift over supported Pt catalysts," *Science (80-.).*, vol. 350, no. 6257, pp. 189–192, 2015, doi: 10.1126/science.aac6368.

[14] J. Raskó, "CO-induced surface structural changes of Pt on oxide-supported Pt catalysts studied by DRIFTS," *J. Catal.*, vol. 217, no. 2, pp. 478–486, 2003, doi: 10.1016/S0021-9517(03)00147-7.

[15] A. Bourane and D. Bianchi, "Heats of adsorption of the linear CO species on Pt/Al2O 3 using infrared spectroscopy: Impact of the Pt dispersion," *J. Catal.*, vol. 218, no. 2, pp. 447–452, 2003, doi: 10.1016/S0021-9517(02)00183-5.

[16] P. T. Fanson, W. N. Delgass, and J. Lauterbach, "Island formation during kinetic rate oscillations in the oxidation of CO over Pt/SiO2: A transient Fourier transform infrared spectrometry study," *J. Catal.*, vol. 204, no. 1, pp. 35–52, 2001, doi: 10.1006/jcat.2001.3369.

[17] A. Bourane, O. Dulaurent, and D. Bianchi, "Heats of adsorption of linear and multibound adsorbed CO species on a Pt/Al2O3 catalyst using in situ infrared spectroscopy under adsorption equilibrium," *J. Catal.*, vol. 196, no. 1, pp. 115–125, 2000, doi: 10.1006/jcat.2000.3030.

[18] A. Bourane, O. Dulaurent, K. Chandes, and D. Bianchi, "Heats of adsorption of the linear CO species on a Pt/Al2O3 catalyst using FTIR spectroscopy: Comparison between TPD and adsorption equilibrium procedures," *Appl. Catal. A Gen.*, vol. 214, no. 2, pp. 193–202, 2001, doi: 10.1016/S0926-860X(01)00483-5.

[19] P. S. F. Mendes, G. Lapisardi, C. Bouchy, M. Rivallan, J. M. Silva, and M. F. Ribeiro, "Hydrogenating activity of Pt / zeolite catalysts focusing acid support and metal dispersion influence," *"Applied Catal. A, Gen.*, vol. 504, pp. 17–28, 2015, doi: 10.1016/j.apcata.2015.03.027.

[20] H. Daly, A. Goguet, C. Hardacre, F. C. Meunier, R. Pilasombat, and D. Thompsett, "The effect of reaction conditions on the stability of Au / CeZrO 4 catalysts in the low-temperature water – gas shift reaction," *J. Catal.*, vol. 273, no. 2, pp. 257–265, 2010, doi: 10.1016/j.jcat.2010.05.021.

[21] M. Mihaylov, H. Knözinger, K. Hadjiivanov, B. C. Gates, and J. Weitkamp, "Characterization of the Oxidation States of Supported Gold Species by IR Spectroscopy of Adsorbed CO," *Chemie Ing. Tech.*, vol. 79, no. 6, pp. 795–806, 2007, doi: 10.1002/cite.200700029.

[22] Y. Jugnet, F. J. C. S. Aires, C. Deranlot, L. Piccolo, and J. C. Bertolini, "Surface Science Letters CO chemisorption on Au (1 1 0) investigated under elevated pressures by polarized reflection absorption infrared

spectroscopy and scanning tunneling microscopy," *Surf. Sci.*, vol. 521, no. 1–2, pp. L639–L644, 2002.
[23] F. J. Cadete Santos Aires, C. Deranlot, Y. Jugnet, L. Piccolo, and J.-C. Bertolini, "METALLIC SURFACES UNDER ELEVATED GAS PRESSURE STUDIED IN SITU BY SCANNING TUNNELING MICROSCOPY: O 2 , H 2 /Au(111); CO/Au(110)," *B. N. Dev (Ed.), Proc. Int. Conf. Phys. Surfaces Interfaces, World Sci. Publ. Singapore*, no. lll, pp. 13–21, 2003, doi: 10.1142/9789812704221_0002.
[24] M. Ruff, S. Frey, B. Gleich, and R. J. Behm, "Au-step atoms as active sites for COadsorption on Au and bimetallic Au/Pd(111) surfaces," *Appl. Phys. A Mater. Sci. Process.*, vol. 66, no. SUPPL. 1, pp. 513–517, 1998, doi: 10.1007/s003390051193.
[25] J. Pischel and A. Pucci, "Low-Temperature Adsorption of Carbon Monoxide on Gold Surfaces: IR Spectroscopy Uncovers Different Adsorption States on Pristine and Rough Au(111)," *J. Phys. Chem. C*, vol. 119, no. 32, pp. 18340–18351, 2015, doi: 10.1021/acs.jpcc.5b05051.
[26] B. J. Keene, "Review of data for the surface tension of pure metals," *Int. Mater. Rev.*, vol. 38, no. 4, pp. 157–192, 1993, doi: 10.1179/imr.1993.38.4.157.
[27] A. Bourane, O. Dulaurent, and D. Bianchi, "Comparison of the coverage of the linear CO species on Pt/Al2O3 measured under adsorption equilibrium conditions by using FTIR and mass spectroscopy," *J. Catal.*, vol. 195, no. 2, pp. 406–411, 2000, doi: 10.1006/jcat.2000.2962.
[28] T. Elgayyar, R. Atwi, A. Tuel, L. Burel, Y. Schuurman, and F. C. Meunier, "Evidencing Pt-Au alloyed domains on supported bimetallic nanoparticles using CO desorption kinetics," *Appl. Catal. A Gen.*, vol. 639, no. April, p. 118643, 2022, doi: 10.1016/j.apcata.2022.118643.
[29] C. J. Heard and D. Hou, "Migration of zeolite-encapsulated Pt and Au under reducing environments," vol. 12, pp. 1598–1609, 2022, doi: 10.1039/d1cy02270a.
[30] F. Garin, "Mechanism of NOx decomposition," *Appl. Catal. A Gen.*, vol. 222, no. 1–2, pp. 183–219, 2001, doi: 10.1016/S0926-860X(01)00827-4.
[31] H. Wise and M. F. Frech, "Kinetics of decomposition of nitric oxide at elevated temperatures. I. Rate measurements in a quartz vessel," *J. Chem. Phys.*, vol. 20, no. 1, pp. 22–24, 1952, doi: 10.1063/1.1700189.
[32] Q. Ge, W. A. Brown, R. K. Sharma, and D. A. King, "NO monomer and (NO)x polymeric chain chemisorption on Pt{110}: Structure and energetics," *J. Chem. Phys.*, vol. 110, no. 24, pp. 12082–12088, 1999, doi: 10.1063/1.479143.
[33] T. Ishihara *et al.*, "Direct decomposition of NO into N2 and O2 over La(Ba)Mn(In)O3 perovskite oxide," *J. Catal.*, vol. 220, no. 1, pp. 104–114, 2003, doi: 10.1016/S0021-9517(03)00265-3.

Chapter 5. Alumina-supported Pt-Au nanoparticles

1. Introduction

Various groups have already reported promoted/modified reactivities of metal nanoparticle catalysts while alloying the active metal with Au. For instance, an enhanced oxidation resistance was reported over Pt-Au [1] and Pd-Au nanoalloy catalysts [2][3]. Also, a synergistic effect was observed over Pd-Au and Cu-Au/TiO_2 used for glucose oxidation [4]. Alloying Pd with Au also modified the CO adsorption on Pd [5][6]. Hence, A similar effect would be expected with Pt.

The characterization by CO adsorption can give information about the structure of the catalyst, the oxidation state of the metal(s), and alloying. Monitoring CO desorption could also be informative about the potential alloying state in bimetallic catalysts since CO should desorb differently from alloyed and pure metal surfaces. Several groups studied CO adsorption behavior over Pt-Au catalysts [7][8][9][10][11] and other Pt-based catalysts [12][13][14][15]. The authors [9] reported modified CO adsorption and desorption patterns over bimetallic Pt-Au samples compared to the monometallic Pt sample but there was no clear evidence of alloying. Therefore, the effect of alloying Pt with Au on the CO adsorption on Pt is still unclear.

The formation of alloyed PtAu nanoparticles is challenging due to the large miscibility gap existing between these metals [16]. However, at the nanoscale, a better miscibility could be expected. Several methods can be used for the preparation of supported bimetallic nanoparticles such as co-impregnation [17], successive wet impregnation [5] and the surface redox method [18].

This chapter aims at characterizing γ-Al_2O_3-supported Au, Pt and Pt-Au nanoparticles using CO adsorption/desorption by DRIFTS. This work investigates the effect of alloying Pt with Au in the bimetallic samples on the CO adsorption and desorption behaviors as compared to the monometallic Pt and Au samples, as a tool of characterizing bimetallic nanoparticles. This characterization technique could be useful since the other characterization techniques also display limitations.

Three γ-Al_2O_3-supported samples are investigated in this report. The three samples include two monometallic Au and Pt samples and two Pt-Au bimetallic samples. My colleague Ranin ATWI had prepared the samples and performed their characterization by the ICP elemental analysis, TEM-EDX and PXRD [19] and these results are briefly recalled here (Section 2) for the sake of completeness. Ranin ATWI also tested the samples for the deNO_X activity and these were inactive.

2. Sample characterizations

2.1. ICP elemental analysis

Table 5.2.1 shows the elemental analysis of the three γ-Al_2O_3-supported samples. The actual loading of Pt in the monometallic samples (1.3 wt.%) is lower than the target loading (2 wt.%). The reason could be an improper impregnation.

Table 5.2.1 : ICP elemental analysis results of the Al_2O_3-supported Au, Pt and Pt-Au samples. [19]

Sample code	**Measured loading (wt. %)**		**Au/Pt atomic ratio**
	Au	Pt	
Pt(1.3)	----	1.3	0
Au(2)	2.13	----	----
Pt(2)Au(0.3)	0.3	2.1	0.14

2.2. TEM-EDX analysis

2.2.1. The monometallic samples

Fig. 5.2.1 shows the TEM images and the corresponding particles size distributions of the monometallic Pt(1.3) and Au(2) samples. Au(2) displayed a narrow particle size distribution (up to 7 nm) with a d_{SW} of 3.9 nm and a dispersion of 35%. Pt(1.3) displayed a wider particle size distribution (up to 14 nm) corresponding to a higher d_{SW} of 7.1 nm and a dispersion of 20%.

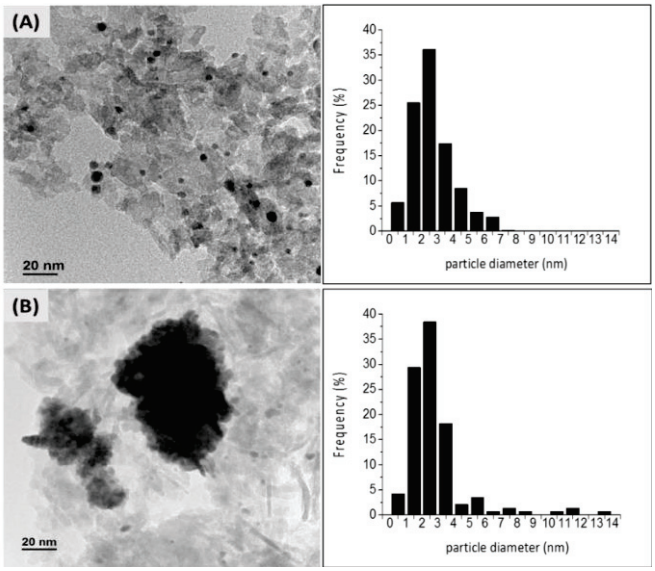

Figure 5.2.1 : TEM images of (A) Au(2), (B) Pt(1.3) and their particle size distributions. [19]

2.2.2. Pt(2)Au(0.3)

Fig. 5.2.2 shows the TEM images and the corresponding particles size distributions of Pt(2)Au(0.3). The sample displayed a narrow particle size distribution (up to 6 nm) with a d_{SW} of 3.4 nm and a dispersion of 38%.

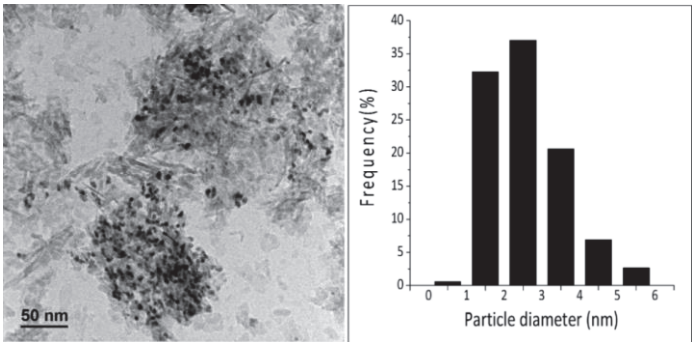

Figure 5.2.2 : TEM image and the corresponding particle size distribution of Pt(2)Au(0.3). [19]

Fig. 5.2.3 shows the EDX analysis collected over several particles of the sample. Most particles displayed the presence of both metals indicating a successful alloying. The average Au/Pt atomic ratio shown by the EDX analysis (0.13) was in agreement with the ICP analysis result (0.14).

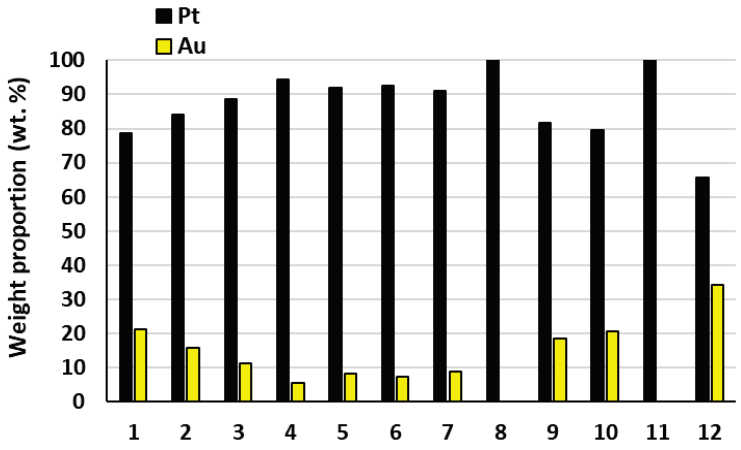

Figure 5.2.3 : EDX analysis over several particles of Pt(2)Au(0.3). [19]

2.2.3. Comparing between all the three samples

Pt(1.3) displayed a wide particle size distribution and the highest d_{SW}, while the Au-containing samples displayed smaller particles and narrower size distributions. Table 5.2.2 shows the particle sizes and metal dispersions of all samples.

Table 5.2.2 : Particle size distributions of the Al_2O_3-supported Au, Pt and Pt-Au samples. [19]

Sample code	Au/Pt atomic ratio	TEM particle size (nm)[a]	Metal dispersion (%)[b]
Pt(1.3)	0	7.3 ± 3	20
Au(2)	----	3.9 ± 1	35
Pt(2)Au(0.3)	0.14	3.4 ± 1	38

[a] Surface-weighted mean diameter (incertitude based on the standard deviation of the distribution-200 nanoparticles counted).

[b] Metal dispersion is estimated using a cuboctahedral model and a calculation method according to Van Hardeveld and Hartog [20].

2.3. PXRD analysis

Fig. 5.2.4 shows the PXRD patterns of the three samples, accompanied with the PDF reference files of metallic Au and Pt. The figure focuses on the range of (2θ = 34-43°) where the 111 peak is located. The monometallic samples displayed peaks perfectly matching with the corresponding reference files. The bimetallic sample displayed a peak in between the expected positions of Au and Pt indicating the presence of an alloyed phase which is Pd-rich. Using Vegard's law, the approximate alloy composition corresponded to $Au_{0.13}Pt_{0.87}$ i.e. with a Au/Pt atomic ratio of 0.15. This value matches perfectly with the actual value of 0.14 obtained from the ICP-OES analysis. The average crystallite size of Pt was 7.5 nm and for Au was 3.2 nm, which are in a good agreement with the TEM particle sizes (7.3 and 3.9 nm, respectively) mentioned in table 5.2.2.

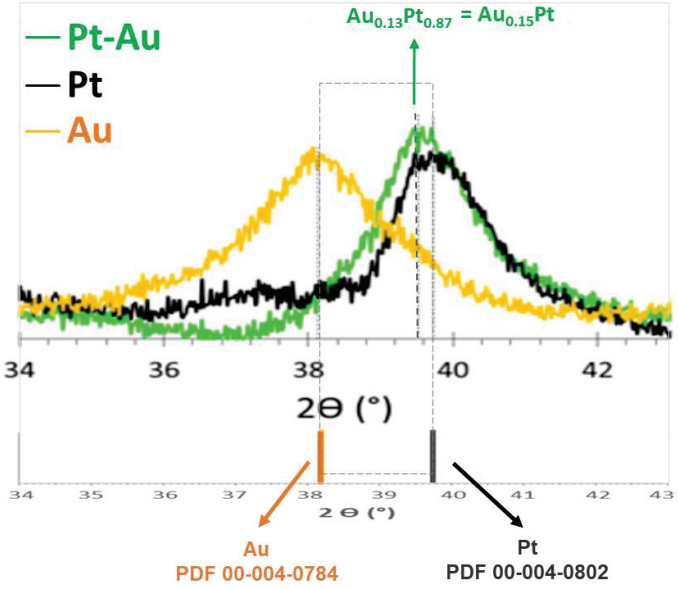

Figure 5.2.4 : PXRD analysis of the three alumina-based samples. [19]

3. CO adsorption by DRIFTS

3.1. Spectra collected before CO adsorption

Fig. 5.3.1 and 5.3.2 show the spectra collected over the three samples with respect to the KBr background before and after the pre-reduction, respectively. Before reduction, the spectra were quite similar. The spectra displayed the Al-O vibrations bands (below 1160 cm^{-1}) due to the alumina framework vibrations. The spectra also showed the presence of adsorbed water (the bands at 2105 and 1650 cm^{-1}) and the resulting large H-bonding band (at 3580 cm^{-1}). The bands at (1340-1650 cm^{-1}) were assigned to adsorbed carbonates [21] that could form due to the exposure to the ambient CO_2 during storage. These bands were pronounced the most in the case of Pt(2)Au(0.3).

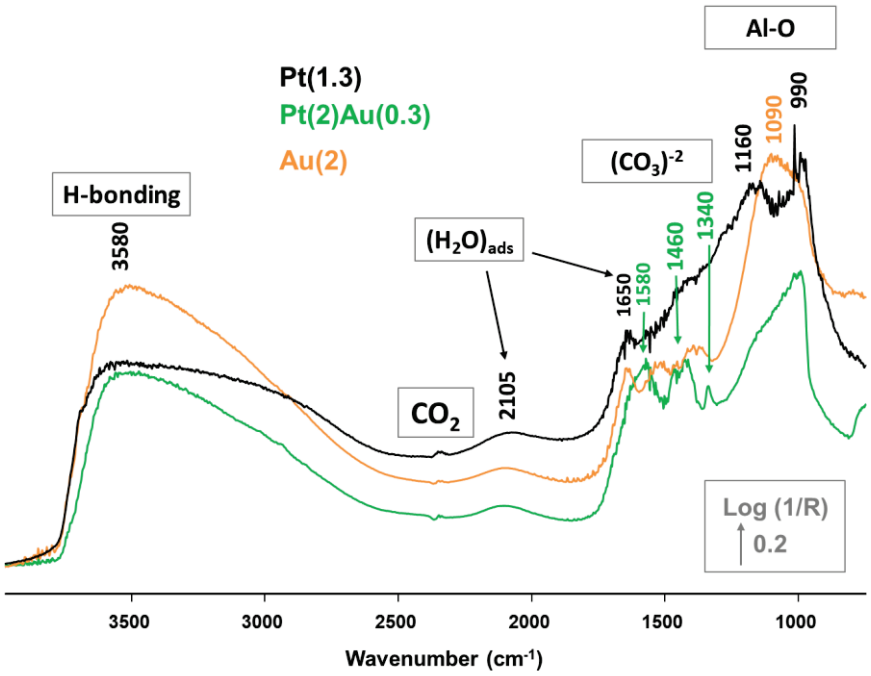

Figure 5.3.1 : Spectra collected at room temperature before reduction over the four samples with respect to KBr background.

The reduction pre-treatment in H_2 at 300°C induced significant changes to the spectra. The bands due to the adsorbed carbonate species became more pronounced especially in the case of Pt(2)Au(0.3). The bands due to the adsorbed water were eliminated due to heating at 300°C. Moreover, the H-bonding band (at 3580 cm^{-1}) became of a lower intensity and the bands due to Al-OH groups (at 3730 and 3680 cm^{-1}) became more pronounced. Interestingly, a new band was observed at 2085 cm^{-1} corresponding to CO adsorbed on Pt in the case of Pt(1.3) and Pt(2)Au(0.3) and not in the case of the the Au sample. This could be due to a partial reduction of the adsorbed carbonates by H_2 leading to the formation and adsorption of CO on Pt. This reaction might not be promoted by an excess Au. The

reaction of H_2 with carbonates to form hydrocarbonaceous deposits could also explain the bands observed around 3000 cm^{-1} (the stretching frequency of C-H in hydrocarbons).

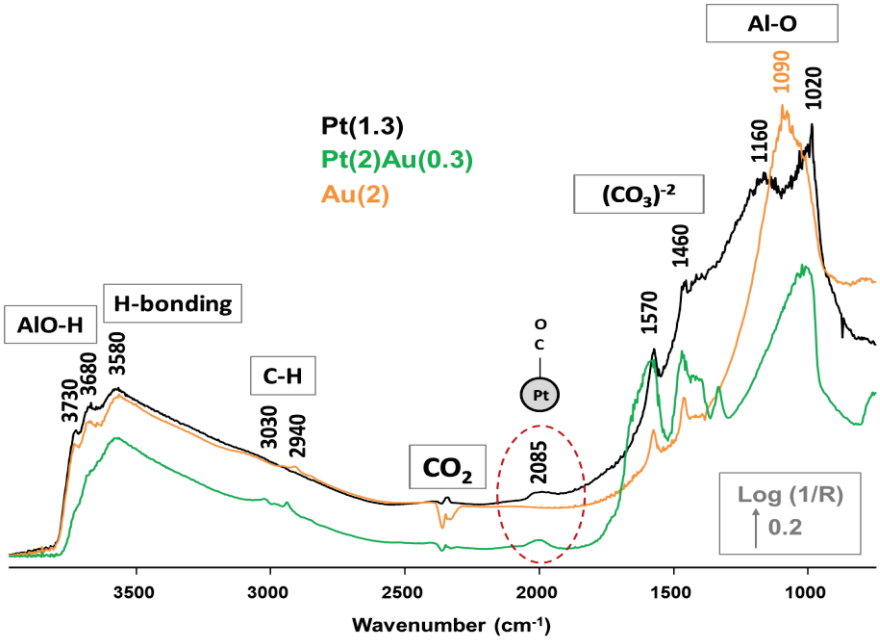

Figure 5.3.2 : Spectra collected after cooling to 50°C after the pre-reduction in H_2 at 300°C over the four samples with respect to KBr background.

3.2. CO adsorption/desorption spectra

3.2.1. Pt(1.3)

Fig. 5.3.3 and 5.3.4 show the CO adsorption profile on the monometallic Pt sample. Two major adsorption bands were observed:

(i) The linearly adsorbed CO [22][23][24][25] (referred to as Pt L-CO) observed as two overlapping bands at 2082 and 2050 cm^{-1}. The band at 2082 cm^{-1} could be assigned to the linear CO adsorption on high coordination sites (essentially large Pt nanoparticles [24][25]). The band at 2050 cm^{-1} could be assigned to the linear CO adsorption on kinks [23], corners [22] or low coordination sites (essentially small Pt clusters [24][25] corresponding to a high metal dispersion [26]). As reported [24][25], small Pt particles display a red shift in the linear adsorption band as compared to the larger particles. This could be explained based on the increased metal back bonding with the CO $2\pi^*$ orbital for smaller particles [27].

(ii) The bridge adsorbed CO [23][24][25] (referred to as Pt B-CO) observed as two overlapping bands at 1847 and 1793 cm^{-1}. The presence of the overlapping adsorption bands indicated a distribution of particle sizes.

The minor band at 1650 cm^{-1} could be due to adsorbed carbonates or water, most likely carbonate-type species because the intensity of hydroxyl bands in the region 3800-3000 cm^{-1} remained negligible. All bands almost stabilized after 5 min under CO.

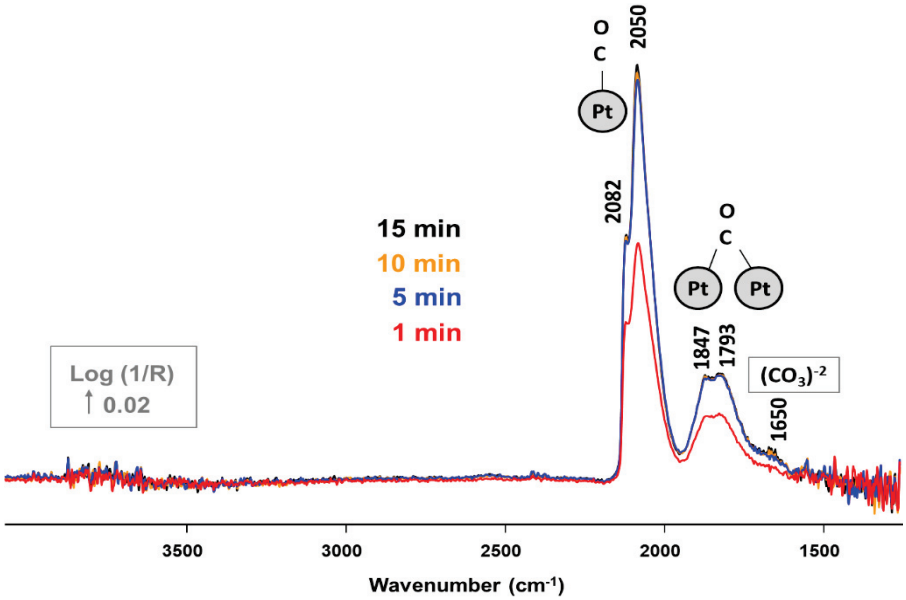

Figure 5.3.3 : The evolution of the CO adsorption profile over Pt(1.3) after introducing CO. Feed: 1% CO/He, 50 mL/min, 50°C.

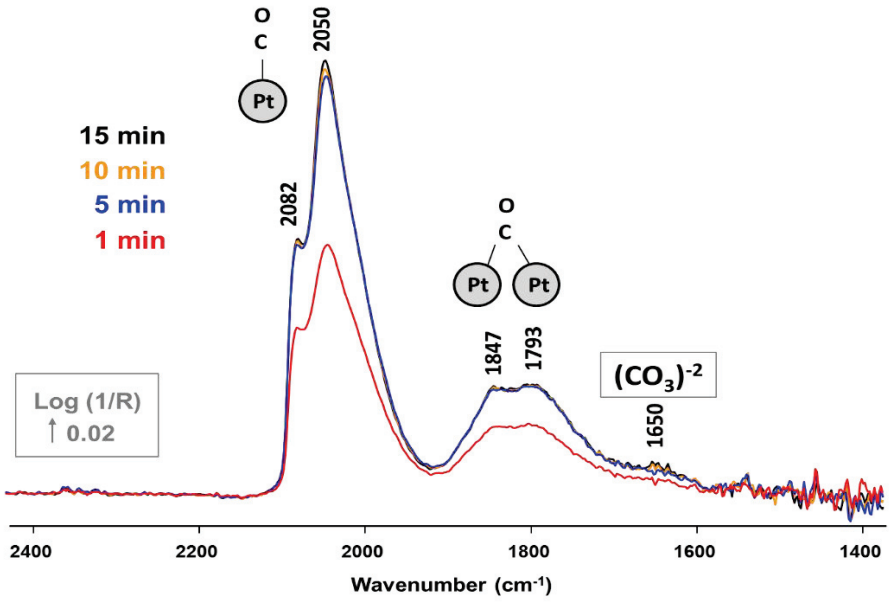

Figure 5.3.4 : The evolution of the CO adsorption profile over Pt(1.3) (1400-2400 cm^{-1}). Feed: 1% CO/He, 50 mL/min, 50°C.

The CO adsorption profile was mainly linear as also observed earlier [28] and could be due to the much stronger adsorption compared to the bridge adsorption mode. The heat of the linear CO

adsorption on Pt is 206-115 kJ/mol at θ = 0-1 [28][29] or 220-106 kJ/mol at θ = 0-1 [24] which is much higher than the heat of bridge CO adsorption on Pt of 94-45 kJ/mol at θ = 0-1 [28][29]. Moreover, the band at 2050 cm^{-1} was significantly larger than that at 2082 cm^{-1} indicating an abundance of small Pt prticles. This is consistent with the TEM analysis where the particle sizes were mostly 1-4 nm with few large particles up to 14 nm (Fig. 5.2.1 B).

Fig. 5.3.5 monitors the CO desorption spectra over the Pt sample after stopping CO.
Pt B-CO displayed continuous decay, red shift and band area decrease. Pt B-CO desorbed rather fast due to its low heat of adsorption as explained before. The band initially desorbed rapidly and reached 0.65 times its initial band area within 1 h before a slower desorption was attained for 4 h more. The intensity of the band at 1650 cm^{-1} decreased slightly for 10 min possibly due to the desorption of adsorbed water before it became stable for 5 h.

Pt L-CO displayed a continuous decrease in the intensity along with a continuous red shift. The overall effect was a slight increase in the band area few min after stopping CO, which then remained stable for 5 h (Fig. 5.3.6). This could indicate that some linearly adsorbed CO were modified by surface migration or desorption/re-adsorption on different sites or due to less dipole interactions following the desorption of most bridged species.

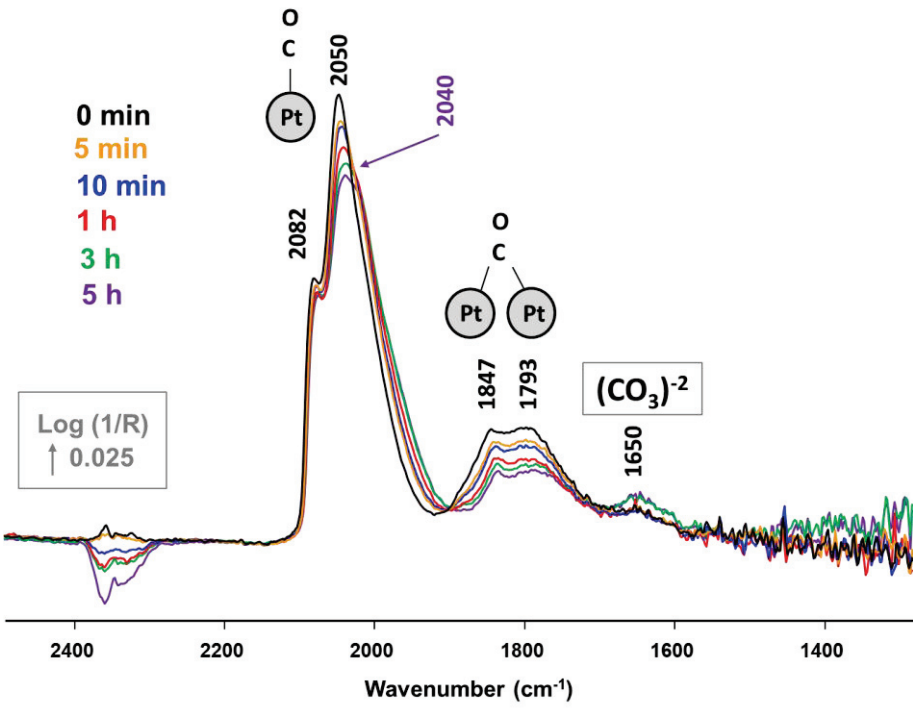

Figure 5.3.5 : The evolution of CO adsorption profile over Pt(1.3) with time after stopping CO. Feed: He, 100 mL/min, 50°C. The sample was previously left under O for 15 min.

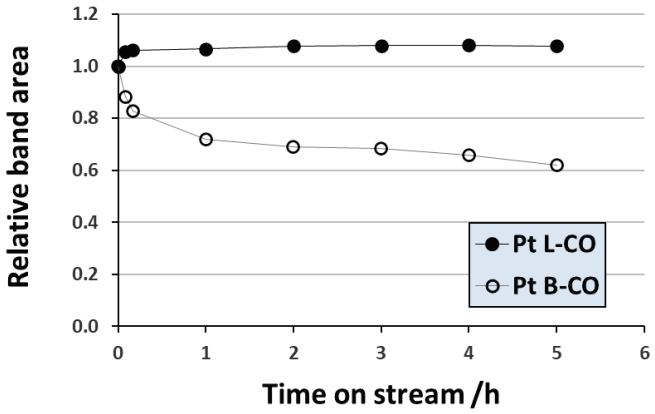

Figure 5.3.6 : The change in the relative band area during the desorption time of the two CO adsorption bands on Pt after stopping CO over the Pt(1.3) sample: linear adsorption (Pt L-CO) and bridge adsorption (Pt B-CO). Feed: He, 100 mL/min, 50°C.

3.2.2. Au(2)

Fig. 5.3.7 and 5.3.8 monitor the evolution of the adsorption spectra over the Au sample.

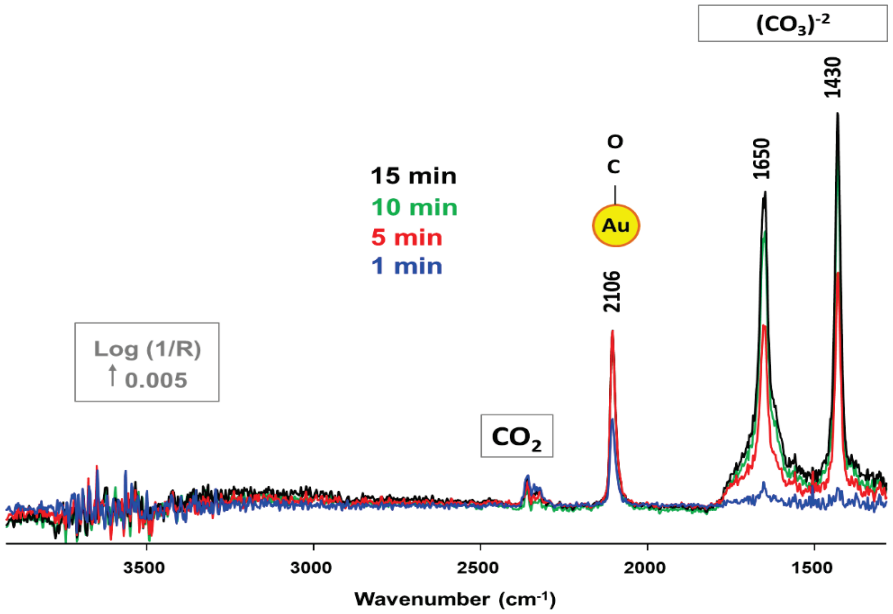

Figure 5.3.7 : The evolution of the CO adsorption profile over Au(2) after introduciong CO. Feed: 1% CO/He, 50°C, 50 mL/min.

Three major adsorption bands were observed: (i) at 2106 cm^{-1} corresponding to CO adsorbed linearly on metallic Au (referred to as Au L-CO) [5][30][31][32][33], (ii) at 1650 cm^{-1} and (iii) at 1430 cm^{-1} corresponding to adsorbed carbonates. Au L-CO stabilized rapidly within 5 min under CO whereas the formation of carbonate continued. The significant formation of carbonates could proceed via several steps of side reactions such as the WGS ($CO + H_2O \rightarrow H_2 + CO_2$) due to water traces or the

dissociation of CO via Boudouard reaction (2 CO → C + CO_2). The dissociation of CO on Au(110) was previously reported [34][30]. It is important to stress that carbonate formation was not observed in the case of the Pt sample, showing that those observed in the case of Au were not due to the presence of CO_2 impurities.

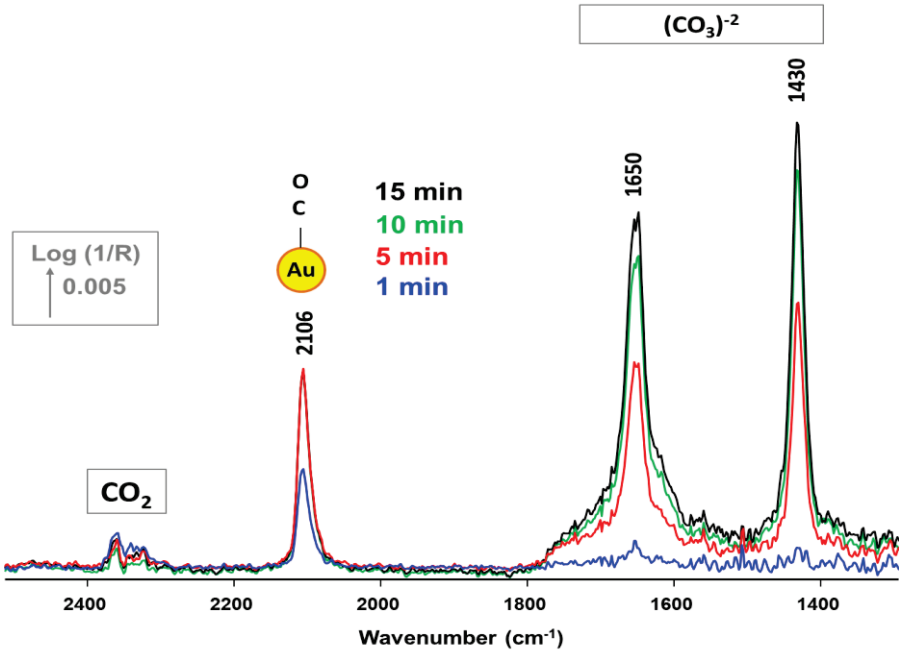

Figure 5.3.8 : The evolution of the CO adsorption profile over Au(2) after introduciong CO) (1300-2500 cm^{-1}). Feed: 1% CO/He, 50 mL/min, 50°C.

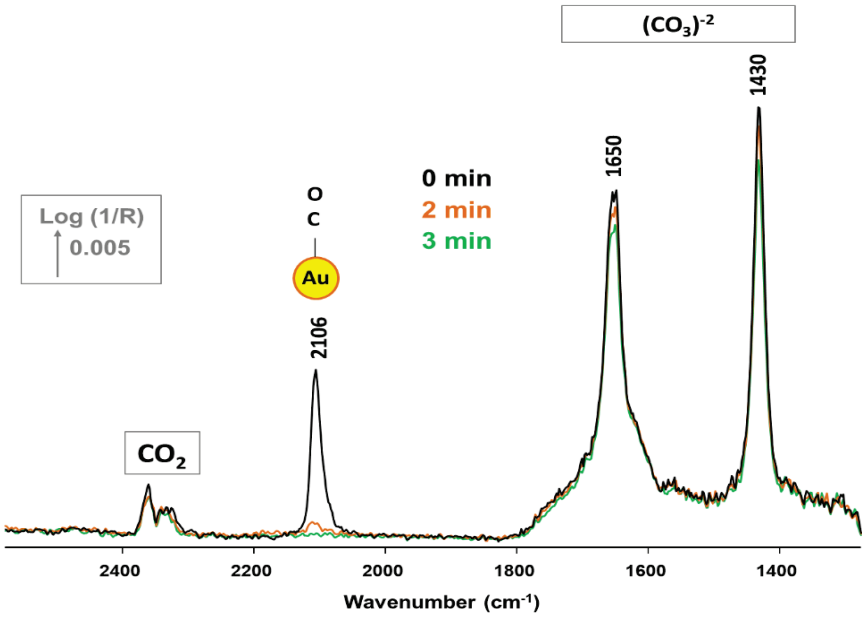

Figure 5.3.9 : The evolution of the CO adsorption profile over Au(2) with tile after stopping CO. The sample was previously left under CO for 15 min. Feed: He, 100 mL/min, 50°C.

Fig. 5.3.9 shows the CO desorption spectra over the Au sample after stopping CO. The Au L-CO band takes ~3 min till full desorption. CO adsorption on Au is rather weak and features low heats of adsorption of 43-62 kJ/mol at θ = 1-0 [35] or 47-74 kJ/mol at θ = 1-0 [36]. The bands of adsorbed carbonates showed a slight decrease in intensity.

3.2.3. Pt(2)Au(0.3)

Fig. 5.3.10 and 5.3.11 show the evolution of the adsorption profile over Pt(2)Au(0.3). Three adsorption bands were observed: (i) the minor band / shoulder at 2106 cm^{-1} assigned to Au L-CO, (ii) the band at 2068 cm^{-1} corresponding to Pt L-CO [23][22] , and (iii) the band at 1836 cm^{-1} assigned to Pt B-CO. Au L-CO and Pt B-CO stabilized within 2 min under CO, whereas Pt L-CO stabilized after 10 min. This could partly be due to Pt surface segregation as reported earlier [37][38]. No adsorbed carbonates were observed, in contrast to the case of pure Au.

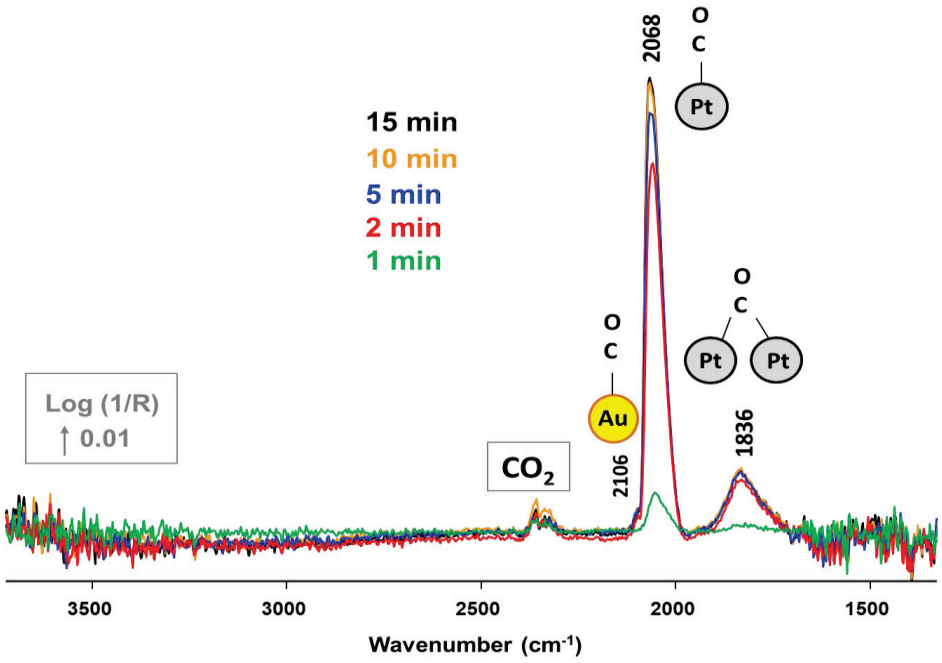

Figure 5.3.10 : The evolution of the CO adsorption profile over Pt(2)Au(0.3) after introducing CO. Feed: 1% CO/He, 50 mL/min, 50°C.

Fig. 5.3.12 and 5.3.13 shows the evolution of the adsorption profile after stopping CO. Au L-CO disappeared after 10 min due to the weak CO adsorption on Au. Pt L-CO and Pt B-CO displayed continuous decay and red shift upon CO desorption with the decay of Pt B-CO being faster. Both bands decayed rapidly for 1 h before a slower decay was maintained for 3 h more. After these 4 h, an abrupt decrease was observed for both bands. After 5 h, Pt B-CO almost disappeared.

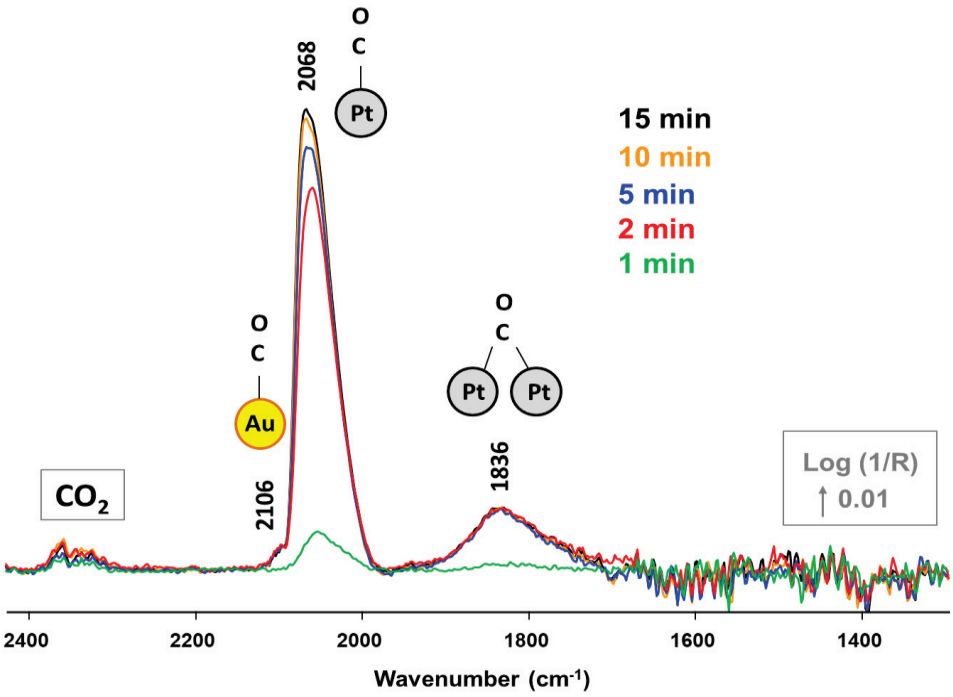

Figure 5.3.11 : The evolution of the CO adsorption profile over Pt(2)Au(0.3) after introducing CO (1300-2400 cm^{-1}). Feed: 1% CO/He, 50 mL/min, 50°C.

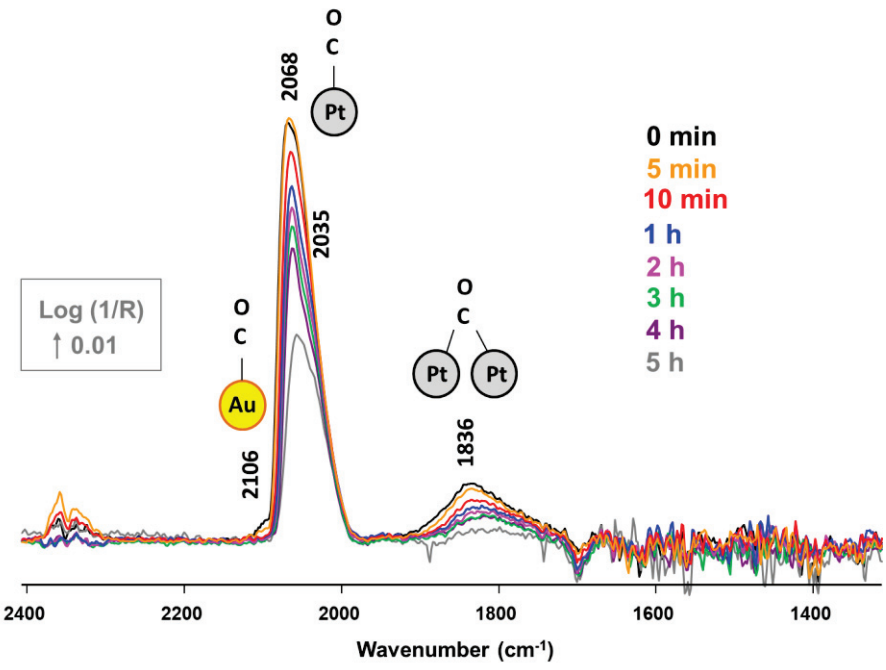

Figure 5.3.12 : The evolution of the CO desorption profile over Pt(2)Au(0.3) after stoppiong CO. The sample was previously left under CO for 15 min. Feed: He, 100 mL/min, 50°C.

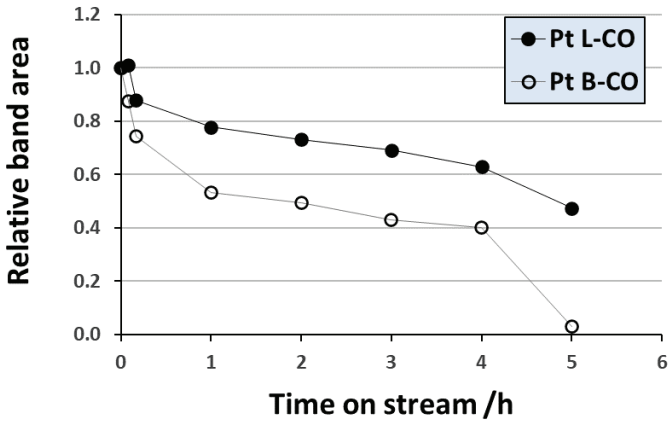

Figure 5.3.13 : The change in the relative band area during the desorption time (in Fig. 5.3.11) of the two CO adsorption bands on Pt after stopping CO over the Pt(2)Au(0.3) sample: linear adsorption (Pt L-CO) and bridge adsorption (Pt B-CO). Feed: He, 100 mL/min, 50°C.

3.2.4. Comparison between all the three samples

Fig. 5.3.14 compares between the final adsorption spectra (15 min under CO) over the three samples. The bimetallic sample displayed a lower band intensity (possibly related to lower optical pathlengths in the samples) and a blue shift of Pt L-CO compared to the monometallic Pt sample. The blue shift could indicate that Au could preferably be located at low coordination sites of the Pt surface in the bimetallic samples. It is also noteworthy that the surface tension of Au (1145 mN/m) is lower than that if Pt (1763 mN/m) [39].

The lower intensity of Pt L-CO in the bimetallic sample (compared to the Pt sample) was not accompanied with a similar increase in Au L-CO. This could not be explained based on the different dispersions of the bimetallic samples since those displayed higher Pt loadings and dispersions than the Pt sample. However, the molar absorption coefficient of Au L-CO could be lower than that of Pt L-CO. Moreover, some Au sites adsorb CO very weakly at room temperature such as the terraces [40][41]. These could also explain the very low Au L-CO in the Au(2) sample.

The bridge CO adsorption seemed more limited in the bimetallic sample, suggesting an efficient dilution of Pt by alloying with Au. Fig. 5.3.15 also shows the ratio between the band area of Pt L-CO and the overall area of the two CO adsorption bands on Pt (linear + bridged) for the three Pt-containing samples. The figure shows an increasing fraction of the linear adsorption mode upon increasing the amount of Au. This demonstrates the dilution of Pt by alloying with Au.

Importantly, the formation of carbonates was apparently only promoted over the Au sample, suggesting that only those promoted the WGS or Boudouard reaction at this low temperature.

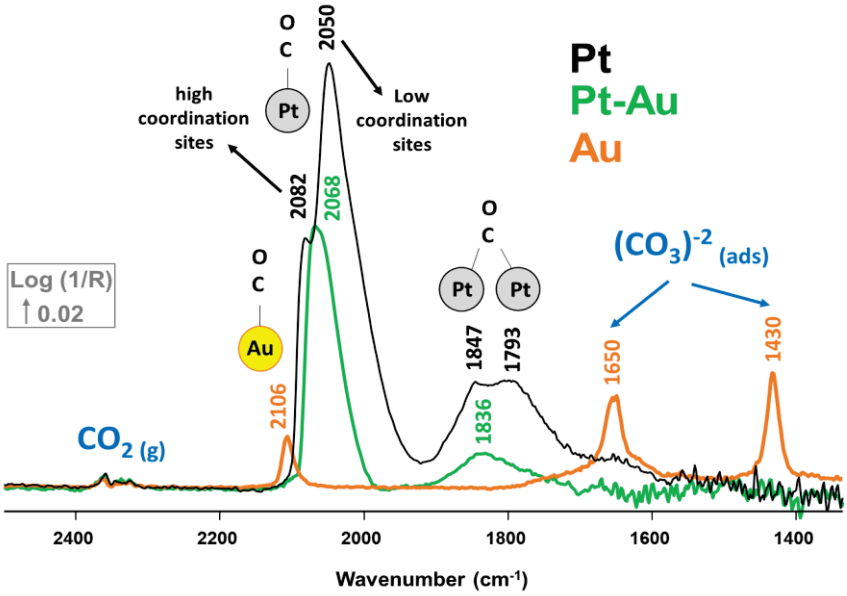

Figure 5.3.14: Final adsorption profiles over the alumina-based samples (15 min under CO). Feed: 1% CO/He, 50 mL/min, 50°C.

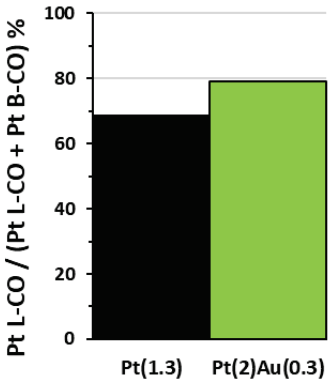

Figure 5.3.15 : The ratio between the band area of the linear CO adsorption on Pt (Pt L-CO) and the overall area of the two CO adsorption bands on Pt for the two Pt-containing samples.

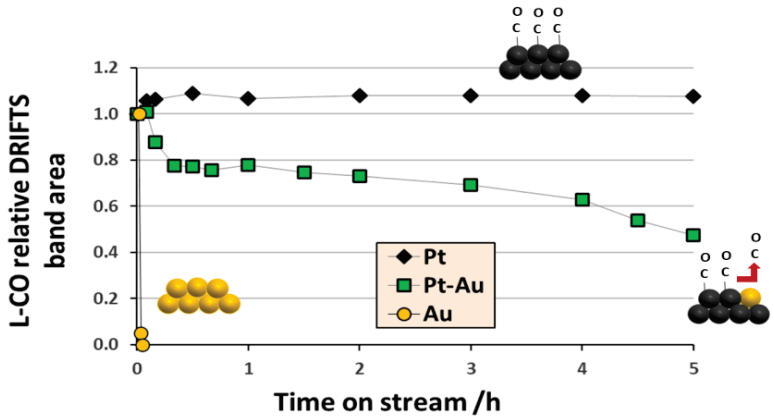

Figure 5. 3.16 : The change in the relative band areas during the desorption time of Pt L-CO on Pt after stopping CO over Pt(1.3) and Pt(2)Au(0.3), and the desorption of Au L-CO over Au(2). Feed: He, 100 mL/min, 50°C.

Fig. 5.3.16 compares between the relative band areas of Pt L-CO during CO desorption over all the three Pt-containing samples; the evolution of Au L-CO in the Au(2) sample is shown for the sake of comparison. Over Pt(2)Au(0.3), Pt L-CO desorbs faster than over the monometallic Pt sample. This could be explained by surface migration of CO from Pt to Au sites, from which facile desorption occurs. Au could also result in a weaker linear adsorption of CO on Pt and facilitate desorption directly from Pt sites. This could be explained based on an electronic effect induced due to alloying Pt with Au. Moreover, the Au surface enrichment was previously observed in Pd_3Au/C nanoparticles while treated under air or Ar at 200°C [42]. Fig. 5.3.17 shows a schematic representation of these three possible explanations.

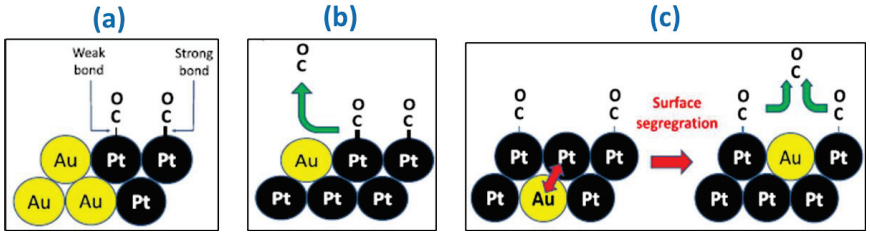

Figure 5.3.17 : Possible explanations of the faster CO desorption over the bimetallic Pt-Au sample: (a) via electronic effect due to alloying Pt with Au, (b) via geometric effect due to CO migration from a Pt atom to the adjacent Au atoms followed by a rapid desorption, or (c) via the surface enrichment with Au under the flow of He. [43]

Fig. 5.3.18 compares the relative band areas of Pt B-CO during CO desorption over Pt(1.3) and Pt(2)Au(0.3). Over the bimetallic sample, Pt B-CO desorbed faster than over the monometallic Pt sample. As concluded from the previous figure, this could be explained based on an electronic effect induced due to alloying Pt with Au, resulting in a weaker bridge adsorption of CO on Pt.

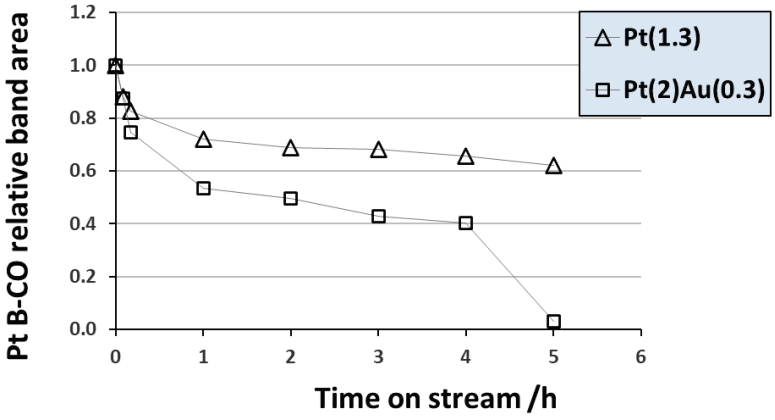

Figure 5.3.18 : The change in the relative band area during the desorption time of the bridge CO adsorption mode on Pt after stopping CO over Pt(1.3) and Pt(2)Au(0.3). Feed: He, 100 mL/min, 50°C.

3.3 Comparison with the Pt-Au@LTA samples

Fig. 5.319, 5.3.20 and 5.3.21 compare the CO adsorption profile over the three alumina-based samples and their LTA-based counterparts after CO exposure for 15 min. In all cases, the signal intensity is different and could be merely due to a different beam pathlength or the different metal loadings and dispersions.

Over the bare support, alumina was not interactive towards CO, whereas LTA displayed linear CO adsorption bands. Moreover, unlike alumina, the LTA support lead to the partial oxidation of the metals, and the formation of CO_2. No carbonates were observed over the LTA-based samples.

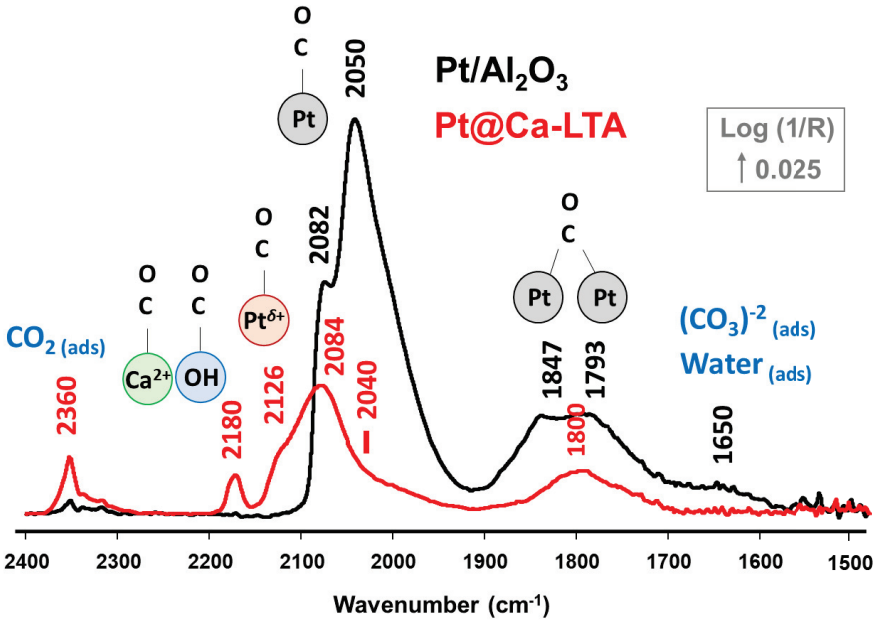

Figure 5.3.19 : CO adsorption profiles over Pt/Al_2O_3 vs. Pt@Ca-LTA (15 min under CO). Feed: 1% CO/He, 50 mL/min, 50°C.

Over the two supports, Pt displayed linear and bridge CO adsorption on metallic Pt (Fig. 5.3.19). Over alumina, the linear adsorption was mainly over the low coordination sites, while over the high coordination sites over LTA. This is probably counterintuitive since the average particle size of Pt/alumina (7.3 nm) is higher than that of Pt@Ca-LTA (1.7 nm). The LTA support probably lead to the formation of oxidized Pt small clusters, leaving only the larger clusters in the metallic state.

The alloying in the bimetallic samples probably was not as efficient over LTA as over alumina. The samples displayed equal loadings of Au (0.3 wt.%) and different loadings of Pt (2.1 wt.% over alumina vs. 0.18 wt.% over LTA). Over LTA (Fig. 5.3.21), the bimetallic sample displayed a lower bridge adsorption, yet a linear adsorption similar to that of the Pt sample. In contrast, over alumina, the bimetallic sample displayed a limited bridge adsorption and blue-shifted linear adsorption

compared to the Pt sample, as a result of the efficient alloying between Au and Pt. As observed over the two monometallic samples, LTA lead to the partial oxidation of Au and Pt.

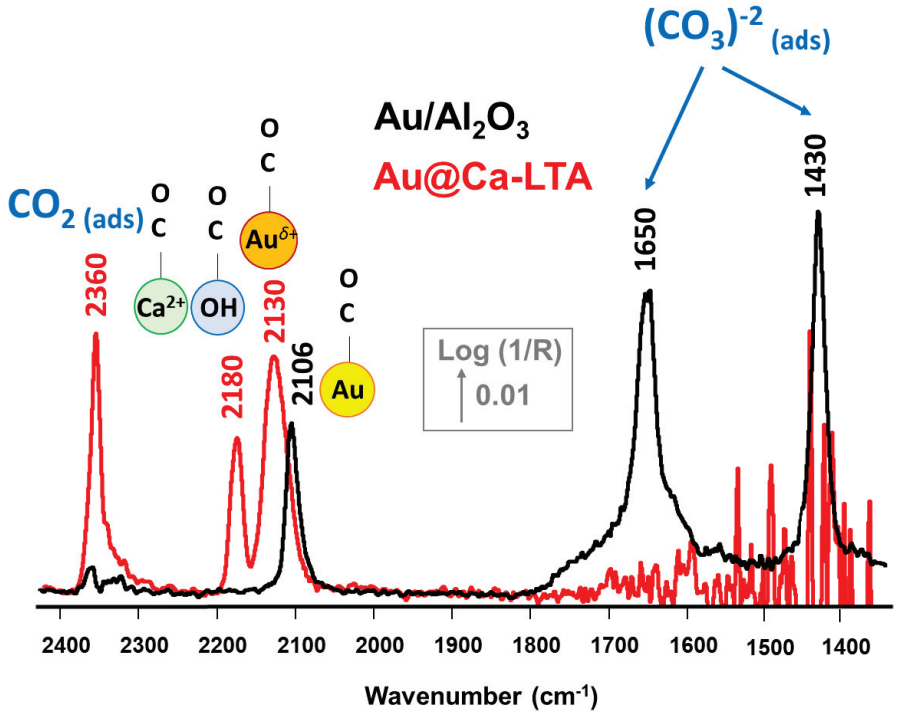

Figure 5.3.20 : CO adsorption profiles over Au/Al_2O_3 vs. Au@Ca-LTA (15 min under CO). Feed: 1% CO/He, 50 mL/min, 50°C.

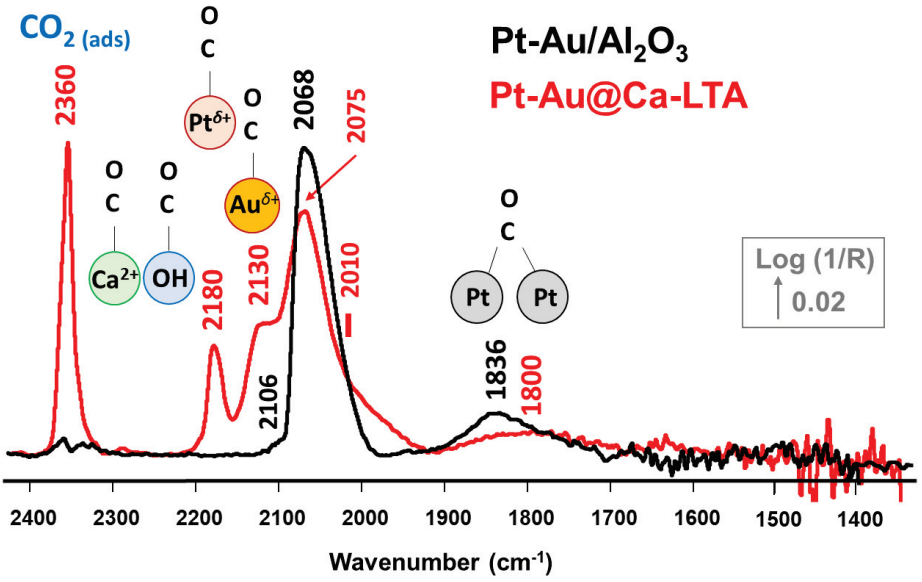

Figure 5.3.21 : CO adsorption profiles over $Pt(2)Au(0.3)/Al_2O_3$ vs. Pt-Au(2)@Ca-LTA (15 min under CO). Feed: 1% CO/He, 50 mL/min, 50°C.

Conclusions

Al_2O_3-supported monometallic Pt and Au samples were prepared using wet impregnation. In addition, a bimetallic Pt-Au samples was prepared by co-impregnation. The samples were characterized by ICP-OES, TEM-EDX, and CO adsorption by DRIFTS.

TEM analysis indicated the formation of mostly small particles in all samples. The Pt sample displayed few large particles possibly due to an imperfect impregnation. TEM-EDX analysis indicated the presence of alloyed regions of the metals in the bimetallic samples.

Pt displayed a high tendency towards the linear CO adsorption. TEM analysis and CO adsorption agreed on the abundance of small Pt particles (mostly 1-4 nm). After removing CO from the flow, the L-CO band was stable while the bridge adsorption band displayed a gradual decay. Au displayed a limited linear CO adsorption, and a significant formation of carbonates possibly via Boudouard or WGS reaction. Au L-CO decayed within 3 min after stopping CO.

The bimetallic sample displayed a lower intensity and a blue shift in Pt L-CO. This indicated that Au would preferably be located on low coordination sites of the Pt surface. The sample also displayed a lower bridge adsorption indicating the dilution of Pt by Au. The decay of the CO adsorption bands over Pt(2)Au(0.3) was faster than that observed over the Pt sample. This could indicate a weaker CO adsorption on Pt due to alloying with Au.

The overall conclusion was that the formation of PtAu alloy nanoparticles was successful via the co-impregnation preparation method. Alloying Au with Pt resulted in the dilution of Pt (geometric effect), and a weaker CO adsorption and hence a faster desorption on Pt (electronic effect). This stresses the benefit of using CO adsorption and monitoring desorption kinetics as a means to characterize Au-Pt nanoalloys.

The major difference with the LTA-based samples was that those featured very small nanoparticles (1-2 nm) and displayed the partial oxidation of the metals. Moreover, the bimetallic sample probably did not feature an efficient alloying and did not display such an intermediate CO desorption behavior.

References

[1] A. Morikawa, K. Okumura, M. Ishii, K. Kikuta, A. Suda, and H. Shinjo, "Characterization of termetallic Pt-Ir-Au catalysts for NO decomposition," *Rare Met.*, vol. 30, no. 1, pp. 53–57, Feb. 2011, doi: 10.1007/s12598-011-0196-6.

[2] A. M. Venezia, V. La Parola, V. Nicolì, and G. Deganello, "Effect of gold on the HDS activity of supported palladium catalysts," *J. Catal.*, vol. 212, no. 1, pp. 56–62, 2002, doi: 10.1006/jcat.2002.3778.

[3] T. Elgayyar *et al.*, "Au-Modified Pd catalyst exhibits improved activity and stability for NO direct decomposition," *Catal. Sci. Technol.*, vol. 11, no. 8, pp. 2908–2914, 2021, doi: 10.1039/d1cy00301a.

[4] J. Sha, S. Paul, F. Dumeignil, and R. Wojcieszak, "Au-based bimetallic catalysts: How the synergy between two metals affects their catalytic activity," *RSC Adv.*, vol. 9, no. 51, pp. 29888–29901, 2019, doi: 10.1039/c9ra06001d.

[5] G. X. Pei *et al.*, "Promotional effect of Pd single atoms on Au nanoparticles supported on silica for the selective hydrogenation of acetylene in excess ethylene," *New J. Chem.*, vol. 38, no. 5, pp. 2043–2051, 2014, doi: 10.1039/c3nj01136d.

[6] L. Zhang *et al.*, "Efficient and durable Au alloyed Pd single-atom catalyst for the Ullmann reaction of aryl chlorides in water," *ACS Catal.*, vol. 4, no. 5, pp. 1546–1553, 2014, doi: 10.1021/cs500071c.

[7] D. Mott, J. Luo, A. Smith, P. N. Njoki, L. Wang, and C. J. Zhong, "Nanocrystal and surface alloy properties of bimetallic Gold-Platinum nanoparticles," *Nanoscale Res. Lett.*, vol. 2, no. 1, pp. 12–16, 2007, doi: 10.1007/s11671-006-9022-8.

[8] F. Boccuzzi, E. Guglielminotti, F. Pinna, and G. Strukul, "Surface composition and reactivity of bimetallic Au-Pt /ZrO samples," *Surf. Sci.*, vol. 377, pp. 728–734, 1997.

[9] C. Mihut, C. Descorme, D. Duprez, and M. D. Amiridis, "Kinetic and Spectroscopic Characterization of Cluster-Derived Supported Pt – Au Catalysts," *J. Catal.*, vol. 212, no. 2, pp. 125–135, 2002, doi: 10.1006/jcat.2002.3770.

[10] M. Eyrich, T. Diemant, H. Hartmann, J. Bansmann, and R. J. Behm, "Interaction of CO with structurally well-defined monolayer PtAu/Pt(111) surface alloys," *J. Phys. Chem. C*, vol. 116, no. 20, pp. 11154–11165, 2012, doi: 10.1021/jp302469c.

[11] D. Mott, J. Luo, P. N. Njoki, Y. Lin, L. Wang, and C. Zhong, "Synergistic activity of gold-platinum alloy nanoparticle catalysts," *Catal. Today*, vol. 122, no. 3–4, pp. 378–385, 2007, doi: 10.1016/j.cattod.2007.01.007.

[12] M. Carosso *et al.*, "Gas phase vs. liquid phase: monitoring H2 and CO adsorption phenomena on Pt/Al2O3 by IR spectroscopy," *Catal. Sci. Technol.*, 2022, doi: 10.1039/d1cy02233d.

[13] Q. Wang, D. Tichit, F. Meunier, and H. Guesmi, "Combined DRIFTS and DFT Study of CO Adsorption and Segregation Modes in Pt-Sn Nanoalloys," *J. Phys. Chem. C*, vol. 124, no. 18, pp. 9979–9989, 2020, doi: 10.1021/acs.jpcc.0c01296.

[14] C. Lentz, S. P. Jand, J. Melke, C. Roth, and P. Kaghazchi, "DRIFTS study of CO adsorption on Pt nanoparticles supported by DFT calculations," *J. Mol. Catal. A Chem.*, vol. 426, pp. 1–9, 2017, doi: 10.1016/j.molcata.2016.10.002.

[15] Q. Zhang *et al.*, "In situ DRIFT spectroscopy insights into the reaction mechanism of CO and toluene co-oxidation over Pt-based catalysts," *Catal. Sci. Technol.*, vol. 9, no. 17, pp. 4538–4551, 2019, doi: 10.1039/c9cy00751b.

[16] H. Okamoto and TB. Massalski, "Phase Diagrams of Binary Gold Alloys," *ASM Int.*, 1987.

[17] X. Yang *et al.*, "An effective Pd-promoted gold catalyst supported on mesoporous silica particles for the oxidation of benzyl alcohol," *Appl. Catal. B Environ.*, vol. 140–141, pp. 419–425, 2013, doi: 10.1016/j.apcatb.2013.04.029.

[18] F. Gauthard, F. Epron, and J. Barbier, "Palladium and platinum-based catalysts in the catalytic reduction of nitrate in water: Effect of copper, silver, or gold addition," *J. Catal.*, vol. 220, no. 1, pp. 182–191, 2003, doi: 10.1016/S0021-9517(03)00252-5.

[19] R. A. (PhD Dissertation), "NO direct decomposition in the presence of excess oxygen over gold-based catalysts," 2021.

[20] R. Van Hardeveld and F. Hartog, "The statistics of surface atoms and surface sites on metal crystals," *Surf. Sci.*, vol. 15, no. 2, pp. 189–230, 1969, doi: 10.1016/0039-6028(69)90148-4.

[21] F. C. Meunier, R. Kdhir, N. Potrzebowska, N. Perret, and M. Besson, "Unravelling Platinum − Zirconia Interfacial Sites Using CO Adsorption," *Inorg. Chem.*, vol. 58, no. 12, pp. 8021--8029, 2019, doi: 10.1021/acs.inorgchem.9b00774.

[22] A. Garnier, S. Sall, F. Garin, M. J. Chetcuti, and C. Petit, "Site effects in the adsorption of carbon monoxide on real 1.8 nm Pt nanoparticles: An Infrared investigation in time and temperature," *J. Mol. Catal. A Chem.*, vol. 373, pp. 127–134, 2013, doi: 10.1016/j.molcata.2013.02.029.

[23] J. Raskó, "CO-induced surface structural changes of Pt on oxide-supported Pt catalysts studied by DRIFTS," *J. Catal.*, vol. 217, no. 2, pp. 478–486, 2003, doi: 10.1016/S0021-9517(03)00147-7.

[24] A. Bourane and D. Bianchi, "Heats of adsorption of the linear CO species on Pt/Al2O 3 using infrared spectroscopy: Impact of the Pt dispersion," *J. Catal.*, vol. 218, no. 2, pp. 447–452, 2003, doi: 10.1016/S0021-9517(02)00183-5.

[25] P. T. Fanson, W. N. Delgass, and J. Lauterbach, “Island formation during kinetic rate oscillations in the oxidation of CO over Pt/SiO2: A transient Fourier transform infrared spectrometry study,” *J. Catal.*, vol. 204, no. 1, pp. 35–52, 2001, doi: 10.1006/jcat.2001.3369.
[26] A. D. Allian *et al.*, “Chemisorption of CO and mechanism of CO oxidation on supported platinum nanoclusters,” *J. Am. Chem. Soc.*, vol. 133, no. 12, pp. 4498–4517, 2011, doi: 10.1021/ja110073u.
[27] A. Bourane, O. Dulaurent, and D. Bianchi, “Comparison of the coverage of the linear CO species on Pt/Al2O3 measured under adsorption equilibrium conditions by using FTIR and mass spectroscopy,” *J. Catal.*, vol. 195, no. 2, pp. 406–411, 2000, doi: 10.1006/jcat.2000.2962.
[28] A. Bourane, O. Dulaurent, and D. Bianchi, “Heats of adsorption of linear and multibound adsorbed CO species on a Pt/Al2O3 catalyst using in situ infrared spectroscopy under adsorption equilibrium,” *J. Catal.*, vol. 196, no. 1, pp. 115–125, 2000, doi: 10.1006/jcat.2000.3030.
[29] A. Bourane, O. Dulaurent, K. Chandes, and D. Bianchi, “Heats of adsorption of the linear CO species on a Pt/Al2O3 catalyst using FTIR spectroscopy: Comparison between TPD and adsorption equilibrium procedures,” *Appl. Catal. A Gen.*, vol. 214, no. 2, pp. 193–202, 2001, doi: 10.1016/S0926-860X(01)00483-5.
[30] Y. Jugnet, F. J. C. S. Aires, C. Deranlot, L. Piccolo, and J. C. Bertolini, “Surface Science Letters CO chemisorption on Au (1 1 0) investigated under elevated pressures by polarized reflection absorption infrared spectroscopy and scanning tunneling microscopy,” *Surf. Sci.*, vol. 521, no. 1–2, pp. L639–L644, 2002.
[31] D. C. Meier, V. Bukhtiyarov, and D. W. Goodman, “CO Adsorption on Au (110) - (1 × 2): An IRAS Investigation,” *J. Phys. Chem. B*, vol. 107, no. 110, pp. 12668–12671, 2003, doi: 10.1021/jp030499u.
[32] F. Vindigni, M. Manzoli, A. Chiorino, and F. Boccuzzi, “Catalytically active gold sites: Nanoparticles, borderline sites, clusters, cations, anions? FTIR spectra analysis of 12CO and of 12CO-13CO isotopic mixtures,” *Gold Bull.*, vol. 42, no. 2, pp. 106–112, 2009, doi: 10.1007/BF03214920.
[33] F. Menegazzo *et al.*, “Highly dispersed gold on zirconia: Characterization and activity in low-temperature water gas shift tests,” *ChemSusChem*, vol. 1, no. 4, pp. 320–326, 2008, doi: 10.1002/cssc.200700152.
[34] F. J. Cadete Santos Aires, C. Deranlot, Y. Jugnet, L. Piccolo, and J.-C. Bertolini, “METALLIC SURFACES UNDER ELEVATED GAS PRESSURE STUDIED IN SITU BY SCANNING TUNNELING MICROSCOPY: O 2 , H 2 /Au(111); CO/Au(110),” *B. N. Dev (Ed.), Proc. Int. Conf. Phys. Surfaces Interfaces, World Sci. Publ. Singapore*, no. lll, pp. 13–21, 2003, doi: 10.1142/9789812704221_0002.
[35] E. Roze, P. Gravejat, E. Quinet, J. L. Rousset, and D. Bianchi, “Impact of the reconstruction of gold particles on the heats of adsorption of linear CO species adsorbed on the au sites of a 1% Au/Al2O 3 catalyst,” *J. Phys. Chem. C*, vol. 113, no. 3, pp. 1037–1045, 2009, doi: 10.1021/jp8062838.
[36] S. Derrouiche, P. Gravejat, and D. Bianchi, “Heats of adsorption of linear CO species adsorbed on the Au° and Ti+δ of a 1% Au/TiO2 catalyst using in situ FTIR spectroscopy under adsorption equilibrium,” *J. Am. Chem. Soc.*, vol. 126, no. 40, pp. 13010–13015, 2004, doi: 10.1021/ja0470719.
[37] K. Ďckers, K. C. Prince, H. P. Bonzel, V. Chab, and K. Horn, “Adsorption-induced surface core-level shifts of Pt(110),” *Phys. Rev. B*, vol. 36, no. 12, pp. 6292–6301, 1987, doi: 10.1103/PhysRevB.36.6292.
[38] S. A. Tenney *et al.*, “Adsorbate-induced changes in the surface composition of bimetallic clusters: Pt-Au on TiO2(110),” *J. Phys. Chem. C*, vol. 114, no. 49, pp. 21652–21663, 2010, doi: 10.1021/jp108939h.
[39] B. J. Keene, “Review of data for the surface tension of pure metals,” *Int. Mater. Rev.*, vol. 38, no. 4, pp. 157–192, 1993, doi: 10.1179/imr.1993.38.4.157.
[40] M. Ruff, S. Frey, B. Gleich, and R. J. Behm, “Au-step atoms as active sites for COadsorption on Au and bimetallic Au/Pd(111) surfaces,” *Appl. Phys. A Mater. Sci. Process.*, vol. 66, no. SUPPL. 1, pp. 513–517, 1998, doi: 10.1007/s003390051193.
[41] J. Pischel and A. Pucci, “Low-Temperature Adsorption of Carbon Monoxide on Gold Surfaces: IR Spectroscopy Uncovers Different Adsorption States on Pristine and Rough Au(111),” *J. Phys. Chem. C*, vol. 119, no. 32, pp. 18340–18351, 2015, doi: 10.1021/acs.jpcc.5b05051.
[42] S. Y. Lee *et al.*, “Surface-rearranged Pd3Au/C nanocatalysts by using CO-induced segregation for formic acid oxidation reactions,” *ACS Catal.*, vol. 4, no. 8, pp. 2402–2408, 2014, doi: 10.1021/cs500227j.
[43] T. Elgayyar, R. Atwi, A. Tuel, L. Burel, Y. Schuurman, and F. C. Meunier, “Evidencing Pt-Au alloyed domains on supported bimetallic nanoparticles using CO desorption kinetics,” *Appl. Catal. A Gen.*, vol. 639, no. April, p. 118643, 2022, doi: 10.1016/j.apcata.2022.118643.

Conclusions and Perspectives

The goal of the "DecompNOx" project was the formulation of supported Au-based bimetallic nanoparticles active for NO direct decomposition below 500°C.

Throughout the project, several methods were used for the preparation of Pd-Au and Pt-Au bimetallic nanoparticles supported on several supports (namely SiO_2, LTA and Al_2O_3). SiO_2 and LTA-based catalysts were characterized and tested for the deNO_X activity to investigate the effect of alloying the active noble metals with Au. Al_2O_3-based catalysts were prepared and characterized by my colleague Ranin Atwi [1]. In this work, the samples were investigated for the CO adsorption/desorption kinetics by DRIFTS, as a means to characterize Pt-Au nanoalloys.

SiO_2-based monometallic Pd and Au and bimetallic Pd-Au nanoparticles (with Au/Pd molar ratio of 0.12 and 0.55) were prepared using the wet impregnation (the monometallic samples) and surface redox (the bimetallic samples) methods. The samples were characterized by ICP-OES, TEM-EDX and PXRD. The samples were also tested for the deNO_X catalytic activity. TEM analysis showed the formation of small Au nanoparticles (<5 nm) while the Pd-containing samples displayed the presence of a significant fraction of larger particles (10 nm). The TEM-EDX analysis of the bimetallic samples showed the presence of alloyed regions.

In situ and *ex situ* PXRD patterns were collected over the catalysts after calcination, reduction, and NO exposure. The samples initially displayed a poor crystallinity before any treatment. Au did not undergo an apparent change after any of the treatments. The calcination treatment lead to the full oxidation of Pd, while over the bimetallic samples, a $Pd_{0.2}Au_{0.8}$ alloy was observed after calcination which is resistant to oxidation. Heating to 450°C under H_2 lead to an increased crystallinity and a thermal lattice expansion of Pd, in addition to an increased alloying in the bimetallic samples.

Prior to the catalytic test, the catalysts were calcined under (NO + O_2) to remove the organic moieties used during the preparation. Then, the catalysts were regenerated by reduction in H_2 at 450°C and tested under NO at 450°C in the absence of O_2. Au was inactive. Pd showed a measurable activity and high N_2 selectivity, though continuously deactivated due to surface poisoning by the produced oxygen, while negligible PdO was observed by XRD. In contrast, the bimetallic samples displayed stable catalytic activities; albeit lower N_2 selectivities. Moreover, at the lower Au/Pd ratio, the activity was higher than that over the Pd sample. These observations suggested the protection of Pd against oxidation due to alloying with Au. However, increasing the Au loading lead to a lower catalytic activity and an enhanced N_2 selectivity, which was probably related to a decrease in the Pd dispersion

(the dilution of Pt). This suggested that the reaction probably proceeded via a NO dimer formation mechanism. The higher Au loading probably inhibited the dimer formation and enhanced the decomposition of the formed N_2O into N_2 and O_2.

LTA-based monometallic Pt and Au and bimetallic Pt-Au nanoparticles (with Au/Pt molar ratio of 2, 1, 0.5 and 0.25) were prepared by the simultaneous encapsulation of the metals during the preparation of the LTA structure. A Ca^{2+} ion exchange process was also performed so as to increase the pore size of the LTA structure. The samples were characterized by ICP-OES, TEM-EDX, PXRD, CO adsorption by DRIFTS. The samples were also tested for the deNO_X catalytic activity. The LTA structure was evidenced by XRD. TEM showed the presence of well dispersed nanoparticles of the order of 2-3 nm in diameter encapsulated in the LTA structure. The post-preparation treatments were not successful at removing S and Cl used during the preparation.

All the samples displayed the CO adsorption on -OH groups and/or Ca^{2+} ions of the basic LTA support. Pt adsorbed CO mostly linearly, in addition to some bridge adsorption. The Au sample displayed a linear CO adsorption on Au atoms. The bimetallic sample (with the Au/Pt molar ratio of 2) displayed all adsorption bands observed with the two monometallic samples and the LTA support. The sample also featured the dilution of Pt by the excess Au. Some CO_2 was formed over the metals possibly via Boudouard reaction or WGS.

All the samples displayed deactivation under NO at 350°C, possibly due to the oxidation of Pt by NO or due to the observed residual S and Cl. The bimetallic samples displayed lower NO conversions than the monometallic Pt sample. Apparently, the presence of Au did not enhance the activity in the bimetallic samples. Moreover, the possible pore blockage due to adsorbed carbonates or nitrates might limit the accessibility of the metals. The use of such material is apparently challenging and requires extra precautions so as to avoid the deactivation observed.

Al_2O_3-based monometallic Pt and Au and bimetallic Pt-Au nanoparticles (with Au/Pt molar ratio of 0.14 and 1.1) were prepared (by wet impregnation or co-impregnation), characterized (by ICP-OES and TEM-EDX), and tested for the deNO_X activity by my colleague Ranin Atwi. In this work, the samples were investigated for the CO adsorption/desorption kinetics by DRIFTS. TEM analysis indicated the formation of mostly small nanoparticles (<4 nm diameter) in all samples. TEM-EDX analysis indicated the presence of alloyed regions in the bimetallic samples. Au displayed a limited and weak linear CO adsorption, and a significant formation of carbonates possibly via Boudouard or WGS reaction. Pt displayed a high tendency towards the linear CO adsorption. After stopping CO, the Pt L-CO band was stable while Pt B-CO gradually decayed.

The bimetallic sample displayed a blue shift in Pt L-CO, suggesting that Au would preferably be located on low coordination sites of the Pt surface. The limited bridge adsorption also indicated the dilution of Pt by Au. The decay of the CO adsorption bands over the bimetallic sample was faster than that observed over the Pt sample. This could indicate a weaker CO adsorption on Pt due to alloying with Au. By this work, we managed to use monitoring CO adsorption/desorption kinetics to characterize Au-Pt nanoalloys.

In addition to the promising catalytic results obtained over the silica-based catalysts, interesting results were obtained during the characterization performed on the catalysts. We were able to publish four articles in peer-reviewed journals:

1- **Contributions and limitations of IR spectroscopy of CO adsorption to the characterization of bimetallic and nanoalloy catalysts** [2]**.**
2- **Au-Modified Pd catalyst exhibits improved activity and stability for NO direct decomposition** [3]**.**
3- **Evidencing Pt-Au alloyed domains on supported bimetallic nanoparticles using CO desorption kinetics** [4]**.**
4- **Stability of Pt-adsorbed CO on catalysts for room temperature oxidation of CO** [5]**.**

As a matter of fact, we had published another article discussing the restructuring of Au nanoparticles under CO [6]. However, we had to retract this paper since we were not able to reproduce our results after changing the DRIFTS cell which was found to have corroded. We discovered that the evolution of the adsorption profile over Au was merely due to Ni contamination from the corroded cell material. CO lead to the formation of $Ni(CO)_4$ which was deposited on the catalyst and was also detected in the effluent gas. This finding was also consistent with what was recently reported elsewhere [7]. Therefore, we also submitted a retraction note [8] to the publishing journal stressing the major data misinterpretation that could result from the possible contaminations in the feed. Such an observation would be of great importance for several groups working on CO adsorption on metals.

This work has proven the ability of alloying Au with noble metals (Pd) to promote their activity towards direct NO_X decomposition below 500°C. However, the best activity achieved is still limited compared to other catalytic substances reported in the literature such as Cu-ZSM5. Therefore, other formulations and/or activation methods need also to be considered.

For instance, further investigation of the significance of (Au/noble metal) atomic ratio could lead to a better catalyst. Moreover, performing the reaction under UV or visible light could be of great advantage while using titania as support which exhibits excellent photocatalytic activity. Pd-Au/TiO_2

were reported to be active photocatalysts under visible light for benzyl alcohol oxidation [9]. Also, other noble metals such as Pt or Rh could prove more active than Pd. Furthermore, using termetallic catalysts could also be beneficial. Such catalysts would comprise the active noble metal, Au for oxidation resistance, and another metal with a better N adsorption (which is poor over noble metals) that would lead to better NO decomposition as suggested earlier [10]. Most importantly, carrying out operando NO adsorption by DRIFTS over the catalysts could be highly informative regarding the catalyst active sites and structure evolution under NO.

References

[1] R. A. (PhD Dissertation), "NO direct decomposition in the presence of excess oxygen over gold-based catalysts," 2021.

[2] T. Elgayyar, R. Atwi, A. Tuel, and F. C. Meunier, "Contributions and limitations of IR spectroscopy of CO adsorption to the characterization of bimetallic and nanoalloy catalysts," *Catal. Today*, vol. 373, pp. 59–68, 2021, doi: 10.1016/j.cattod.2021.01.009.

[3] T. Elgayyar *et al.*, "Au-Modified Pd catalyst exhibits improved activity and stability for NO direct decomposition," *Catal. Sci. Technol.*, vol. 11, no. 8, pp. 2908–2914, 2021, doi: 10.1039/d1cy00301a.

[4] T. Elgayyar, R. Atwi, A. Tuel, L. Burel, Y. Schuurman, and F. C. Meunier, "Evidencing Pt-Au alloyed domains on supported bimetallic nanoparticles using CO desorption kinetics," *Appl. Catal. A Gen.*, vol. 639, no. April, p. 118643, 2022, doi: 10.1016/j.apcata.2022.118643.

[5] F. C. Meunier, T. Elgayyar, K. Dembélé, and H. Kaper, "Stability of Pt-Adsorbed CO on Catalysts for Room Temperature-Oxidation of CO," *Catalysts*, vol. 12, no. 5, pp. 1–12, 2022, doi: 10.3390/catal12050532.

[6] R. Atwi, T. Elgayyar, F. J. Cadete Santos Aires, A. Tuel, and F. C. Meunier, "Revisiting the Evolution of IR Spectra of CO Adsorbed on Au Nanoparticles Supported on Non-reducible Supports," *Top. Catal.*, vol. 63, no. 15–18, pp. 1596–1605, 2020, doi: 10.1007/s11244-020-01372-2.

[7] Y. Yao, L. Chen, X. Mao, Y. Yang, J. Chen, and L. Zhou, "In Situ PM-IRRAS Study of CO Adsorption on Au Surfaces: Solving the Puzzle," *J. Phys. Chem. C*, vol. 125, no. 16, pp. 8606–8619, 2021, doi: 10.1021/acs.jpcc.1c01638.

[8] R. Atwi, T. Elgayyar, F. J. Cadete Santos Aires, A. Tuel, and F. C. Meunier, "Retraction Note to: Revisiting the Evolution of IR Spectra of CO Adsorbed on Au Nanoparticles Supported on Non-reducible Supports," *Top. Catal.*, vol. 64, no. 17–20, pp. 1054–1055, 2021, doi: 10.1007/s11244-021-01467-4.

[9] T. Jiang *et al.*, "Gold and gold-palladium alloy nanoparticles on heterostructured TiO2 nanobelts as plasmonic photocatalysts for benzyl alcohol oxidation," *Nanoscale*, vol. 7, no. 1, pp. 209–217, 2015, doi: 10.1039/c4nr05905k.

[10] H. Falsig, T. Bligaard, J. Rass-Hansen, A. L. Kustov, C. H. Christensen, and J. K. Nørskov, "Trends in catalytic NO decomposition over transition metal surfaces," *Top. Catal.*, vol. 45, no. 1–4, pp. 117–120, 2007, doi: 10.1007/s11244-007-0250-7.

List of figures

List of tables